The prompt emission of Gamma-Ray Bursts : analysis and interpretation of Fermi observations

Manal Yassine

▶ **To cite this version:**

Manal Yassine. The prompt emission of Gamma-Ray Bursts : analysis and interpretation of Fermi observations. High Energy Astrophysical Phenomena [astro-ph.HE]. Université Montpellier, 2017. English. NNT : 2017MONTS006 . tel-01739257

HAL Id: tel-01739257

https://theses.hal.science/tel-01739257

Submitted on 20 Mar 2018

HAL is a multi-disciplinary open access archive for the deposit and dissemination of scientific research documents, whether they are published or not. The documents may come from teaching and research institutions in France or abroad, or from public or private research centers.

L'archive ouverte pluridisciplinaire **HAL**, est destinée au dépôt et à la diffusion de documents scientifiques de niveau recherche, publiés ou non, émanant des établissements d'enseignement et de recherche français ou étrangers, des laboratoires publics ou privés.

Thesis

To obtain the grade of

Doctor

Delivred by the **University of Montpellier**

Prepared within the doctoral school **I2S**
and the research unity **UMR 5299**

Speciality : **Physics**

Presented by **Manal Yassine**

The prompt emission of Gamma-Ray Bursts: analysis and interpretation of *Fermi* observations

Defended on Septembre 11, 2017 in front of the jury composed by :

Mrs.	Ana Palacios	**President**
Mrs.	Sheila McBreen	**Referee**
M.	Diego Götz	**Referee**
Mrs.	Valerie Connaughton	**Examiner**
M.	Bertrand Cordier	**Examiner**
M.	Francesco Longo	**Examiner**
M.	Frédéric Piron	**Supervisor**

Contents

Remerciements

Déjà trois ans sont passées pour réaliser ce travail de thèse... Ils ont été très courts pour achever tout ce que je pensais faire, mais aussi longs en ces moments de stress, de travail et de challenge. A la fin de cet effort, je recueille le fruit de mon travail, mais je n'aurais pas eu la chance d'en arriver là sans le soutien de beaucoup de personnes que j'ai rencontrées durant cette période. Je remercie d'abord Frédéric Piron, mon directeur de thèse, pour sa disponibilité, sa patience, sa responsabilité qu'il a gardé jusqu'au dernier moment de correction de mon manuscrit. J'ai appris beaucoup grâce à toi Fred, tant au niveau professionnel qu'au niveau personnel. Je te remercie aussi de m'avoir donné l'occasion de faire partie de la collaboration international Fermi. Je souhaite aussi remercier Denis Puy, directeur du LUPM, pour sa gentillesse, ses conseils et ses conversations régulières avec nous les doctorants et en nous incluant au laboratoire de façon active.

Un grand merci aux membres de jury qui ont accepté d'examiner mon manuscrit. Merci à Diego Götz et Sheila McBreen pour avoir accepté d'être rapporteurs et pour tous leurs commentaires complémentaires. Je souhaite aussi remercier Valérie Connaughton, Francesco Longo, Anna Palacios et Bertrand Cordier pour avoir accepté de faire partie du jury.

Je tiens à remercier toutes les personnes du service administratif du laboratoire, en particulier Amel, Sylviane, Lydie, Carole et Denis Cortes. Sans oublier le service informatique, je remercie d'abord Nicolas ainsi que Samuel qui m'ont aidée à résoudre des problèmes techniques et informatiques et à utiliser les machines virtuelles du Cloud. Je remercie aussi Stéphane pour sa disponibilité pour résoudre mes problèmes d'installation de logiciels, ainsi que Claude, Joris, Michèle, Luisa pour leurs gentillesse et leurs aides complémentaires.

Je n'oublie pas tous les membres des équipes du laboratoire "EMA", "AS" et

"IFAC" pour leur gentillesse et pour les discussions ainsi que pour les moments de détente et de joie passés ensemble lors de pots conviviaux organisés au laboratoire. Bon courage aux thésards actuels du LUPM: Benjamin, Justine, Duncan, Ronan, Martin et Michelle. Merci à ma collègue de bureau Grazia pour les beaux moments passés ensemble pendant deux ans et pour les expressions italiennes que tu m'as apprises de temps en temps! Je te remercie aussi pour nos discussions au niveau personnel, ainsi pour ton aide dans la recherche des solutions à mes questions sans fin. Je n'oublie pas non plus Johann, avec qui j'ai partagé un bureau durant la première année, et qui m'a aidé au début de ma thèse à comprendre les techniques d'analyse.

En tant que membre de la collaboration Fermi, j'ai eu la chance d'avoir des discussions intéressantes avec des spécialistes du domaine. Je tiens à remercier tous les membres du groupe "sursauts gamma" de la collaboration et plus particulièrement Giacomo et Nicolas qui n'ont pas hésité à répondre à mes questions par mails.

J'adresse un grand merci à mon amie Rihab, qui est comme ma soeur et qui m'a accompagnée pendant ma première année à l'étranger. Merci pour tous tes conseils qui m'ont servi non seulement en master mais aussi durant la thèse même s'il nous était difficile de nous retrouver pendant ces dernières années. Je te remercie pour avoir effectué un long trajet pour assister à ma soutenance.
Je t'envoie un grand coucou Johanna! Je n'oublierai jamais les petits quarts d'heure que nous avons pris presque chaque matin pour discuter de tout! Je te remercie pour tes conseils, ton aide et je te souhaite plein de succès dans ta vie personnelle ainsi que professionnelle! Tu le mérites bien! Je remercie d'ailleurs le groupe Fermi qui m'a permis de rencontrer de nouveaux amis! Merci Soheila pour les jolis moments passés ensemble lors d'une réunion du groupe, et pour la merveilleuse amitié qu'on garde malgré la grande distance! J'adresse un spécial et grand merci à mon mari qui a supporté avec moi les moments de stress et d'inquiétude les plus durs durant toute la thèse et surtout durant la période de réalisation de ce manuscrit. Tu m'as donné le courage de faire cette thèse et m'as aidé à dépasser les difficultés malgré l'occupation de ta thèse. Merci pour tous les bons moments que nous avons passés ensemble à apprendre, découvrir, voyager, nous amuser et rêver d'un joli futur.

Par dessus tout je voudrais remercier mes parents qui nous ont appris à moi et toute la famille la façon de parcourir les difficiles chemins vers le succès. Un chaleureux merci à vous ma mère et mon père! Pour toutes mes soeurs que j'aime du fond de mon coeur, je vous souhaite une pleine réussite dans vos vies personnelles et professionnelles. Pour toi mon frère, je te souhaite bonne chance dans ton projet pour devenir un brillant médecin.
J'espère n'avoir oublié personne...

Introduction

I performed my thesis work in the "Laboratoire Univers et Particules de Montpellier" (LUPM, CNRS/IN2P3) within the "Expériences et Modélisation en Astroparticules" (EMA) team. The members of the EMA team conduct their research in the field of gamma-ray astronomy with an expertise in the observation, analysis and modeling of celestial gamma-ray sources, in relation with the acceleration and propagation of cosmic rays. The researchers of the EMA team are involved in international collaborations that exploit ground or space-based instruments, like *Fermi* and HESS. The future projects of the team include the CTA (Cherenkov Telescope Array) and the SVOM (Space Variable Objects Monitor) mission, which is dedicated to the study of Gamma-Ray Bursts.

The Gamma-Ray Burst (GRB) field is a domain of modern gamma-ray astronomy, which evolves rapidly. Discovered fifty years ago, GRBs are very energetic and brief flashes of high-energy radiations which are emitted in a short time scale (fraction of a second to several minutes). The GRB bright emission is thought to be powered by a newly formed stellar-mass black hole that is accompanied by a collimated outflow (i.e. a jet) moving at a relativistic speed. The emission is observed as two successive phases: the high energy "prompt" phase and the late and less luminous "afterglow" phase. Understanding the GRB high-energy emission is one of the scientific goals of the *Fermi* mission.

The *Fermi* observatory was launched by the NASA in 2008 and it is still in operation. It carries two instruments which were constructed by two international collaborations that are comprised of research institutions in the United States, in Europe and in Japan. Together, its two instruments, the GBM (Gamma-ray Burst Monitor) and the LAT (Large Area Telescope), cover seven decades in energy (8 keV - 300 GeV). Thanks to the high performance of the LAT telescope, it becomes possible to study the GRB properties at high energies, which were difficult to iden-

tify and to characterize by previous instruments. Based on the experience gained since launch, the LAT collaboration released publicly a new set of data in June 2015. These data, called Pass 8, were generated using improved algorithms of reconstruction and classification of gamma-ray events.

The main topic of my thesis is the study of the spectral and temporal properties of the prompt emission phase of the Gamma-Ray Bursts observed by *Fermi*. Quantifying how the LAT Pass 8 data, especially in the sub-100 MeV energy range, improve the quality of GRB spectral reconstruction is one of the goals of my thesis. The interpretation of the observed properties of the GRB prompt phase using theoretical and physical models constitutes the main objective of my work.

As a full member of the LAT collaboration and of the *Fermi* GRB group, I contributed to several common efforts. In particular, I used the LAT Pass 8 data to analyze and localize new GRB candidates in real time. I performed this "Burst Advocate" activity several times during the three years of my thesis.

GRB 090926A is a very bright burst with unique properties and it was jointly detected by the GBM and the LAT from keV energies up to the GeV domain. I characterized the extreme variability of its prompt emission, and I performed a detailed time-resolved analysis of its broadband spectrum, focusing on the spectral break observed at GeV energies. I discuss the theoretical implications of the characteristics of this GRB in the framework of the internal shock model that has been developed by collaborators from the "Institut d'Astrophysique de Paris" (IAP).

The spectral models that are usually employed to characterize GRB prompt spectra are based on phenomenological or mathematical functions. However, understanding the physical processes at work in GRB jets requires the comparison of their spectral and temporal properties with dedicated theoretical models. For this purpose, I made use of the IAP internal shock model, which simulates the GRB jet dynamics and the radiation from a population of shock-accelerated electrons. I explored this physical model and proposed a new parametric function, which is representative of the model and can be used as a proxy to fit the keV-MeV spectrum of GRBs. Using this function, I compared the predictions of the IAP model to a large sample of GBM-detected GRBs, including GRB 090926A.

This thesis manuscript is organized as follows. The properties of GRBs that have been revealed since their discovery are presented in chapter 1. This chapter describes also the main ingredients of the physical scenarios that are being investigated by the GRB community, and it gives a brief overview of the GRB observations with the actual and the future GRB multi-wavelength and multi-messenger telescopes. The design of the two *Fermi* instruments and their performance are described in chapter 2. Chapter 3 deals with the detection and localization techniques that

are implemented in the on-board and on-ground analyses of GRBs with the GBM and the LAT. The spectral analysis methods are also described in this chapter. Chapter 4 explains how the "Burst Advocate" on-duty activities are organized in the *Fermi* GRB group. This chapter shows my contribution of general interest for this group. Chapter 5 presents the in-depth analysis and the interpretation of the prompt emission of the remarkable GRB 090926A. Finally, the IAP internal shock model is explored and compared with observations in chapter 6.

CHAPTER 1

Gamma-ray bursts: the most powerful explosions in the Universe

Contents

1.1 Introduction

Gamma-Ray Bursts (GRBs) are the most powerful explosive events ever observed in the known Universe. They are brief flashes of high-energy radiations, which release an energy amount of 10^{51-55} erg (assuming an isotropic emission) in a short time scale (fraction of seconds to several minutes). This energy is equivalent to hundred times the total electromagnetic energy radiated by a supernova ($\sim$ to the energy that our Sun would radiate during its entire lifetime). Redshift measurements of some GRBs confirmed the extragalactic origin of these objects making them the most luminous events in the Universe and one of the most major astrophysical scientific topics nowadays.
This chapter aims at introducing the Gamma-Ray Bursts. Sect.1.2 shows a brief historical overview of GRB observations in pre-*Fermi* era. Their phenomenology as well as the theoretical interpretations based on their observations are presented in Sect.1.3 and 1.4 respectively. Finally, Sect.1.5 is dedicated to presenting a detailed review of the *Fermi* observations especially at high energy.

1.2 A brief history of GRB observations

1.2.1 The early times

GRBs were first discovered in the second half of the 1960's by the *Vela* satellites. These satellites had been launched by the American National Aeronautics and Space Administration (NASA) following the *Test Ban Treaty* signed with the Soviet Union and the United Kingdom in 1963, which prohibited nuclear weapon tests in the atmosphere, in outer space and under water. *Vela* consisted of a series of 12 satellites equipped with X-ray (3-12 keV) and γ-ray (0.2-1.5 MeV) detectors. Each pair of satellites was placed on the same orbit in opposite orbital positions (see a pair of satellites in Fig.1.1, left panel) ensuring a complete view of the globe.

While searching the Earth atmosphere for gamma-ray and neutron radiations that could be emitted by nuclear weapons, *Vela* detected an intense and brief flash of gamma rays on July 2, 1967. The direction of the emitting source was estimated using the triangulation technique with a precision of order of tens of degrees (see more details in Fig.1.2). The source direction excluded an origin from the Earth or the Sun. Together, these results revealed a new type of gamma-ray flashes of cosmic origin. After this discovery and during its 10-year operation period, *Vela* recorded 73 similar flashes, called later "Gamma Ray Bursts (GRBs)", confirming their natural and extra-terrestrial origin. The announcement of the first burst detected by *Vela*, called GRB 670702[1], was published for the first time in 1973 [Klebesadel et al., 1973].

[1]The name of a GRB consists of its detection date yy/mm/dd. Later, a letter A, B, C, .. was added to the GRB name to report if the burst was the first, second, third, .. detected during the

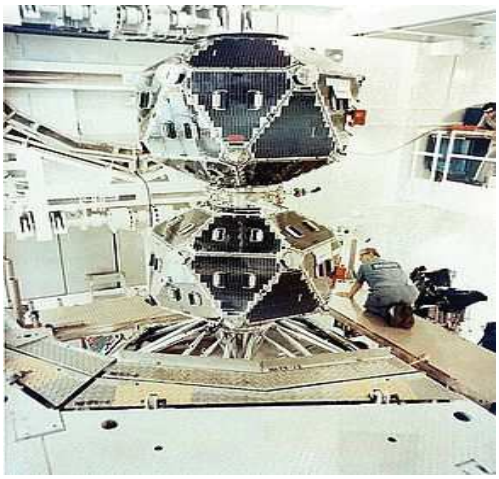

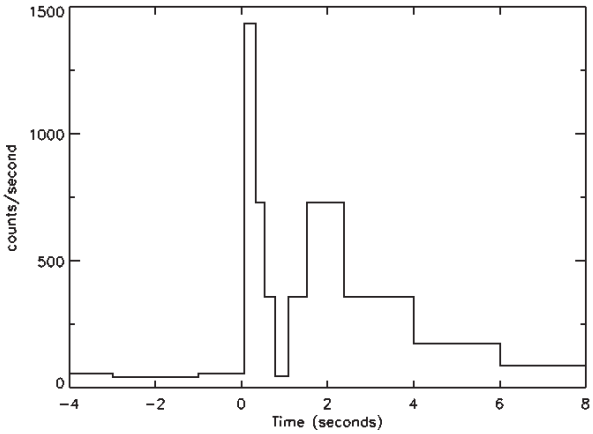

Figure 1.1: ***Left:*** *The twin satellites Vela-5A and Vela-5B in a clean room (from HEASARC [2003a]). In space, the two satellites were placed on opposite sides of the Earth (∼118 000 km orbit radius).* ***Right:*** *Count light curve of GRB 670602 [Bonnell, 1995].*

The Soviet satellites and the Inter-Planetary Network

By the end of 1978, a scientific cooperative Soviet-French program, called "Signe 2M" [Niel et al., 1976], was launched aiming to search for GRBs and to perform accurate localizations, with a precision of $\sim 5'$ based on the triangulation technique [Estulin et al., 1981]. This experiment offered the possibility of obtaining a more accurate determination of the GRB positions by increasing the spacing of the satellites. However, this strategy has a disadvantage of the long waiting time needed for collecting data from the distant satellites. In this case, notifying the detection information to other instruments took at least a few days following the GRB detection.

The Signe 2M experiment was based on the observations of the three Soviet satellites Venera-11, Venera-12 (each of which orbiting Venus) and Prognoz-7 (orbiting the Earth) covering an energy range of 20 keV - 1 MeV. Initially launched to explore the Venus atmosphere, each of the two Venera satellites carried two γ-ray detectors. Prognoz-7 was one of a series of 12 satellites launched initially to monitor the solar activity and emission in X rays and γ rays.

Soon, the first Inter-Planetary Network (*IPN*, [Hurley et al., 2003]) was organized, collecting data from the 3 Soviet satellites of the Signe 2M experiment, the German satellite "Helios 2" (orbiting the Sun), and the NASA's Pioneer Venus Or-

current day.

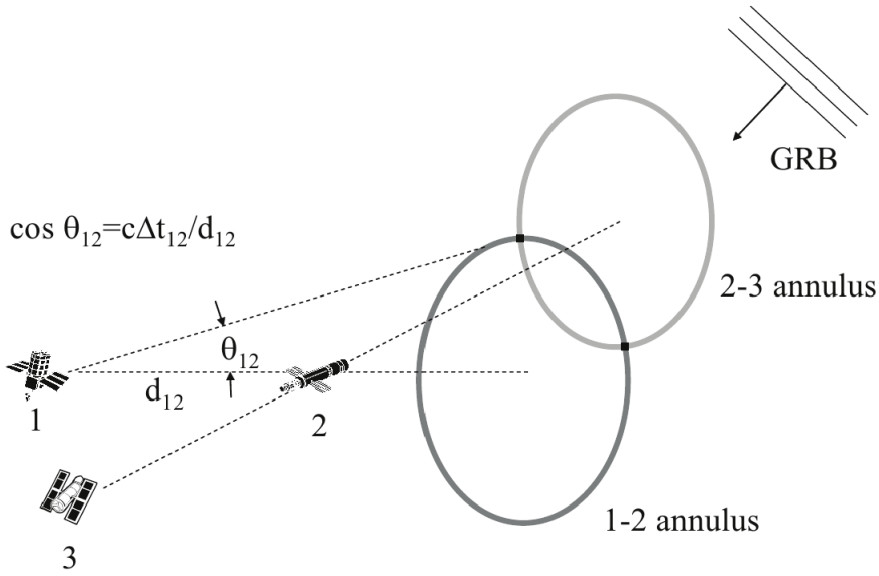

Figure 1.2: *The localization of a celestial source by the triangulation technique is based on the delay (Δt) in the photon arrival times measured by different satellites, combined with their relative distances (d). Each pair of satellites provides a localization annulus with an opening angle θ such that $\cos(\theta)=c\Delta t/d$. The intersection of the two annuli obtained with three satellites provides two possible directions. A fourth satellite is required to select the final position.*

biter, in addition to the *Vela* satellites. Interestingly, the observations of these satellites over the period 1978-1980 started to reveal the diversity of the GRB temporal profiles [Estulin et al., 1981]. The most important result from the *IPN* observations was the discovery of the isotropic distribution of the GRBs in the celestial sphere based on a sample of 82 *IPN* GRBs [Atteia et al., 1987].

The Burst And Transient Source Experiment

Launched in 1991 by the NASA, the *Compton Gamma Ray Observatory* (*CGRO*[2]) carried four instruments covering a wide energy range, with improved sensitivity with respect to past experiments: *OSSE* (*Oriented Scintillation Spectrometer Experiment*, 100 keV - 10 MeV), *COMPTEL*[3] (*Compton Telescope*, 1 MeV - 30 MeV), *BATSE* (*Burst and Transient Source Experiment*, 20 keV - 2 MeV), and *EGRET* (*Energetic Gamma Ray Experiment Telescope*, 20 MeV - 30 GeV).

The *BATSE* [Fishman et al., 1992] instrument was dedicated to the monitoring of the high-energy transient sky and, more specifically, to the search for GRBs. *BATSE*

[2] https://heasarc.gsfc.nasa.gov/docs/cgro/cgro.html
[3] https://heasarc.gsfc.nasa.gov/docs/cgro/cgro/comptel.html

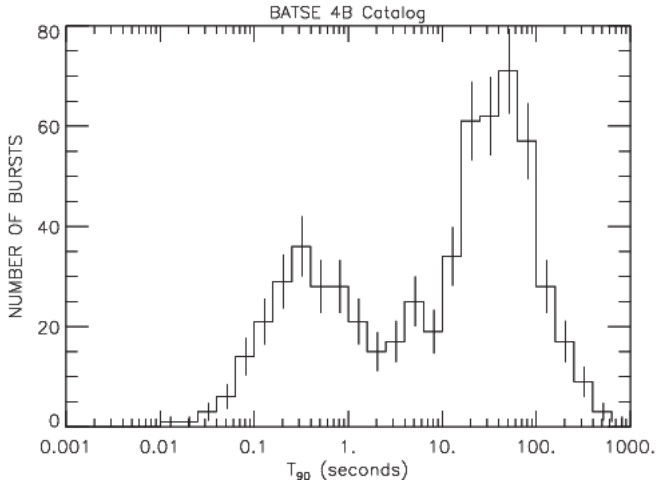

Figure 1.3: *Distribution of GRB duration in the BATSE 4th catalog [Meegan et al., 1996]*

consisted of eight detecting modules placed at the eight corners of the satellite with different orientations, allowing to cover a wide field of view of $\leq 4\pi$ sr (i.e., the entire sky that is not occulted by the Earth) and to localize GRBs with a few degree accuracy. Each detecting module included two NaI(Tl) scintillators: a Large Area Detector (2025 cm^2 $\times$ 1.27 cm) to observe in the 40 keV - $\sim$ 2 MeV energy range, and a Spectroscopic Detector (127 cm^2 $\times$ 7.62 cm) to observe in the 0.015-20 MeV energy range. Thanks to its unprecedented sensitivity, *BATSE* detected $\sim$ 2700 bursts during its 9-year lifetime ($\sim$ 1 GRB/day). Based on a large sample of 1005 *BATSE* GRBs, Briggs et al. [1996] firmly established the isotropic distribution of these sources on the celestial sphere.

Before the first observations of GRB afterglows by *BeppoSAX* (see further below), the distance scale of GRBs was unknown. During the first years of the *BATSE* era, considering GRBs as galactic sources was a viable possibility, while others preferred to place them at cosmological distances. The galactic models explained the GRB phenomena as the ones observed on the surface of neutron stars (NS[4]) [Hurley, 1986]. The brief lifetime of GRBs was indeed compatible with the characteristics of such compact objects emitting at high energies. The claim for the existence of cyclotron lines in the spectra of some GRBs by [Mazets et al., 1981], reinforced a few years later by Ginga observations [Fenimore et al., 1988; Murakami et al., 1988], provided support for the NS paradigm. The existence of these lines implies a mag-

[4]NSs are the compact cores of dead massive stars under the gravitational collapse of the stars at the end of their life. They are the densest and smallest stars known to exist in the Universe with a radius of only about 12-13 km and a very large density of roughly $\sim 10^{14}$ times the density of the Sun.

netic field of order $\sim 10^{13}$ Gauss, which is one of the characteristics of magnetized NS surfaces. However, these lines were never confirmed by the *BATSE* observations [Palmer et al., 1994].

In the same period, *BATSE* confirmed the isotropic distribution of GRBs on the celestial sphere, which reinforced the extragalactic scenarios for their origin. However, galactic scenarios, e.g. involving a large galactic halo, remained viable until 1997. This question motivated the organization of a "Great Debate on the distance scale to Gamma-Ray Bursts" in 1995[5], which revealed the preference of the astronomical community for the second class of scenarios. Actually, even before measuring the redshift of the GRBs, it was possible to seek their origin based on their density distribution and using the V/Vmax test. This test constrains the radial distribution of a population of objects within the volume that is probed by the instruments, due to their limited flux sensitivity. For a uniform distribution in a local volume, V/Vmax has a uniform distribution between 0 and 1 with $\langle V/V_{max} \rangle = 0.5$ [Schmidt et al., 1988]. This average value is less than 0.5 for a non uniform distribution and/or a cosmological distribution. With the increase of the number of the bursts detected by *BATSE*, the γ-ray flux distribution did not show a uniform distribution but rather a decreasing density of GRBs at large distances. Specifically, Meegan et al. [1992] found $\langle V/V_{max} \rangle = 0.348 \pm 0.024$. This lack of faint GRBs, along with the good flux sensitivity of *BATSE*, strongly disfavored the galactic scenarios, yet it could not firmly confirm the extragalactic origin of GRBs. A larger halo than that of the Galaxy had to be invoked to cover the total distribution of GRBs.

Another important result from the *BATSE* experiment was the classification of GRBs in two different categories, which was the first step in understanding their characteristics. Using *BATSE* data over only 2-year period, Kouveliotou et al. [1993] established the bimodality of the GRBs based on their duration. Dezalay et al. [1992] distinguished a subset of short GRBs among a sample of GRBs that were detected by the French-Soviet PHEBUS experiment[6]. Introducing a new notation T_{90}[7], which is the time interval over which 90% of the radiation is recorded in a given energy range, this study showed two distinct classes with a separation at $\sim$2 seconds: a population of short GRBs (SGRBs) with an average duration of about 0.3 s and a larger population of long GRBs (LGRBs) with an average duration of about 30 s.

[5] The first astronomical debate occurred in 1920 between H. Curtis and H. Shapley about the "Scale of the Universe". H. Curtis argued that the Universe is composed of many galaxies like our own, however, Shapley claimed that it is composed of only a big galaxy where we are belonging. Seventy five years later, B. Paczynski and D. Q. Lamb debated "The distance scale of the GRBs" in the same auditorium where the first debate has been organized. During this conference, B. Paczynski argued for a cosmological origin of GRBs while D. Q. Lamb defended the galactic scenario (see more in `https://apod.nasa.gov/debate/debate95.html`)

[6] Instrument onboard the GRANAT telescope which was launched in 1989 aiming to observe the Universe in the X-ray and γ-ray energy ranges (see HEASARC [2004] for more details).

[7] T_{90} is the time interval which includes 5% to 95% of the integrated burst counts.

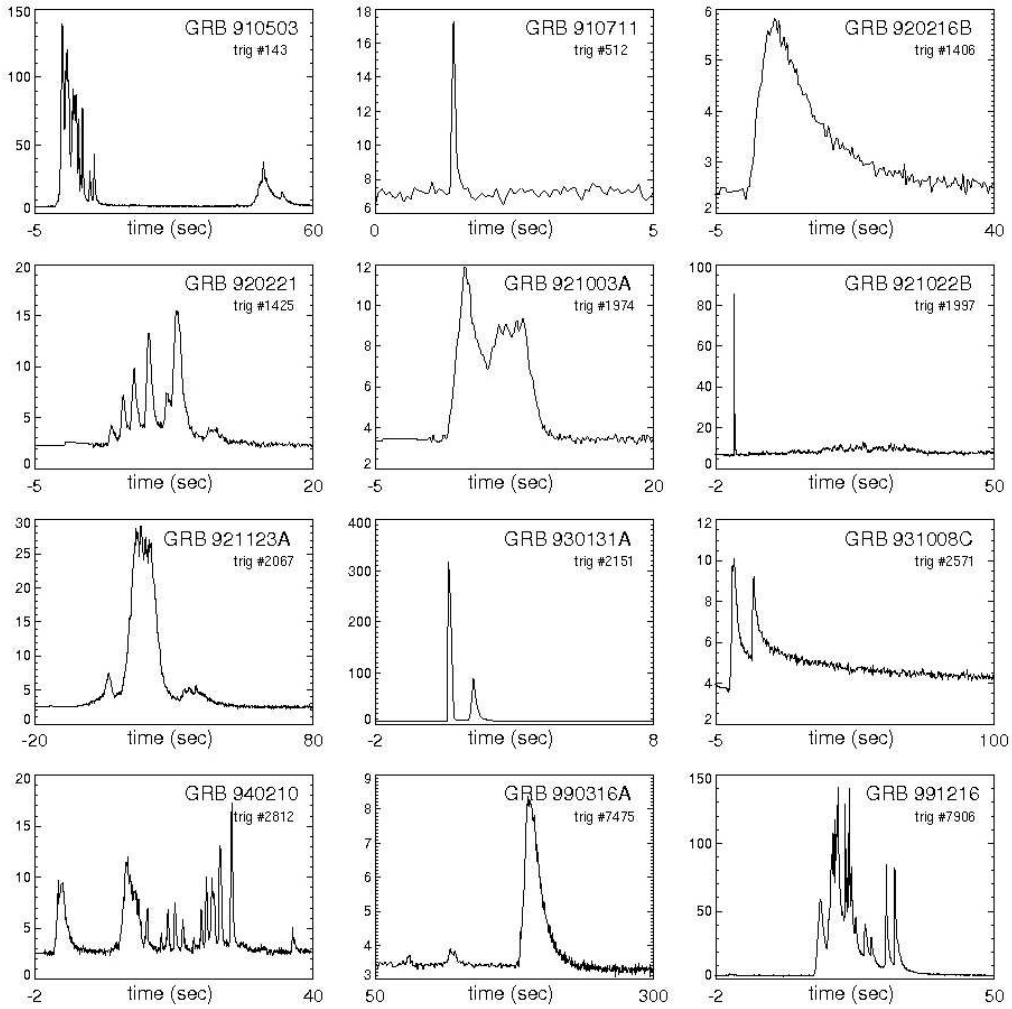

Figure 1.4: *BATSE light curves of selected GRBs. From HEASARC [2003b].*

This result was confirmed later using the *BATSE* 4th GRB catalog (see Fig.1.3)

Furthermore, the large sample of *BATSE* GRBs revealed the diversity of their temporal properties. The light curves of *BATSE* GRBs showed different variability time scales, ranging from milliseconds to minutes. Some GRBs had an isolated peak in their time profile showing a fast rise followed by an exponential decay. Whilst others showed multiple peaks with extreme variability (see Fig.1.4). These observations also revealed that the spectra of GRBs are non-thermal, evolving with time from hard to soft, with a peak energy of the spectral energy distribution (E_p) of several hundred keV. These keV-MeV spectra are well reproduced by the phenomenological `Band` function [Band et al., 1993], which consists of two smoothly-connected power laws and is often attributed to the synchrotron emission from shock-accelerated elec-

trons. These characteristics and others of the early emission phase of GRBs will be discussed in details in Sect.1.3.1.

Despite the success of *BATSE* in establishing key characteristics of GRBs, a rapid and accurate localization of GRBs was not possible with its instrumentation. Its large error box ($> 4°$) around the estimated position of the detected burst, made follow-up observations difficult by other instruments searching for counterparts at larger wavelengths.

1.2.2 The afterglow era

BeppoSAX

This localization issue was solved with the launch of the Italian-Dutch satellite *BeppoSAX* in 1996 [Boella et al., 1997]. *BeppoSAX* satellite carried on board a set of instruments called *NFIs* (*Narrow Field Instruments*, 0.1-300 keV) as well as the *WFC* (*Wide Field Cameras*, 2-26 keV) which were both used to monitor GRBs [Boella et al., 1997]. The *NFIs* consisted of Medium Energy Concentrator Spectrometers (MECS), Low Energy Concentrator Spectrometer (LECS), High Pressure Gas Scintillation Proportional Counter (HPGSPC) and Phoswich Detector System (PDS). They were devoted to long observations, looking at the same direction in the sky with a field of view of about 1.5°. The four lateral active shields of the PDS were used as gamma-ray burst monitor (*GRBM*) dedicated to observe in the γ energy range, 40-700 keV [Boella et al., 1997]. The *GRBM* was composed of four identical CsI(Na) scintillators, with a total effective area of 4400 cm^2 and with an open field of view, including the *WFC* field of view. This instrument had poor localization capabilities, and could only provide rough source positions. The *WFC* instrument consisted of two cameras pointed at opposite directions, with a 40×40 deg^2 field of view. The two cameras, each covering 4% of the sky, were equipped with a coded mask (see more details in [Ballesteros, 2001; Cieslak, 2016]) which allowed to obtain better localizations ($\sim$ 1-3 arcminutes).

Thanks to the completeness of the instruments, in terms of their energy ranges, it was possible to follow-up the detected bursts at different wavelengths. Once the *GRBM* triggered on a GRB, a rough localization of the GRB could be estimated from the analysis of the *WFC* data on ground. In case of a *WFC* detection, the refined localization was used to trigger *NFI* observations. This strategy required at least a few hours before pointing the *NFI* [Feroci, 1999]. This alert strategy and observation sequence led to the discovery of GRB counterparts in X-ray [Costa et al., 1997] and visible domains [Groot et al., 1997].

On February 28, 1997, the *GRBM* triggered on GRB 970228 which was also seen in the field of view of a *WFC* camera. The *WFC* localized the burst within $3'$. Due

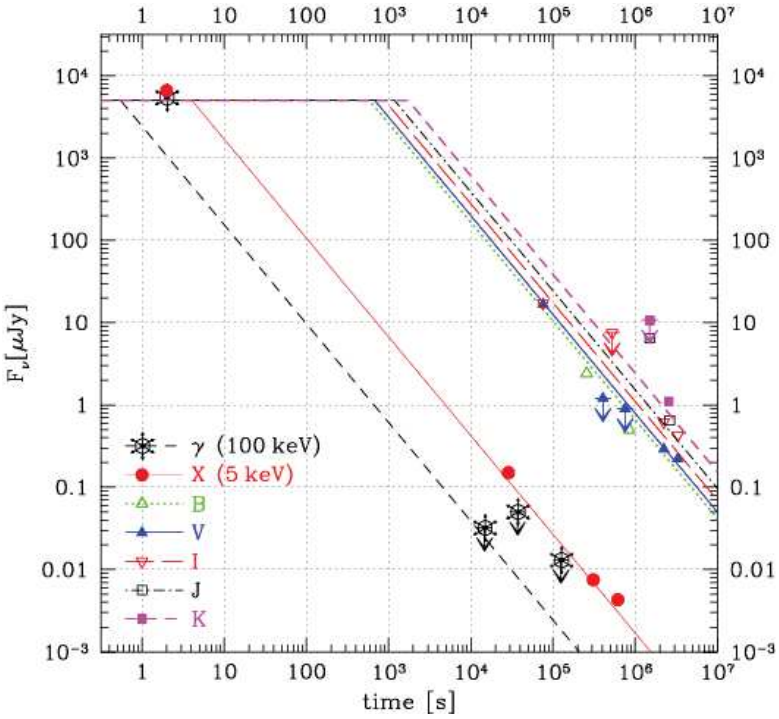

Figure 1.5: *GRB 970228 afterglow light curves detected by the WFC and NFI on board BeppoSAX in the 2-10 keV energy range. The figure shows the light curves in X-rays, visible and infrared. From Wijers et al. [1997].*

to the human intervention needed to repoint the satellite, the *NFI* observations started 8 hours after the initial GRB alert. The flux of the X-ray source appeared to decrease in time following a power law ($t^{-\alpha}$) with index $\alpha = 1.3 \pm 0.1$ [Costa et al., 1997] (see Fig.1.5). In parallel, a counterpart was also detected in the visible domain in the same night by the ground telescopes, the INT[8] (Isaac Newton Telescope) and the WHT[9] (William Herschel Telescope). This long-lasting and fading emission (later called the "afterglow" emission) contrasts with the bright and variable emission (the GRB "prompt" emission) that had been known for years. These novel observations opened a new era for the understanding of the GRB phenomenon.

Following this discovery, *BeppoSAX* detected GRB 970508 which was sufficiently bright to be seen at all wavelengths up to the radio domain. The spectroscopic observations performed by the Keck telescope (Hawaii) showed highly redshifted FeII and MgII absorption lines, and led to the first measurement of a GRB distance. They placed the burst at redshift $z = 0.835$ [Reichart, 1998]. This discovery was a great breakthrough in the field of GRB which closed the distance debate and clearly

[8] `http://astrolapalma.com/en/william-herschel-telescope`
[9] http://www.ing.iac.es/Astronomy/telescopes/wht/

established the extragalactic origin of GRBs, ruling out the galactic models. This distance also implied a huge amount of energy released at the source, making GRBs the most luminous objects in the Universe.

Intriguingly, the detection of GRB 980425 by the GRBM and the *WFC* brought indication of the properties of long GRBs. One day after the detection of this GRB, the Australian Mount Stromlo Observatory (MSO) announced the detection of the type-Ic supernova SN98bw within the error box of the *WFC* [Galama et al., 1998]. This was the first hint of a possible connection between LGRBs and core-collapsed supernovae, i.e. of massive stars as GRB progenitors.

HETE-2

Due to the time needed to download the *WFC* data and to compute an accurate position on the ground, the localization of GRBs with *BeppoSAX* was not optimized for triggering follow-up observations. In 2000, the *HETE-2* satellite was successfully launched, with the capability to detect and quickly localize GRBs onboard. The satellite carried three main instruments: *FREGATE* (*French Gamma-ray Telescope*, 6 - 400 keV), *WXM* (*Wide field X-ray Monitor*, 2 - 25 keV) and *SXC* (*Soft X-ray Camera*, 0.5 - 10 keV). With an effective area of 120 cm^2, *FREGATE* consisted of four NaI(Tl) γ-ray detectors, dedicated to the GRB detection and their spectro-temporal study. The *WXM* was equipped with two coded masks with an effective area of 175 cm^2 each. The *SXC* operated in the soft X-ray domain, and consisted of two X-ray imagers with a total effective area of 7.4 cm^2.

HETE-2 was the first satellite that could quickly localize GRBs on board and therefore deliver GRB positions to the follow-up community within a few tens of seconds. Thanks to this capability, it was possible to observe the afterglow after a short delay from the γ-ray detection. The first exciting result of *HETE-2* was the detection of the afterglow of GRB 021004 only 3 minutes after its detection [Fox, 2002]. This observation showed variability in the afterglow light curve at early times, which contrasted with the smooth decay seen for the late afterglow.

Thanks to *HETE-2*, the connection between LGRBs and the supernovae (SNe/Ic), already seen by the *BeppoSAX* observation of GRB 980425, was firmly confirmed by the detection of GRB 030329 [Stanek et al., 2003] (see Fig.1.6). This GRB was followed by spectroscopic observations during nine days after its detection, confirming, with accurate spectroscopic measurements, the association of this long GRB to the type-Ic SN2003dh.

All of the afterglows detected by *BeppoSAX* and also by *HETE-2*, during 5 years after launch, were associated to long GRBs. One had to wait until 2005 for the first

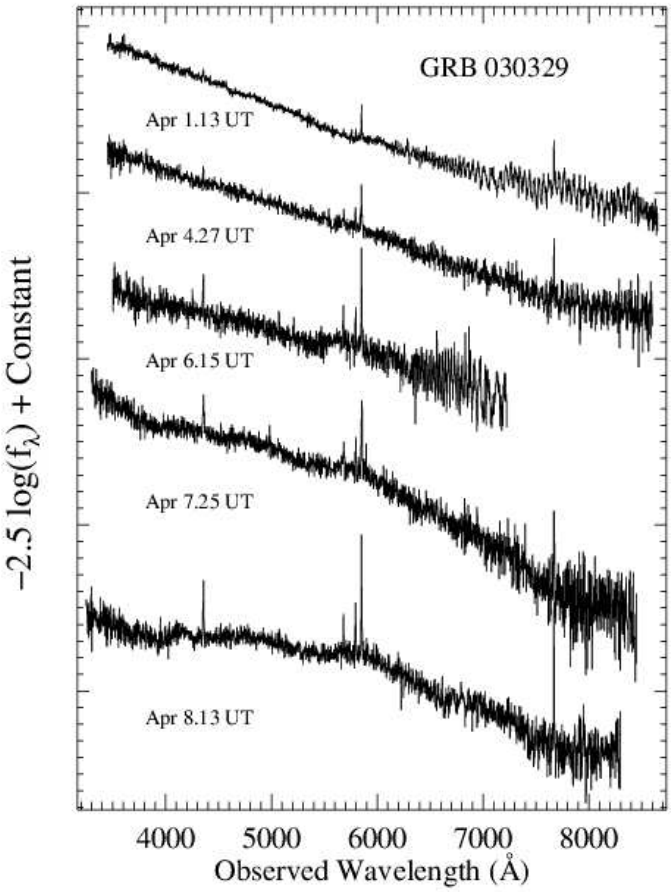

Figure 1.6: *Time evolution of the GRB 030329 visible spectrum (top to bottom: 2.64 to 9.64 days after the burst), with a progressive appearance of broad peaks which are characteristic of a supernova. From Stanek et al. [2003]*

detection of a SGRB optical afterglow. The follow-up observations of the short GRB 050709 placed this *HETE-2* burst in a star-forming galaxy at z=0.160 [Fox et al., 2005].

Thanks to its low-energy detection threshold, *HETE-2* also revealed the existence of other classes of GRBs which emit in soft X-rays, the so-called XRFs (for X-ray flashes, [Barraud et al., 2003]) and XRRs (X-Ray Rich GRBs, [Sakamoto et al., 2005]).

Swift

The launch of the *Swift* satellite in 2004 [Gehrels et al., 2004] (still in operation) marked the start of a new era in GRB studies. It is dedicated to answering questions that were left unresolved by its predecessors, in particular: what are the properties of the GRB afterglow? what are the progenitors of GRBs? *Swift* consists of three instruments: the *BAT* (for *Burst Alert Telescope*, [Barthelmy et al., 2005]), the *XRT* (*X-Ray Telescope*, [Burrows et al., 2005]) and the *UVOT* (*UltraViolet/Optical Telescope*, [Roming et al., 2005]) instruments.

BAT is a wide field of view (∼2 sr) coded-mask imager which detects GRBs in the 15-150 keV energy domain and provides a quick and accurate estimate of their positions with $1'$-$3'$ error radii. This accurate localization is good enough to autonomously slew the spacecraft and point the other two instruments of the satellite for follow-up observations. Thanks to this repointing capability and to the rapid slewing, the observation of the transition phase between the prompt and the afterglow emissions became possible. As a result, the early afterglow emission could be followed by the *XRT* a couple of minutes only after the end of the prompt emission. Thanks to its wide field of view, *BAT* is able to detect ∼80 GRBs per year, and it gathered ∼1000 bursts in its 11 years of operations [Lien et al., 2016].

The *XRT* is a sensitive X-ray imaging telescope, covering an energy range 0.2-10 keV. It has a narrow field of view of $23' \times 23'$. The main role of the *XRT* is to refine the localization of *BAT*-detected GRBs (within $\sim 3''$), and to observe their X-ray afterglow.

The *UVOT* is a 30 cm telescope, dedicated to the observation of the UV and visible GRB afterglow. It has 6 bandpass filters covering the 170-650 nm range. It has a narrow field of view $17' \times 17'$ and a point source localization accuracy of $0.3''$.

Thanks to the rapid slew of *Swift*, the accurate localization estimated by its instruments is delivered to the ground within 20-200 s after the detection. The GRB position and light curves are downlinked via the TDRSS system (Tracking and Data Relay Satellite System) [Sakamoto et al., 2008]. Because of this rapidity, the afterglows of most of *Swift* detections have been followed by ground-based telescopes looking for optical counterparts. About 60% of *Swift* GRBs have been followed in the visible, and only 30% have spectroscopic redshift measurements [Coward et al., 2013]. Recent studies show that *Swift* GRBs cluster around a redshift of 2-2.5 [Lien et al., 2016; Perley et al., 2016] (see Fig.1.7). The largest spectroscopic redshift so far was recorded for GRB 090423, at z=8.3, detected by *Swift* [Tanvir et al., 2009] i.e. when the Universe was only 600 million year old. Using photometric observations with the Gemini-North, the Very Large Telescope, and the GRB Optical and Near-infrared Detector, Cucchiara et al. [2011] placed GRB 090429B at z = 9.4.

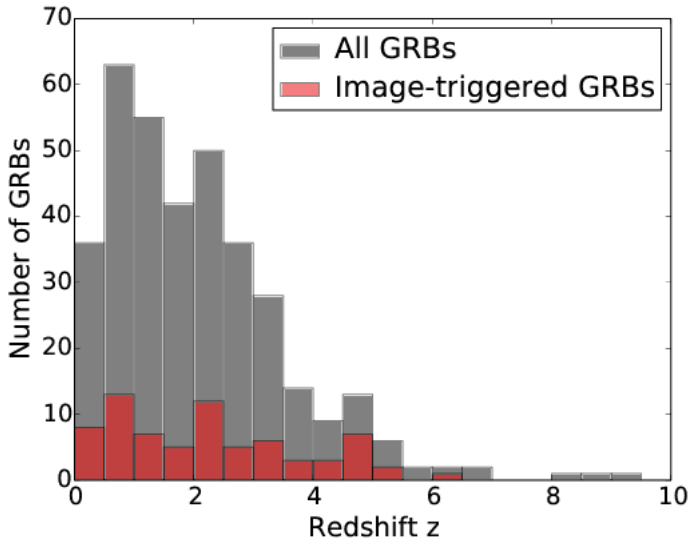

Figure 1.7: *Redshift distribution for the BAT GRBs which have spectroscopic redshift measurements (gray bars). To detect GRBs, the BAT searches either for an increase of the count rate in the light curves, or for the appearance of a new source in successive sky images. The latter method is called "image trigger", and the bursts detected by this method are shown in red bars. From Lien et al. [2016].*

However, this estimation could be affected by large uncertainties due to the less accurate photometric redshift measurements compared to spectroscopic ones.

One of the most important discovery of *Swift* is the observation of a canonical light-curve of the X-ray afterglow. It was believed that the afterglow emissions follow a simple decaying power law as was seen by *BeppoSAX* for late afterglow emissions. However, the *XRT* observations showed instead a complex light curve behavior in the transition phase between the prompt and afterglow phases, which raised new questions about the GRB emission mechanisms. The canonical afterglow light curve consists of several power law segments separated by 2-3 break times (see more details in Sect.1.3.2). Morover, bright flares have been observed in a fair fraction (30% [Chincarini et al., 2010]) of X-ray afterglows, adding to the complexity of GRB light curves. The afterglows of SGRBs are fainter than that of LGRBs, and thus more difficult to observe. While the distance of short GRBs was unknown before 2005, the number of SGRBs with known redshift has dramatically increased thanks to *Swift*. About 10% of the *Swift* GRBs are SGRBs where ∼25% of them have redshift measurements with an average of 0.85 [D'Avanzo, 2015]. These GRBs can occur in late-type (non-star-forming) or early-type (star-forming) galaxies, whereas LGRBs occur in star-forming galaxies only [Gehrels, 2007].

1.2.3 The high-energy missions

INTEGRAL

On October 17, 2002, the European Space Agency (ESA) launched the *INTEGRAL* (*INTErnational Gamma-Ray Astrophysics Laboratory*, [Winkler et al., 2003]) satellite with contributions from Russia (launcher) and from the USA (Goldstein ground station). Gamma-ray observations with *INTEGRAL* are performed by two complementary instruments onboard: the *SPI* spectrometer (*SPectrometer on INTEGRAL*, [Vedrenne et al., 2003]) in the energy range 15 keV to 8 MeV and the imager *IBIS* (*Imager on Board the INTEGRAL Satellite*, [Ubertini et al., 2003]) in the energy range 20 keV to 10 MeV, in addition to two monitoring instruments operating in the X-ray (JEM-X) and visible (OMC) domains. All of these instruments are co-aligned, but have different fields of view.

The *SPI* spectrometer has a fully coded field of view of 16° and an energy resolution of 2.5 keV at 1.3 MeV. Its angular resolution of 2.5° allows for a typical point-like source localization of 10-20′. It consists of a coded mask with an array of 19 Germanium (Ge) detectors. An anti-coincidence system (ACS) is made from 91 bismuth-germanate (BGO) crystals arranged on a cylinder that is placed between the mask and the detection plane to reduce the background induced by charged cosmic rays (CR). This veto system has a large effective area of 0.3 m^2 and can be also used for GRB studies. However, the energy of the interacting gamma-ray photons is not measured, and only GRB light curves can be produced [Rau et al., 2005].

The *IBIS* imager consists of a coded mask with two layers of pixel detectors (ISGRI [Lebrun et al., 2003] and PICsIT [Labanti et al., 2003]) optimized for low (15 keV - 1 MeV) and high (175 keV - 10 MeV) energies. Both detection planes can be used together as a Compton polarimeter.

Based on the capabilities of both instruments, a system called "IBAS" (for *INTEGRAL* Burst Alert System) has been running on ground with the aim to detect and localize GRBs in real time [Mereghetti et al., 2004]. Thanks to *IBIS*, the GRBs can be localized within 2′ uncertainty radius (90% confidence level). In most cases, these localizations are transmitted to the other telescopes[10] within a few tens of seconds after the GRB detection [Mereghetti, 2013]. Light curves with high photon statistics are produced with the *SPI*/ACS system. Thanks to its performance, this software detected more than 90 GRBs during the first 10 years of the *INTEGRAL* mission including 4 SGRBs [Mereghetti, 2013].

[10] *INTEGRAL* is one of satellites which contribute to the *IPN*. The main satellites which contribute to the *IPN* are: WIND, Mars Odyssey, Messenger, RHESSI, *Swift*, Suzaku, *AGILE*, and *Fermi* in addition to *INTEGRAL*

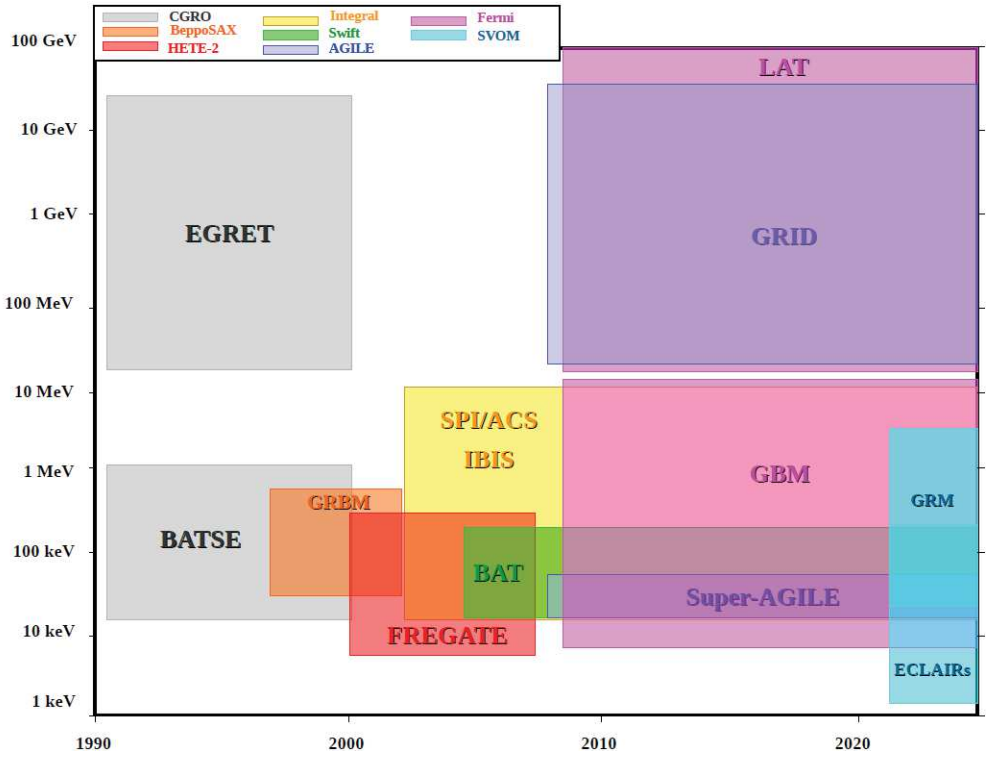

Figure 1.8: *Missions and satellites dedicated to observing GRBs since 1990. The energy ranges of the satellites correspond to the energy ranges of their instruments which have wide fields of view.*

An interesting and promising result was the polarization measurement for GRB 041219A with *IBIS*. A polarization study of this GRB was performed as well by McGlynn et al. [2007] with the *SPI* instrument. For this bright GRB detected by *INTEGRAL*, it was possible to study the emission polarization in different time intervals, which is extremely difficult for fainter GRBs. This study allowed to detect an evolution of the polarization with time [Götz et al., 2009]. Most of the theoretical models of GRBs emission predict polarization assuming different magnetizations corresponding to different ordering of the magnetic fields in the jet [Ghisellini and Lazzati, 1999; Lyutikov and Blandford, 2003].

EGRET

In addition to its prolific observations in the keV-MeV range, *CGRO* offered for the first time an opportunity to look at the GRBs at high energies via its *EGRET* instrument. *EGRET* [Hartman et al., 1992] was devoted to high-energy observation of gamma ray sources up to 30 GeV. It was a pair-conversion spark chamber telescope equipped with a calorimeter and a plastic anti-coincidence scintillator. The conversion of the high-energy photons into electrons and positrons was occurring within 28

Missions	**operation period**	**Instruments**	**E/WL range**	**Typical GRB localization accuracy**
Vela	1965 - 1979	multiple satellites	200 keV - 1.5 MeV	$10'$
IPN	1978 - 1980	multiple satellites	20 keV - 1 MeV	$5'$
CGRO	1991 - 2000	*BATSE*	20 keV - 1 MeV	3-4°
		EGRET	20 MeV - 30 GeV	
BeppoSAX	1996 - 2002	GRBM	40 - 700 keV	
		WFC	2 - 26 keV	$1\text{-}3'$
		NFIs	0.1 - 300 keV	
HETE-2	2000 - 2006	*FREGATE*	6 - 400 keV	
		WXM	2 - 25 keV	
		SXC	0.5 - 10 keV	3 - 15"
INTEGRAL	2002 -	*SPI*/ACS	15 keV - 10 MeV	$10\text{-}20'$
		IBIS	20 keV - 10 MeV	$< 1'$
Swift	2004 -	*BAT*	15 - 150 keV	$1\text{-}3'$
		XRT	0.2 - 10 keV	3"
		UVOT	170 - 650 nm	0.3"
AGILE	2007 -	*GRID*	30 MeV-50 GeV	$5\text{-}20'$
		SA	15-45 keV	$1\text{-}3'$
Fermi	2008 -	LAT	20 MeV- 300 GeV	0.2-0.5°
		GBM	8 keV- 40 MeV	∼10-15°

Table 1.1: *GRB-monitoring satellites up to 2017*

Tantalum foils interleaved with spark chamber modules to measure their direction. It had an effective area of 1500 cm^2 at 300 - 1000 MeV and an angular resolution of 0.54° above 1 GeV. A total absorption spectrometer crystal (TASC) made of NaI, was placed below the spark chamber to measure the photon energy. All detectors were covered by an anti-coincidence shield to reject part of the background induced by charged cosmic rays. Due to its limited effective area, *EGRET* could detect a few GRBs only. On January 31, 1993, it recorded the first GeV photon from a GRB [Sommer et al., 1994a]. Before this date, the highest energy photon did not exceed the 100 MeV energy range.

With the observation of the high-energy emission of GRB 941017, the interpretation of GRB spectra was confronted to new difficulties. The keV-MeV spectrum of this burst is still fitted by the `Band` function (defined further in Eq.1.2) which could point to synchrotron emission from shock-accelerated electrons. The high-energy emission showed a deviation from the low-energy spectrum where an additional

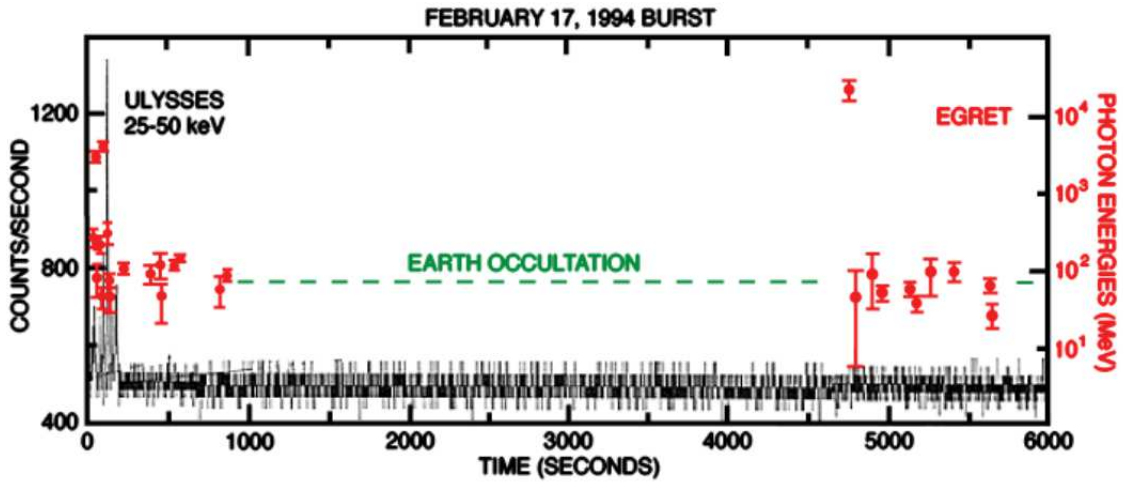

Figure 1.9: *The light curve and count spectrum of GRB 940217 as seen by EGRET and by the ULYSSES probe. A photon of 18 GeV was observed with a delay of ∼75 mn after the trigger time. From Hurley et al. [1994].*

power law component was observed up to 200 MeV [González et al., 2003a]. The large fluence of this additional component with respect to the low-energy one, as well as its steadiness that contrasts with the slow decay of the first component, questioned the standard synchrotron shock model and suggested additional emission mechanisms at high energies, e.g. the inverse Compton component from the forward and reverse shock system[11] [Granot and Guetta, 2003]. Finally, thanks to the sensitivity of *EGRET*, a high-energy photon of energy of 18 GeV was detected from GRB 940217 [Hurley et al., 1994]. This photon was detected ∼75 minutes after the *BATSE* detection time. The delayed high-energy emission was observed up to ∼90 minutes, and its origin remains elusive (see Fig.1.9).

AGILE

Seven years after the end of the *CGRO* mission, the small Italian satellite *AGILE* (*Astro-rivelatore Gamma a Immagini LEggero*" [Tavani et al., 2008]) was launched with the aim to explore the γ-ray Universe carrying on board the two instruments *GRID* (for *Gamma Ray Imaging Detector*, 30 MeV-50 GeV) and *SA* (*Super-AGILE*, 15-45 keV). The *GRID* is a pair-conversion telescope with a sensitivity which is comparable to that of *EGRET*. It consists of a silicon tracker with 12 layers, 10 of which include tungsten foils for the pair conversion, and a CsI calorimeter. The

[11] The forward shock corresponds to the external shock between the jet and the circum-burst medium, which creates a reverse shock that propagates inward.

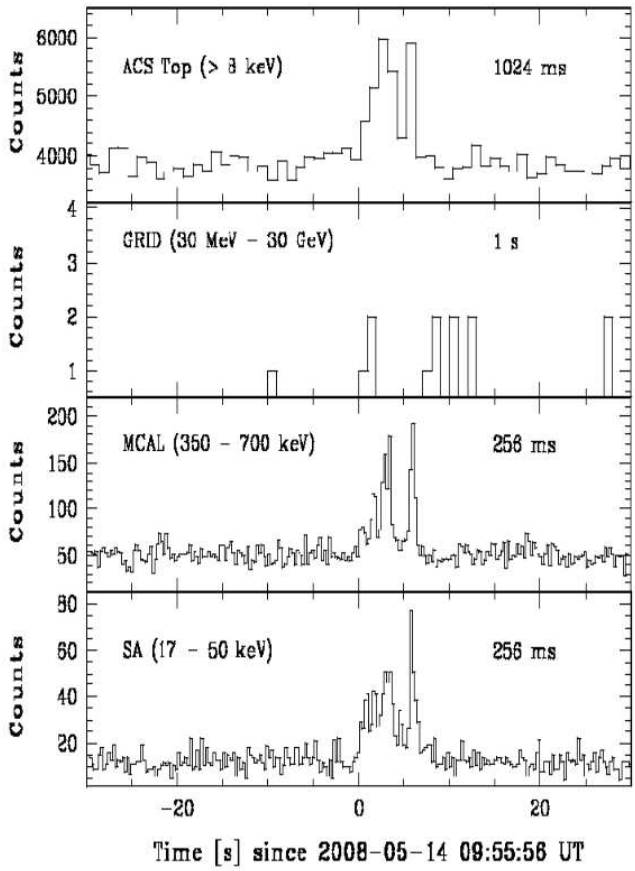

Figure 1.10: *Light curve of GRB 080514B as seen by the AGILE instruments. The second light curve shows the delayed onset of the high-energy emission (30 MeV - 30 GeV) with respect to the peaks seen by MCAL (third panel) and SA (bottom panel). From Giuliani et al. [2008]*

innovative technology of *AGILE/GRID* lies in the integration of silicon detectors in the instrument [Tavani et al., 2006]. This allows to an optimal imaging capability in high-energy range from 100 MeV to 50 GeV. However, its small effective area (more than 200 cm^2 above 30 MeV) with respect to *EGRET* limits its sensitivity in this domain. A part of *GRID* called *MCAL* (*Cesium-Iodide Mini-Calorimeter*) can also independently trigger on GRBs in the energy range between 300 keV and 100 MeV [Galli et al., 2013]. The *SA* detector is a hard X-ray imager, a coded-mask system comprising silicon detectors and a thin Tungsten mask with an angular resolution of $6'$ and an optimal source positioning of 1-$3'$. All of the *AGILE* instruments are surrounded by a segmented anti-coincidence shield for rejecting charged particles.

Over the first 3 years of operation, *AGILE* detected ∼130 GRBs [Marisaldi et al.,

2009], among which 85 were only observed above 300 keV [Galli et al., 2013]. Interestingly, the detection of GRB 080514B revealed a time delay of its GeV emission, as seen by the *GRID*, with respect to its keV-MeV prompt emission [Giuliani et al., 2008] (see Fig.1.10). A similar delay was seen later from the short GRB 090510 detected by *Fermi* [Giuliani et al., 2010].

Fermi

Known formerly as *GLAST* (*Gamma-ray Large Area Space Telescope*), the *Fermi* satellite was launched in June 2008. One important scientific goal of the mission is the study of GRBs from keV up to GeV energies. Together, its main instrument called LAT (*Large Area Telescope*, 20 MeV- 300 GeV, Atwood et al. [2009]) and its GBM (*Gamma-ray Burst Monitor*, 8 keV- 40 MeV, Meegan et al. [2009]) instruments, cover seven decades in energy.

The γ-ray detection principle with the LAT is similar to that of *EGRET*. A pair-conversion and tracking system is used in combination with a calorimeter to detect and characterize the incident photons, and an anti-coincidence detector rejects the charged cosmic particles. The tracker of the LAT instrument (see more details in Chap.2) benefits from the silicon strip detector (SSD) technology, which allows to achieve a high angular resolution (0.2° at 10 GeV, see [Bellazzini et al., 2003]). The LAT instrument consists of 18 converter-tracker planes. This provides a large effective area of $\sim$0.9 m^2 and a wide field of view of 2.4 sr. The LAT anti-coincidence detector is segmented in order to address the issue of "self-veto" which affected the detection efficiency of *EGRET* (see Sect.2.4.1). Covering the whole unocculted sky, similarly to the *BATSE* instrument, the GBM complements the LAT for the observation of transient sources especially GRBs.

In addition, the *Fermi* satellite benefits from a repointing capability (see Sect.2.2). This observational mode occurs when the GBM detects a bright and/or fluent burst. In this case, the spacecraft slews in order to place the GRB within the LAT field of view for a duration of $\sim$2.5 hours. This allows to observe the high-energy emissions of the GRB afterglow for several hours after its detection. With all these capabilities *Fermi* is helping to answer a long list of questions concerning the GRBs:

- What are the main acceleration processes of the particles: shocks or magnetic reconnection?
- What are the accelerated particles responsible for the high-energy radiations: electrons or protons?
- Where are these particles accelerated: below, near or above the photosphere?
- At which distance from the central engine do the prompt emission end and the afterglow emission start?

- What are the main radiative processes? Are they purely non thermal (e.g., synchrotron, inverse Compton emissions)? What is the contribution of the thermal emission?
- How relativistic are GRB jets and what is the distribution of their bulk Lorentz factor?
- What is the maximum photon energy that can be emitted by GRBs and what is the shape of their spectrum at the highest energies?

1.3 GRB Phenomenology

Thanks to the *BATSE* observations and later to the *BeppoSAX* ones, it was discovered that the GRB emissions occur in two different successive phases: the high-energy "prompt" phase and the temporally extended "afterglow" phase.

1.3.1 Observational properties of the prompt emission

The prompt emission is a short and intense phase of hard X-ray and γ-ray radiations. Its light curve has an irregular profile and important variations from burst to burst. Some light curves show clear and well-separated pulses, whereas other light curves showed extreme variabilities with a typical time-scale $\delta t_{\rm v}$ significantly shorter than the total duration of the burst (see Fig.1.4). The GRBs that have isolated pulses, being asymmetric in most cases, often show a fast rise and an exponential decay (FRED) profile [Norris et al., 2005]. In this case $\delta t_{\rm v}$ is thus comparable to the total duration of the burst. Considering the different durations of the GRB light curves, the so-called T_{90} quantity was introduced to define the duration of the prompt emission, corresponding to the time interval that contains 90% of the received flux. Despite the difference of the prompt phase T_{90} between long and short GRB classes, the shape of their light curves is almost the same, but only contracted in time for the latter [Gruber et al., 2014].

Assuming that the energy released by a GRB is isotropically distributed, one can compute this energy denoted by $\mathrm{E}_{\gamma,iso}$ following the equation:

$$E_{\gamma,iso} = \frac{4\pi D_l^2}{1+z} S. \tag{1.1}$$

where S is the time-integrated energy flux of the burst, z is its redshift and D_l is its luminosity distance. In order to facilitate the comparison between different bursts, the energy flux S is usually integrated over an energy range $[\mathrm{E}_1, \mathrm{E}_2]$ in the observer frame, which corresponds to a fixed energy band in the source rest frame $[\mathrm{E}'_1, \mathrm{E}'_2]$= $[\mathrm{E}_1, \mathrm{E}_2]\times(1+\mathrm{z})$, namely: $\mathrm{S}=\mathrm{T}_{obs}\times\int_{E'_1/(1+z)}^{E'_2/(1+z)} \mathrm{E}\Phi(\mathrm{E})\mathrm{dE}$, where $\Phi(\mathrm{E})=\mathrm{dN}/\mathrm{dE}$ is the

differential photon spectrum (in units of $\mathrm{keV}^{-1}\,\mathrm{cm}^{-2}\,\mathrm{s}^{-1}$) averaged over the observation time interval T_{obs} (see eq.2 of [Ghirlanda et al., 2004]). The isotropic energy E_{iso} can reach $10^{(54-55)}$ erg, which is difficult to account for, even in theoretical models involving an accreting compact object. As we will see in Sect. 1.4.1, a possible solution is to assume that the GRBs emit their radiations in a form of collimated outflow, i.e. a jet, although the jet opening angle is still unknown (see Sect.1.4.1).

The keV-MeV prompt emission spectrum

Conversely to the diversity seen in their light curves, the spectra of GRBs often show similar shapes. The *BATSE* observations firmly established that GRB prompt spectra in the keV-MeV energy range are non-thermal, showing a good agreement with the phenomenological `Band` function [Band et al., 1993]. This function is composed of two smoothly-connected power laws with four parameters A_{Band}, α, β and E_p (see Fig.1.11), and it is defined as:

$$\frac{dN_{\texttt{Band}}}{dE} = A_{\texttt{Band}} \begin{cases} \left(\frac{E}{100\,\mathrm{keV}}\right)^{\alpha} \exp[-\frac{E\,(2+\alpha)}{E_p}], & E \leq E_p \frac{\alpha-\beta}{2+\alpha} \\ \left(\frac{E}{100\,\mathrm{keV}}\right)^{\beta} \left[\frac{E_p}{100\,\mathrm{keV}} \frac{\alpha-\beta}{2+\alpha}\right]^{\alpha-\beta} \exp[\beta-\alpha], & E > E_p \frac{\alpha-\beta}{2+\alpha} \end{cases} \tag{1.2}$$

$A_{\texttt{Band}}$ is the amplitude parameter, in units of $\mathrm{keV}^{-1}\,\mathrm{cm}^{-2}\,\mathrm{s}^{-1}$and E_p is the peak energy which corresponds to the maximum of the νF_ν ($E^2 \times dN/dE$) spectrum. As reported in the *BATSE* catalog [Goldstein et al., 2013], the α and β parameters of the `Band` function show relatively narrow distributions clustering around -1 and -2.4, respectively. On the other hand, the peak energy has a wider distribution, ranging from $\sim$ 40 keV to $\sim$3 MeV, with a typical value of $E_p \sim 200$ keV.

In the pre-*Fermi* era, the `Band` function was usually sufficient to reproduce the keV-MeV spectrum of most GRBs, which is often attributed to the synchroton emission of shock-accelerated electrons. However, complementary analyses showed that a thermal spectral component could adequately fit the data for some GRBs as well. The presence of a thermal component has been investigated on various samples of *BATSE* GRBs (see, e.g., Ghirlanda et al. [2003] and Ryde [2004]), in the form of a single Black Body (BB) contribution that reproduces the whole spectrum, or sometimes associated to a non thermal power-law component. Thanks to its broad coverage of the prompt emission spectrum, it was expected from *Fermi* to bring significant clues to the presence of a thermal contribution. The spectroscopic results obtained with the *Fermi*/GBM show a good agreement of the `Band` function with most of the observed spectra [Gruber et al., 2014]. However, an additional thermal component was observed in several cases (GRB 1000724B [Guiriec et al., 2011], GRB 120323A [Guiriec et al., 2013], GRBs 080916C and 090926A [Guiriec et al., 2015a], GRB 131014A [Guiriec et al., 2015b]). Moreover, some GRB spectra exhibit a flux excess at low energy ($<$ 50 keV), featuring an additional power law

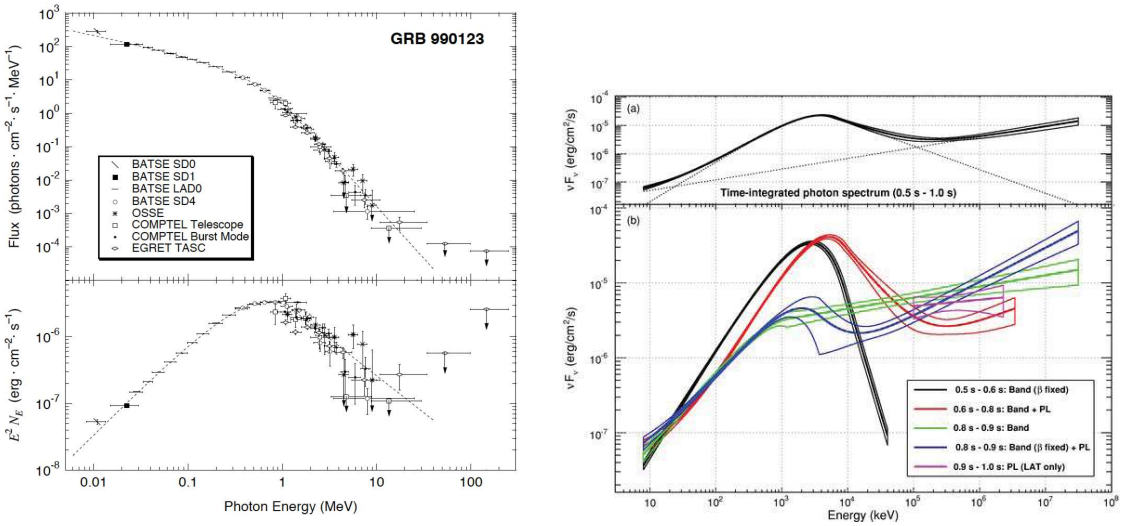

Figure 1.11: ***Left:*** *(top to bottom) photon spectrum and spectral energy distribution of GRB 990123 as measured by the four instruments of CGRO [Briggs et al., 1999].* ***Right:*** *spectral energy distribution of GRB 090510 as measured by* Fermi *[Ackermann et al., 2010]. Each spectrum is represented by a 68% confidence level contour corresponding to the best fitted spectral shape (i.e., a* `Band` *function with an extended power law at high energies).*

component which can dominate the `Band` component, as in the case of GRB 090510 [Ackermann et al., 2010; Tierney et al., 2013] (see the right panel of Fig.1.11). The BB and the PL components that are seen at low energy by the *Fermi*/GBM show the complexity of the GRB prompt emission spectra.

In addition to the duration of SGRBs and LGRBs, it has been found that the hardness of their prompt emission can be used as an indicator to distinguish these two classes of GRBs. The hardness ratio (HR) of a spectrum is defined as the ratio of the fluence in two non-overlapping energy bands. The fluence (in units of erg cm^{-2}) is defined as the integral of the energy flux over energy and time. Studying the hardness of a *BATSE* GRB sample, [Qin et al., 2000] showed that SGRBs are harder (with an HR average of $\sim$0.8 between the two energy bands 100-300 keV and 50-100 keV) than the long ones (HR average $\sim$0.5) (see Fig.1.12). An interesting analysis of the time evolution of the hardness parameter made by [Ford et al., 1995] showed that LGRBs exhibit a hard-to-soft evolution with time, that reflects the cooling of the prompt emission spectrum.

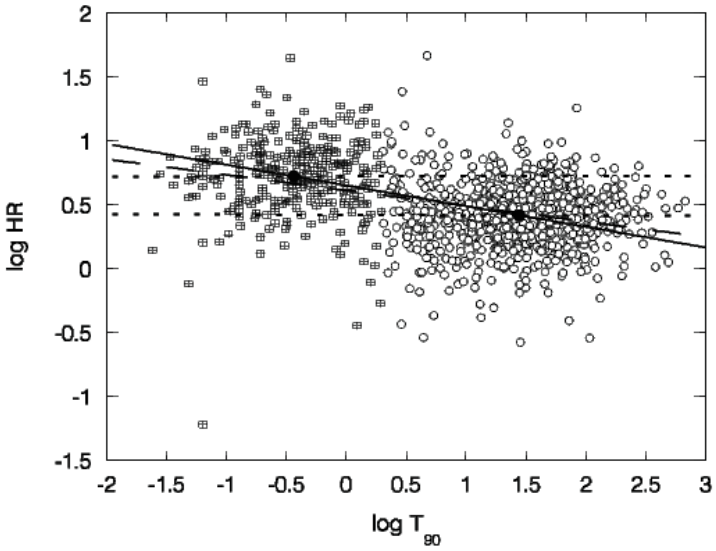

Figure 1.12: *The hardness versus duration diagram of BATSE GRBs. The hardness is calculated as the ratio of the fluence in two energy ranges: HR= $F_{(100-300)keV}/F_{(50-100)keV}$. This figure shows two sets of short and long GRBs connected by a straight line. The dotted lines are the regression lines for both sets while the dashed line is the regression line for the whole sample. From Qin et al. [2000].*

The high-energy prompt emission

The high-energy prompt emission was seen firstly by *EGRET* from a few GRBs (GRBs 930131 [Sommer et al., 1994b], 940217 [Hurley et al., 1994], 940301 and 941017 [González et al., 2003b]). While the high-energy emission detected from GRB 930131 could be accounted by the extrapolation of the `Band` function, the spectrum of GRB 941017 showed an additional power-law component which lasted much longer (∼200 s) than the keV-MeV component.

The *Fermi*/LAT has a much larger effective area than *CGRO/EGRET*. Therefore, the LAT observations of GRBs revealed the behavior of their high-energy prompt emission with greater precision. All of the bright bursts detected by the LAT show an extra-component at high energy. This extended component is fitted either with a power law (e.g. the short GRB 090510 [Ackermann et al., 2010], GRB 080916C [Abdo et al., 2009b], GRB 090902B [Abdo et al., 2009a]) or with a power law attenuated by an exponential cutoff (like GRB 090926A, [Ackermann et al., 2011]). For long GRBs, the fluence of this component is sub-dominant and represents ∼10% only of the keV-MeV component [Ackermann et al., 2013b], whereas both fluences seem to be comparable for short GRBs (e.g. GRB 090510). However, the confirmation of the latter result needs a larger sample of short GRBs detected

at high energies.

On the other hand, some *Fermi* GRBs did not show any evidence for emission above 100 MeV and only flux upper limits were derived. More interestingly, [Ackermann et al., 2012b] revealed high-energy spectral breaks at ∼50 MeV for six of the brightest and hardest GBM GRBs (e.g., GRB 091127). In a more recent work, [Vianello et al., 2017] measured sharp spectral cutoffs in the energy range 20 - 60 MeV and 80 - 150 MeV for the two GRBs 100724B and 160509A.

The delayed high-energy emission seen by *EGRET* has been also confirmed by the LAT observations. It was found to start significantly later than the keV-MeV prompt emission and to persist at much longer time scale. The possible origins of this delayed emission will be discussed in Sect.1.5.1.

1.3.2 Observational properties of the afterglow emission

Unlike the prompt emission, the afterglow radiation has smooth temporal and spectral variabilities. It extends on a broad band of energy (radio to X-rays) and can last days to months after the prompt emission. It has, like the prompt emission, a non-thermal spectrum, which is well described by synchrotron emission, although an inverse Compton (IC) component may also contribute to the X-ray and high-energy afterglow emissions. The first afterglow detected by *BeppoSAX* in 1997 was associated with a long GRB [Costa et al., 1997; Frail et al., 1997]. The observations of the afterglow emission of short GRBs became possible only after the launch of *Swift*, which detected in 2005 the afterglow of the short GRB 050509B [Gehrels et al., 2005].

In the pre-*Swift* era, the afterglow emission was observed a few hours only after the end of the prompt emission due to the manual slewing technique of *BeppoSAX* (as seen in Sect.1.2). At that time, only the late emission part of the afterglow was detected, showing a smooth flux decay usually following a simple power law. Thanks to the automatic slewing of the *Swift* spacecraft, the observations of the early afterglow emission became possible. These observations allow to understand the properties of the GRB emission, especially in the transition phase between the prompt and the afterglow phases.

The X-ray afterglow light curve shows a steep power-law flux decay (as t^{-3}) during hundreds of seconds (phase I in Fig. 1.13). This decay is followed by a plateau phase (phase II, $t^{-0.5}$ to t^{-1}) typically lasting 10^{3-4} s and a power-law decay phase already observed pre-*Swift* (phase III, t^{-1} to $t^{-1.5}$) [Nousek et al., 2006]. In addition to the decay phases, *Swift* revealed the existence of X-ray flares, which can occur during any of the light-curve phases [Butler and Kocevski, 2007; Krimm et al., 2007]. The X-ray afterglow was detected for almost 93% of the BAT GRBs [Kann et al., 2010], and more than 30% of them have observed flaring emissions [Chincarini et al.,

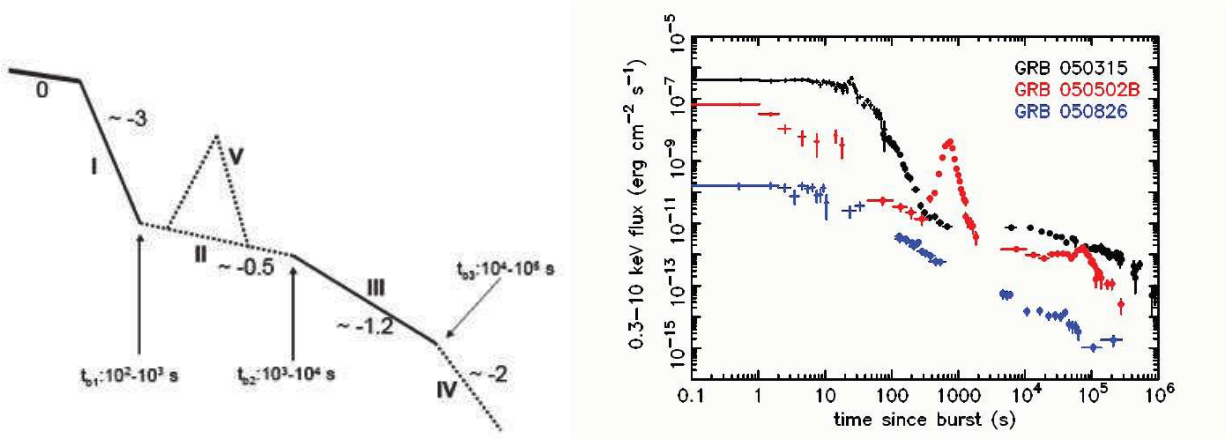

Figure 1.13: ***Left:*** *Schematic canonical X-ray afterglow light curve. Figure taken from Zhang et al. [2006].* ***Right:*** *X-ray light curves of three bursts as seen by BAT (crosses) and XRT (filled circles) on board the Swift telescope. Figure taken from O'Brien et al. [2006].*

2010].

The first optical afterglow was detected for the long GRB 970228 after a few days from the first X-ray afterglow detection [Frail et al., 1997]. The light curves of long GRBs show a typical power-law decay $t^{-\alpha}$ with -1.2 < α < -0.5 [Oates et al., 2011, 2009], and it lasts sometimes one to few days after the detection time. The spectroscopic observations in the optical domain are crucial for computing the distance of GRBs. Only ∼60% of the *Swift* GRBs have detected optical counterparts and only half of them have known redshifts [Gehrels and Razzaque, 2013]. The radio afterglow is the last and the longest phase of the GRB emissions lasting several weeks or months [Berger et al., 2004; van der Horst et al., 2008]. The first radio afterglow was detected from GRB 970508 [Frail, 1997]. The radio observations, if available, allow to study the overall energy of the GRBs. Due to the capabilities of *Swift*, the number of GRBs with radio data has been increased. Almost one-third of all *Swift* GRBs have been detected in radio [Chandra, 2016].

1.4 Physical scenarios

This section is devoted to presenting some of the GRB properties which are revealed by the observations as the existence of a collimated jet of the GRB and the identification of the progenitors of GRBs. The acceleration mechanisms, together with the possible radiative processes that can explain the GRB emissions are described in this section as well.

1.4.1 A relativistic and collimated outflow

The short time scales of the detected GRBs (few milliseconds to seconds) as well as their extreme variability, put strong constraints on the size R of the emission region following the causality relation $R < ct_v$. Assuming an isotropic emission, the large luminosity (L_{iso} 10^{51-55} erg/s) that is measured implies a very large density of photons confined in such a small region. Such a density would increase the gamma-ray opacity to pair production ($\gamma+\gamma \rightarrow e^+ + e^-$) which is due to the annihilation of high-energy gamma rays (of energy E) with softer photons (of energy E'). This annihilation takes place under the condition that the product of the two photon energies is of order $E \times E' \simeq m_e^2 c^4$. In the Thomson regime with a cross-section $\sigma_T = 0.665 \times 10^{-28}$ m^2, the $\gamma\gamma$ opacity can be approximated as:

$$\tau_{\gamma\gamma}(E) \simeq n(E')\sigma_T R = \sigma_T \frac{L_{iso,E'}}{4\pi m_e c^3 R} > 10^{13} \left(\frac{L_{iso,E'}}{10^{51}\,\mathrm{erg\,s^{-1}}}\right)\left(\frac{t_v}{10\mathrm{ms}}\right)^{-1} \quad (1.3)$$

with $n(E')$ is the soft photon number density. For typical $L_{iso,E'}$ $\sim 10^{51}$ erg/s and $t_v \sim 10$ ms, the $\gamma\gamma$ opacity is larger than 10^{13}. This huge opacity would produce a thermal spectrum. However, the observed spectra of GRBs show non-thermal emissions, which can reach a few GeV for some bursts. This well known "compactness problem" can be solved by assuming a relativistic motion of the emitting source [Meszaros and Rees, 1993]. In this case, the opacity is reduced by a factor $\Gamma^{2(1-s)}$ if one assumes a power-law spectrum of index s for the soft photons (see [Granot et al., 2009] for more details). For a typical high-energy index of the `Band` spectrum (s$\sim$-2.3), the opacity is thus reduced by a factor $\sim \Gamma^7$ and it can be less than unity for a minimum value of the jet Lorentz factor $\Gamma > \Gamma_{min} \sim 100$. A detailed calculation of Γ_{min} will be shown in Chap.5 (Eq.5.4). This calculation shows the dependence of the minimum Lorentz factor with the variability timescale (t_v), the redshift (z) and the energy of the most energetic photon (E_{max}) as follows:

$$\Gamma_{min} \propto t_v^{\frac{1}{(s-1)}} (1+z)^{\frac{(s+1)}{(s-1)}} E_{max}^{\frac{(s+1)}{2(s-1)}} \quad (1.4)$$

Assuming an isotropic emission, the energy radiated by a GRB can be as high as $E_{\gamma,iso} \sim 10^{54-55}$ erg (one million times the total energy radiated by a supernova, $\sim 10^{49}$ erg). As discussed in the case of the most energetic GRB 080916C ($E_{\gamma,iso} = 8.8 \times 10^{54-55}$ erg, see [Abdo et al., 2009b]), this puts severe constraints on the energy budget that is required from the source. In order to account for the extreme power of GRBs, it was suggested that their emission occur within a conical, collimated jet with an opening angle θ_j of a few degrees. In this case, the equivalent isotropic energy must be replaced by the energy emitted from the corresponding solid angle, with the following ratio:

$$\frac{E_\gamma}{E_{\gamma,iso}} = \frac{2\Omega}{4\pi} = \frac{2 \times (2\pi \times (1 - \cos(\theta_j)))}{4\pi} \simeq \frac{\theta_j^2}{2} \quad (1.5)$$

which is equal to 4.10^{-3} for $\theta_j = 5°$. A consequence of the jet collimation hypothesis is the prediction of achromatic breaks in the afterglow light curves. Because of the relativistic motion of the jet (see the discussion above), the observer receives only the photons which are emitted with an angle $\theta \sim 1/\Gamma$. As the jet decelerates during the afterglow phase, this angle increases until reaching the geometrical size of the jet (i.e., for $\Gamma \sim 1/\theta_j$), which makes the flux decay more rapidly at later times as the entire emitting surface is visible. In the pre-*Swift* era, these so-called achromatic jet breaks had been observed in a few X-ray afterglow light curves, e.g. for GRB 990510 ([Harrison et al., 1999]). Using a model to convert the jet break time into a jet opening angle θ_j, Frail et al. [2001] found that the corrected energy E_γ for long GRBs clusters around 10^{50-51} erg, which relaxes the constraint on the energy budget. However, later observations by *Swift* showed that only a small fraction of GRBs exhibit achromatic breaks in X-rays and in the visible domain [Kocevski and Butler, 2008; Racusin et al., 2009]. To accommodate the observation of such chromatic jet breaks, Ghisellini et al. [2007] introduced a late prompt emission mechanism which can produce different patterns of the observed light curves in the X-ray and visible domains. While the existence of a jetted emission in GRBs is a natural explanation for their apparent high luminosities, whether jet achromatic breaks are required is still a matter of debate in the GRB community. Answering this question certainly needs more observational constraints in order to built detailed models of the jet's geometry and evolution throughout the burst emission phases.

1.4.2 Progenitors and host galaxies

In this section, we focus on the main proposed scenarios to explain the origin of GRBs: the collapsar and the merger models.

The collapsar model

This model is usually invoked to explain the origin of LGRBs. The association of GRB 980425 detected by *BeppoSAX* with SN98bw [Galama et al., 1998] was the first evidence of a possible link between LGRBs and core-collapsed supernovae (SNe), which correspond to the final collapse and explosion of massive stars at the end of their lifetime. This connection appeared again with the detection of *HETE-2* of GRB 030329 associated, thanks to spectroscopic observations, to SN 2003dh [Stanek et al., 2003]. Since these pioneering observations, most of the nearby, LGRBs have been associated to type-Ic SNe, whose spectra show no hydrogen and helium lines.

This model is based on the gravitational collapse of a massive star, which can lead to the formation of a black hole surrounded by an accretion disk and relativistic ejecta. The progenitor in this collapsar model [MacFadyen and Woosley, 1999] is thought to be a Wolf-Rayet star, namely a massive (>30 $M_\odot$ typically) and rotating star. To a large extent, the physical conditions that are required to form a GRB

following a core-collapse supernova are still unclear. In order to avoid strong stellar winds and to maintain a high angular momentum at the end of the star life, a low metallicity could be required. However, such a condition would also be less favorable for the escape of the jet out of the stellar envelope (R. Hascoet's thesis, [Hascoet, 2012], section 2.3.1).

In the collapsar model, the progenitors of LGRBs are expected to lie within their host galaxies, in the most active and star forming regions. The association of LGRBs with late-type and star-forming galaxies is now well established, as in the case of GRB 970508 [Bloom et al., 1998]. Direct observations of the radial position of some LGRBs in their galaxies also showed that these bursts are more concentrated in the brightest regions of their hosts [Fong et al., 2010; Fruchter et al., 2006].

The merger model

Unlike LGRBs, SGRBs were not found to be associated with SNe [Hjorth et al., 2005]. Since the advent of *Swift*, the observation of their afterglows helped to assess the nature of their host galaxies, which show a greater diversity than that of LGRBs. SGRBs are found to be far from the center of their host galaxies, in low-density environments [Fong et al., 2010]. These characteristics point to the merger of compact object binaries as the most popular progenitor model for SGRBs. This model involves the presence of a binary system of two compact objects (neutron stars, or neutron star / black hole), as initially proposed by Paczynski [1986]. As the binary system looses its energy in the form of gravitational radiation, the two compact objects get closer and eventually merge together, releasing a huge amount of energy. While this scenario remains essentially speculative, recent observations tend to support it. The most notable case is the detection of a so-called "kilonova" [12] associated with GRB 130603B [Tanvir et al., 2013]. In the merger model, a substantial emission of gravitational waves is also expected, which could be detected by the new generation of gravitational wave detectors in the forthcoming years [Connaughton et al., 2016].

1.4.3 The GRB paradigm

In both the collapsar and the merger models, the central engine of a GRB is assumed to be a compact stellar mass black hole surrounded by an accretion disk. The rotational energy of this compact object powers a collimated outflow of radiation released in a small volume.

[12] A faint transient event produced by NS-NS or NS-BH mergers due to the decay of the radioactive species created by the merger

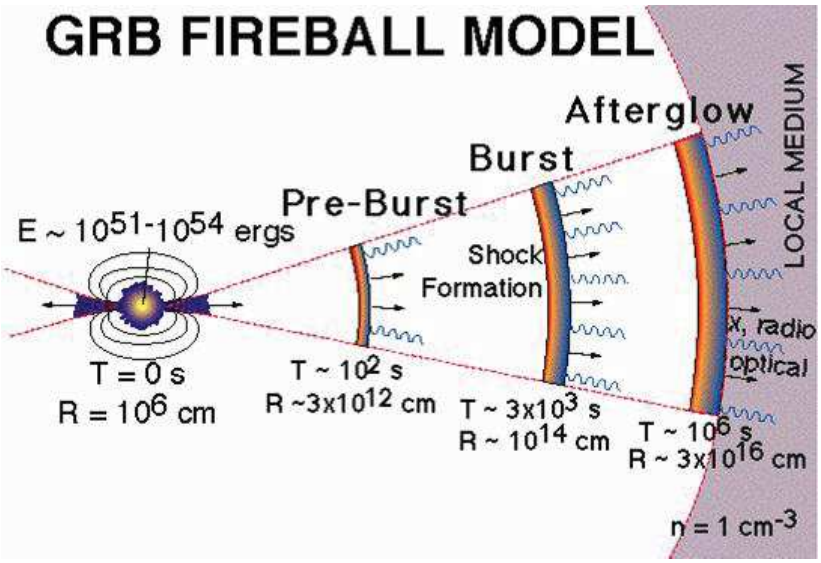

Figure 1.14: *Schema of the fireball standard model of GRBs showing the photospheric radius (order of 10^{12} cm), the internal shock radius (order of 10^{14} cm) and the afterglow radius (order of 10^{16} cm). From Mészáros [2006].*

Acceleration mechanisms

A model proposed to accelerate this outflow to relativistic velocities is the "fireball" model [Cavallo and Rees, 1978], where the term "fireball" refers here to an opaque plasma whose initial energy is significantly greater than its rest mass. Due to its opacity, the plasma expands under its own pressure and cools until it becomes optically thin and the photons escape freely. In the meantime, the fireball is accelerated and it is expanding relativistically outwards. In addition to radiation and pairs, the fireball may also include some baryonic matter which may be injected with the original radiation or may be present in an atmosphere surrounding the initial explosion. These baryons are accelerated with the rest of the fireball and convert part of the initial energy into bulk kinetic energy. The kinetic energy is then dissipated via shocks that accelerate the particles that in turn emits the observed radiation, mainly as synchrotron emission. Internal shocks arise due to shocks within the flow when fast moving particles catch up with slower ones at radius $\sim 10^{13-14}$ cm from the central engine (see Fig.1.14), and they are thought to be the mechanism responsible for the prompt emission. Although this scenario can explain most of the GRB observations, it has some difficulties which will be discussed further below. There is another possible dissipation mechanism to explain the prompt emission phase, the magnetic reconnection model [Lyutikov, 2006; Thompson, 1994; Zhang and Mészáros, 2002]. In this scenario most of the energy is carried by pointing flux. The energy is dissipated via magnetic reconnection driven by, e.g., magnetic instabilities.

Within the fireball model, at large distance from the central engine (radius of order 10^{16-17} cm) the outflow starts to decelerate and interacts with the circumstellar medium via an external shock, that is responsible for the afterglow phase. This simple scheme is successful to interpret the general features of the prompt and the late afterglow emission. However, *Swift* revealed the complexity of the transition zone between these two phases, challenging the standard scenario.

Radiative processes

The prompt radiation is likely related to synchrotron emission from a population of accelerated electrons in a magnetic field amplified by the internal shocks [Meszaros et al., 1994]. An additional component due to inverse Compton (IC) scattering is also expected at high energy (of the order of GeV) [Bošnjak et al., 2009]. However, *Fermi* observations showed that this additional component is detected in only a few GRBs and, thus, that it is subdominant with respect to the synchrotron emission. Thermal emission is also expected at the photosphere when the outflow become transparent. Depending on the details of the acceleration process, this emission may be bright [Rees and Mészáros, 2005].

The pure synchrotron model predicts that the the low-energy index of the photon number spectrum is -3/2 in the fast cooling regime. This index could increase to -2/3 in the slow cooling regime, which is less favored for GRBs because of their high luminosities on short timescales. In any case, the latter limit is violated (the so-called synchrotron "line of death", [Preece et al., 1998]) for a large fraction of GRBs that have even harder indices. One of the possible solution to this issue is to invoke a "jitter" process which is equivalent to a synchrotron scenario in a disordered magnetic field at small scales [Medvedev, 2000]. Alternatively, the IC scatterings in the Klein-Nishina regime may modify the low-energy index of the synchrotron spectrum [Daigne et al., 2011]. The addition of a thermal (photospheric) component to the synchrotron spectrum may also produce a low-energy photon index harder than the one obtained by the simple synchrotron model [Guiriec et al., 2011].

Also the protons can be accelerated by shocks and contribute to the observed radiation, either via their synchrotron emissions of via their interaction with the jet photons (proton-photon interaction) creating an electromagnetic cascade [Asano et al., 2009; Razzaque et al., 2010]. This possibility has been considered to explain the delayed onset of the GeV emission compared to the MeV prompt emission, observed by EGRET and *Fermi*/LAT, since the proton acceleration timescales are much longer than for electrons. However, it cannot explain the extreme variability seen in GRB light curves.

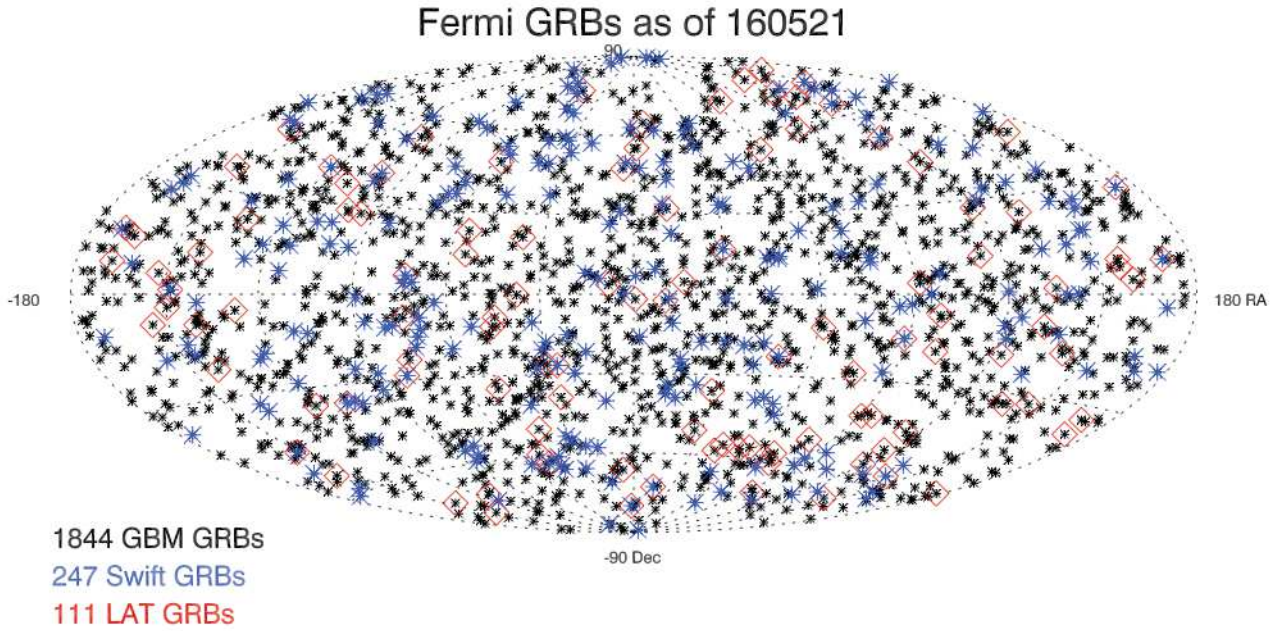

Figure 1.15: *Position of GBM and LAT detected GRBs on the celestial sphere. As of May 21, 2016, the GBM detected 1844 GRBs among which 111 were detected by the LAT and 247 were also triggered by Swift.*

1.5 GRB observations with *Fermi* and with future experiments

1.5.1 GRB observations with *Fermi*

In nine years of operations, the *Fermi* space telescope performed a deep exploration of the GRB domain, providing invaluable observations that shed new light on their properties at high energies. With 12 NaI (sodium iodide) scintillators and 2 BGO (bismuth germanate) detectors pointing to different directions, the GBM instrument onboard the *Fermi* satellite observes the whole unocculted sky. It detects 1 GRB every ∼1.5 days [Narayana Bhat et al., 2016a] (∼ 250 GRBs/year [Goldstein et al., 2012; Paciesas et al., 2012]) observing up to now ∼ 2000 bursts including more than 300 short GRBs (∼ 17%) [von Kienlin et al., 2014]. Almost half of the GBM GRBs appear in the LAT field of view, the main instrument on board *Fermi* telescope which detects only ∼8-10% of them. The LAT, not surprisingly, detects the brightest and/or the most fluent GBM GRBs (Fig.1.16, left). Up to March 2017, it collected 123 GRBs[13] (see Fig.1.15), including 12 short GRBs (second LAT

[13] https://fermi.gsfc.nasa.gov/ssc/observations/types/grbs/lat_grbs/table.php

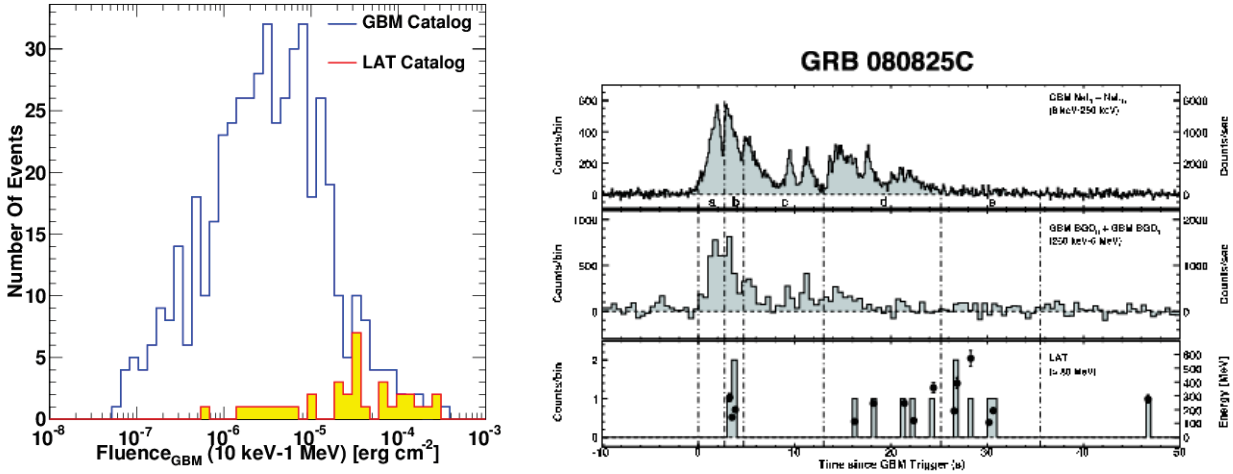

Figure 1.16: ***Left:*** *Fluence distribution of GRBs seen by the LAT and GBM instruments [Ackermann et al., 2013b].* ***Right:*** *Multi-detector light curve of the first GRB detected by the LAT, GRB 080825C [Abdo et al., 2009c].*

GRB catalog, in preparation). Due to the large error box of the GBM ($<15°$ [Connaughton et al., 2015; Meegan et al., 2009]), the follow-up of its detected GRBs by other instruments with more accurate localization, e.g. by the LAT ($\lesssim 1°$) and then by the *Swift*/XRT (a few arsec), is required to facilitate the measurement of their redshifts by ground telescopes. Most of the LAT bright GRBs with accurate localizations have been followed-up by *Swift* and by optical telescopes allowing to determine their redshift. The redshift distribution of LAT GRBs covers a wide range starting from 0.145 (for GRB 130702A) up to 4.35 (for GRB 080916C).

Soon after its launch, the LAT telescope started to reveal peculiar properties of the GRBs, individually and as a whole. The first LAT detection was the long weak GRB 080825C with a significance of $\sim 6\sigma$. This burst had two main peaks in the GBM light curve with a coincidence of the first photon seen by the LAT with the second peak (see Fig.1.16, right panel). No spectral feature was detected for this GRB unless a weak contribution of a cutoff at high energy with only 4.3σ [Abdo et al., 2009c]. Its highest energy photon (0.57 GeV), among the 10 detected photons above 100 MeV, was observed ~ 28 s after the keV-MeV emissions (see more details in [Abdo et al., 2009c]) showing some evidence for a temporally-extended emission, while the GBM signal started to weaken. This, despite the faint detection of this burst, was a sign of a long-lived emission at high energy as was already seen by the *EGRET* and *AGILE* telescopes.

GRB 080916C was the first long and bright burst seen by the LAT. Its high-

energy emission extended for more than 20 minutes, much longer than the GBM duration ($\sim$ 65 s) and its high-energy photon (27.4 GeV with Pass 8, see Sect.2.4.3) was observed $\sim$ 17 s after the GBM trigger time. This burst shows a slight deviation from the `Band` function, providing a marginal detection of a power law at high energy (4-5σ, [Ackermann et al., 2013b]). Thanks to the rapidity in communicating the GRB information with the on ground algorithms, this burst was analysed by the GBM and LAT team and a follow-up request was sent to the *Swift*/XRT instrument. The localization of this GRB by *Swift*/XRT allowed for follow-up observations by the ground-based telescope GROND (Gamma-Ray Optical/Near-infrared Detector) which measured a photometric redshift of z=4.35 $\pm$ 0.15 [Greiner et al., 2009]. The high fluence of GRB 08916C, combined with its large distance, led to an isotropic equivalent energy (following Eq.1.1) $E_{\gamma,iso} \approx 8.8 \times 10^{54}$ erg in the 10 keV-10 GeV energy range, making it the most energetic GRB ever detected [Abdo et al., 2009b]. Within only one year after launch, the *Fermi*/LAT increased the number of GRBs detected above 100 MeV, collecting 9 long bursts (including the two GRBs mentioned above) and 2 short GRBs. The first short burst GRB 081024B detected by the LAT was faint but it was the first short GRB detected above 1 GeV [Abdo et al., 2010]. Its highest energy photon of 3 GeV was detected $\sim$ 0.49 s post-trigger. This burst was detected by the GBM for 0.8 s below 5 MeV, however, its high-energy emission ($>$ 100 MeV) lasted for $\sim$3 s revealing evidence for a temporally-extended emission.

GRB 090510 is the first short bright burst seen by the LAT. Its highest energy photon was detected during its prompt emission with an energy of $\sim$31 GeV, the highest energy photon ever detected from a short GRB [Ackermann et al., 2010]. It shares the same properties as the GRBs described above (delayed and extended emission). The new interesting feature detected in the spectrum of this GRB was the extended power law which contributes not only at high energy but also in low-energy range (see the top panel of Fig.1.11, right). This component dominates the `Band` function on both sides, a characteristic which had not been seen for long GRBs before. The energy throughput of the GRB 090510 GeV spectrum is comparable to the one in the keV-MeV energy range (see Fig. 1.17). A large sample of SGRBs is required to check if this characteristic is common for SGRBs and, therefore, could be used to characterise this class of bursts.

In addition to the mentioned GRBs, the pocket of the LAT is full of interesting GRBs, which often reveal new features. The long bright GRB 090902B [Abdo et al., 2009a] spectrum has similar characteristics to the bursts presented above. The most energetic photon detected from GRB 090902B was received 82 s after the GBM trigger. The burst spectrum showed an extended power law which contributed from low-energy range up to high energy, similarly to the short GRB 090510. This spectrum showed a hard low-energy index (α_{Band}=0.07) which is difficult to explain by the usual synchrotron model [Abdo et al., 2009a]. This motivated to interpret the

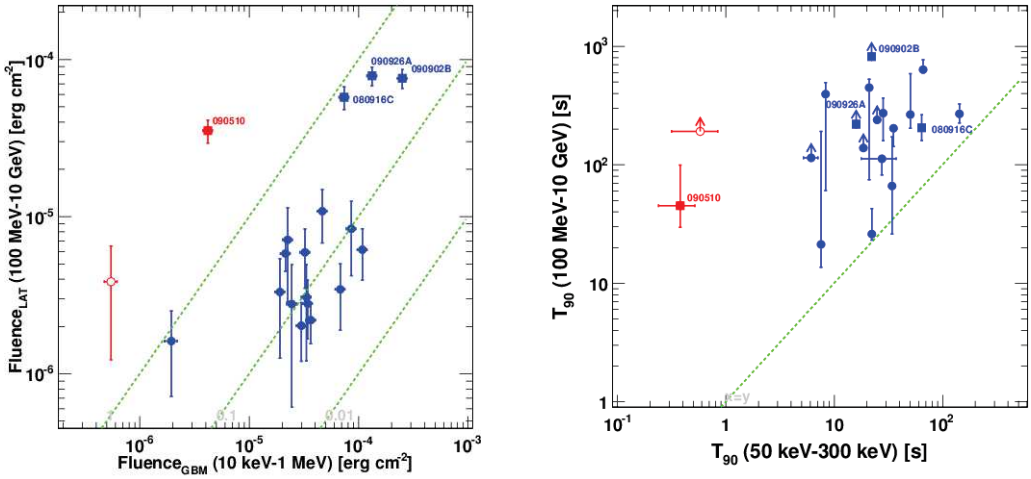

Figure 1.17: ***Left:*** *Fluence of the GRBs of the first LAT GRB catalog measured in the LAT energy range (100 MeV - 10 GeV) with respect to that measured by the GBM (10 keV - 1 MeV) during the T_{90} determined by each instrument.* ***Right:*** *The 90% emission duration determined by the LAT and GBM for the GRBs of the 1rst LAT GRB catalog. This figure shows evidence for a long-lived emission at high energies. Both figures are taken from Ackermann et al. [2013b]*

spectrum of this GRB by a pure photospheric model [Ryde et al., 2010]. The origin of this contribution still needs to be clarified with more GRB statistics and with detailed physical models dedicated to understanding the broadband GRB spectra.

In the light of the GRB properties discussed so far, it appears that their prompt keV-MeV spectrum has a different origin than the MeV-GeV spectrum. These observations show a good agreement with the prediction of the forward shock model, associating the LAT emission to the afterglow phase. The delayed onset in this model is assumed to be the time required for the flux to increase during the early afterglow phase [Razzaque, 2010]. However, this model cannot explain the fast variability observed in most of the bright GeV light curves e.g. GRBs 090510A, 090902B and 090926A. Furthermore, one of the evidence for an internal origin of the GeV radiation was the detection of GRB 090926A. The multi-detector light curve of GRB 090926A, presented in Fig.1.18 (left), shows a sharp spike at 10 s post-trigger that was observed by all *Fermi* detectors (GBM NaIs and BGOs, LAT), with an unprecedented synchronization (within 50 ms) between all energy bands. This feature as well as the extreme variability seen in its light curve suggest that both the low- and high-energy emissions, which both occur during the keV-MeV prompt emission, have an internal origin (e.g., internal shocks). More interestingly, this burst was the first to show a spectral break at high energy ($\sim$ 400 MeV) which was detected during the sharp spike in a coincidence with the apparition of the extended power-

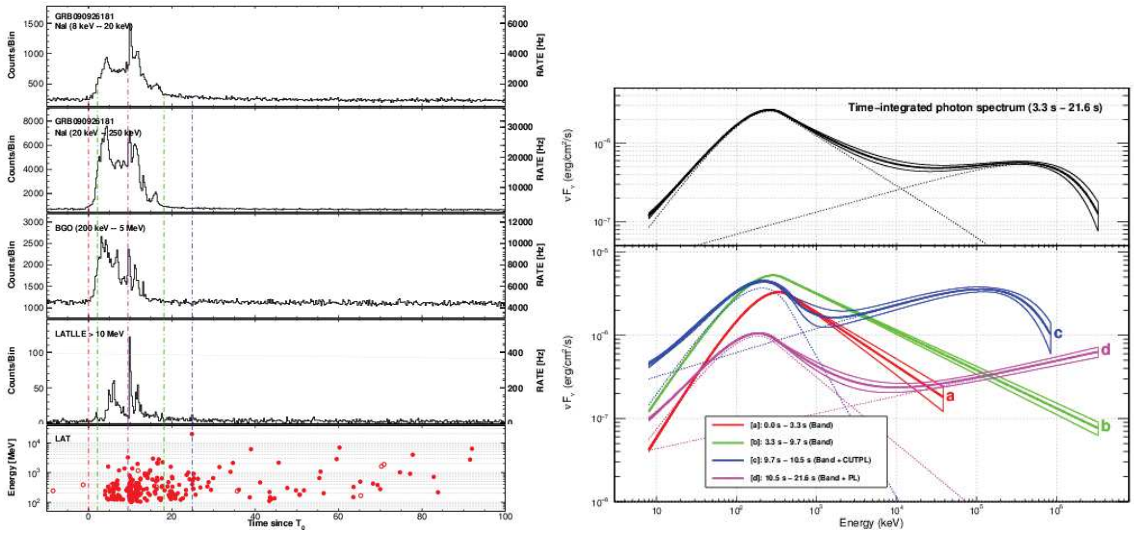

Figure 1.18: ***Left:*** *Multi-detector light curve of GRB 090926A as seen by the GBM and the LAT: summed GBM/NaI detectors (first two panels), GBM/BGO (third panel), Low LAT Energy data above 10 MeV (fourth panel) and LAT events above 100 MeV.* ***Right:*** *Spectral energy distribution of GRB 090926A as seen by the Fermi instruments in a time-integrated analysis (top) and a time-resolved analysis (bottom). Both figures are taken from Ackermann et al. [2013b]*

law component (Fig.1.18, right). This spectral break was used in [Ackermann et al., 2011] to estimate directly the Lorentz factor of the jet using different $\gamma\gamma$ absorption models. Using the $\gamma\gamma$ opacity described in Sect.1.4.1, with the variability time scale of the keV-MeV component of this GRB, the obtained values for Γ range from 200 to 700. Follow-up observations of this burst by the Very Large Telescope (VLT) [Rau et al., 2010] were used to estimate its redshift, z=2.1071 $\pm$ 0.0004. This redshift was confirmed by D'Elia et al. [2010] using the X-Shooter observations (z=2.1071 $\pm$ 0.0001). As a result, the isotropic equivalent energy $E_{\gamma,iso} \approx 2.4\times 10^{54}$ ergs in 10 keV - 10 GeV within the GBM T_{90} ($\sim$16s) places it among the most energetic bursts seen by the LAT.

The long GRB 100724B is an interesting burst in various respects. This burst was the most fluent burst in the GBM sample used for the first LAT GRB catalog, but was not that bright in the LAT energy range [Ackermann et al., 2013b]. Its most energetic photon of 0.22 GeV was detected $\sim$62 s post-trigger. Unlike all the reported bursts, GRB 100724B did not show any extra component at high energy and its spectrum is attenuated in the LAT energy range, with an observed cutoff at $\sim$40 MeV [Vianello et al., 2017]. Moreover, a detailed analysis of this burst made by [Guiriec et al., 2011] revealed the existence of a weak thermal component with a Black Body (BB) spectrum at low energy (kT= 615$\pm$29 keV), in addition to the

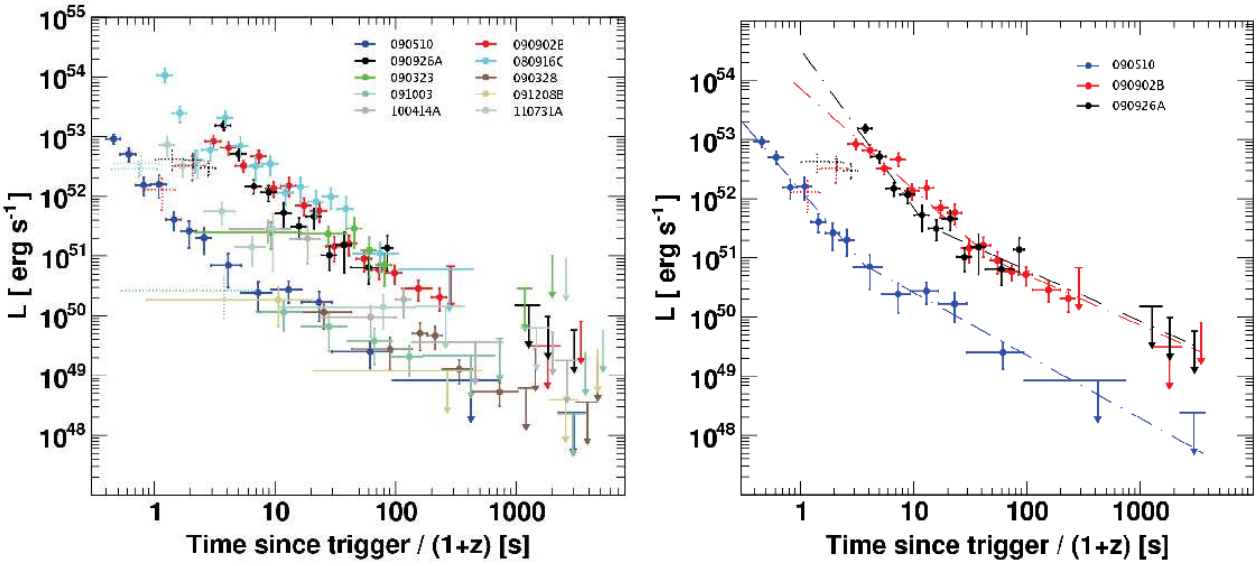

Figure 1.19: ***Left:*** *Light curve of the luminosity above 100 MeV for the GRBs with known redshift in the first LAT catalog.* ***Right:*** *Luminosity light curves of GRBs 090510, 090902B and 090926A with a broken power law. Both figures are taken from Ackermann et al. [2013b]*

non-thermal Band function. A thermal component has been also detected in the spectra of GRBs 110721A [Axelsson et al., 2012] and 120323A [Guiriec et al., 2013].

All of these components at low- and high-energy, show that GRB spectra in the keV-MeV domain are more complicated than the synchrotron spectrum predicted by the internal shock model. The thermal component has been predicted since a long time ([Daigne and Mochkovitch, 2002], see also the recent work in [Hascoët et al., 2013]), but is has been detected only in a few GRB spectra. However, it might be present in the spectra of all GRBs but hard to detect. The delayed onset as well as the detection of GeV emission at early times still also to be explained. Complete broadband physical models which are devoted to answer these questions and to understand the properties of the GRBs are imperious needs. Detailed spectro-temporal analyses of the detected GRBs are also required for this aim (see a detailed analysis of the bright GRB 090926A in Chap.5).

At later times, the GRB spectra at GeV energies can be more easily explained. The luminosity evolution with time of most of the GRBs studied in the LAT first catalog shows a simple power-law decay ($L(t) \propto t^{\delta}$) with an index $\delta \simeq -1$ (see Fig.1.19, left panel). It is also found that the photon index λ of the GeV spectra of the studied GRBs clusters around a constant value of $\sim$-2. This apparent non-variation of the index of these spectra is in contrast with the extreme variability

seen in the keV-MeV emissions, which are likely related to internal processes (e.g., internal shocks). Both these results ($\delta \simeq$-1 and $\lambda \sim$-2) are a clear evidence for an external origin of the high-energy emission due to the forward shock of the jet with the circum-burst medium during the afterglow phase. Only three bursts in the first LAT catalog (GRBs 090510, 090902B and 090926A) showed temporal breaks in their luminosity light curve (Fig.1.19, right). The increase of the temporal index δ (from $\sim$-2 to $\sim$-1 after the break time) for these GRBs suggests a transition between the prompt phase of the GeV emission to its afterglow phase.

GRB 130427A shows a different behavior than the other LAT brigh GRBs. The GeV emission of this burst starts only after the end of the keV-MeV emission. This burst is the brightest and the most fluent GRB ever seen by the LAT, with a GeV emission lasting for $\sim$19 hours [Ackermann et al., 2014]. Its highest energy photon of 95 GeV was detected $\sim$4 minutes post-trigger, and it is the most energetic photon ever detected from a burst. More than 15 photons were recorded above 10 GeV including a photon of 73 GeV detected 19 s post-trigger and another photon of energy 32 GeV detected $\sim$9.5 hours later. This burst is occurred at a redshift z=0.34 which explains its huge fluence ($\sim 4.2\times10^{-3}$erg cm^{-2}). The high-energy emission started after the end of the keV-MeV emission in the GBM. This differs considerably from all other LAT bright bursts, for which the GeV emission onset occurred before the end of the prompt keV-MeV emission. Its GeV light curve showed a soft evolution at early times, before the start of the X-ray afterglow as observed by the *Swift*/XRT. At later times, the GeV flux decays with a temporal index δ=1.17$\pm$0.06, and the spectral photon index remains constant and close to -2 (see the middle panel of Fig.1.20). These observations indicate that the high-energy emission of GRB 130427A is associated with the afterglow phase. The detection of this burst questioned the synchrotron model which is thought to be the dominant process responsible for the high-energy emission during the afterglow phase. In the synchrotron emission model it is expected that all the high-energy photons should be less than the maximum synchrotron photon energy $E_{syn,max}$. Assuming a single acceleration and emission region, this energy is derived by equating the electron acceleration and synchrotron radiative cooling timescales, t_{acc} and t_{syn}. The former can be obtained as the timescale of an electron Larmor gyration ($2\pi R_L/c$). In the case of GRB 130427A, $E_{syn,max} \sim 80\ \Gamma(t)$ MeV, which is represented in Fig.1.21 as a function of time, using a prescription for the decrease of the jet Lorentz factor Γ (see more details in [Ackermann et al., 2014]). This figure shows that the two most energetic photons at 73 GeV and 95 GeV are incompatible with this synchrotron limit. The absence of a detection of an Inverse Compton component in the LAT energy range shows that the canonical forward-shock synchrotron model is not able to explain the spectrum of this burst, suggesting a new emission process and/or a new acceleration mechanism, e.g. magnetic reconnection [Ackermann et al., 2014].

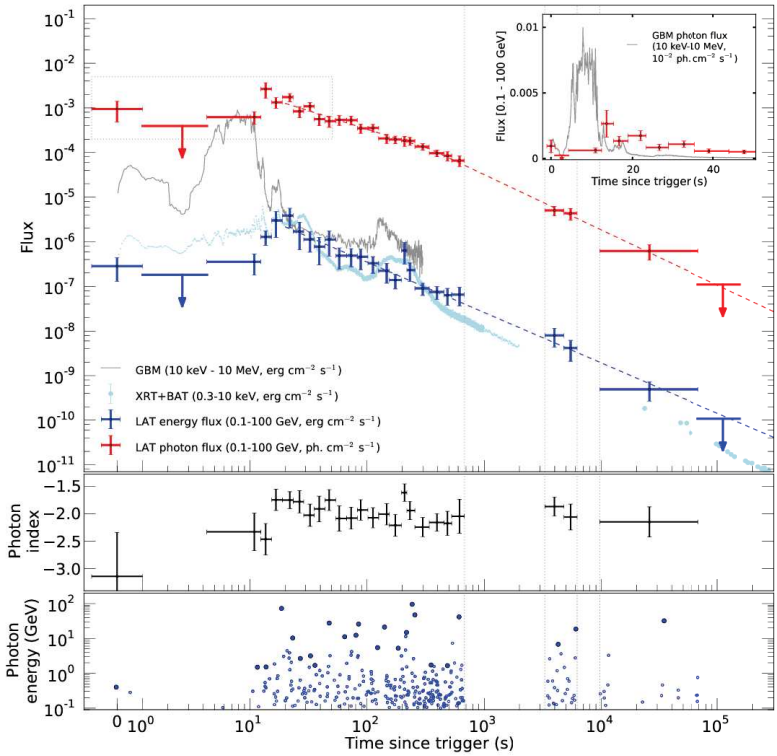

Figure 1.20: *Temporal profile of GRB 130427A as seen by Fermi and Swift.* ***Top:*** *LAT energy flux (blue), LAT photon flux (red), GBM energy flux (gray) and XRT+BAT (light blue) energy flux light curves. The photon flux light curve from the GBM is presented in the inset (gray) in a linear scale with an expanded view of the first 50 seconds. Middle: LAT photon index.* ***Bottom:*** *Energies of all the photons associated with the GRB with probabilities >90%. Filled circles correspond to the photons with the highest energy for each time interval. The vertical gray lines indicate the two time intervals during which the burst was occulted by the Earth. Figure taken from Ackermann et al. [2014]*

1.5.2 Future GRB multi-wavelength and multi-messenger observations

After nearly fifty years of research, the GRB field is not completely explored and the debates about their origins and physical mechanisms remain to be settled. The fascinating properties of GRBs make them the observational targets of a lot of instruments in a wide range of wavelengths. Following on the success of the missions presented in the previous sections, a new generation of instruments will be devoted to completing the puzzle.

Observations of GRBs in the very high energy range (VHE, $\sim$ tens of GeV up

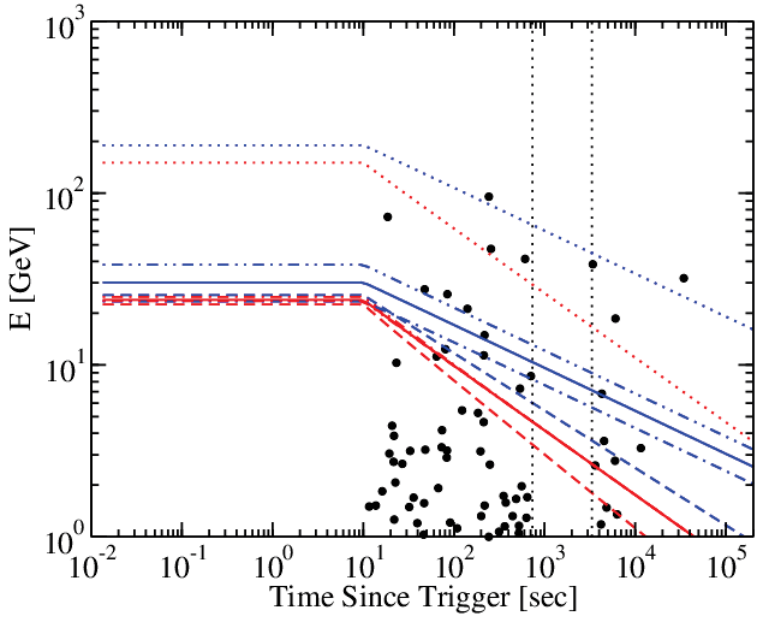

Figure 1.21: *Maximum synchrotron energy in the forward-shock model for GRB 130427A as a function of time. The red and blue colors correspond respectively to a uniform density of the inter-stellar medium and massive star wind environment. The different line styles correspond to different hypotheses on the initial value of the jet Lorentz factor. Black dots indicate the high-energy photons detected by the Fermi/LAT. Figure taken from Ackermann et al. [2014]*

to TeV) will help to identify the main particles (leptons or hadrons) responsible for the high-energy emission, as well as their acceleration mechanisms. The detection of high-energy photons by the LAT, for instance the 73 GeV and 95 GeV photons from GRB 130427A, is promising for future GRB detections in the VHE range. However, due to the low photon flux that is expected in the VHE domain, instruments with large effective areas are needed to collect enough signal. Since this condition is difficult to fulfill in space (the largest detector in space is the *Fermi*/LAT, with a $\sim$1m^2 area), ground-based imaging atmospheric Cherenkov telecopes (IACTs) must be employed. VHE particles (gamma rays and charged cosmic rays) create showers of charged particles by interacting with the upper atmosphere. The secondary particles, which travel faster than the speed of light in the atmosphere, produce a flash of Cherenkov light (mostly at blue-UV wavelengths) that is recorded from the ground by dedicated telescopes equipped with fast electronics. In this detection technique, the atmosphere is used as a big calorimeter, therefore, it is considered an essential part of the instrumentation. Several Imaging Atmospheric Cherenkov Telescopes (IACTs) are in operations nowadays: H.E.S.S.[14] (High-Energy Stereoscopic System)

[14] `https://www.mpi-hd.mpg.de/hfm/HESS/`

in Namibia, MAGIC[15] (Major Atmospheric Gamma-ray Imaging Cherenkov telescopes) in the Canary Islands and VERITAS[16] (Very Energetic Radiation Imaging Telescope Array System) in Arizona. In the future, the two Cherenkov Telescope Arrays (CTA, [Actis et al., 2011]), each comprising several tens of telescopes, will cover the two celestial hemispheres with unprecedented sensitivity in the VHE range.

Starting from the bright bursts detected by the LAT (e.g., GRB 090902B) Gilmore et al. [2013] and Inoue et al. [2013] assumed different GRB spectral shapes (extrapolation of the `Band` function, or flat SED) to estimate a GRB detection rate with CTA that is close to 1 or 2 per year. The main reasons for such low detection rates are the low duty cycle (∼10%), the limited field of view of CTA (a few degrees per telescope) and the Extragalactic Background Light (EBL) which absorbs the photons of distant GRBs above 10 GeV.

An alternative technique is used for the HAWC[17] experiment (High-Altitude Water Cerenkov detector, 250 km East of the Mexico city), a synoptic detector which consists of ∼300 water tanks to sample the atmospheric showers on the ground, with a large FoV and a high duty cyle [HAWC Collaboration, 2012]. Since this experiment has a higher energy threshold and a smaller sensitivity than the CTA telescopes, it is well suited to the detection of the shortest GRBs, whose emission is more distinguishable from the cosmic-ray background events.

It is commonly known that the acceleration mechanisms presumed for GRBs, i.e. shock acceleration or magnetic reconnection, are also considered for producing cosmic rays at ultra high energies (>PeV[18]) [Vietri et al., 2003]. Over the past decade, the spectrum, composition, and sky distribution of these particles have been measured with unprecedented precision by the Pierre Auger Observatory in Argentina [Abraham et al., 2010; Abreu et al., 2011]. Moreover, astrophysical secondary neutrinos have been seeked by the IceCube[19] in Antarctica and ANTARES[20] in the Mediterranean Sea, which will be followed by the KM3NeT[21] telescope in the near future. In 2013, Aartsen et al. [2013] announced the detection by IceCube of the first PeV neutrinos with an extragalactic origin, while their origin (for which GRBs are good candidates) is still unknown. Recently, the IceCube collaboration announced the detection of a very rare neutrino triplet, but did not find any electromagnetic counterpart based on multi-wavelength observations including *Swift*/XRT, *Fermi*/LAT, VERITAS and HAWC data [Aartsen et al., 2017].

[15] `https://magic.mpp.mpg.de/`

[16] `https://veritas.sao.arizona.edu/`

[17] `http://www.hawc-observatory.org/`

[18] 1 TeV= 10^{12} eV. 1 Petaelectron volts (PeV) = 10^{15} eV. 1 eV= $1.602176565 \times 10^{-19}$ joules (J).

[19] `https://icecube.wisc.edu/`

[20] Astronomy with a Neutrino Telescope and Abyss environmental RESearch in France, `http://antares.in2p3.fr/`

[21] `http://www.km3net.org/`

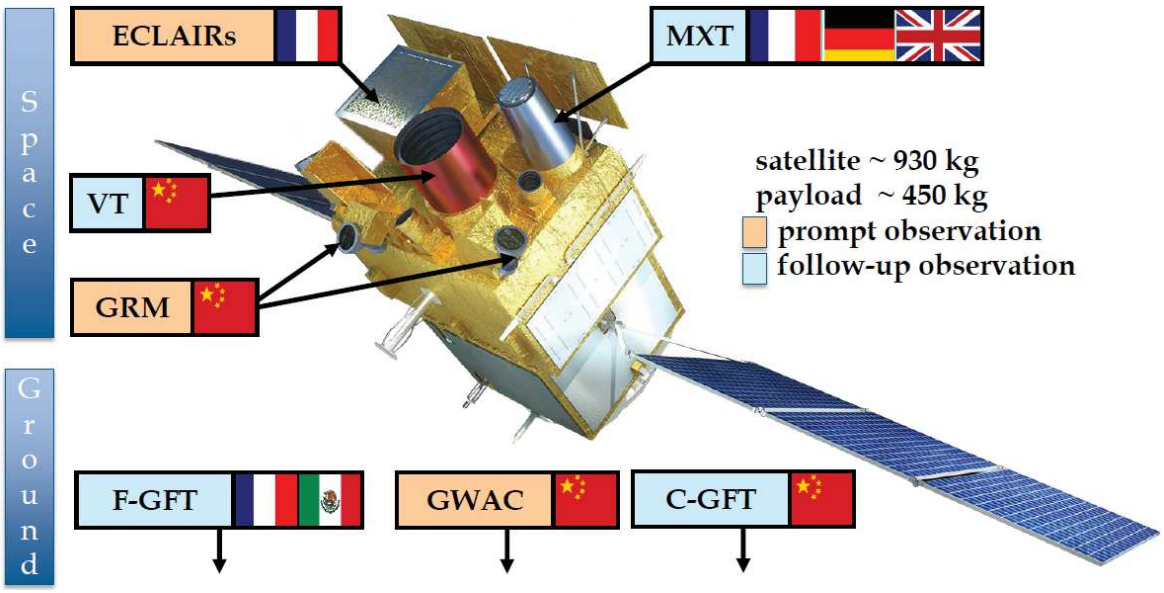

Figure 1.22: *The 7 instruments of the SVOM mission. Figure taken from Wei et al. [2016]*

The short-type GRBs are considered to be good candidates for Gravitational Wave (GW) emission, as mentioned in Sect.1.4.2. The two interferometers of the LIGO experiment in the USA [Abbott et al., 2009] and the VIRGO interferometer in Italy [Accadia et al., 2012] have been in operations for several years. Thanks to the advanced-LIGO detector, the first gravitational wave source was detected in 2015 and it was interpreted as the merger of two massive black holes [Abbott et al., 2016]. Searches for a GRB counterpart were performed, in particular using the archival data of the LAT [Ackermann et al., 2016] and of the GBM [Connaughton et al., 2016]. However, the localization of the GW was outside the LAT FoV, therefore only flux limits on a possible counterpart were derived at later times. On the other hand, the GBM team announced the detection of a weak transient signal, 0.4 s after the GW detection with less than 3σ of significance [Connaughton et al., 2016]. The *INTEGRAL/SPI*-ACS observations at the LIGO trigger time allowed to derive strong upper limits on the gamma-ray emission associated with the GW event for the whole localization region [Savchenko et al., 2016]. As shown by the second firm detection of a GW event by LIGO in 2017 [Abbott et al., 2017], more discoveries of GW sources are expected in the near future. In some cases, the simultaneous detections of short GRBs with optical or gamma-ray telescopes will put strong constraints on the merger model and help to understand the nature of this class of GRBs.

GRB observations with *Swift* led to important discoveries regarding their afterglow emission phase and their host galaxies, while the *Fermi* instruments improved significantly the spectro-temporal coverage of their prompt emission phase. However, the connection between both emission phases, as well as the acceleration mechanisms and radiative processes which occur throughout the GRB, are far from being fully understood. Besides, most of the *Fermi* GRBs have unknown redshifts. The SVOM (Space-based multi-band astronomical Variable Objects Monitor) mission will be launched in a few years (end of 2021). It comprises four instruments on the satellite payload, and three ground optical telescopes (Fig.1.22). One of the main objectives of SVOM is to build a sample of GRBs of all types with a high fraction of redshift determination and with a complete observation of each event, from the prompt phase to the late afterglow phase. SVOM is a collaborative project between the Chinese and the French space agencies and the Chinese Academy of Sciences. It will cover the prompt γ-ray emissions from 4 keV up to 5 MeV thanks to its two instruments ECLAIRS and GRM. It will also observe the afterglow emissions in the X-rays (0.3-6 keV) and in the visible domain (400 - 950 nm) with its two narrow-field instruments, the MXT and the VT, respectively. Furthermore, with its ground-based wide camera GWAC and the two robotic instruments C-GFT and F-GFT, it will be able to follow-up both the prompt and afterglow emissions of the detected GRBs at larger wavelengths (400 - 1700 nm) providing an accurate localization. After the detection of a GRB by ECLAIRS, the initial localization with an accuracy better than $12^{'}$ will be sent immediately to the ground, and also used to repoint the satellite and the narrow-field instruments within 5 minutes in case of a bright signal. The MXT and the VT telescopes are devoted to localize the burst more precisely with an accuracy better than $\sim 30^{''}$ and $\sim 1^{''}$ respectively. Thanks to the wide fields of view of the GRM ($>$2 sr) and ECLAIRS (2 sr) as well as to the rapid slewing capability of the whole system, 70 to 90 GRBs are expected to be detected in gamma rays per year, and $\sim$60 bursts are expected to be detected by the MXT and the VT. These multi-wavelength observations will facilitate the redshift measurement of a significant fraction (50 %) of the detected GRBs, increasing the possible detection of high-redshift GRBs of z $>$5 (3-4 GRBs/year) and 6$<$ z $<$ 7 ($\sim$1 GRB/year) [Wei et al., 2016]. The sample of softer bursts will include a good fraction of XRF and XRR bursts, allowing to better identify and characterize the different types of GRBs. In addition, the SVOM observations are expected to increase the fraction of short GRBs with measured redshift, thanks to the nearly antisolar pointing, and to the rapidity and the follow-up capability of the system. Together all the instruments of SVOM will allow to observe the whole GRB spectrum from the first prompt emissions up to the afterglow covering the transition zone between the two phases which has not been well explored. Therefore, the SVOM observations are expected to help understand the emission mechanisms of both the prompt and afterglow emissions answering questions like [Wei et al., 2016]:

- Is the prompt phase the product of internal shocks or reconnection? What are the main energy reservoirs of the jet?

- Is the forward external shock the main mechanism for the afterglow emission? What is the contribution from the reverse shock?
- What are the different spectral components of the jet emissions?

As was shown in Sect.1.5.1, the GBM observations revealed a thermal component and/or an additional power-law component at low energy in some GRB spectra. With the low-energy limit of the coded-mask detector ECLAIRS (4 keV), it will become possible to collect more statistics at low energy and therefore to better constrain the spectral features in this energy range. Moreover, this low-energy spectral reach will provide better constraints on the spectral parameters, particularly the α parameter of the `Band` function which suffers from the death line problem (see Sect.1.4.3).

CHAPTER 2

The *Fermi* Gamma-ray Space Telescope

Contents

This chapter is dedicated to describe the *Fermi* Gamma-ray Space Telescope. The properties of the *Fermi* satellite are described in Sect.2.1. In Sect.2.2, the two observing modes of the *Fermi* observatory are presented. The two instruments carried by the satellite, the GBM and the LAT, are described in Sects.2.3 and 2.4 respectively. The performance of these instruments is as well discussed in these sections.

2.1 The *Fermi* observatory

The *Fermi* observatory, formerly known as GLAST (for Gamma-ray Large Area Space Telescope) has been launched on June 11, 2008, by the NASA in order to

Figure 2.1: *The Fermi spacecraft and its payload: the LAT instrument at the top is here covered by its anti-meteorite shield, while the GBM scintillators are visible at the bottom (left) side.*

study the γ-ray sky (Fig.2.1). The two instruments of *Fermi* (GBM and LAT) were developed by international collaborations gathering several laboratories in the USA, Germany, France, Italy, Sweden and Japan. The satellite has been put on a circular orbit at an altitude of 565 km with an inclination of 25.6° from the equator. Its orbit has a period of ∼96 minutes and it precesses with respect to the celestial pole every 53.4 days (for more details see [Ackermann et al., 2012a]). Both the altitude and the inclination angle were chosen in order to minimize the background of cosmic rays.

2.2 Observing modes

The *Fermi* satellite has two observing modes: the "scanning" and the "pointing" modes. The scanning (survey) mode is the default observation mode of *Fermi* which is an all-sky survey. It is optimized to provide relatively uniform coverage of the entire sky every three hours (two orbits) observing each point on the sky for roughly 30 minutes. In this mode of observation, the satellite is inclined from the local Zenith by a certain angle called *rocking angle* switching either to the North or to the South pole at the beginning of each new orbit. During the first three months of operations, the *rocking angle* was 35°, but was changed to 50° to decrease the temperature of the satellite's batteries [Ackermann et al., 2012a].

In addition, *Fermi* is able to perform pointed observations which allow to maximize the exposure time on selected parts of the sky. In this mode, the target is

placed near the center of the field of view to maximize the effective detection area. This observation mode called Target of Opportunity (ToO) is manually scheduled and transmitted to the satellite. The ARR (Autonomous Repoint Request), another pointed observation mode, is an automatic request which is sent to the LAT on board when a GRB is detected by the GBM with sufficient brightness and/or fluence (two different configurable thresholds). During the ARR, the spacecraft slews within minutes to place the GBM-detected GRB near the center of the LAT field of view (at 10° from the center of the LAT field of view).

During each orbit, the *Fermi* satellite passes in the South Atlantic Anomaly (SAA) area where the Earth's inner Van Allen belt[1] is the closest to the Earth's surface than elsewhere dipping down to an altitude of 200 km. The SAA is a direct consequence of the difference between the terrestrial geographic pole and the magnetic pole. Due to the high cosmic radiation level, the *Fermi* detectors are switched off during the passages within the SAA, which decreases the total observing time by ∼15% on average [Ackermann et al., 2012a]. In practice, the on board definition of the SAA zone is different for the two instruments of *Fermi*. The SAA contours for the LAT are represented by the polygon shown in Fig.2.2 (see more details in [Atwood et al., 2009]).

2.3 The Gamma-Ray Burst Monitor

The GBM [Meegan et al., 2009] is a detector of X-rays and γ-rays in the energy range 8 keV-40 MeV aiming at studying transient sources such as GRBs and solar flares. It consists of 12 sodium iodide NaI(Tl) scintillators and 2 bismuth germanate (BGO) scintillators. Each of the 12 NaI detectors consists of a crystal of 1.27 cm thickness and 12.7 cm diameter with an aluminum housing and a photo-multiplier (PM) (Fig.2.3, top left). The NaI detectors cover the energy range 8 keV - 1 MeV with an energy resolution of ∼10 keV at 70 keV. The effective area of a typical NaI detector is ∼100 cm^2 between 20 keV and 1 MeV [Meegan et al., 2009]. The 12 NaI detectors are distributed around the *Fermi* spacecraft (see Fig.2.3, bottom left). Each of the 2 BGO detectors covers the energy range 150 keV- 40 MeV with an energy resolution of 100 keV at 1 MeV. The crystal of each BGO is surrounded by two PMs and it has a thickness and a diameter of 12.7 cm. The effective area of each BGO detector reaches ∼110 cm^2 for energies between 200 keV and 2 MeV. The 2 BGOs are positioned on opposite sides of the spacecraft so that at least one of them can observe any source detected by a NaI scintillator.

The placement of the GBM detectors all around the satellite (bottom left panel of Fig.2.3) offers to the GBM the possibility to observe a large portion of the sky with a FoV of 9.5 sr, i.e. the part of the sky that is not occulted by the Earth.

[1] belt of charged particles trapped by the Earth's magnetic field

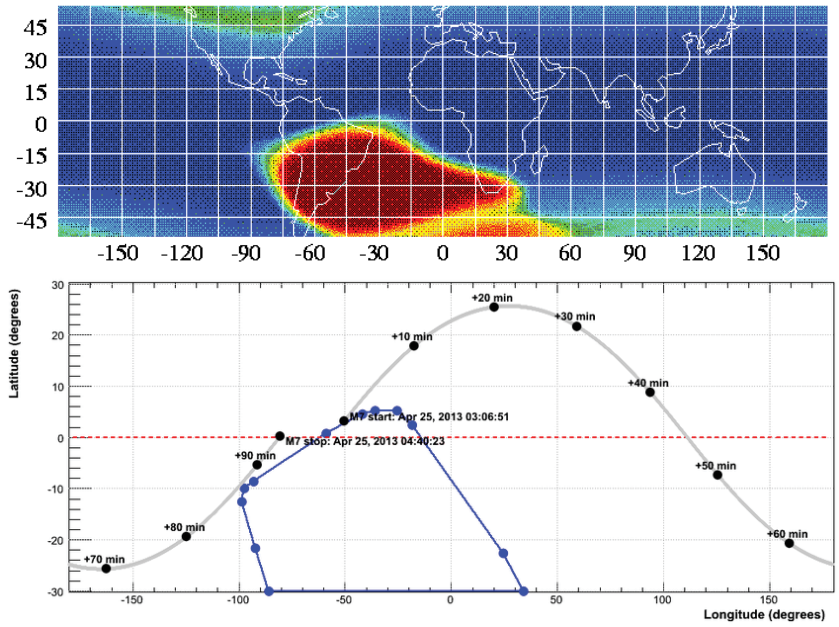

Figure 2.2: ***Top:*** *Position of the South Atlantic Anomaly at 560 km seen by ROSAT satellite in 1990 (taken from* `http://heasarc.gsfc.nasa.gov/docs/rosat/gallery/misc$_$saad.html` *).* ***Bottom:*** *Orbit of Fermi, the polygon in blue shows the SAA contour adopted for the LAT. This figure shows that a LAT data acquisition (or "run") starts after exiting the SAA region or crossing the equator, until the next entry in the SAA or crossing of the equator. From an internal data quality monitoring page.*

The energy domain of both the NaI and BGO together (8 keV - 40 MeV, 5 decades) covers the emission of a typical GRB spectrum with a resolution of 15% at 100 keV and 10% at 1 MeV [Goldstein et al., 2012]. The net dead time per event of the GBM instrument is nominally 2.6 μs, which is adapted to the study of sources with high variability such as GRBs. The performance of the GBM is summarized in Tab.2.1. The detection and the identification of a transient source is based on the NaI detectors. The difference between the detected events and the expected background of the NaI detectors, allows to claim or not a detection of a transient source. The onboard trigger algorithm scans various energy bands and timescales and it requires two or more NaI detectors to exceed a specific threshold that is set with respect to the background rate (see section 3.1.1). An onboard classification is also performed for each triggered event to estimate its probability of belonging to known classes of transients (GRBs, solar flare, particle event). The comparison of the relative ratios between the different NaI detectors that have seen the GRB from different angles, provides a localization within an error box of ∼10-15° [Connaughton et al., 2015; Meegan et al., 2009] (see more details in Sect.3.1). The rapid detection

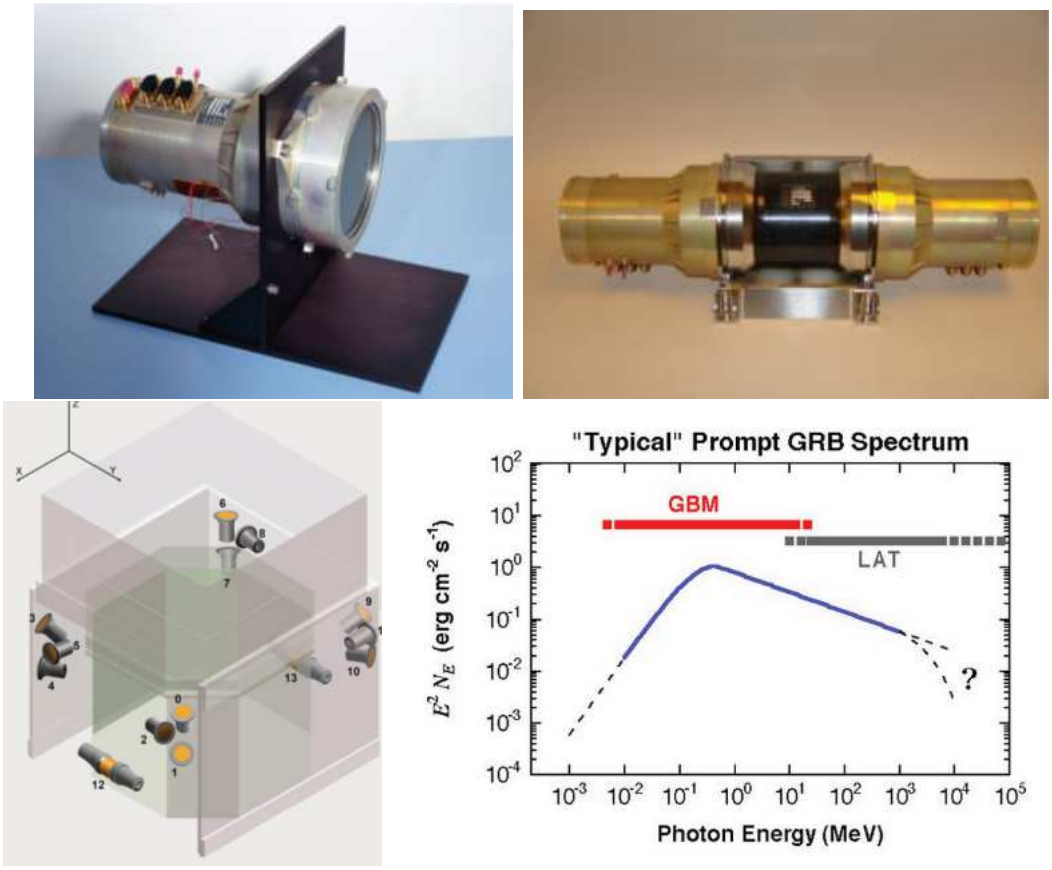

Figure 2.3: ***Top:*** *NaI (left) and BGO (right) detectors of the GBM.* ***Bottom:*** *(Left) Positions of the GBM detectors around the satellite (12 NaI and 2 BGO detectors (12-13)), (Right): The GBM energy range covers most of a typical GRB spectrum. Both the GBM and the LAT cover 7 decades of energy.*

capability of the GBM in wide energy and time ranges allows it to detect 2 bursts every 3 days. As of today, the GBM has detected more than 2000 GRBs including 300 SGRBs ($\sim$ 250 GRBs/year [Goldstein et al., 2012; Paciesas et al., 2012]). In addition to the GRBs, the GBM observes other types of transient sources such as magnetars and terrestrial gamma-ray flashes.

The NaI and BGO counts are recorded in three different data files: CSPEC, TTE, and CTIME. The CSPEC data has 128 PHA (for Pulse Height Analysis) bins i.e. energy bins, and has a default time binning of 4.096 s which drops to 1.024 s after a GRB trigger. The Time-Tagged Events (TTE) data has, like CSPEC, 128 PHA bins, but it contains individual events (unbinned in time) with 2 μs time resolution. Prior to November 2012 the TTE data were recorded from $\sim$ 30 s before to 300 s after the trigger time for every GRB detection. Since then, the TTE data are continuously

Characteristics	Capability
Energy range	8 keV to 40 MeV
Field of view	9.5 sr
Energy resolution (FWHM)	$\sim$ 15% at 100 keV ;$\sim$ 10% at 1 MeV
On-board trigger threshold	$\sim$0.7 $cm^{-2}\,s^{-1}$
On-board burst location error	$<$15°
Ground burst location error	$<$5° (+ few-15° syst.)
Burst trigger rate	$\sim$ 250 per year
Dead time per event	2.6 μs

Table 2.1: *Performance of the GBM onboard Fermi (From Meegan et al. [2009])*

recorded during the scanning operation mode. The CTIME data has a minimum temporal resolution of 64 ms with a bad energy resolution (8 PHA bins) which is not relevant for spectroscopy. All of these data are transferred via the Tracking and Data Relay Satellite System (TDRSS) to the GBM Instrument Operations Center (GIOC) in Huntsville, Alabama and to the Burst Alert Processor (BAP) at the NASA Goddard Space Flight Center (GSFC) to be processed on ground.

2.4 The Large Area Telescope

The Large Area Telescope (LAT, [Atwood et al., 2009]) is the main instrument on board the *Fermi* satellite. This gamma-ray imager is a pair-conversion telescope, which covers the energy range from $\sim$20 MeV to more than 300 GeV. Its performance are summarized in Tab.2.2. The LAT has a large effective area ($\sim$0.9 m^2 above $\sim$1 GeV), a wide field of view (2.4 sr, i.e. 20% of the sky), a low dead time ($\sim$27 μs) that is much lower than the *EGRET* one (100 ms), and a good angular resolution ($<$0°.15 above 10 GeV). As a result, the LAT detects more GRBs at high energy than *EGRET*, with more photons for each detected GRB. The LAT also observes, among others, AGNs, pulsars, pulsar wind nebulae and supernova remnants. Fig.2.4 shows the distribution on the sky of the 3033 sources listed in the third LAT catalog Acero et al. [2015].

The LAT consists of a 4×4 array of converting-tracking towers (see Fig.2.5, left) placed above 4×4 calorimeter modules. The tracker towers are covered by an anti-coincidence detector (see Fig.2.5, right) to reject most of the incident charged cosmic-rays. The main role of the tracker is to convert an incident γ-ray to an e^+e^- pair and to reconstruct the γ-ray direction from the tracks of the pair. The photon energy is principally measured by the calorimeter. These three sub-systems are described in section 2.4.1. The LAT trigger and filtering stage, the event reconstruction, and the event classification are described in Sects.2.4.2, 2.4.3 and 2.4.4 respectively. In Sect.2.4.5, I present the LAT instrument response functions, which are used in the

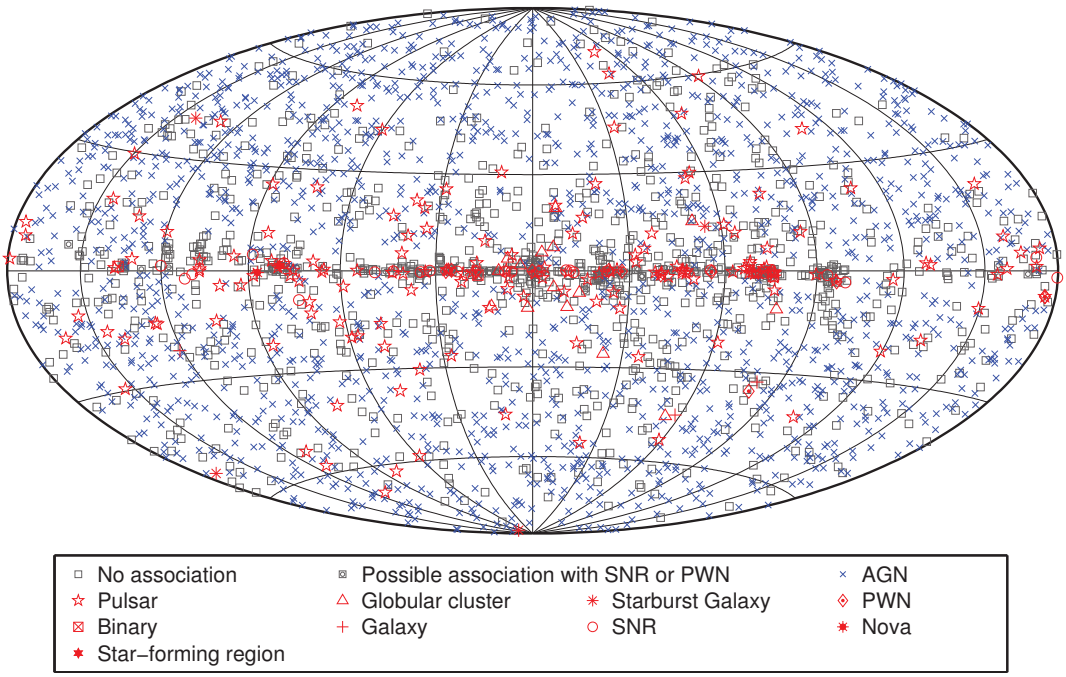

Figure 2.4: *Positions (in galactic coordinates) of 3033 galactic and extragalactic sources as seen by the* Fermi *telescope during the first four year of operation. Figure taken From the LAT 3FGL catalog Acero et al. [2015]*

GRB analysis described in the next chapter.

Characteristics	Capability
Energy range	20 MeV to 300 GeV
Field of view	2.4 sr
Energy resolution (on axis)	$\sim$ 9%-15% (100 MeV - 1 GeV)
	8%-9% (1 GeV - 10 GeV)
	8.5%-18% (10 GeV - 300 GeV)
Energy resolution ($>60°$ incidence)	$\leq$6% ($>$ 10 GeV)
On-board burst location error	$< 10'$
Ground burst location error	$< 1°$
Burst trigger rate	$< \sim$ 15 per year
Dead time per event	26.5 μs
Effective area at normal incidence	9500 cm^2

Table 2.2: *Performance of the LAT onboard Fermi after launch (From Atwood et al. [2009])*

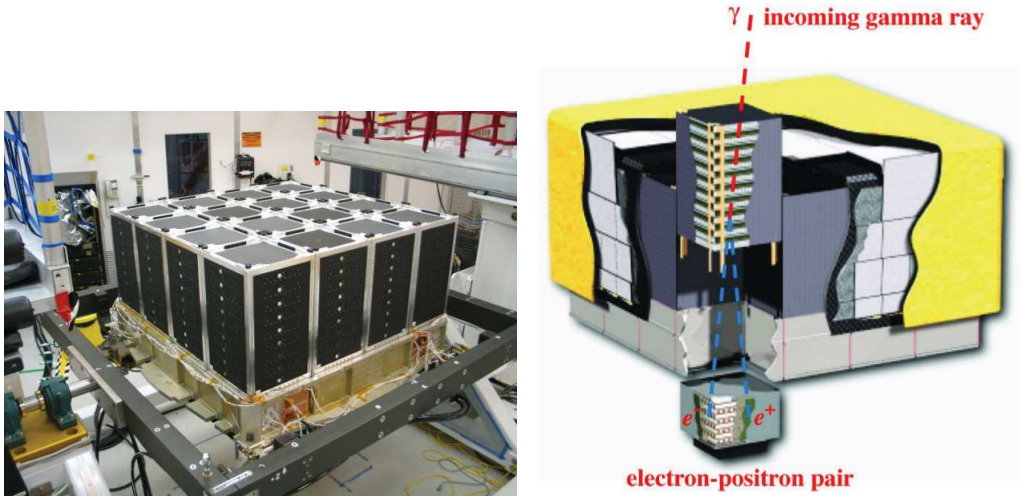

Figure 2.5: ***Left:*** *The 16 TKR towers and CAL modules during the LAT integration.* ***Right:*** *Passage of an incident photon in the tracker and its conversion into an e^+e^- pair. The pair deposits its energy in the calorimeter at the bottom of the tracker. The Anti-Coincidence Detector is represented in light grey, it is protected by an anti-meteorite shield represented in yellow.*

2.4.1 The LAT sub-systems

The converting and tracking system (TKR)

The converting and tracking sub-system of the LAT (TKR hereafter) consists of 16 towers. Each tower has a surface of 37^2 cm^2 and a height of 85 cm, and includes 18 planes of Silicon Strip Detectors (SSDs) (see Fig.2.6, left). Each plane has two SSD layers that are separated by a small space of 2 mm [Bellazzini et al., 2003], and oriented in X and Y in order to record the passage of charged particles. The pitch between two neighbor strips in an SSD layer is 228 μm. Each of the 16 planes placed in the upper part of the TKR is situated below a tungsten foil. Most of the time, the γ-rays that are detected by the TKR interact with one of the tungsten foils, producing an e^+e^- pair. The trajectories of the electron and positron are tracked by the following SSD planes (see Fig.2.6, right). The particles of the pair enter the calorimeter in most cases because of the low aspect ratio (0.4) of the TKR. The wide field of view of the LAT also results from this low height/width ratio.

The cross-section of the pair conversion process is proportional to the atomic number Z of the target material. Therefore, using tungsten (Z=74) foils in the LAT TKR ensures a high conversion probability. However, the tungsten foils of the first 12 planes (the "FRONT" section) have a small thickness (0.03 radiation length) to minimize the multiple scattering of the e^+e^- pair and to keep a good angular resolution. Indeed, the LAT angular resolution is determined by the multiple scattering

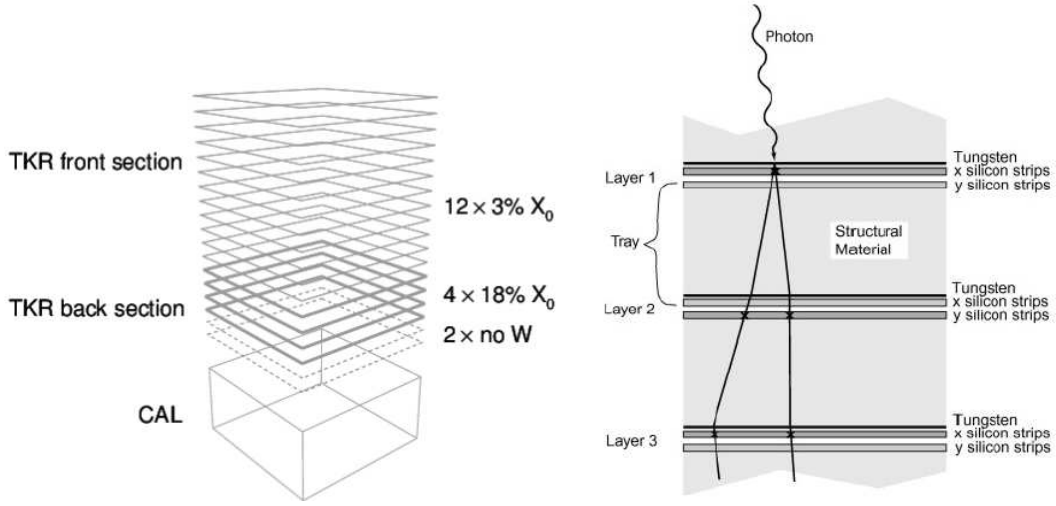

Figure 2.6: ***Left:*** *FRONT and BACK sections of a tower with a CAL module at the bottom [Ackermann et al., 2012a].* ***Right:*** *Pair conversion of an incident photon in the TKR. The silicon strip planes are used to localize the charged particles.*

at low energies, where it depends strongly on the photon energy as can be seen in Fig.2.10 (bottom, right). The foils in the following 4 planes (the "BACK" section) are thicker (0.18 radiation length) in order to increase the conversion probability and to recover the photons that did not convert in the upper part of the TKR. For these events, the angular resolution is worse. The last two planes do not have tungsten foils and are used only for the event reconstruction.

The calorimeter (CAL)

Each of the 16 TKR towers sits on top of a calorimeter (CAL) module. Each CAL module contains 8 layers of 12 CsI(Tl) crystals ($2.7 \times 2.0 \times 32.6$ cm^2), for a height of 8.6 radiation lengths. In total, the CAL has 1536 crystals and weighs $\sim$1800 kg. All crystals in a layer are aligned in the same direction (X or Y). The layers are arranged in a hodoscopic configuration, i.e. the preferred orientation of the crystals in a layer is orthogonal to that of the previous and next layers (see Fig.2.7). Two photo-diodes, with two gains each, are placed at each extremity of each crystal to collect the scintillation light. The large photo-diode covers the low-energy depositions ($< \sim$2 GeV) in the crystal while the small one is suitable for the high-energy depositions ($< \sim$70 GeV). The difference in the light intensities between the two extremities allows to localize the barycenter of the energy deposition in the crystal, with an accuracy that depends on the deposited energy (from less than 1 mm to a few mm).

An electromagnetic particle shower is produced in the CAL when the e^+e^- pair

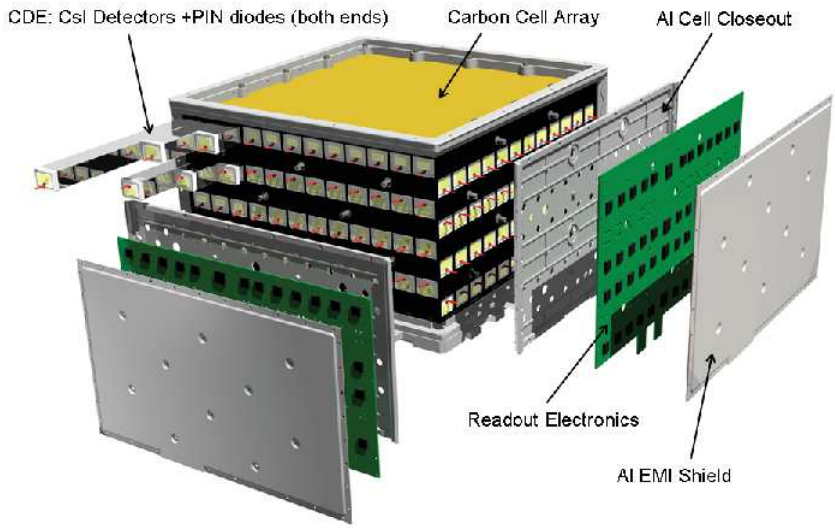

Figure 2.7: *Module of a calorimeter which containing 8 layers of 12 CsI(Tl) scintillators each.*

reaches a module. The energy depositions in the shower are recorded and localized by the CAL thanks to the hodoscopic configuration described above. This provides a 3D image of the shower that is used for the photon energy measurement. In addition to measuring the energy, the CAL also contributes to the identification and rejection of the charged cosmic-ray background.

The Anti-Coincidence Detector (ACD)

The *Fermi* satellite is exposed to an intense flow of charged particles which interact with the LAT. To limit this important background, the top and the sides of the TKR are covered by an Anti-Coincidence Detector (ACD, [Moiseev et al., 2007], see Fig.2.8) with an excellent efficiency to identify and reject the charged particles. The ACD is formed by 89 plastic scintillators (tiles) of thickness 1 cm and 8 ribbons. The tiles overlap in one direction to minimize the space between them and the 8 ribbons are implemented to cover the gaps in the other direction. The main function of the ACD is to veto the charged cosmic rays, which loss energy by ionization while crossing the tiles. In case of high-energy photons reaching the calorimeter, secondary particles created in the electromagnetic shower can propagate backward and hit the ACD. This so-called "backsplash" effect was the main reason for the self-veto of *EGRET*, and for the decrease of its γ-ray detection efficiency at high energies (with an effective area twice smaller at 10 GeV than that at 1 GeV). To limit the self-veto effect in the LAT instrument, its ACD is segmented in tiles, which permits to ignore the ACD veto in case of an incompatibility of the ACD hits with the TKR information. In the on board trigger algorithm, this comparison is simply based

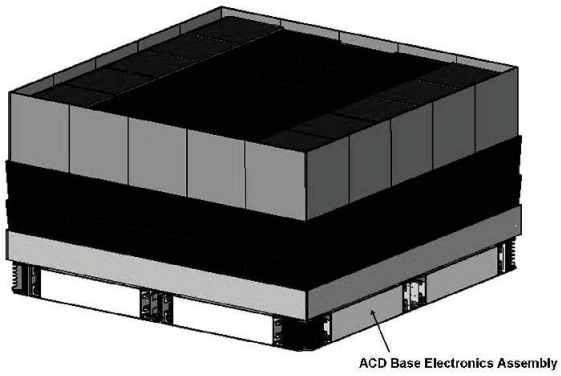

Figure 2.8: *Anti Coincidence Detector design. The ACD has a total of 89 plastic scintillator tiles with a 25 array on the top and 16 tiles on each of the four sides. In order to minimize gaps between tiles, the tiles overlap in one direction. In the other direction, scintillating fiber ribbons are used to cover the remaining gaps.*

on a list of ACD tiles associated with each TKR tower. In addition, the bottom skirt of the ACD tiles is not included in the trigger logic. In the on-ground event processing algorithms, the ACD hits are compared with the full information on the reconstructed direction of the incident particle. With this technique, the ACD vetoes only less than 20% of photon events at 300 GeV [Atwood et al., 2009].

2.4.2 On board trigger and filtering

The interaction of a particle with the LAT can lead to a trigger request activation. In order to pass the triggering stage, an event must fulfill specific combinations (called trigger engines) of trigger conditions (or primitives). Eight trigger condition can be combined together, in particular the `TKR`, `ROI`, `CNO`, `CAL_LO` and `CAL_HI` conditions (see [Ackermann et al., 2012a] for more details):

- The `TKR` trigger condition, also known as "three-in-a-row", is the most important one as it allows the LAT to trigger on the gamma-rays that converted in the TKR. It requires at least three (x,y) hits in three consecutive planes of a TKR tower.

- The `ROI` (for Region Of Interest) condition requires a hit in one of the ACD tiles associated with the TKR tower that triggered (see Sect.2.4.1). It is used by the trigger logic to identify the charged primary particles that cross the ACD before triggering the TKR.

- The `CNO` (for Carbon Nitrogen Oxygen) condition requires a large energy deposition in the ACD. It is used to identify the cosmic ions (Z>=6).

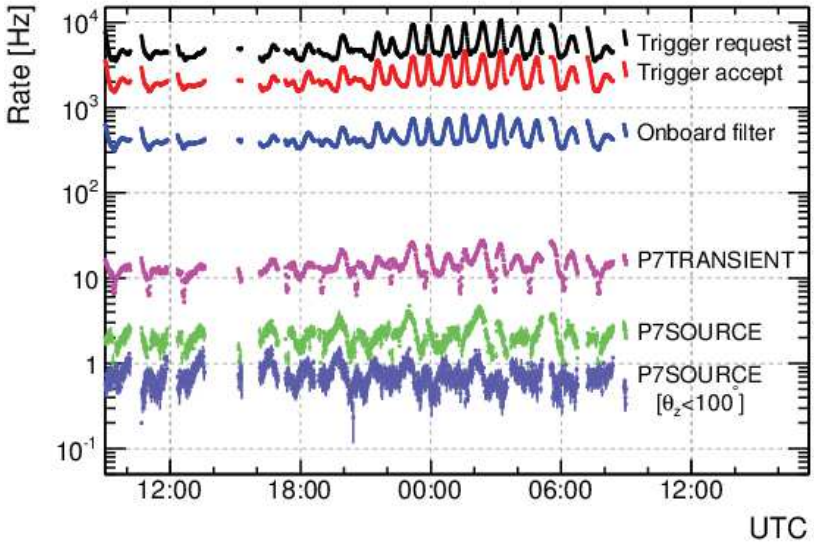

Figure 2.9: *Time modulation of the LAT event rates for a period of one day. From [Ackermann et al., 2012a]*

- The `CAL_LO` (resp. `CAL_HI`) condition requires more than 100 MeV (resp. 1 GeV) in any of the CAL crystals. Events that first satisfy the `CAL_LO` condition are discarded by the trigger logic since they correspond to primary particles entering the CAL from below or from its sides. The `CAL_HI` primitive is used to keep most of the high-energy events, which have low flux and trigger rate.

Astrophysical photons typically satisfy the `TKR` trigger condition, possibly one of the two CAL conditions, but not the `ROI` and `CNO` conditions.

At the end of the triggering process, each event is presented to several filtering algorithms. The main purpose of these filters is to reject a large part of the charged-cosmic ray background (without discarding γ-rays) and to decrease the data volume to be downlinked. In addition, the filters select samples of events that are useful for the instrument monitoring and calibrations. The GAMMA filter is the most important one since it has been designed to select most of the γ-rays (see more details [Ackermann et al., 2012a]). This selection is based on a simple track reconstruction performed on board. Above 20 GeV, all events are accepted by this filter owing to their relatively low event rate.

The LAT event rate decreases from a few kHz at the trigger level down to $\sim$400 Hz after filtering (see Fig. 2.9). The data are then downlinked to the ground through the TDRSS, 6 to 8 times per day. On ground, these data are transmitted to the ISOC (Instrument Science Operations Center) at the Stanford Linear Accelerator Center (SLAC), where the reconstruction and the classification of each event are

performed.

2.4.3 Event reconstruction

Since 2009, the LAT data have been released to the world-wide community as different versions of the data called "passes". Each pass corresponds to different reconstruction and/or classification algorithms, i.e. to different data sets and instrument responses. Soon after launch, the LAT collaboration realized that the instrument was affected by a new type of background events. These so-called "ghosts" are events which pass through the LAT during, or a few μs before, the trigger window opened by another event, producing residual electronic signals in all the LAT subsystems. In the initial Pass 6 data set, which was released in 2009, the ghost events were not handled by the reconstruction and classification software. However, these events were properly taken into account in the Monte-Carlo simulations (based on the Geant4 toolkit, [Agostinelli et al., 2003]), which are used to calculate the instrument responses. The Pass 7 data set was released after August 2011. It was based on an selection algorithm that had been re-optimized in order to take the ghosts into account [Ackermann et al., 2012a]. However, the reconstruction technique remained unchanged. In the same period, the LAT collaboration started to rebuild the event reconstruction and classification algorithms entirely. The most recent Pass 8 data set was released in June 2015, after years of dedicated efforts aimed at separating the ghost contributions from real events.

In Pass 8, the event-level analysis was improved in different areas and in all of the three LAT sub-systems. The previous reconstruction algorithms were based on identifying the hits in the TKR that were compatible with the centroid and main axis of the energy depositions in the CAL. However, this method was not suitable enough for low-energy events, which are the most affected by the ghosts. The Pass 8 approach is based on a "tree-based tracking" technique which searches for tree-like structures in the TKR independently of the CAL information. The back-splash effect is reduced, which improves the accuracy of the direction determination. In order to identify the ghosts in the CAL, a clustering algorithm was also introduced. This algorithm takes full advantage of the CAL hodoscopic configuration to measure the photon energy and direction from the electromagnetic shower. Another novelty in the Pass 8 reconstruction software is the search for a connection between the shower imaged by the CAL and possible hits in the ACD, independently of the TKR information. This allows to better identify the charged particle background. As a result the LAT acceptance and effective area have increased over its entire energy band between Pass 7 and Pass 8, especially below 100 MeV where the effect of the ghosts was more pronounced (see Fig.2.10).

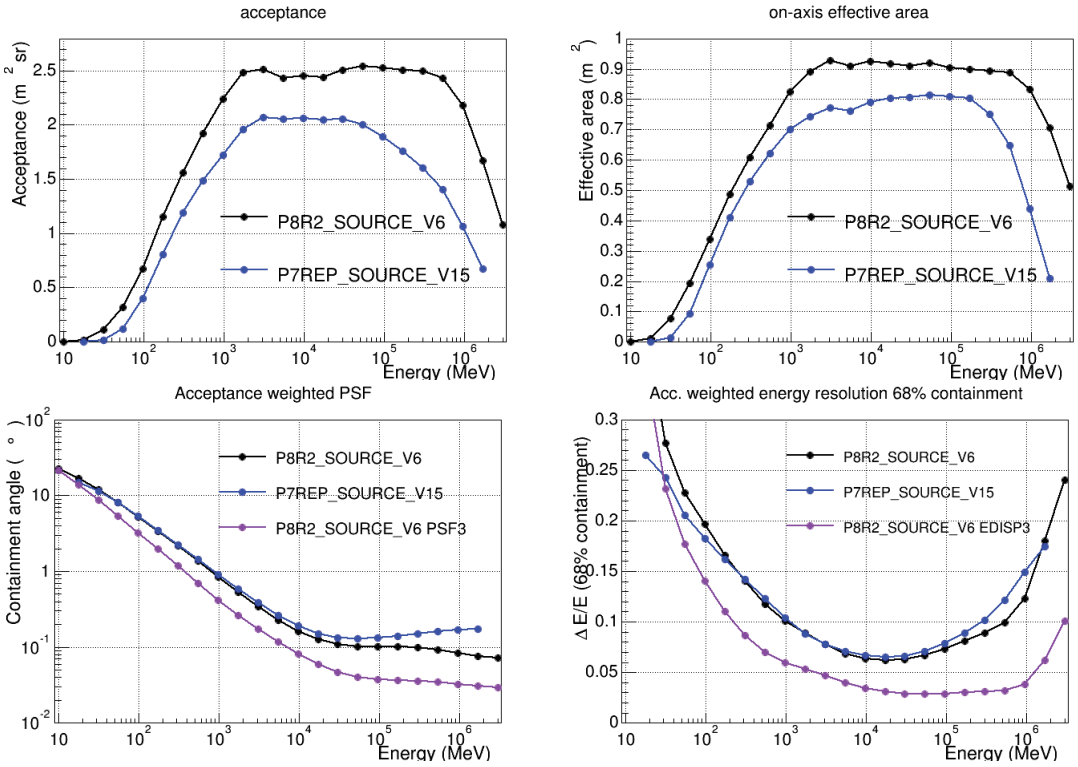

Figure 2.10: ***Top:*** *Comparison of the acceptance (effective area integrated over the field of view) and the effective area between the Pass 7 REP and Pass 8* `SOURCE` *event classes. Pass 7 REP is the reprocessed version of the first Pass 7 algorithm.* ***Bottom:*** *Comparison of the angular resolution and the energy resolution between the Pass 7 and Pass 8* `SOURCE` *event classes. Pass 8 PSF3 and EDISP3 correspond to the sub-classes of events with the best angular and energy resolutions, respectively. Taken from* `http://www.slac.stanford.edu/exp/glast/groups/canda/lat_Performance.htm`*. The four figures show a clear improvement of the performance of the LAT with Pass 8.*

2.4.4 Event classification

Based on the quality of the reconstructed events, selection cuts have been defined by the LAT collaboration to classify the data in different classes corresponding to different levels of residual backgrounds. Five classes of photon candidates are defined with a decrease of the signal contamination by the cosmic-ray background:

- `TRANSIENT` class: this class has the largest effective area with respect to the other classes since it is obtained with less stringent selection cuts. Therefore, this class corresponds to the highest background rate, of the order of ∼10 Hz or more (see Fig.2.9). This class is recommended for transient sources such as the GRB prompt emission and solar flares, whose durations are short enough

to limit the number of background events. Several `TRANSIENT` classes have been defined corresponding to different background levels. The `TRANSIENT100` event class has the larger background rate with respect to `TRANSIENT020` and `TRANSIENT010`. The background rates in these event classes are equal to 10, 2 and 1 times the isotropic diffuse γ-ray background, respectively.

- `SOURCE` class: this class is a sub-class of the `TRANSIENT` class, with a background event rate less than 1 Hz. It is useful for the analyzes of point sources and recommended for GRB afterglow analyses.

- `CLEAN` class: this class has a lower background rate than the `SOURCE` class (with a rate of ~ 0.1 Hz). It is recommended for the analysis of diffuse sources.

- `UltraClEAN` class: this class was developed to study the extragalactic diffuse γ-ray emission. The residual contamination in this class is roughly 10% less than in the `CLEAN` class at 100 MeV. It has the best signal-to-noise ratio, and it corresponds to the smaller effective detection area.

- `UltraCLEANVETO` class: this class was developed to study diffuse emissions which require low CR contamination, and to check for CR-induced systematic effects.

In addition to the standard event classes listed above, the LAT Low Energy (LLE) event class includes all events that pass the GAMMA filter, further requiring only minimal information such as the existence of a reconstructed track in the TKR. As a result, this class is enriched by low-energy events and is suitable only for the analysis of short duration intervals (GRB prompt emission, solar flares).

The LAT data sets are publicly available at the FSSC[2] (*Fermi* Science Support Center). The data files can be retrieved in FITS[3] format (Flexible Image Transport System). The first file "FT1" is an event file which contains the list of events that have passed the selection cuts, along with their characteristics, such as their arrival time in MET (Mission Elapsed Time, since January 1rst, 2001), their energy, direction and event class. The second file "FT2" contains information related to the satellite position and orientation as functions of time, and the observation mode. This file also lists the moments when the LAT is inactive during its passages in the SAA zone (see Sect.2.2).

2.4.5 The LAT instrument response functions

The LAT instrument response functions (IRFs) represent the performance of the LAT to detect and to characterize the incident photons. These functions describe

[2] `http://fermi.gsfc.nasa.gov/ssc/data/access/`
[3] Standard format of data useful in astrophysics domain.

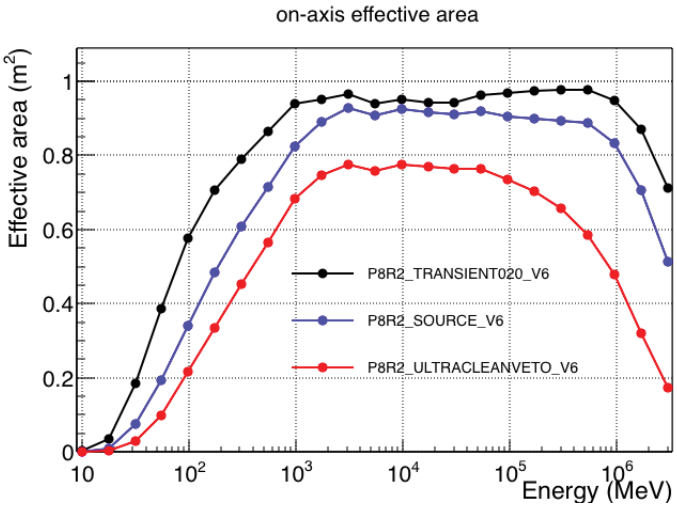

Figure 2.11: *Effective detection area as a function of the photon energy, for the three event classe* `TRANSIENT020`, `SOURCE` *and* `ULTRACLEANVETO`. *Taken from* `http://www.slac.stanford.edu/exp/glast/groups/canda/lat_Performance.htm`

the capacity of the instrument to detect and to identify a γ-ray, to measure its energy E and its direction $\hat{p}$. Therefore, they are usually expressed as functions of these key parameters as follows:

- The effective detection area $A_{eff}(\hat{p},E)$ depends on the geometry of the instrument (e.g., the projected area for events entering the LAT from the top side), weighted by its efficiency to detect (i.e., at the trigger and filtering levels) and to identify (i.e., at the reconstruction and classification levels) a gamma-ray photon. It can be formally defined as the quantity that relates the differential spectrum $[d^2N/dEd\hat{p}](\hat{p},E)$ (in units of $\mathrm{cm}^{-2}\,\mathrm{s}^{-1}\,\mathrm{sr}^{-1}$) of a source (here assumed steady) observed during T_{obs}, to the number of photons N_γ detected in a true energy interval $[E_{min}, E_{max}]$:

$$N_\gamma = T_{obs} \int_{E_{min}}^{E_{max}} \int_\Omega \left[\frac{d^2N}{dEd\hat{p}}\right](\hat{p},E)\, A_{eff}(\hat{p},E)\, d\hat{p}\, dE \tag{2.1}$$

  where Ω is the angular size of the source. For a point-like source at the position $\hat{p}_0$, e.g. a GRB, $[d^2N/dEd\hat{p}](\hat{p},E) = [\mathrm{dN/dE}](E)\ \delta(\hat{p}-\hat{p}_0)$, therefore:

$$N_\gamma = T_{obs} \int_{E_{min}}^{E_{max}} \left[\frac{dN}{dE}\right](E) A_{eff}(\hat{p}_0,E) dE \tag{2.2}$$

  The function $A_{eff}(E)$ is represented in the top right panel of Fig.2.10 for a source at normal incidence. Below $\sim$1 GeV, the effective detection area increases with energy, mainly because of the increase of the probability to

convert, reconstruct and identify γ rays. Above 1 GeV, A_{eff} is approximately constant and equals $\sim$0.9 m^2.

- The Point Spread Function PSF($\hat{p'}$,$\hat{p}$,E) is the probability density of reconstructing a direction $\hat{p'}$ for an incident photon of direction $\hat{p}$ and energy E. At a given energy E, the width of the PSF characterizes the LAT angular resolution. It is usually expressed as the 68% containment angle r_{68}(E). This angle is represented in Fig.2.10 (bottom, left), averaged over the LAT FoV and weighted by the acceptance. This figure shows that the containment angle decreases rapidly from $\sim$10° at 30 MeV to $\sim$0.1° above 10 GeV, which reflects the weakening of the multiple scattering of the e^+e^- pair in the TKR.

- The energy redistribution function $D(E', \hat{p}, E)$ is the probability density of reconstructing an energy E' for an incident photon of direction $\hat{p}$ and energy E. At a given energy E, the width of the redistribution function characterizes the LAT energy resolution. It is usually expressed as the 68% containment energy interval, relatively to the energy E. This δ_E/E ratio is represented in Fig.2.10 (bottom, right), averaged over the LAT FoV and weighted by the acceptance. This figure shows that the energy dispersion spans from $\sim$6% to $\sim$20% between 100 MeV and 10 GeV.

For the LAT analysis of point-like sources that will be presented in the next chapter, it is useful to define the product of the IRFs as:

$$R(\hat{p}', E', \hat{p}, E) = A_{eff}(\hat{p}, E) \times PSF(\hat{p}', \hat{p}, E) \times D(E', \hat{p}, E) \tag{2.3}$$

Due to the different selections used in the event classification, each of the event classes defined in Sect.2.4.2 has its own set of IRFs. These IRFs were calculated by Monte-Carlo simulations of γ rays at various energies and angles using the GEANT4 toolkit [Agostinelli et al., 2003].

The evolution of $A_{eff}(\hat{p}$,E) with the inclination angle of the source defines the Field of View (FoV) which depends on the type of the selected events and on their energies. For a specific energy, the FoV is defined as the ratio between the acceptance $A(E)$ (i.e., the effective area integrated over the solid angle) and the effective area at normal incidence ($\hat{p}$=0).

$$FoV(E) = \frac{A(E)}{A_{eff}(\hat{p} = 0, E)} = \frac{\int A_{eff}(\hat{p}, E) d\Omega}{A_{eff}(0, E)} \tag{2.4}$$

The FoV of the LAT is 2.4 steradians.

2.5 The LAT IRF systematics

The spectral analysis of the LAT GRBs will be described in Sect.3.4.2. The uncertainties on the fitted parameters can be classified in two distinct categories:

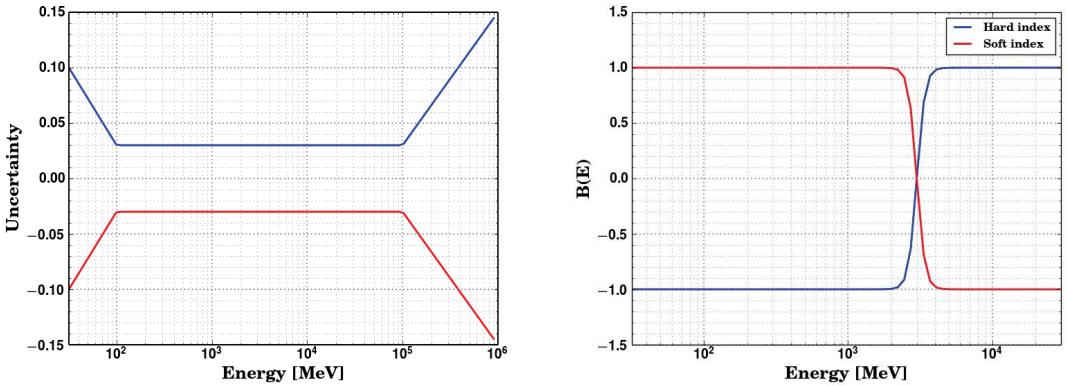

Figure 2.12: ***Left:*** *Containment interval of the relative systematic uncertainty on the LAT effective area as a function of the photon energy. The limits of the interval are defined as $\epsilon(E)\times B(E)$, with $B(E)$=1 (blue) or -1 (red).* ***Right:*** *the hyperpolic tangent $B(E)$ bracketing factor that maximizes the systematic uncertainty on the spectral index, for a reference energy E_0=3 GeV and K=0.13.*

- Statistical error: this uncertainty is related to the size of the event sample. The more data are available, the more accurate are the fit results, and the smaller are the parameter errors.

- Systematic error: this uncertainty is related to the biases that arise from the analysis procedure. Possible sources of systematic errors are the software implementation of the fitting method, or disagreements between the representation of the instrument responses and reality.

A large fraction of the systematic errors comes from the imperfect understanding of the IRFs, which are defined in Sect.2.4.5. The LAT collaboration found[4] that the inaccuracies related to the detection effective area have the most important systematic effect on the spectral analysis results. To estimate the IRF systematics and to propagate them to the measured spectral parameters, the collaboration defined a set of bracketing IRFs. In this new IRF package, the relative systematic uncertainty on A_{eff} is provided as a function of energy $\epsilon(E) = \frac{\delta A_{eff}(E)}{A_{eff}(E)}$. This factor can be mutiplied by a bracketing factor $B(E)$, which is arbitrarily chosen to vary between -1 and +1. The bracketing effective areas are thus defined as:

$$\tilde{A}_{eff}(E) = A_{eff}(E) \times (1 + \epsilon(E) \times B(E)) \tag{2.5}$$

The ϵ(E) function was estimated from the systematic errors on the efficiency of the event selection cuts (see Sect.2.4.4). Comparing the results between real and

[4] `https://fermi.gsfc.nasa.gov/ssc/data/analysis/LAT_caveats.html`

Energy	uncertainties
E < 100 MeV	10%
100 MeV < E < 100 GeV	3%
E > 100 GeV	15%

Table 2.3: *Maximum amplitude of the relative systematic error on the LAT detection effective area area with respect to the energy for the Pass 8* `SOURCE` *event class of Pass 8 data.*

simulated data, it was found out that the uncertainties ϵ(E) are contained within a limited range which changes as a function of the energy (see Fig.2.12, left). For the Pass 8 `SOURCE` event class, the relative uncertainty is 10% below 100 MeV, 15% above 100 GeV and 3% in between (Tab.2.3 and Fig.2.12, left).
The bracketing factor B(E) can be arbitrarily chosen to check the effect of the systematics on the spectral parameters. To maximize the effect on the normalization parameter of the spectral model, the bracketing factor must be constant (B(E)=$\pm$1) [Ackermann et al., 2012a]. Regarding the spectral index of a power law model, this factor was found to depend on the energy as B(E)=$\pm\tanh(\ln(E/E_0)/k)$ with E_0 the reference energy and k a constant to control the smoothness of the function (see Fig.2.12, right).

CHAPTER 3

GRB observation and analysis with *Fermi*

Contents

This chapter describes the techniques of detection and localization of GRBs observed by the *Fermi* instruments, together with the spectral analysis methods. The detection and localization techniques with both the on board and on ground algorithms of the GBM are described in Sect.3.1. Sect.3.2 describes the LAT data

preparation as well as the LAT maximum likelihood analysis method. The techniques of detection and localization of GRBs observed by the LAT are presented in Sect.3.3. Sect.3.4 describes the spectral analysis technique that is applied to the GBM and LAT data. Finally, the main sources of systematic uncertainties of the LAT are discussed in Sect.2.5.

3.1 GRB detection and localization with the GBM

3.1.1 On board detection

The flight software (FSW) of the GBM on board *Fermi* includes GRB detection and localization algorithms which are run in real time. The concept of the GBM trigger is similar to the one used for its predecessor *BATSE*. The GBM FSW implements much more trigger algorithms (up to 119), each based on a specific energy range and timescale. The GBM is capable to trigger γ-ray sources in four energy ranges [25 - 50 keV], [50 - 300 keV], [100 - 1000 keV] and [300 - 1000 keV] within 10 different time intervals, from 16 ms to 8.192 s in steps of a factor 2. This increases the detection probability of short and long GRBs with different hardnesses [Narayana Bhat et al., 2016b; Paciesas et al., 2012]. The GBM trigger is based on the comparison of the count rates of its NaI detectors with their background rates. A trigger is produced when the GBM FSW detects an excess of 4.5σ significance. This excess must be detected in at least 2 NaI detectors to be considered as a GRB detection. The count rate for each detector is calculated in a given energy range within a given time window, while its background rate is integrated over the same energy range during the previous 17 seconds of the current time window [Narayana Bhat et al., 2016b]. The major contributions to the background come from the cosmic X-ray diffuse emission at low energies, and from the Earth gamma-ray albedo at high energies [Meegan et al., 2009]. The on board GBM algorithm can provide a rough localization of the detected GRB, with an error radius less than 15° for strong bursts (fluence > 10 photons cm^{-2}) [Meegan et al., 2009].

The world-wide community is notified of each GBM alert via the GCN (Gamma-ray burst Coordinates Network[1]) system which runs at the GSFC. The GBM alert notice is followed by a series of messages ("flight position" notices), which contain updated information such as the trigger time and intensity, the coordinates of the GRB candidate and the localization uncertainty, the hardness, the trigger classification with the associated probabilities for the two most likely categories (e.g., GRB, solar flare, particle event, etc).

[1] `https://gcn.gsfc.nasa.gov/gcn`

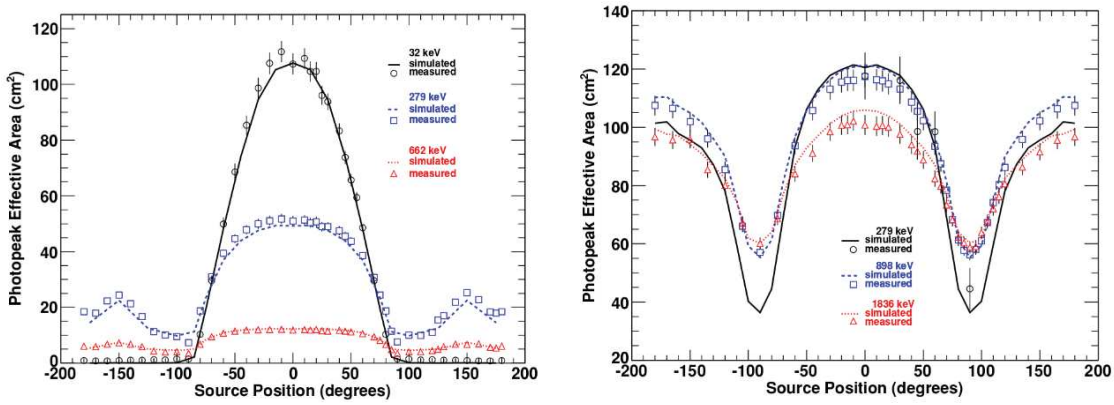

Figure 3.1: *Left to right: The effective area of the NaI and BGO detectors as a function of the angle between the detector axis and the source direction. Figures taken from Meegan et al. [2009]*

3.1.2 Localization

The distribution of the 12 NaI detectors around the *Fermi* spacecraft with different orientations allows to localize the detected GRBs within a radius of more than 10 degrees. The localization of a burst is performed by comparing the relative count rates of all the NaI detectors [Connaughton et al., 2015]. The detection area of a NaI detector is roughly proportional to the cosine of the angle between the source direction and the detector axis, as shown in Fig.3.1. The relative count rate is calculated as the ratio of the background-subtracted counts (flux) observed in two detectors with different angles. A comparison of the $N-1$ ratios with the expected relative ratios (see further below) of the N NaI detectors is performed to estimate the GRB direction. To compute the theoretical (expected) count rates for each detector, one must know the effective area of this detector, the incidence angle of the GRB, an estimation of the background that should be excluded from the expected burst counts depending on the detector response. One should also assume the spectral shape of the source (for more details see [Connaughton et al., 2015]). With all these ingredients, one can determine the coordinates of a burst provided that this burst is seen by at least 4 detectors (which yields 3 count ratios and thus leaves 1 degree of freedom). Usually, the GBM localization is done using a χ^2 minimization process for which the source is placed at different positions in the sky. The best position is thus the one that minimizes the χ^2. This localization is converted into GRB coordinates (Right Ascension, Declination) using the information of the spacecraft position [Meegan et al., 2009]. The uncertainty on the GRB localization at 68 % confidence level is calculated as the radius of the circular region that is obtained from the contour $\Delta\chi^2=\chi^2\text{-}\chi^2_{min}=2.3$ around the minimum. This calculation is performed by the localization algorithms which are run on board and on the ground.

3.1.3 On-ground automated processing

The Burst Alert Processing (BAP) of the GBM is run at the mission operations center at the GFSC, with an identical system available in Huntsville for redundancy [Meegan et al., 2009]. It takes ∼10-15 min to process the GBM data with the BAP. In many respects, the localization algorithm of the BAP is more performant than the one that is implement onboard. It provides improved estimates of the rates in each detector. In particular, the scattering of the GRB signal on the Earth's atmosphere is better treated, using the orientation of the satellite. The algorithm also uses a finer celestial grid, with an angular binning of 1° instead of 5° onboard. Finally, it uses three spectral models for the source instead of one. As a result, GRBs are localized more accurately on ground with an error radius of a few to ∼10 degrees.

Each time the GBM algorithm finds a localization that is more accurate than the previous one, this new localization is communicated to the world-wide community with updated GCN notices. Once the complete real-time data set arrives on-ground, a Burst Advocate[2](BA) of the GBM team repeats the analysis manually in order to improve upon the results previously obtained by the automated processing. The BA localizes the GRB based on the counts in the peak flux time interval or the energy fluence (integral of energy flux over a period of time), both measured in the energy range [50 - 300] keV.

3.2 The LAT maximum likelihood analysis method

The analysis of an astrophysical source with the LAT starts from the distribution in energy, space and time of the detected events (counts). The photon distribution in energy and space is different from their true distribution because of the dispersion that is caused by the instrument response. The migrations from the true energies and directions to the measured ones are characterized by the LAT energy redistribution function and PSF, respectively (see Sect.2.4.5). Since the spectra of typical gamma-ray sources are steep and amplify these migrations, a direct deconvolution of the LAT responses is a very difficult task and may be even risky. Instead, the standard analysis method that is used to reconstruct the spectrum and the position of a source is based on the comparison of the observed counts with theoretical predictions, taking into account the instrument responses. In this technique, also known as "forward-folding", one convolves a theoretical source model with the instrument responses. The comparison between the predicted and the measured count distribution allows to determine the model parameters that best fit the observations. In this section I describe how the source model and the data are prepared (Sect.3.2.1). Then I present the maximum likelihood method that is used for the model comparison (Sect.3.2.2).

[2]person in charge of the manual GRB spectral analysis (see Chap.4)

3.2.1 Source model and data preparation

The LAT data-model comparison can be performed in the whole sky or, for most cases, in a selected Region Of Interest (ROI) which is usually defined as a circular area that is assumed to include the position of the source to study. In general, the total spectrum $S(E,\hat{p})$ (in units $\mathrm{cm^{-2}\,s^{-1}\,keV^{-1}\,sr^{-1}}$) of the source model is the sum of the spectra from point-like sources (S_l) that may contribute to the signal in the ROI, from the galactic diffuse sources (S_G) and from the extragalactic and/or isotropic diffuse emissions (S_{EG}). In practice, all of these components are defined in an XML (eXtensible Markup Language) file, which specifies which spectral or position parameters are left free to vary in the fitting procedure. In this procedure, the fluxes of the sources are assumed to be constant, i.e. they are time-averaged.

For a point-like source l, the spectral and spatial dependencies in $\mathrm{S}_l(E,\hat{p})$ can be factored as $\mathrm{S}_l(E)\delta(\hat{p}-\hat{p}_l)$ where $\hat{p}_l$ is the position of the source in the sky. Therefore, the total spectrum is:

$$S(E,\hat{p},\Lambda) = \sum_l S_l(E)\delta(\hat{p}-\hat{p}_l) + S_G(E,\hat{p}) + S_{EG}(E,\hat{p}) \tag{3.1}$$

where $\Lambda = \{\lambda\}$ is the set of the model parameters. The convolution of this model with the IRFs gives the measured count spectrum (see Sect.3.2.2). More details on the model will be given in the next sections.

The FT1 event file and the FT2 spacecraft file (see Sect.2.4.4) are required to start the analysis. These files are public[3] since August 2009 for Pass 7 data and since June 2015 for Pass 8 data. For GRB analyses, it is recommended to use the `TRANSIENT` event class, which includes the largest number of events compared with the other event classes (see Sect.2.4.4). To select and analyse this data, I have used the version 10-00-02 of the suite of science tools that have been developed by the LAT collaboration[4]. The first step consists in creating a new event file (*selectfile*) using the ***gtselect***[5] tool, which selects the `TRANSIENT` events within specified criteria:

- **Time interval:** the time interval desired for the analysis.
- **Energy range:** before the release of Pass 8 data, the systematics at low energy (< 100 MeV) were significant because of the "ghost" events (see Sect.2.4.3). Therefore, it was not recommended to include low energy events in the spectral analyses. This systematic issue is resolved with Pass 8 data, and it becomes possible to include events with energies < 100 MeV to the spectral analysis as long as the effect of the energy dispersion, which is more pronounced at low energies, is taken into account properly.

[3] `https://fermi.gsfc.nasa.gov/ssc/data/access`

[4] `http://fermi.gsfc.nasa.gov/ssc/data/analysis/software`

[5] `https://fermi.gsfc.nasa.gov/ssc/data/analysis/scitools/help_v9r23p1/gtselect.txt`

- **Region of Interest (ROI):** it is recommended to define a large ROI around the source in order to take into account the extension of the PSF at low energies and to better constrain the level of the background components. This region is typically defined with a size of 10 to 15 degrees.
- **Zenith angle:** at high zenith angles ($\theta_z > 110°$) the terrestrial albedo contaminates the signal in the ROI. Therefore, it is recommended to keep only the time intervals during which the ROI is entirely contained below a threshold angle of θ_z^{max}=105°.

Then, one must use the ***gtmktime***[6] tool which creates *Good Time Intervals (GTI)* as sub-intervals of the selected time interval. This tool can filter the observations in various ways. Usually one would exclude from the analysis the time sub-intervals during which the ROI is not entirely contained within θ_z^{max}, or during which the spacecraft was in the SAA zone.

The third step before the spectral analysis consists of computing the livetime (exposure time) which is the time during which the LAT was looking at a given position in the sky and a given inclination. This time is required to account for the deadtime of the instrument. It is computed with the ***gtltcube***[7] tool, which creates a new file called *livetime cube* based on the *selectfile* and FT2 file.

3.2.2 The likelihood formalism and its implementation

The analysis of LAT data is performed through the maximum likelihood (ML) method. The likelihood is the probability of obtaining a set of data given a model. The maximum likelihood method is the procedure of finding the values of the model parameters which maximize the likelihood function. This estimation can be performed in two ways. The first is the "unbinned" analysis, which consists of applying the model probability to each event individually. The second, called "binned", compares the model with the data sampled in energy and direction.

The unbinned likelihood analysis

For the unbinned likelihood method, the events can be considered as binned into infinitely small bins containing only one or no event. This method is CPU time consuming and is recommended for analyses of point sources, extended or faint sources with a small number of events. The likelihood is computed from the reconstructed energy and direction of each individual event, given a sky model convolved with the IRFs of the instrument $R(E, \hat{p}; E', \hat{p}')$. The log-likelihood function is given by:

$$\ln \mathcal{L}(\{x_i\}, \Lambda) = \sum_i \ln M(E'_i, \hat{p}'_i, t_i) - N_{pred} \tag{3.2}$$

[6] https://fermi.gsfc.nasa.gov/ssc/data/analysis/scitools/help/gtmktime.txt
[7] https://fermi.gsfc.nasa.gov/ssc/data/analysis/scitools/help/gtltcube.txt

where $\{x_i\}$ is the list of events, and $M(E_i, \hat{p}_i, t_i)$ is the probability density of a photon arrived at time t_i, at the measured energy E_i and direction $\hat{p}_i$ (Eq.A.1). N_{pred} is the number of the photons predicted by the model (see more details in App.A.1).

The ***gtexpmap***[8] tool computes the number of events associated with the diffuse components of the spectral model. This tool integrates the product of the response functions (Eq.2.3) over the measured energies and directions (ROI). Because of the large angular resolution at low energy ($\sim$3.5° at 100 MeV), this calculation must be done at each point of a source region (SR) which is larger than the ROI by $\sim 10°$ in order to take into account all sources that may contribute to the signal observed in the ROI. This tool requires the *selectfile* event file, the FT2 file, the *livetime cube*, the IRFs, a number of longitude and latitude points (n_L, n_l) and the desired number of energy bins (n_e). The output fits file of this tool contains a cube of $n_L \times n_l \times n_e$ exposure maps for the defined ROI.

The contribution to the expected signal from each component of the source model is computed at each step of the likelihood maximization. To speed up the fitting procedure, the spectral and spatial dependencies of each diffuse component are assumed to factor, which allows to precompute the integral of their spatial part convolved with the IRFs for each individual event. This calculation is performed by the ***gtdiffrsp***[9] tool which requires, in addition to the event and spacecraft files, the XML source model file. This step can be ignored for the standard analyses with some sets of IRFs, where the diffuse responses have been pre-computed and stored in the FT1 file.

Finally, the maximum likelihood analysis is performed using the ***gtlike***[10] tool in "UNBINNED" mode. In addition to the source model and the FT2 files, this tool uses the files generated by the ***gtselect***, ***gtltcube*** and ***gtexpmap*** tools. The output of ***gtlike*** is a new source model file, which contains the fitted parameters and their errors. The error of each parameter λ is obtained from the likelihood profile $\ln \mathcal{L}(\lambda)$, where the likelihood function at each value of λ is maximized with respect to all other free parameters. As an example, the 68% confidence level interval corresponds to a decrease $\Delta \ln \mathcal{L}(\lambda)$=0.5 from the maximum likelihood value [Rolke et al., 2005].

The binned likelihood analysis

For the binned likelihood method, the data are sampled in energy and direction. This method is simpler than the unbinned method, yet it is less accurate since the

[8] https://fermi.gsfc.nasa.gov/ssc/data/analysis/scitools/help/gtexpmap.txt
[9] https://fermi.gsfc.nasa.gov/ssc/data/analysis/scitools/help/gtdiffrsp.txt
[10] https://fermi.gsfc.nasa.gov/ssc/data/analysis/scitools/help/gtlike.txt

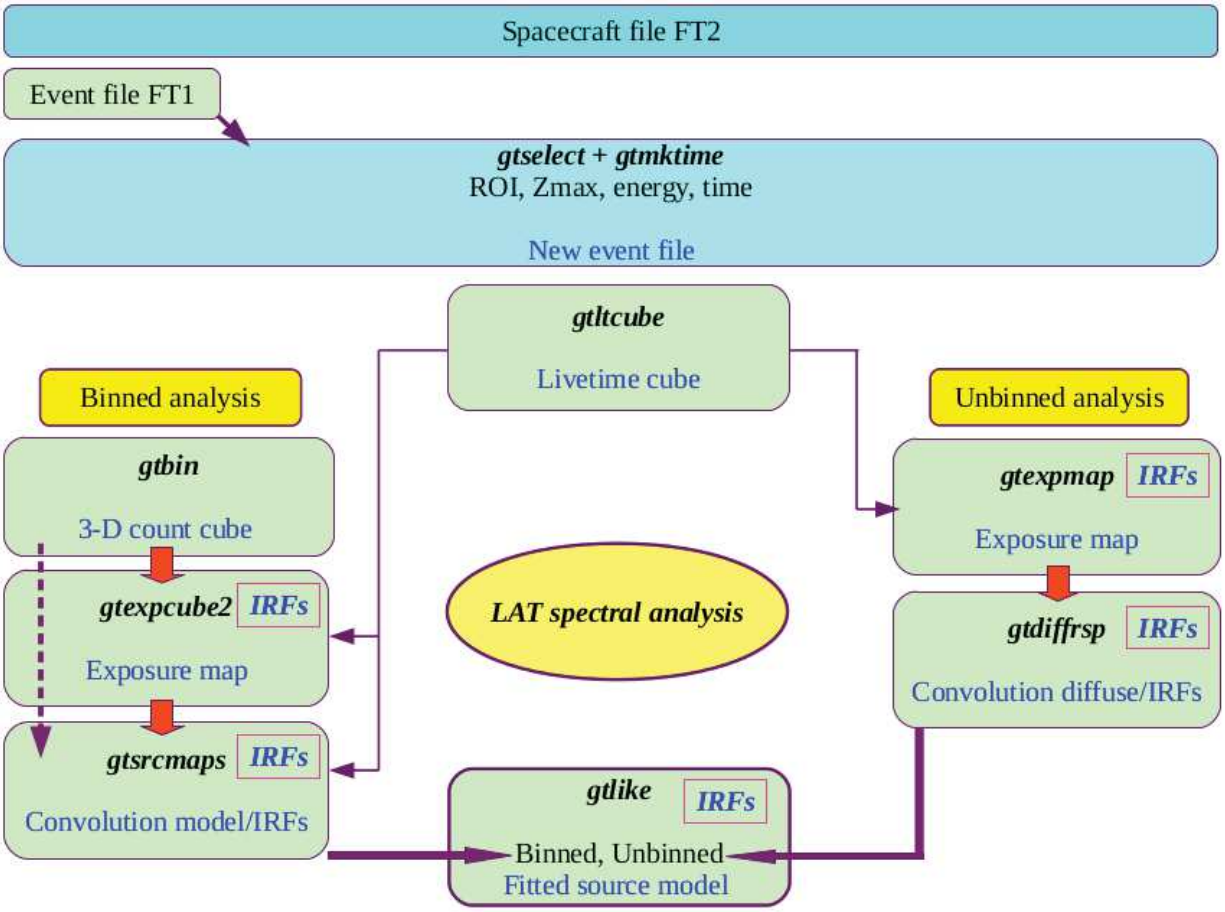

Figure 3.2: *GRB spectral analysis with the LAT science tools.*

information on individual events is lost. The binned likelihood function reads:

$$L(\{x_i\}, \Lambda) = \prod_{k=1}^{n_k} \frac{H_k^{n_k} \exp^{-H_k}}{n_k!} \tag{3.3}$$

where n_k is the number of observed counts in the energy bin k and H_k is the number of photons predicted by the model (Eq.A.7). The log-likelihood function is thus given by:

$$\ln \mathcal{L}(\{x_i\}, \Lambda) = \sum_k n_k \ln H_k - N_{pred} \tag{3.4}$$

The first step in the binned likelihood analysis is to create a data cube binned in space and energy, using the CCUBE option of the ***gtbin***[11] tool. Then, one has to use

[11] `https://fermi.gsfc.nasa.gov/ssc/data/analysis/scitools/help/gtbin.txt`

the ***gtexpcube2***[12] tool to create exposure maps for different energies, that account for the livetime determined by ***gtltcube***.

After this step, the ***gtsrcmaps***[13] tool convolves the different components of the source model file (XML file) with the instrument response functions. This tool requires the FT2 file in addition to the data cube file and the binned exposure map created for this analysis. The last step is the spectrum fitting which is performed with ***gtlike*** using its "BINNED" option.

For both types of analysis (unbinned or binned), one can use the ***gtsrcprob***[14] tool to compute the probabilities of associating the detected events to each of the sources in the XML file. This tool requires the FT2 file, the XML file, the IRFs and the *selectfile* file provided that the latter has been processed by the ***gtdiffrsp*** tool in case of the presence of diffuse components.

Energy redistribution effect

The energy redistribution function is the widest at low energies (< 100 MeV). Therefore, any analysis using low-energy data will be biased by large uncertainties if the energy dispersion is not properly accounted for. To check the effect of the energy dispersion function on the spectral reconstruction, I simulated a point-like source with a power-law spectrum dN/dE, observed during T_{obs}. This simulation was done with the ***gtobssim***[15] tool using the Pass 8 IRFs. The total number of counts in the interval of measured energy $[E'_{min},E'_{max}]$ is given by:

$$N = T_{\rm obs} \int_{E'_{min}}^{E'_{max}} dE' \int_0^{+\infty} \frac{dN}{dE} A_{eff}(E) D(E,E') dE \tag{3.5}$$

where $D(E,E')$ is the energy redistribution function defined in Sect.2.4.5. This number of events can be compared with the one obtained for an instrument with a perfect energy measurement, i.e. $D(E,E') = \delta(E-E')$:

$$N_{ideal} = T_{\rm obs} \int_{E_{min}}^{E_{max}} \frac{dN}{dE} A_{eff}(E) dE \tag{3.6}$$

Fig.3.3 shows the simulated count spectrum (red dots) and the expected counts spectrum with and without including the energy redistribution effect (red and blue solid lines respectively). This figure shows that the energy dispersion has to be accounted for in the spectral analysis. The energy redistribution has been implemented in the science tools for the binned likelihood analysis following Eq.A.1. It is thus possible

[12] https://fermi.gsfc.nasa.gov/ssc/data/analysis/scitools/help/gtexpcube2.txt
[13] https://fermi.gsfc.nasa.gov/ssc/data/analysis/scitools/help/gtsrcmaps.txt
[14] https://fermi.gsfc.nasa.gov/ssc/data/analysis/scitools/help/gtsrcprob.txt
[15] https://fermi.gsfc.nasa.gov/ssc/data/analysis/scitools/help/gtobssim.txt

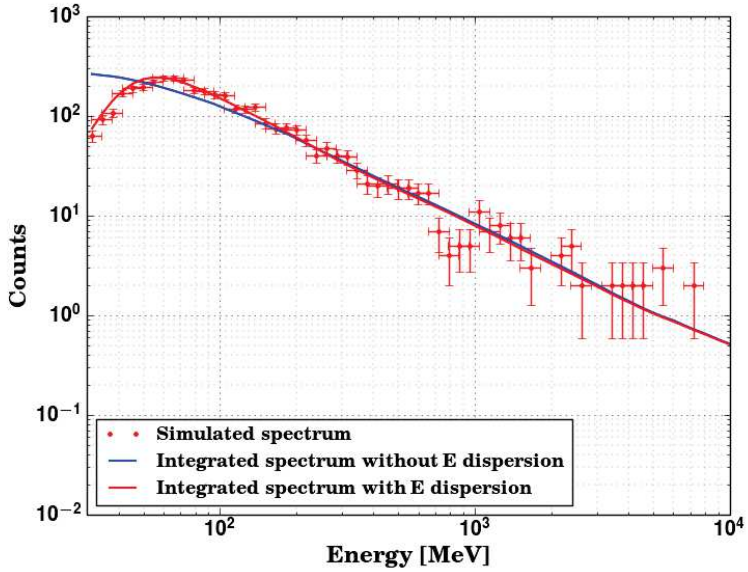

Figure 3.3: *Comparison of the simulated count spectrum (red dots) with the expected distribution obtained with (red line) and without (blue line) including the energy dispersion.*

to include low-energy data in this analysis method. However, this option is not available in the unbinned likelihood analysis, which would be too CPU time consuming. In this work, I will use both ML methods following the steps described in this section and summarized in Fig.3.2.

3.3 GRB detection and analysis with the LAT

3.3.1 On board detection

The LAT telescope has its own on board detection algorithm. This algorithm has two search modes: the first one searches within the LAT data for spatial and temporal clusters of events, while the other is seeded by the detection time and position which are computed on board by the GBM [McEnery et al., 2010]. In case of GRB detected on board by the LAT, the trigger information is sent through automated messages (i.e., GCN notices) to other telescopes in less than a few minutes, fostering follow-up observations. In case of a remarkably bright and/or fluent burst detected by the GBM, an ARR (Sect.2.2) is automatically sent to the spacecraft to place the GRB near the center of the LAT FoV provided that the GRB is far away from the horizon (above the Earth avoidance angle of 20°). This pointing mode is maintained for a maximum of 2.5 hours (5 hours formely) after trigger. The GRB emissions

detected by the LAT usually last for hundreds of seconds post-trigger (with the exception of 130427A which was detected for ∼19 hours).

The LAT on board algorithm rarely detects GRBs (e.g. GRB 090510 [Ohno and Pelassa, 2009], GRB 160509A [Longo et al., 2016a]). When the GBM detects a burst on board, it sends an alert message to the LAT via the spacecraft bus within less than a second. If the burst occured in the LAT FoV, the LAT flight software uses this message to search for a possible detection and remains in trigger mode during 5 minutes. This search is performed from different starting times (2, 5, 10, 20, 30, 60, 90, and 150s) after the GBM trigger, to account for the delayed onset of the high-energy emission that has been observed for most of the LAT bright bursts [McEnery et al., 2010]. Any LAT trigger passes through a filtering stage on ground to limit the number of false alerts. Thanks to its good angular resolution, the LAT is able to localize the detected GRBs on board with an accuracy of 0.1-0.5° [McEnery et al., 2010].

3.3.2 On ground detection and localization

The statistical method that is used to detect and to localize a GRB with the LAT is based on the likelihood ratio test (LRT, [Neyman and Pearson, 1928]). This test confronts the data to two different statistical hypotheses. In the null hypothesis (H_0), one computes the maximum likelihood of the data for a sky model that does not include the GRB, while the GRB is added to the model in the alternative hypothesis (H_1). In the following, I label $\hat{b}$ the free parameters of the background components (diffuse galactic and extragalactic emissions, point-like sources). Similarly, I label $\hat{p}$ the two coordinates of the GRB, and $\hat{s}$ its spectral parameters (e.g., the two parameters of the power-law spectrum). With these notations, the test statistic (TS) that is used to compare the two hypotheses is defined as:

$$TS = -2 \ln \frac{max_{\hat{b}} \mathcal{L}(\hat{b})}{max_{\hat{b},\hat{s},\hat{p}} \mathcal{L}(\hat{b},\hat{s},\hat{p})} \tag{3.7}$$

The higher the TS, the higher the detection significance N_σ, as can be seen from this equation. However, deriving the exact relation between TS and N_σ is not straightforward and out of the scope of this work. For a complete discussion, one can refer to the section devoted to the source detection in the first LAT GRB catalog article (section 3.2.1 of [Ackermann et al., 2013b]). In the following, I will use an approximated relation, which is based on the Wilks theorem (Wilks, 1938). This theorem states that the TS follows a χ^2 distribution with k degrees of freedom under the null hypothesis and in the large sample limit, where k is the number of additional parameters between the two hypotheses, i.e. the GRB parameters. If an accurate position is given by an external instrument (e.g., the *Swift*/BAT or XRT), then one can fix the position parameters in the above equation. Moreover, if the GRB spectrum is

described by a power law with a fixed photon index (typically -2 for LAT GRBs), then k=1 and N_σ=$\sqrt{TS}$. I will use this approximation in the following chapters, requiring N_σ >5 (TS>25) to consider a GRB as successfully detected. It is worth to mention that the TS value and the detection significance are strongly dependent on the background parameters. Therefore, an accurate estimation of these parameters is required. Finally, if the GRB position is not known or not accurate enough (e.g., in case of a GBM trigger), then the GRB position and its detection significance must be estimated together, as described below.

The localization of a GRB with the LAT is performed by computing the test statistic at fixed positions $\hat{p}_i$ on a grid in celestial coordinates:

$$TS(\hat{p}_i) = -2\ln\frac{max_{\hat{b}}\mathcal{L}(\hat{b})}{max_{\hat{b},\hat{s}}\mathcal{L}(\hat{b},\hat{s}|\hat{p}_i)} \tag{3.8}$$

The grid is centered near an input position, which is either provided by an external instrument or pre-computed with LAT data (see further below). The TS map is generated with the ***gttsmap***[16] tool, in a binned or unbinned likelihood mode. The estimated position of the GRB corresponds to the position that maximizes its detection significance. Namely, the best position corresponds to the maximum value of the test statistic on the map, i.e. to the TS given in Eq.3.7:

$$TS_{max} = -2\ln\frac{max_{\hat{b}}\mathcal{L}(\hat{b})}{max_{\hat{b},\hat{s},\hat{p}}\mathcal{L}(\hat{b},\hat{s},\hat{p})} \tag{3.9}$$

The localization errors are derived from the confidence level contours around the maximum TS. At a given position $\hat{p}_i$, the difference with the maximum TS is:

$$\Delta TS = TS_{max} - TS(\hat{p}_i) = -2\ln\frac{max_{\hat{b},\hat{s}}\mathcal{L}(\hat{b},\hat{s}|\hat{p}_i)}{max_{\hat{b},\hat{s},\hat{p}}\mathcal{L}(\hat{b},\hat{s},\hat{p})} \tag{3.10}$$

which corresponds to an LRT between $\hat{p}_i$ and the best position. According to the Wilks theorem, ΔTS follows a χ^2 distribution with 2 degrees of freedom, i.e. the two GRB coordinates. The localization error contour for a 68% (resp. 90%) confidence level is thus defined as ΔTS=2.3 (resp. 4.61) [Mattox et al., 1996]. Most of the detected GRBs have shapeless or elliptical contours. Nonetheless, the size of these contours are converted to circular uncertainties in order to provide simple and meaningful localization errors. The 68% (resp. 90%) error radius is thus defined as the radius of a disk whose area is equal to the area within ΔTS=2.3 (resp. 4.61).

The GRB localization with ***gttsmap*** can be time consuming if the chosen grid is too large and/or its binning is too small. In order to reduce the computation time, one can first localize the GRB with a less accurate but faster method implemented in the ***gtfindsrc***[17] tool. This method computes the unbinned likelihood profile

[16] https://fermi.gsfc.nasa.gov/ssc/data/analysis/scitools/help/gttsmap.txt
[17] https://fermi.gsfc.nasa.gov/ssc/data/analysis/scitools/help/gtfindsrc.txt

$max_{\hat{b},\hat{s}} L(\hat{b},\hat{s}|\hat{p}_i)$ at different positions $\hat{p}_i$ to find the best position. In this procedure, the spectral index of the GRB is fixed to a typical value (-2) and the normalizations of the GRB and of the background components are left free to vary. The localization error is calculated by fitting the likelihood profile by a paraboloid that is symmetric around the best position, i.e. assuming that the localization error contour is circular and deriving the Gaussian error radius from the second derivative of the parabola. As a result, this method gives only an approximate localization, especially for GRBs with low event statistics and/or non circular contours. For this reason, the position and localization error obtained with ***gtfindsrc*** are often used to optimize the size and binning of the grid in ***gttsmap***, which provides the final results.

3.3.3 On-ground automated processing

It takes ∼6-8 hours for the LAT data to be downlinked and processed. Once available on ground, they are processed at the ISOC and the reconstructed events enter the Automatic Science Processing (ASP). The ASP searches for a LAT counterpart following each GRB detection by the GBM or other observatories (e.g., *Swift*/BAT). It also performs a continuous blind search for new transient sources independently of any external trigger. When the ASP algorithms detect a new GRB candidate, an alert is sent internally to the *Fermi* GRB group in view of a manual analysis by the LAT BA (see Chap.4).

3.4 Spectral analyses

As described in the previous sections, the analysis of a LAT-detected GRB is based on the forward-folding technique. Using the suite of LAT science tools, one can assess its detection significance, localize it, and measure its spectrum. This technique is also used to combine the GBM and LAT data in joint spectral analyses. In both types of spectral analysis (LAT or GBM+LAT), a theoretical photon spectrum is convolved with the instrument response, and its parameters are estimated through the maximization (or minimization) of a fit statistic. In this section I present the parametric models for the GRB prompt emission spectra that I studied during my thesis work (Sect.3.4.1). Then I present how the likelihood fit statistics is used to measure the GRB spectra at high energy with the LAT (Sect.3.4.2). Finally, I describe how GBM and LAT data are combined in joint spectral fits, as well as the fit statistics that are used in these analyses (Sect.3.4.3).

3.4.1 Spectral models

For both the GBM and the LAT analyses, the spectral model of the source is the differential photon flux dN/dE (in units of $\mathrm{MeV}^{-1}\,\mathrm{cm}^{-2}\,\mathrm{s}^{-1}$). In addition to the `Band` function described in Eq.1.2, we used the spectral models reported below.

- **Power law (PL):**

$$\frac{dN_{PL}}{dE} = A_{pl}\left(\frac{E}{E_0}\right)^{-\gamma} \tag{3.11}$$

where A_{pl} is the amplitude, γ is the photon index and E_0 is a fixed reference energy.

- **Power law with an exponential cutoff (CUTPL):**

$$\frac{dN_{CUTPL}}{dE} = A_{cutpl}\left(\frac{E}{E_0}\right)^{-\gamma}\exp\left(-\frac{E}{E_f}\right) \tag{3.12}$$

where A_{cutpl} is the amplitude and E_f is the folding energy of the exponential cutoff.

- **Broken power law with an exponential cutoff (CUTBPL):**

$$\frac{dN_{CUTBPL}}{dE} = A_{cutbpl}\begin{cases}\left(\frac{E}{E_0}\right)^{\gamma_0}\exp\left(-\frac{E}{E_f}\right), & E \le E_b \\ \left(\frac{E_b}{E_0}\right)^{\gamma_0}\left(\frac{E}{E_b}\right)^{\gamma}\exp\left(-\frac{E}{E_f}\right), & E > E_b\end{cases} \tag{3.13}$$

with A_{cutbpl} the amplitude, E_b the break energy, γ_0 the photon spectral index below E_b and γ the photon spectral index above this energy.

- **Black body spectrum (BB):**

$$\frac{dN_{BB}}{dE}(E) = \mathtt{K}\ 8.0525\frac{E^2 dE}{(\mathtt{kT}^4(\exp(E/\mathtt{kT})-1))} \tag{3.14}$$

where kT is the temperature in keV, K=L_{39}/ D_{10}^2, with L_{39} the source luminosity in units of 10^{39} ergs^{-1}and D_{10} the distance to the source in units of 10 kpc.

- **Multiplicative broken power law (MBPL):**

$$MBPL(E) = \begin{cases}1, & E \le E_b \\ \left(\frac{E}{E_b}\right)^{\beta}, & E > E_b\end{cases} \tag{3.15}$$

This function is a multiplicative term with E_b the break energy and β the change in the spectral index.

It is generally recommended to minimize the correlation between the model parameters. In case of a power-law model, the correlation between the amplitude and the index parameters can be entirely suppressed by fixing the reference energy E_0 (Eq.3.11) at the value of the decorrelation energy E_{dec}, at which the error on the differential flux dN/dE is minimal. The error (σ_F) on F=dN/dE is obtained via the error propagation method, which uses its first derivatives with respect to the spectral parameters, their 68% uncertainties (σ_A and σ_γ respectively) and the covariance between them ($C_{A\gamma}$). It is expressed as follows:

$$\sigma_F^2 = \left(\frac{\partial F}{\partial A_{pl}}\right)^2 \sigma_{A_{pl}}^2 + \left(\frac{\partial F}{\partial \gamma}\right)^2 \sigma_\gamma^2 + 2\left(\frac{\partial F}{\partial A_{pl}}\right)\left(\frac{\partial F}{\partial \gamma}\right) C_{A_{pl}\gamma} \tag{3.16}$$

From this equation we obtain:

$$\frac{\sigma_F^2}{F^2} = \left[\left(\frac{\sigma_{A_{pl}}}{A_{pl}}\right)^2 + \ln^2\left(\frac{E}{E_0}\right)\sigma_\gamma^2 + 2\ln\left(\frac{E}{E_0}\right)\frac{C_{A_{pl}\gamma}}{A_{pl}}\right] \tag{3.17}$$

The decorrelation energy is obtained by solving $\partial(\sigma_F^2/F^2)/\partial u = 0$ for $u = \ln(E_{dec}/E_0)$. The E_{dec} that we find for a PL model takes the form:

$$E_{dec} = E_0 \exp\left(-\frac{C_{A_{pl}\gamma}}{A_{pl}\sigma_\gamma^2}\right) \tag{3.18}$$

3.4.2 Spectral analysis with the LAT

Before starting a GRB analysis, one must define a region in the sky around the burst position and a source region that is larger than the ROI due to the fact that the LAT PSF is finite (see Sect.3.2.2). The source model contains the galactic diffuse gamma-ray emission, the isotropic emission and the GRB. The galactic component can be implemented as a template which is provided by the LAT collaboration. This template depends on the data used in the analysis. For the Pass 8 data set, the galactic template used for the `TRANSIENT` event class is the *gll_iem_v06.fit*[18]. The spectral model for the isotropic emission can be simply described by a power law, with a normalization that is free to vary and a spectral index that is fixed to a typical value of -2. In addition to the background components, the source model contains the GRB at a fixed position and its spectral model (see Sect.3.4.1) with free parameters.

The results of the likelihood analysis with ***gtlike*** can be used to create the count spectra that are required by the GBM/LAT joint analysis presented in the next section. Firstly, the ***gtbin*** tool must be used to create a PHA file that contains the events binned in energy. This tool requires the selected event file and the FT2 file (see Sect.3.2.1). Together with the *livetime cube*, the exposure map and the output

[18] `https://fermi.gsfc.nasa.gov/ssc/data/access/lat/BackgroundModels.html`

file of ***gtlike*** that contains the fitted model, this PHA file is then used by the ***gtbkg***[19] tool to create the count spectrum of the background.

3.4.3 Spectral analysis with the GBM and the LAT

The comparison between the observed data and the theoretical predictions is performed using a fit statistic. The fit statistics used for the analyses of GRBs observed by *Fermi* are summarized as follows:

- **The χ^2 statistic:** this statistic is only used when the number of events is large enough in each energy interval. In addition to the parameter estimation, it allows to judge the goodness of the fit.

- **The Cash statistic:** this statistic is recommended in case of low counts that are Poisson distributed. It is defined as -2ln $\mathcal{L}$, where $\mathcal{L}$ is the likelihood function [Cash, 1979]. It cannot be used directly to assess the quality of the fit, however it allows to compare between two nested[20] models using their likelihood ratio -2($\ln \mathcal{L}_1 / \ln \mathcal{L}_2$).

- **The Castor statistic (C-stat):** this statistic is a variant of the Cash statistic[21]. It combines the advantages of the Cash and χ^2 statistics. The Castor statistic can be used to judge the goodness and to compare two nested models. The log-likelihood function of the Castor statistic is expressed as:

$$-2 \ln \mathcal{L} = 2 \sum_{i=1}^{N} (y(x_i) - y_i + y_i(\ln y_i - \ln y(x_i))) \tag{3.19}$$

  where y_i are the observed data and $y(x_i)$ the values of the model.

- **The Pgstat statistic:** this statistic is similar to C-stat for a Gaussian and non Poissonian distribution of the background events.

For the spectral analysis, I used the GBM TTE data type which has the largest number of energy bins (see Sect.2.3). In the forward-folding technique, the response of a detector is convolved with a spectral model to produce the expected count spectrum. For each GBM detector, the response file contains a detector response matrix (DRM), which is the product of its effective area and its energy redistribution function (see the example in Fig.3.4). The DRM accounts for all the different interaction processes which occur in the scintillator materials (Compton scatter, X-ray escape, etc.). The background in each GBM detector is estimated from the event rate before

[19] `https://fermi.gsfc.nasa.gov/ssc/data/analysis/scitools/help/gtbkg.txt`

[20] Two models are nested if one of them can be obtained in the limit of the other (or one model is a particular case of the other)

[21] see `https://heasarc.nasa.gov/docs/xanadu/xspec/xspec11/manual/node57.html` for more details

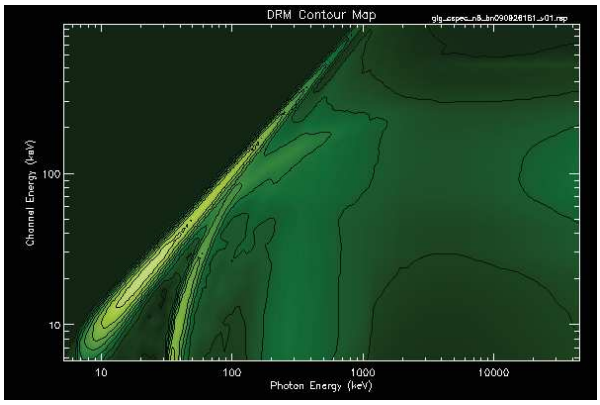

Figure 3.4: *The detector response matrix of a GBM NaI scintillator.*

and after the GRB. These intervals are fitted with a polynomial function (with a degree up to 4). The extrapolation of this background during the "ON" interval (time of the GRB emission) determines the background which is used in the fitting procedure. The LAT data used for the joint analysis are the same used for the only-LAT data analysis described in Sect.3.4.2. The format of the IRFs of the LAT instrument are not suitable for the GBM spectral fit software (see below). Instead, one must use the ***gtrspgen***[22] tool to create a suitable detector response matrix.

The *Fermi* data spectral analysis can be performed either with the *rmfit*[23] tool created by the GBM collaboration or using the *XSPEC*[24] standard fitting software. For the joint GBM/LAT analyses, I used the *rmfit* tool (version 3.2) with the Castor statistic which is recommended because of the limited event statistics in the LAT. I used also *XSPEC* (version 12.8.2) with the Castor or Pgstat statistics. The format of the GBM data files is not compatible with *XSPEC*. To adapt them, I used the *GBMtoolkit* that is available in the *Fermi* GRB group. This tool selects the GBM detectors that see the GRB with an angle less than 50°, and it defines automatically the ON/OFF time intervals that are suitable for the background estimation.

[22] `https://fermi.gsfc.nasa.gov/ssc/data/analysis/scitools/help/gtrspgen.txt`
[23] available at the FSSC `http://fermi.gsfc.nasa.gov/ssc/data/analysis/rmfit`
[24] `https://heasarc.nasa.gov/docs/xanadu/xspec/`

CHAPTER 4

Burst Advocate activities and first GRB analyses

Contents

This chapter is dedicated to presenting my contributions of general interest to the *Fermi* GRB group during my thesis. During this period, I contributed to the LAT Burst Advocate shifts and to the second LAT GRB catalog. I also reanalyzed two bright GRBs with Pass 8 data before they were made public in August 2015. In Sect.4.1 I present the LAT Burst Advocate activities. My contributions for detecting new bursts in real-time are described in Sect.4.2. Crosscheck analyses of GRB candidates for the second LAT GRB catalog are presented in Sect.4.3. Sect.4.4 presents the time-integrated analyses of the long bright GRBs 080916C and 090926A.

4.1 LAT Burst advocate activities

The LAT Burst Advocate (BA) is a person in charge of dealing with the GRB alerts generated by the GBM or other GRB-detecting space instruments (e.g. by the *Swift*/BAT). The LAT BA activity consists in performing a rapid analysis of the LAT data and localizing the detected burst in a timely manner. Once a GRB alert is received from the GBM or the LAT on-board or on-ground algorithms, the LAT BA has to check the GBM wiki page for more details about the burst, and to check the Data Quality Monitoring plots. These plots show the evolution of the event rates which passed the filtering stage presented in Sect.2.4.2. They allow also to control the quality of the data around the time of the alerts. Once the complete data has been processed at the ISOC, the BA has to check the preliminary results of the automatic science processing (ASP, see Sect.3.3.3) on the GRB candidate. The BA is required to communicate directly with the *Fermi* GRB group, notifying the detection of the burst and informing them of any news or issues related to the scientific importance of this burst. He/She has to set up quickly a meeting by teleconference with the GRB group in order to refine the localization and the analysis of the detected GRB. The main tasks of the BA are the determination of the best GRB position and checking his/her result with other people at the meeting. If the GRB localization with the LAT is accurate enough (error radius $<0.5°$), the BA has to submit a *Swift* ToO in order to follow the burst at other wavelengths, provided that this burst is not already detected by *Swift* and that the Sun avoidance condition is fulfilled (see Sect.4.2.1). Afterwards, the LAT BA is expected to write a GCN circular to inform the GRB community as fast as possible about the position of the GRB and the preliminary results of his/her analyses. In case of a confirmed LAT detection, the BA uploads the new GRB to the LAT GRB public table[1]. Once the real-time analyses have been performed, and in case of a bright LAT detection, the GBM and LAT BAs work together to perform in-depth analyses of the burst. For the most interesting bursts, the analysis results and interpretations are published in articles signed by the *Fermi* collaborations, where the author priority is usually given to the BAs to reward them for their service work.

A ***BA tool*** has been developed by the *Fermi* GRB group to facilitate the BA work and to provide near-real time results as quickly as possible. The ***BA tool*** is an interface of the science tools including new scripts, which allow for an interactive analysis in addition to the manual analysis of the BA. The scripts of the ***BA tool*** are run automatically by the ASP system as soon as the data processing is finished. If a new GCN alert notice is generated by the GBM, including an updated localization, the LAT BA can run the ***BA tool*** manually to search for a LAT detection at the new position. The ***gtburst***[2] tool developed by the GRB group also offers the possibility of a quick analysis of the LAT data.

[1] `https://fermi.gsfc.nasa.gov/ssc/observations/types/grbs/lat_grbs/table.php`
[2] `https://fermi.gsfc.nasa.gov/ssc/data/analysis/scitools/gtburst.html`

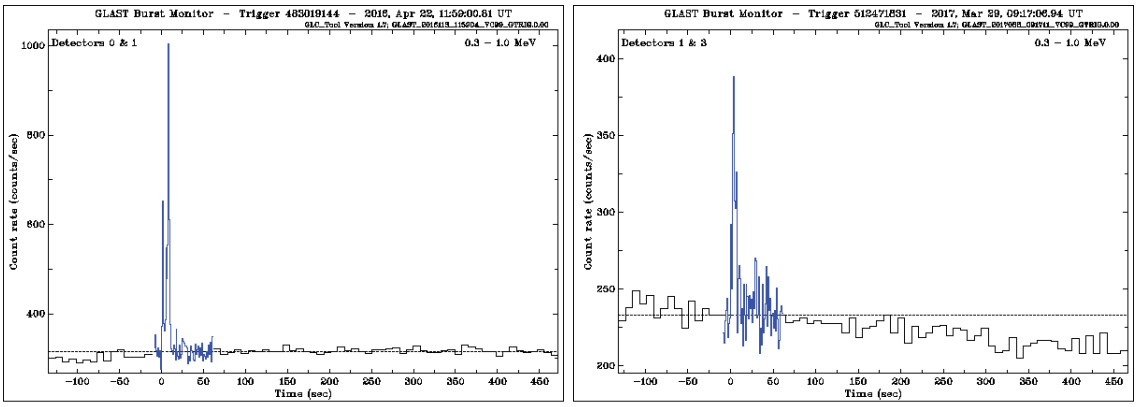

Figure 4.1: *From left to right: GBM light curves of GRBs 160422A and GRB 170329A respectively as seen by the NaI detectors in the energy range [0.3 MeV, 1 MeV].*

The GRB group defined three time zones for the BA (in Europe, United States and Japan) to be covered by the shifters. The BA's work extends during one full week (7 days) of ∼12 hours during each day, while the nights are monitored by a deputy BA in another zone.

4.2 Detection of new bursts

The BA duty is a good opportunity for participating in the interactive detections of GRBs in real time. During my Ph.D., I had the occasion to be the LAT BA for 11 weeks of shifts. During three of these shifts, we detected three GRBs (GRBs 160422A, 170329A and 170728B) for which I am the author of their GCN circulars (see Sect.4.5). The third burst was detected only one month before the thesis defense, hence, it is not described in this manuscript. I contributed as a co-author to the LAT detection and analysis of five other bursts which occured during the shifts of colleagues in the LAT team. All the analyses presented in this section were performed using the Pass 8 dataset (see. Sect.2.4.3).

4.2.1 Detection of GRBs 160422A and 170329A

On April 22, 2016, the GBM detected the long GRB 160422A at 11:59:00.81. It has an extremely impulsive rise in the GBM light curve and has been seen up to 1.5 MeV as shown in Fig.4.1, left. This burst is considered as an ordinary burst compared with the LAT GRBs. It was 53° from the LAT boresight at the time of

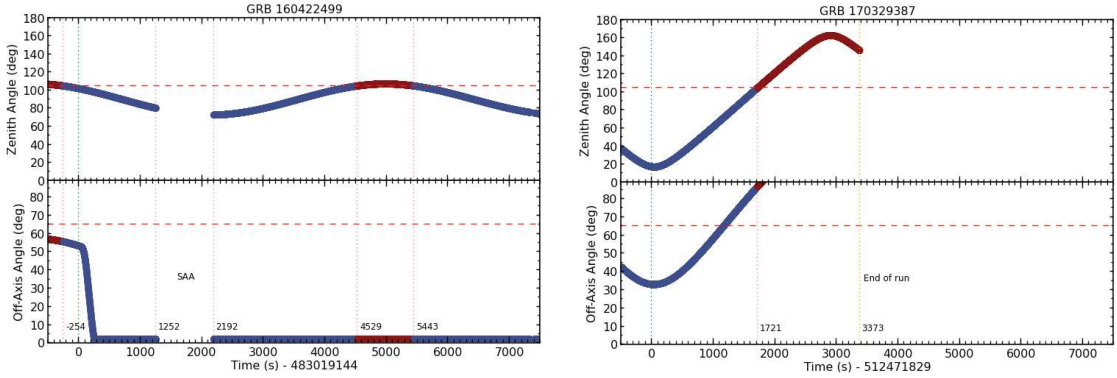

Figure 4.2: *Navigation plots of GRBs 160422A (left) and 170329A (right) showing the zenith angle of the spacecraft in the top panel and the burst off-axis angle with respect to its observation time in the bottom panel.*

the trigger (see Fig.4.2, left, bottom panel) and triggered an ARR of the spacecraft. The burst was contaminated by the Earth's limb emission at the trigger time (see Fig.4.2, left panel). The spacecraft entered the SAA zone at 1200 s post-trigger and it exited this zone at ∼2300 s. A high-energy photon of 12 GeV was detected by the LAT 770 seconds after the GBM trigger. I analyzed GRB 160422A with the unbinned ML method described in Sect.3.2.2. I analyzed the first 1200 s post-trigger, using the `TRANSIENT020` events above 100 MeV which are contained in a 12° radius ROI centered on the position found in the ASP analysis. I suppressed the Earth's limb contamination by excluding all the time intervals with a zenith angle larger than 100° ($\theta_z^{max} = 100°$). I defined a source model containing the galactic template $gll\_iem\_v06.fits$ in addition to the GRB with a PL spectrum. I localized the burst at RA , Dec = 42.06°, -57.90° with a statistical error radius of 0.09° at 90% confidence level, which is compatible with the results from the ***BA tool***. This result was cross-checked by the colleagues of the GRB group who attended the meeting by teleconference. The localization error of this burst is small with respect to the error box of *Swift*/XRT. Consequently, I requested a *Swift* Target of Opportunity (ToO) and submitted a GCN circular [Yassine et al., 2016] (see Sect.4.5). The X-ray and the optical afterglow emission of this GRB were observed by the *Swift*/XRT [Maselli et al., 2016] and UVOT [Marshall, 2016] instruments. The position given by the UVOT instrument confirmed our localization with (R.A., Dec.) = (42.09°, -57.88°) with an estimated 90% error radius of 0.45". The GROND observation of this GRB did not provide a distance measurement and only preliminary magnitudes were estimated [Schweyer et al., 2016].

My spectral analysis of GRB 160422A yielded a photon index γ = -1.66 ± 0.26 and an integrated flux of $(1.44 \pm 0.61) \times 10^{-6}$ cm^{-2} s^{-1}above 100 MeV with a detection significance of 6.5 σ ($\sqrt{TS}$). To extend the analysis of this source, I performed

unbinned likelihood analyses using different ROI and θ_z^{max} cuts in order to check their effects on the analysis results (see Tab.4.1). For a fixed θ_z^{max} at 100°, the analysis shows compatible results for ROI of 10° and 12°. For a fixed ROI radius at 10°, the analysis with a high θ_z^{max} cut at 105° seems to be contaminated by the Earth's limb emission. On the other hand, an extreme cut of θ_z^{max} at 85° decreases the burst statistics down to only 12 photons. This configuration affects the results as can be seen from the large uncertainties on the flux (3.90 ± 2.60)×10^{-6} $cm^{-2}s^{-1}$and on the GRB position (0.88°). The results for (θ_z^{max}=100°, ROI= 10°) are compatible with those for (θ_z^{max}=90°, ROI= 10°). This analysis shows the importance of the selection cut choices, which must be often optimized for an accurate GRB analysis.

The second detected burst, GRB 170329A, triggered the GBM at 09:17:06.94 UT. It was detected by the GBM up to at least 1 MeV (see Fig.4.1, right). This burst was also detected by the LAT. It was 33° from the LAT boresight at the time of the trigger. It exited the LAT FoV at 1000 s (see Fig.4.2, right). The most energetic photon of this GRB has an energy of 0.8 GeV and was detected 4 seconds after the GBM trigger. The LAT localized this GRB at the position (356.6°, 9.8°) with a 90% error radius of 0.6° and with more than 6σ of significance. I asked for a *Swift* ToO at the position found by the LAT, via a LAT offline position GCN notice. This request was declined due to the relatively large error on the LAT position, and to the proximity of the Sun (the burst position was at 13° from the Sun, within the Sun avoidance region of *Swift*[3]). The spectral analysis of this source yielded an index of -2.6 ± 0.4 and a photon flux of (4.66 ± 1.42)×10^{-6} $cm^{-2}s^{-1}$above 100 MeV.

4.2.2 Contribution to other burst detections in real time

Additionally, I contributed to the analyses of five new bursts detected by the LAT outside my BA shifts. The results of these analyses, i.e. localization, highest energy photon, etc., are presented in Tab.4.2 and reported briefly in this section.

GRBs 150210A [Zhu et al., 2015] and 150510A [Racusin et al., 2015] are LAT ordinary bursts which triggered the GBM. The highest energy photon detected by the LAT did not exceed 2 GeV in both cases. The LAT localized GRB 150510A at the position (RA, Dec) = (15.14°, 4.99°) with a 90% error radius of 1.3° which was too large to ask for a *Swift* follow-up. Indeed, part of the data was missing because of the spacecraft repointing (ARR) that caused a delay in their downlink. Based on the complete data, an updated position was obtained later with a 90% error radius of 0.36° (see Tab.4.2). Although the new error radius was smaller than the field of view of the *Swift*/XRT, the burst was not followed up since it was located within the Sun avoidance region of Swift. Both GRBs 150210A and 150510A have a large

[3]The sky region around the Sun that can not be observed by the *Swift* instruments because of safety reasons.

number of LLE events. Using this data selection, these bursts were detected above the background with 20σ and 9σ significance, respectively.

GRBs 160310A [Vianello et al., 2016] and 170228A triggered the GBM at 00:22:58.47 and 19:03:00.71 UT and they were also detected by the LAT. The highest-energy photon detected from GRB 160310A (resp. GRB 170228A) has an energy of 30 GeV (resp. 5 GeV), and it was detected 5800 seconds (resp. 130 s) after the GBM trigger. The significance of their LAT detection was 5.6σ and 5.8σ, respectively. A Swift ToO was requested for each of them owing to the good LAT localizations (see Tab.4.2).

On 2016 May 9, both *Fermi* instruments triggered on the extraordinary GRB 160509A [Longo et al., 2016a]. This burst is one of the rare sources detected by the LAT onboard algorithm. It is very bright, with a flux of $(0.56 \pm 0.06)\times10^{-4}$ cm^{-2} s^{-1}above 100 MeV, and one of the most exciting LAT bursts (see 4.3). The onboard algorithm localized GRB 160509A at (RA,Dec) = (310.1°, 76.0°) with a 90% error radius of 0.5° [Longo et al., 2016b]. After receiving the data on ground, we refined the analysis and found an accurate localization with a 90% error of 0.20°. The burst triggered an ARR of the spacecraft, which started after 2 minutes and allowed to observe the high-energy aferglow for 2.5 hours. My spectral analysis yielded a position that is similar to the one obtained with the ***BA tool***. This burst is detected with more than 17σ significance as shown on the TS map of Fig.4.4. The detection of the X-ray afterglow of GRB 160509A by the *Swift*/XRT motivated ground follow-up observations. Observations of the optical aferglow with the Gemini North telescope on Mauna Kea placed the burst at a spectroscopic redshift z = 1.17 [Tanvir et al., 2016]. A recent analysis made by [Kocevski and Longo, 2016] showed that GRB 160509A underwent a transition from a phase where the jet internal emission is dominant, to a an external shock emission phase.

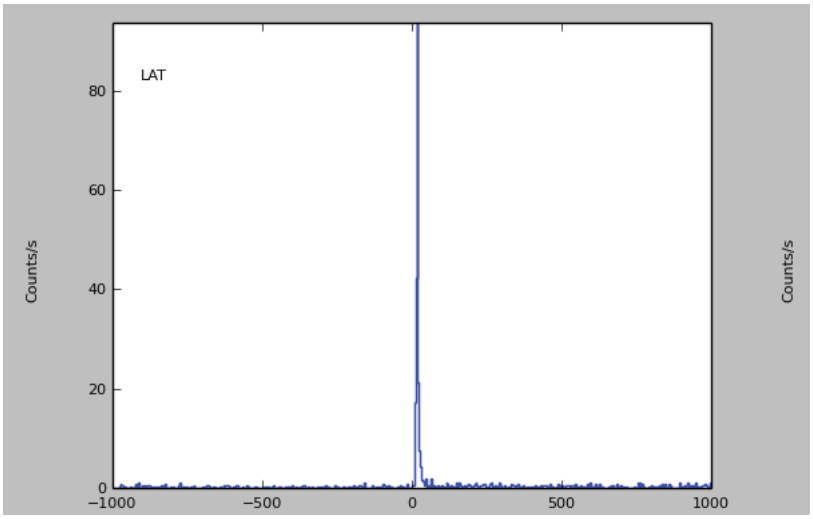

Figure 4.3: *LAT light curve of GRB 160509A.*

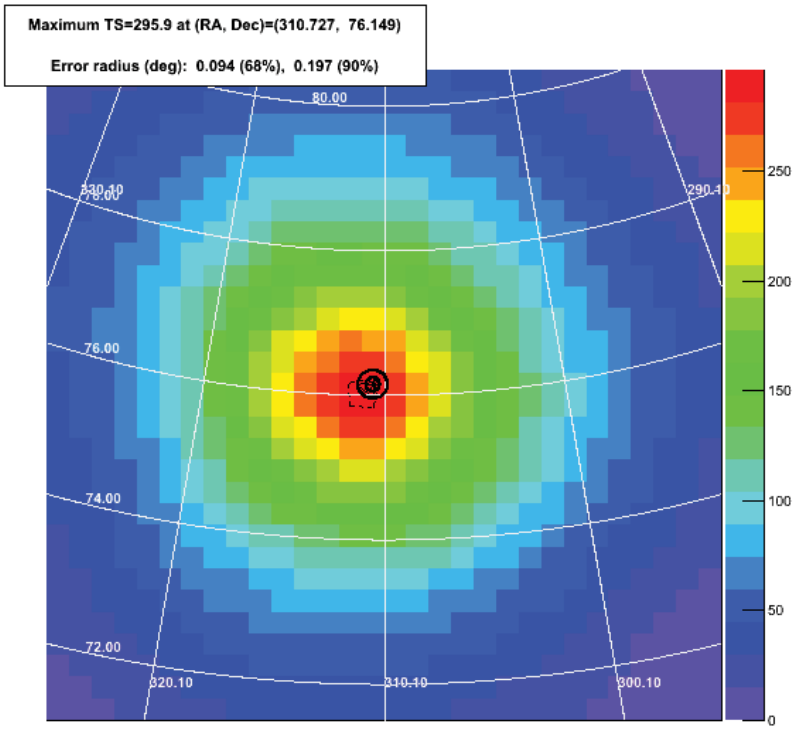

Figure 4.4: *TS map of GRB 160509A. The black circles represent the 68% and the 90% error radii around the position of the GRB.*

Analysis	θ_z^{max} = **100°**		**ROI = 10°**		
ROI/ θ_z^{max}	**12°**	**10°**	**105°**	**90°**	**85°**
Number of events	52	36	61	14	6
Test statistic TS	42	43	51	37	12
RA, Dec (deg)	42.06, -57.90	42.04, -57.89	42.07, -57.91	42.05, -57.90	43.21, -57.60
90% error radius (deg)	0.09	0.08	0.09	0.09	0.88
Photon index γ	-1.66 ± 0.26	-1.69 ± 0.26	-2.02 ± 0.29	-1.35 ± 0.29	-1.64 ± 0.42
Photon flux above 100 MeV $\times 10^{-6}(\mathrm{cm}^{-2}\,\mathrm{s}^{-1})$	1.44 ± 0.61	1.54 ± 0.64	2.73 ± 1.01	1.42 ± 0.79	3.90 ± 2.60

Table 4.1: *Results of the spectral analyses of GRB 160422A during the time interval from 0 s to 1200 s post-trigger using different ROI and* θ_z^{max} *cuts.*

Burst name	GRB150210A	GRB150510A	GRB160310A	GRB160509A	GRB170228A
observation time in the LAT FoV	T_0+(0-1000) s and after T_0+5000 s	T_0+(500-600) s	T_0+(0-500) s and T_0+(5200-7000) s	T_0+(0-2660) s	T_0+(80-800) s
Angle from the LAT boresight at the GBM trigger time	55°	55°	62°	32°	70°
highest-energy photon	1 GeV	1.5 GeV	30 GeV	52 GeV	5 GeV
detection time of	T_0+2 s	T_0+170 s	T_0+5800 s	T_0 + 77 s	T_0 + 130 s
(R.A., Dec)	(112.15°, 13.27°)	(16.16°, 4.79°)	(98.78°, -7.11°)	(311.3°, 76.1°)	(239.55°, -3.59°)
90% error radius (deg)	0.33°	0.36°	0.1°	0.12°	0.3°

Table 4.2: *The observation information and the positions of 5 new bursts detected by the LAT.*

4.3 Contribution to the second LAT GRB catalog

In the first *Fermi*/LAT GRB catalog [Ackermann et al., 2013b], covering a three-year period since the launch, only 35 bursts were detected either by the ML analysis at energies > 100 MeV or using LLE data. Thanks to the improved knowledge of the instrument systematics and to the updated reconstruction / classification algorithms (Pass 8), the LAT detection number has notably increased. In addition, a new LAT detection algorithm called LTF (for "LAT Transient Factory") has been developed to optimize the LAT data analysis methods, e.g. benefiting from a better understanding of the systematic uncertainties of the GBM localizations [Connaughton et al., 2015]. This algorithm helped to increase the number of detections of the LAT GRBs by 40%. As a result, these improvements increased the size of the LAT GRB sample beyond 100. This also motivated a global effort in the *Fermi* group toward the second LAT GRB catalog [Vianello et al., 2015].

The LTF algorithm looks for a GRB by computing TS maps in 10 pre-defined time windows, whose duration ranges from 10 s to 10 ks after the trigger time, around the position provided by the GBM or by *Swift*. Once the maximum of the TS maps is determined, a likelihood analysis is performed to get an accurate position of the GRB taking into account the contributions of the surrounding sources to the ROI (for more details see [Vianello et al., 2015]). This algorithm has an excellent efficiency for detecting and localizing transient sources such as short and long bursts. Over long time scales (kilo-seconds), it can also catch nearby blazars whose flux is in a high state. It is therefore necessary to check every GRB candidate returned by the LTF, and to look for other possible source associations.

The confirmation of a GRB candidate requires several conditions: the burst detection is considered significant enough if a TS larger than 25 is obtained from the manual likelihood analysis, with at least three photons associated with the burst with a probability larger than 90% (calculated with ***gtsrcprob***, see Sect.3.2.2). For long time scale detections (> 1 ks), it is required to check whether the GRB candidate could actually be a flaring blazar. For this purpose, we used the list of flaring sources detected by the FAVA algorithm (for *Fermi* All-Sky Variability Analysis) [Ackermann et al., 2013a]. On the other hand, for short time scale detections ($<$ 1 ks), it is recommended to check a possible association with the Sun. One must keep in mind that a bright GRB is typically detected by the LAT in the first 100 s after the GBM trigger time, which can also help to assess the validity of a GRB candidate. Finally, a careful attention must be paid to the GRB localization error, since a large uncertainty could be, e.g., due to the Earth's limb contamination.

All of these criteria can be applied by using the different tools that are available to the GRB group and to the BAs. As a member of this group, I participated in the manual check of the candidates found by the LTF. In tandem with a col-

Name of the GRB candidate	(R.A, Dec.)	Detection timescale (s)	TS	Detection
GRB081009140	(250.50°, 18.40°)	500	34	√
GRB100414097	(192.11°, 8.69°)	100	183	√
GRB110328520	(121.65°, 41.53°)	500	39	√
GRB121216419	(131.81°, -77.39°)	10	30	√
GRB140511095	(329.76°, -30.06°)	10^4	14	X
GRB140723067	(210.63°, -3.73°)	100	181	√
GRB141012773	(286.82°, -49.88°)	100	76	√
GRB150210935	(112.85°, 12.36°)	100	78	√
GRB160310016	(98.78°, -7.11°)	10^4	30	√
GRB160325291	(15.65° , -72.69°)	100	38	√

Table 4.3: *Detection and localization results for ten burst candidates in the LAT second GRB catalog.*

laborator from the GRB group, I performed the analysis of 10 candidates, which are reported in Tab.4.3. This table shows, for each burst, the detection time window and the significance of the detection presented as a TS value. The likelihood analyses of the 10 bursts were performed using the ***gtburst*** tool within a 12° ROI centered on the position reported by the LTF, and applying a cut on θ_z^{max} at 100°. In all of these likelihood analyses, the background components of the sky model consist of the Galactic template "$gll\_iem\_v06\_cut.fits$" and the isotropic template "$iso\_IRFs\_V6\_v06.txt$" provided by the LAT collaboration, in addition to the point sources from the 2FGL catalog [Nolan et al., 2012] in the source region defined around the ROI. As a result, only one burst over the ten bursts studied in this work was found to be a false detection and, thus, excluded from the catalog. This candidate was associated with a blazar located 1.34° away from the position returned by the LTF algorithm.

4.4 Re-analysis of LAT bright GRBs with Pass 8 data

During the period preceding the public release of LAT Pass 8 data and IRFs, I participated in the evaluation of their performance by re-analyzing several LAT GRBs. Among the bright bursts in the first LAT GRB catalog [Ackermann et al., 2013b], I focused on the long bursts GRB 080916C and GRB 090926A.

4.4.1 Observations of GRBs 080916C and 090926A

GRB 080916C triggered the GBM at 00:12:45.61 UT on 2008 September 16. It is the first very bright burst detected by the LAT [Abdo et al., 2009b]. It appeared at a

large off-axis angle $\theta \sim 49°$ and exited the LAT FoV after ∼20 min. Unfortunately, the repointing capability of the *Fermi* spacecraft (ARR) was enabled a few weeks later, in October 2008. The burst was localized by the LAT at (R.A., Dec.) = (119.88°, -56.58°) with a 90% error radius of 0.13°. The telescope GROND placed this burst at a redshift z= 4.35 ± 0.15 [Greiner et al., 2009]. The highest energy photon in the Pass 7 data was detected at 16.5 s post-trigger with an energy of 13.3 GeV. Interestingly, an even more energetic photon was later discovered in the Pass 8 data, with an energy of 27.4 GeV at 40.5 s post-trigger [Atwood et al., 2013].

GRB 090926A is a remarkable burst due to the extreme variability observed in its light curve at all energies. This burst triggered the GBM at 04:20:26.99 UT on 2009 September 26. It was detected at an off-axis angle of ∼ 48°, and it triggered an ARR of the spacecraft in order to observe its afterglow emission. However, the spacecraft remained in survey mode because the Earth avoidance condition was not fulfilled (see Sect.3.3.1). The burst rose above the horizon 3 ks after trigger. The spacecraft slewed to the GRB and kept it close to center of the LAT FoV during 5 hours. The best LAT on-ground localization of this burst is (R.A., Dec.) = (353.56°, 66.34°), with a 90% error radius of 0.07°. The follow-up observations of the optical afterglow of GRB 090926A led to redshift of 2.1071 ± 0.0001 [D'Elia et al., 2010].

4.4.2 Data selection and analysis method

In this section and the following, I present my analyses of the GeV prompt emission spectra of GRB 080916C and GRB 090926A. These analyses were performed during the whole duration of the LAT emission (i.e., during the LAT T_{90} computed in the first LAT GRB catalog [Ackermann et al., 2013b]), using the P8R2_`TRANSIENT100`_V6 (version 6) IRFs and data above 30 MeV. In order to assess how the LAT sensitivity to spectral features is improved with Pass 8 data, I repeated the analysis above 100 MeV using Pass 8 and Pass 7 data, since the event reconstruction between Pass 6, used in the first GRB catalog [Ackermann et al., 2013b], and Pass 7 remained essentially unchanged.

For these analyses, I selected the `TRANSIENT100` class events, in an ROI with a radius of 12°. In order to avoid any residual contamination from the Earth's limb, I excluded all time intervals with zenith angles larger than 105°. This work was performed using the science tools version 10-00-02. For the analysis of each GRB, I defined a source model which includes the spectra of the GRB and of the background, and I fitted their parameters with ***gtlike*** (Sect.3.4.2). In both GRB analyses, the galactic emission was neglected since most of the background events come from the isotropic background component. The latter not only includes astrophysical photons, but also many residual charged cosmic rays because of the looser selection cuts used to build the `TRANSIENT` event class. Besides, GRB 090926A has

a high galactic latitude (b = -49.4°). The spectrum of the isotropic background was fitted with a simple power law with the two parameters left free to vary. The spectrum of the GRB was fitted using a power-law function with a reference energy E_0 (Eq.3.11) fixed at the decorrelation energy E_{dec} (Eq.3.18). The decorrelation energy was found to be ∼330 MeV and ∼240 MeV for Pass 7 and Pass 8 datasets respectively.

I reanalyzed the spectra of GRBs 080916C and 090926A using Pass 7 and Pass 8 data in order to illustrate the gain in LAT sensitivity with Pass 8. For the spectral analyses above 100 MeV, I used the unbinned maximum likelihood method, which is recommended because of its better performance compared with the binned method (see Sect.3.2.2). Analyses with Pass 7 data are restricted to energies above 100 MeV because of the large systematic effects that are caused by the ghost events at lower energies. Since this issue has been solved in Pass 8 data (see Sect.2.4.3), I could extend the GRB spectral analyses down to 30 MeV using the binned maximum likelihood method, which is the only way to account for the important energy dispersion at low energy (see the end of Sect.3.2.2). For comparison purposes, I also performed binned analyses above 100 MeV with Pass 8 data.

4.4.3 Event statistics and analysis results

The event statistics for GRBs 080916C and 090926A in different energy ranges are presented in Tab.4.4. This table shows that the total number of events is doubled from Pass 7 to Pass 8. The largest gain in statistics is obtained below 100 MeV where the gain in effective area is the largest, with an increase of the event numbers by a factor of 3 to 7 depending on the energy range for each of the two bursts.

Bursts	**GRB 080916C [5 s, 209.8 s]**			**GRB 090926A [5.5 s, 225 s]**		
Datasets	Pass 7	Pass 8	P8/P7	Pass 7	Pass 8	P8/P7
30 MeV-100 GeV	428	991	2.3	447	1088	2.4
30 MeV-50 MeV	47	251	5.3	33	243	7.4
50 MeV-0.1GeV	119	358	3	95	381	4.0
0.1 GeV-0.5 GeV	189	303	1.6	257	391	1.5
0.5 GeV-1 GeV	48	59	1.2	29	40	1.4
1 GeV-10 GeV	23	18	0.8	32	32	1.0
10 GeV- 100 GeV	2	2	1.0	1	1	1.0

Table 4.4: *Event statistics in Pass 7 and Pass 8 data during the LAT T_{90} of GRBs 080916C (from 5 s to 209.8 s) and 090926A (from 5.5 s to 225 s) in different energy ranges.*

The results of the analyses of GRB 080916C and GRB 090926A spectra, using LAT Pass 7 and Pass 8 datasets above 100 MeV during the LAT T_{90} time interval

are reported in Tabs.4.5 and 4.6 respectively. These tables show the unbinned ML analysis of Pass 7 data, and the unbinned and binned analyses of Pass 8 data. All of the three fits above 100 MeV gave consistent results in terms of the photon index. The flux obtained with Pass 8 data for GRB 080916C is slightly larger (23 %) than the flux obtained with Pass 7 data, however both datasets gave identical flux values for GRB 090926A. The unbinned and binned analyses of Pass 8 data show similar results.

In a second step, the burst spectra were analyzed by applying the binned ML to Pass 8 data, including events with energies above 30 MeV. A better accuracy on the spectral parameters was obtained with this configuration (see the last column of Tabs.4.5 and 4.6). This configuration offered a number of events of ∼2.3 times larger than the previous dataset. The analysis in this wide energy range yielded a photon index γ = -2.23 ± 0.04 and an integrated flux of (37 ± 1.3) × 10^{-5} $cm^{-2}\,s^{-1}$for GRB 080916C, and γ = -2.20 ± 0.03 and a flux of (48 ± 1.5) × 10^{-5} $cm^{-2}\,s^{-1}$for GRB 090926A. These results are presented in Fig.4.5 which shows the SEDs of GRBs 080916C and 090926A. The narrowest confidence level contour is obtained with the analysis including data above 30 MeV. This result clearly illustrates the improvement of the spectral reconstruction with Pass 8, which allows to include lower energy events in the likelihood analysis.

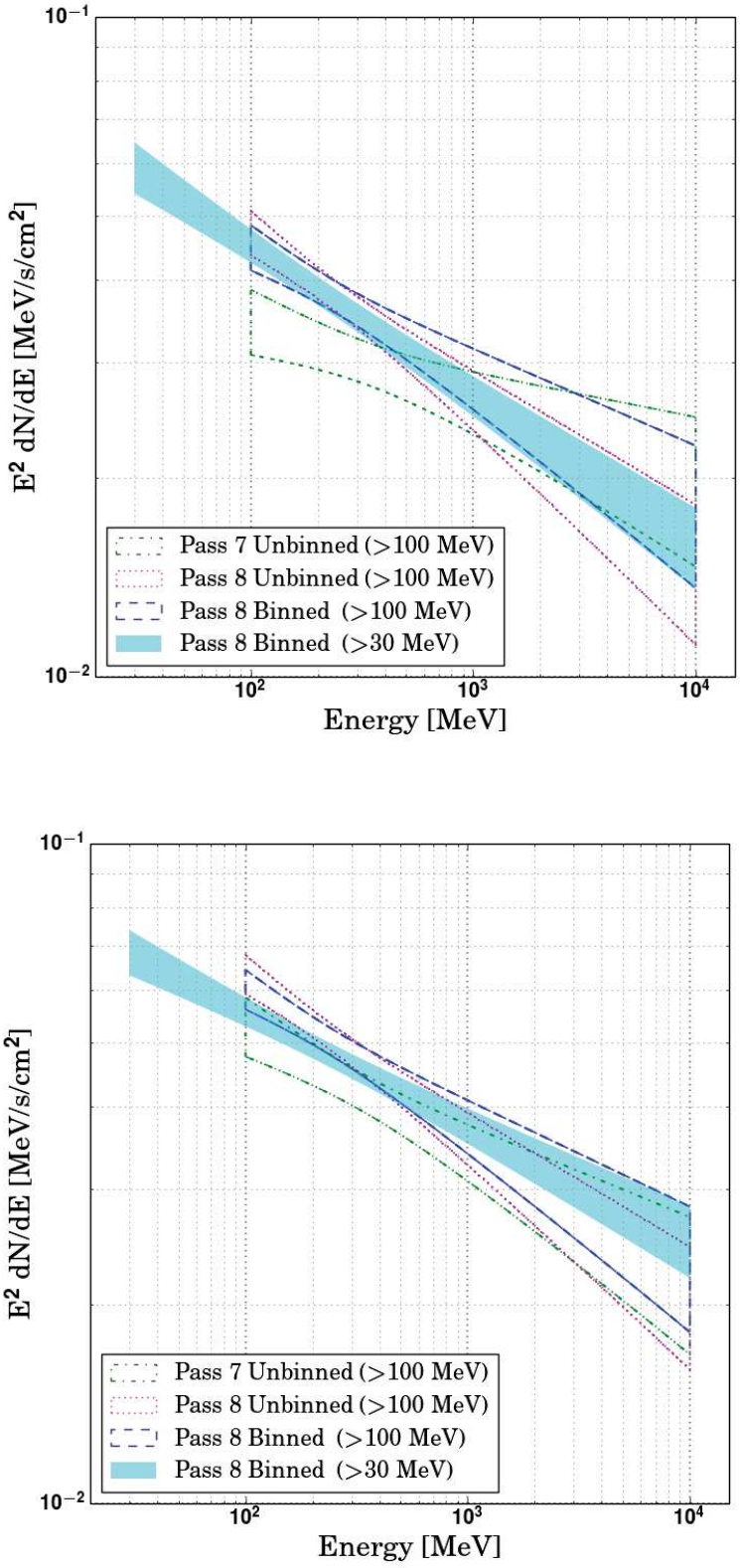

Figure 4.5: *Time-averaged spectral energy distribution of GRB 080916C ttop panel) and GRB 090926A (bottom panel), using Pass 7 (green dotted-dashed butterfly), Pass 8 data above 30 MeV (cyan butterfly) and above 100 MeV (pink dotted and blue dashed butterflies). This figure shows, for each of the four analyses, a 68% confidence level contour which is derived from the errors on the parameters of the fitted power-law function.*

Analysis method	**Unbinned ML**		**Binned ML**	
LAT dataset	Pass 7	Pass 8	Pass 8	Pass 8
LAT energy range	100 MeV-100 GeV	100 MeV-100 GeV	100 MeV-100 GeV	30 MeV-100 GeV
Number of events	262	382	382	991
A_{pl} ($\times 10^{-4}$ keV^{-1} cm^{-2} s^{-1})	2.7±0.2	6.4 ± 0.3	6.4 ± 0.4	6.3 ± 0.3
PL photon index γ	-2.12 ± 0.07	-2.25 ± 0.06	-2.20 ± 0.06	-2.23 ± 0.04
>100 MeV flux (10^{-5} cm^{-2} s^{-1})	31± 2	38 ± 2	37 ± 2	37 ± 1.3

Table 4.5: *Results of the PL fits to LAT data of GRB 080916C during the LAT T_{90} (from 5 s to 209.8 s post-trigger).*

Analysis method	**Unbinned ML**		**Binned ML**	
LAT dataset	Pass 7	Pass 8	Pass 8	Pass 8
LAT energy range	100 MeV-100 GeV	100 MeV-100 GeV	100 MeV-100 GeV	30 MeV-100 GeV
Number of events	319	464	464	1088
A_{pl} ($\times 10^{-4}$ keV^{-1} cm^{-2} s^{-1})	3.8 ± 0.3	8.7 ± 0.4	8.5 ± 0.4	8.1 ± 0.3
PL photon index γ	-2.19 ± 0.07	-2.25 ± 0.06	-2.21 ± 0.06	-2.20 ± 0.03
>100 MeV flux (10^{-5} cm^{-2} s^{-1})	45 ± 3.1	51 ± 2.4	50 ± 2.4	48 ± 1.5

Table 4.6: *Results of the PL fits to LAT data of GRB 090926A during the LAT T_{90} (from 5.5 s to 225 s post-trigger).*

4.5 GCN circulars

TITLE: GCN CIRCULAR
NUMBER: 19329
SUBJECT: GRB 160422A: Fermi-LAT Detection
DATE: 16/04/22 19:26:41 GMT
FROM: Judith Racusin at GSFC <judith.racusin@nasa.gov>

M. Yassine (LUPM, Montpellier), J. L. Racusin (NASA/GSFC), and N. Omodei (Stanford) report on behalf of the Fermi-LAT team:
Fermi LAT detected high-energy emission associated with GRB 160422A, which was also detected by Fermi GBM (trigger 483019143 / 160422499) at 11:59:00.81 on April 22, 2016.

The best LAT on-ground location is found to be: RA, Dec (J2000) = 42.05, -57.9 with an error radius of 0.07 deg (90% containment, statistical error only).

This was 80 deg from the LAT boresight at the time of the trigger, and triggered an autonomous repoint of the spacecraft. The GRB became unocculted by the Earth and entered the LAT field of view at ∼T0+400 seconds.

The data from the Fermi-LAT show a significant increase in the event rate that is spatially correlated with the trigger with high significance.

The highest-energy photon is a 12 GeV event which is observed 770 seconds after the GBM trigger. A Swift ToO has been requested for this burst.

The Fermi-LAT point of contact for this burst is Manal Yassine (manal.yassine@lupm.in2p3.fr).

The Fermi-LAT is a pair conversion telescope designed to cover the energy Band from 20 MeV to greater than 300 GeV. It is the product of an international collaboration between NASA and DOE in the U.S. and many scientific institutions across France, Italy, Japan and Sweden.

TITLE: GCN CIRCULAR
NUMBER: 20942
SUBJECT: GRB170329A: Fermi-LAT detection
DATE: 17/03/29 15:31:29 GMT
FROM: Manal Yassine at IN2P3/LUPM/CNRS <manal.yassine@lupm.in2p3.fr>

M. Yassine (LUPM, Montpellier) ,E. Bissaldi (Politecnico INFN Bari), G. Vianello (Stanford), J. L. Racusin (NASA/GSFC), F. Longo (University and INFN, Trieste) and N. Omodei (Stanford) report on behalf of the Fermi-LAT team:

At 09:17:06.94 UT on March 29, 2017, Fermi-LAT detected high-energy emission from GRB 170329A, which was also detected by Fermi-GBM (170329387/512471831).

The best LAT on-ground location is found to be RA, Dec 356.6, 9.8 (degrees, J2000) with an error radius of 0.6 deg (90% containment, statistical error only). This was 33 deg from the LAT boresight at the time of the trigger.

The data from the Fermi-LAT show a significant increase in the event rate that is spatially and temporally consistent with the GBM emission. More than 37 photons above 100 MeV observed within 1 ks. The highest-energy photon is a 0.8 GeV event which is observed 4 seconds after the GBM trigger.

The Fermi-LAT point of contact for this burst is Manal Yassine (manal.yassine@lupm.in2p3.fr).

The Fermi-LAT is a pair conversion telescope designed to cover the energy Band from 20 MeV to greater than 300 GeV. It is the product of an international collaboration between NASA and DOE in the U.S. and many scientific institutions across France, Italy, Japan and Sweden.

TITLE: GCN CIRCULAR
NUMBER: 21380
SUBJECT: GRB 170728B: Fermi-LAT detection
DATE: 17/07/29 13:03:36 GMT
FROM: Manal Yassine at IN2P3/LUPM/CNRS <manal.yassine@lupm.in2p3.fr>

M. Yassine (LUPM,CNRS,IN2P3) and J. L. Racusin (NASA/GSFC) report on behalf of the Fermi-LAT team:

On July 28, 2017, Fermi-LAT detected high-energy emission from GRB 170728B, which triggered the Fermi-GBM (trigger 522975804) at 23:33:32 UT July, 28 2017. This burst was also detected by Swift (Cenko et al., GCN Circ. 21371).

The best LAT on-ground location is found to be RA, Dec 238.97, 69.74 (degrees, J2000) with an error radius of 0.53 deg (90% containment, statistical error only). This was 30 deg from the LAT boresight at the time of the trigger and triggered an autonomous repoint of the spacecraft.

The data from the Fermi-LAT is spatially and temporally correlated with the GBM emission with high significance. More than 10 photons above 100 MeV are observed within 100 seconds. The highest-energy photon is a 0.6 GeV event which is observed 9.3 seconds after the GBM trigger.

The Fermi-LAT point of contact for this burst is Manal Yassine (manal.yassine@lupm.in2p3.fr).

The Fermi-LAT is a pair conversion telescope designed to cover the energy Band from 20 MeV to greater than 300 GeV. It is the product of an international collaboration between NASA and DOE in the U.S. and many scientific institutions across France, Italy, Japan and Sweden.

CHAPTER 5

Investigation of the GRB 090926A prompt emission

Contents

5.1 Motivations

Among the two bright bursts studied in the previous chapter, I focus now on GRB 090926A owing to the unique properties of its prompt emission spectrum. The extreme variability of its high-energy emission from keV to GeV energies is an evident contradiction to the external forward-shock scenario which is thought to be a good explanation for the delayed onset and of the temporal extension of the LAT emission (see Sect.1.5.1). The observed variability strongly favors an internal origin of the dissipation and radiation mechanisms at the highest energies, during the whole duration (∼22 s) of the keV-MeV prompt emission as seen by the GBM.

The light curve of GRB 090926A during its prompt phase is presented in Fig.5.1. It shows a bright spike at ∼10 s post trigger, which is present in all detectors with a synchronization within less than 50 ms. The temporal correlation between the keV-MeV and GeV emissions during this bright spike suggests that both emissions have a common origin. Moreover, this bright spike coincides with the emergence of an additional power law component at energies greater than 10 MeV. Interestingly, this additional component exhibits a spectral break at a few hundreds of MeV (Fig.1.18). This spectral attenuation has been previously interpreted in terms of γ-ray annihilation, and used to set constraints on the bulk Lorentz factor of the outflow [Ackermann et al., 2011]. Another hint for the internal origin of the GeV emission from GRB 090926A during the first instants is provided by its luminosity decay, which shows a break well after the end of the keV-MeV prompt emission (Fig.1.19, right). This temporal break was observed at 40 s post-trigger with an increase of the luminosity decay index from ∼-2.7 to ∼-1. This break has been interpreted as marking the transition between the prompt and the afterglow phases [Ackermann et al., 2013b].

In this chapter, I present the analyses of the prompt emission spectrum of GRB 090926A. Firstly, a time-resolved spectroscopic analysis using the LAT-only data is presented in Sect.5.2. Secondly, a joint GBM and LAT data analysis is performed in order to characterize the time evolution of the spectrum in a wide energy range (from a few keV to GeV energies). These analyses are presented in

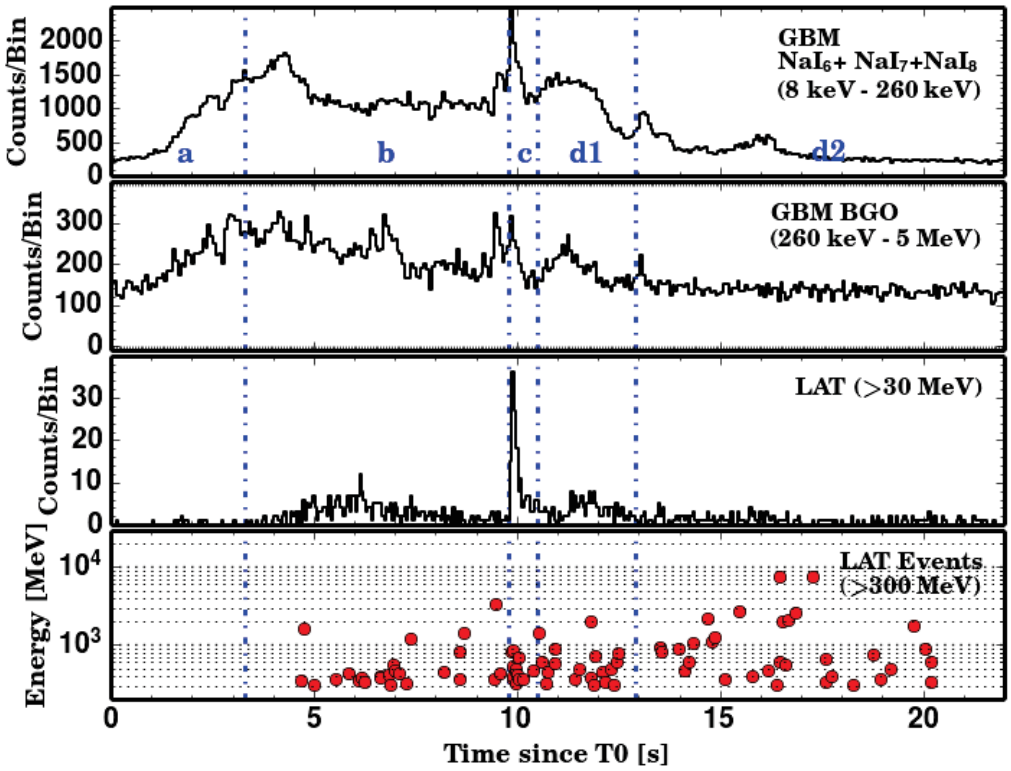

Figure 5.1: *Fermi multi-detector light curve of GRB 090926A during its prompt phase. The vertical dashed lines at T_0 + 3.3, 9.8 s and 10.5 s define the boundaries of the time intervals a, b, c, d_1 and d_2. The vertical dashed line at T_0 + 12.9 s separates the two time intervals (d_1 and d_2) of the time interval d.*

Sect.5.3. Additional contributions to the spectrum have been investigated at low and high energy such as a thermal component, or specific shapes for the high-energy spectral break. These analyses are presented in Sect.5.3.3 and 5.4. Sect.5.5 and 5.6 show my study of the temporal evolution of the high-energy spectral break and the systematic uncertainties on my results, respectively. To constrain the bulk Lorentz factor of the outflow, the variability timescales in the burst multi-detector light curve were derived as detailed in Sect.5.7. Finally, different theoretical interpretations are discussed in Sect.5.8.

5.2 LAT-only time resolved spectral analysis

In the first publication of the Fermi GRB group [Ackermann et al., 2011], the multi-detector light curve of GRB 090926A was split into four time intervals for the spectroscopic analysis (a, b, c and d) with upper boundaries respectively at (3.3, 9.8, 10.5, 21.6) s post-trigger (see Fig.5.1). In this work, I focused my study of the spectral and temporal evolution of this burst on the time period (intervals c and d) where the emission was the brightest in the LAT. The LAT spectral analysis of the two time intervals was performed following the same methodology used in Sect.4.4.2. I selected the Pass 8 `TRANSIENT100` events contained in a RoI of 12°, and I applied a cut on θ_z^{max} at 105°. I performed both an unbinned ML analysis above 100 MeV and a binned ML analysis above 30 MeV. In addition, I analyzed the Pass 7 data above 100 MeV with the unbinned ML method, to compare my results with those of [Ackermann et al., 2011].

5.2.1 Spectral models

In order to fit the spectrum of GRB 090926A in the LAT energy range, I adopted either a power law (PL, Eq.3.11) or a power law with an exponential cutoff (CUTPL, Eq.3.12). Both functions are normalized by a free amplitude parameter in units of $\mathrm{keV}^{-1}\,\mathrm{cm}^{-2}\,\mathrm{s}^{-1}$. To minimize the correlation between the fitted parameters, I fixed the reference energy E_0 at a value close to the decorrelation energy of Eq.3.18. Depending on the analyzed data set, the values for E_0 range from 200 MeV and 500 MeV. To test the detection and the significance of a spectral break at high energy, the likelihood test statistic (TS) was used between a PL and a CUTPL functions. Following Eq.3.9, the TS is computed as $2\,(\ln \mathcal{L}_1 - \ln \mathcal{L}_0)$, where $\mathcal{L}_0$ and $\mathcal{L}_1$ are the maximum values of the likelihood functions obtained with the PL and CUTPL models, respectively. For a detection of the spectral break, I searched for a TS $\geqslant 25$ ($\sigma \geqslant 5$, see Sect.3.3.2).

5.2.2 Results

The fit results above 100 MeV with Pass 7 (unbinned) and Pass 8 (binned and unbinned) data are shown in Tab.5.2 and Tab.5.3 for the time intervals c and d respectively. These tables report also the analyses of Pass 8 data including energy events below 100 MeV. For the time interval c, as can be seen in Tab.5.2, the three fits above 100 MeV of Pass 7 and Pass 8 gave consistent photon index and folding energy E_f with a slight improvement in the reconstruction of the spectral parameters with the last dataset. Due to the low event statistics above 100 MeV, the fitted photon index is poorly constrained. Moreover, no significant spectral break was found in these analyses (only 2.5σ with Pass 8 data). A better accuracy of the spectral index was reached when including Pass 8 events with energies between 30 MeV and 100 MeV, with a marginal detection of the spectral break ($N_\sigma = 4.4$).

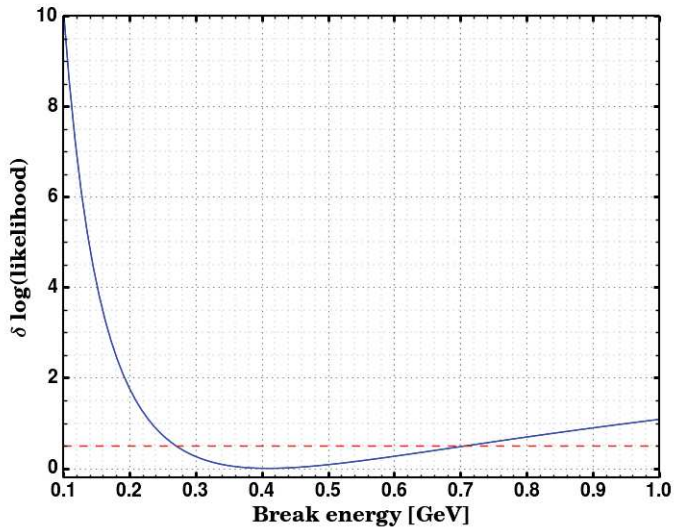

Figure 5.2: *Likelihood profile of the folding energy E_f for a fit in the time interval c of GRB 090926A and a wide LAT energy range (Pass 8 data above 30 MeV). The intersections of the horizontal red dashed line with the likelihood profile provide the asymmetric uncertainties of the folding energy.*

The large number of events in this configuration, as seen in Tab.5.2, yielded a more accurate photon index $\gamma = -1.68 \pm 0.22$ and a folding energy $E_f = 0.41^{+0.27}_{-0.14}$ GeV (see Fig.5.2). This result is fully compatible with the measurements reported in [Ackermann et al., 2011], which has been obtained in a joint spectral fit of GBM and LAT data.

For the time interval d, shown in Tab.5.3, all the fits above 100 MeV gave consistent values of the PL spectral index. Including events data down to 30 MeV doubled the available event statistics, and a more accurate spectral index of $\gamma = -2.10 \pm 0.03$ was obtained in this configuration.

5.3 Joint GBM/LAT analysis

5.3.1 Data preparation and fitting procedure

As seen in the previous section, with the LAT data alone, I could not detect a significant deviation from the simple power law shape at high energy in the time interval c (only a marginal detection was obtained). To characterize the spectral evolution from keV up to GeV energies, I combined the GBM keV-MeV data with the LAT data in joint spectral analyses. In addition to the analyses of time intervals c and d,

	BGO/NaI normalization factor $f_{\rm eff}$	
Spectral models	0.83	0.79
`Band` + **PL**		
`Band`		
$A_{\texttt{Band}}$ ($\times 10^{-2}$ keV^{-1} cm^{-2} s^{-1})	17.8 ± 0.3	18.3 ± 0.4
E_{peak} (keV)	245.6 ± 3.8	240.3 ± 3.6
α	-0.58 ± 0.03	-0.55 ± 0.03
β	-2.46 ± 0.03	-2.50 ± 0.03
PL		
A_{pl} ($\times 10^{-3}$ keV^{-1} cm^{-2} s^{-1})	5.7 ± 0.7	6.2 ± 0.6
Index	-1.813 ± 0.017	-1.815 ± 0.015
C-stat/dof	960.5/541	962.2/541
`Band` + **CUTPL**		
`Band`		
$A_{\texttt{Band}}$ ($\times 10^{-2}$ keV^{-1} cm^{-2} s^{-1})	17.4 ± 0.1	17.9 ± 0.2
E_{peak} (keV)	249.9 ± 0.7	242.9 ± 0.6
α	-0.590 ± 0.008	-0.558 ± 0.009
β	-2.559 ± 0.008	-2.575 ± 0.009
PL		
A_{cutpl} ($\times 10^{-3}$ keV^{-1} cm^{-2} s^{-1})	6.3 ± 0.5	7.0 ± 0.5
Index	-1.75 ± 0.01	-1.76 ± 0.009
CUTPL		
Folding energy (GeV)	1.22 ± 0.28	1.18 ± 0.25
C-stat/dof	901.3/541	902.1/540

Table 5.1: *Results of the* `Band`*+PL and* `Band`*+CUTPL spectral fits to GBM+LAT (Pass 8) data for the prompt emission [3 s, 21 s] of GRB 090926A, using two different BGO/NaI normalization factors f_{eff}.*

a joint analysis of the time interval b [3.3 s - 9.8 s] was performed in order to check the spectral contributions at early time.

Following the analysis reported in [Ackermann et al., 2011], I selected the GBM Time-Tagged Event (TTE) data from the three NaI detectors (N6, N7, N8) and the BGO detector (B1) which have seen the burst. The GBM TTE data are unbinned in time with a good time resolution (2 μs) and they are binned in energy with 128 channels. I used the data prepared in the previous section. The analysis of the time interval b was only performed with the widest LAT energy range ($>$ 30 MeV). To get the count spectrum of the background in the LAT and GBM, I followed the steps described in Sect.3.4.2 and 3.4.3 respectively.

Analysis method	Unbinned ML		Binned ML	
LAT data set	Pass 7	Pass 8	Pass 8	Pass 8
LAT energy range	100 MeV-100 GeV	100 MeV-100 GeV	100 MeV-100 GeV	30 MeV-100 GeV
Number of events	45	65	65	152
A_{cutpl} ($\times 10^{-4}$ keV^{-1} cm^{-2} s^{-1})	3.4 ± 0.9	3.3 ± 0.7	3.1 ± 0.4	3.2 ± 0.6
CUTPL photon index γ	-1.21 ± 0.82	-1.13 ± 0.68	-1.15 ± 0.71	-1.68 ± 0.22
CUTPL folding energy E_f (GeV)	$0.23^{+0.30}_{-0.10}$	$0.24^{+0.22}_{-0.09}$	$0.27^{+0.27}_{-0.10}$	$0.41^{+0.27}_{-0.14}$
Break significance N_σ	2.3	2.7	2.5	4.4

Table 5.2: *Results of the CUTPL fits to LAT data during the time interval c (from 9.8 s to 10.5 s post-trigger) of GRB 090926A. The reference energy E_0 in Eq.3.12 has been fixed to 500 MeV for Pass 7 and Pass 8 data.*

Analysis method	Unbinned ML		Binned ML	
LAT data set	Pass 7	Pass 8	Pass 8	Pass 8
LAT energy range	100 MeV-100 GeV	100 MeV-100 GeV	100 MeV-100 GeV	30 MeV-100 GeV
Number of events	107	154	154	321
A_{pl} ($\times 10^{-4}$ keV^{-1} cm^{-2} s^{-1})	2.9 ± 0.3	3.6±0.3	3.7±0.3	3.6±0.3
PL photon index γ	-2.14 ± 0.10	-2.19 ± 0.10	-2.19 ± 0.10	-2.10 ± 0.07

Table 5.3: *Results of the PL fits to LAT data during the time interval d (from 10.5 s to 21.6 s post-trigger) of GRB 090926A. The reference energy E_0 in Eq.3.11 has been fixed to 306 MeV and 280 MeV for Pass 7 and Pass 8 data respectively.*

The joint spectral analyses were performed with the *rmfit* tool by minimizing the Castor fit statistic (C-stat) (see Sect.3.4). A significant detection of an extra power law, with two dof with respect to a reference model, is claimed if the Δ C-stat value between the two models is greater than 27 (this corresponds to 5 σ for 2 dof). On the other hand, the detection of a spectral cutoff with one dof with respect to a power law is claimed if the Δ C-stat value between the two nested models is greater than 25. The probability of a false detection using these Δ C-stat limits is less than 10^{-6}. Because of the relative uncertainties in the responses of the NaI and BGO detectors, a global effective area correction was applied to the BGO data to match the model normalization given by the NaI data. In order to match the flux given by the NaI detectors, a normalization factor $f_{\rm eff}$ was introduced in the fit between the two types of detectors following the same methodology used in [Ackermann et al., 2011]. In a first step, this parameter was left free to vary and it was estimated estimated by fitting the whole prompt emission spectrum (i.e. from T_0 + 3.3 s to T_0 + 21.6 s). Then, the parameter was held fixed for all subsequent analyses. The fitted value $f_{\rm eff} = 0.825 \pm 0.013$ is marginally compatible with the value of 0.79 reported in [Ackermann et al., 2011]. To check the effect of this slight difference on my results, I performed a joint GBM/LAT analysis for the whole prompt spectrum [3 s, 21 s] with both values (0.79 and 0.83). The spectral component observed in the GBM energy range was fitted by a `Band` function (Eq.1.2) and the LAT spectrum was fitted either with a simple PL or with a CUTPL model. The results of these analyses and their C-stat values are reported in Tab.5.1. This table shows that both values of $f_{\rm eff}$ yield very similar results. Therefore, in all of my joint analyses $f_{\rm eff}$ was held fixed at 0.83.

5.3.2 Results

For the time interval b, in addition to the keV-MeV spectral component (represented by a `Band` function) I searched for a possible extra PL component in the LAT energy range. As shown in Tab.5.4, I found that the `Band` model is sufficient to reproduce the spectrum in this time interval and the extra PL is not required by the data (Δ C-stat=7.5 for 2 d.o.f.).

The extra PL component, however, was found to be very significant in the time intervals c and d. In the time interval c, I increased the complexity of the model by adding a CUTPL component. Comparing the two models (`Band`+PL) and (`Band`+CUTPL), I confirmed the detection of a high-energy spectral break in the extra PL detected previously by [Ackermann et al., 2011]. The results of this analysis are summarized in Tab.5.5 which shows the increased significance of the spectral break from 5.9σ with Pass 7 data above 100 MeV to 7.7σ with Pass 8 above 30 MeV (see also Fig.5.3, top panel). The CUTPL parameters are well constrained and are compatible with the results reported in [Ackermann et al., 2011] with a photon index $\gamma = -1.68^{+0.04}_{-0.03}$ and a folding energy $E_f = 0.37^{+0.06}_{-0.05}$GeV.

Spectral parameters	`Band`	`Band` + **PL**
A_{Band} ($\times 10^{-3}$ keV^{-1} cm^{-2} s^{-1})	309.7 ± 4.4	316.5 ± 6.3
`Band` E_{peak} (keV)	278.7 ± 3.5	273.3 ± 4.4
`Band` α	-0.55 ± 0.01	-0.48 ± 0.03
`Band` β	-2.34 ± 0.01	-2.36 ± 0.02
A_{pl} ($\times 10^{-5}$ keV^{-1} cm^{-2} s^{-1})	-	3.80 ± 1.67
PL index	-	-1.89 ± 0.09
C-stat/dof	892.1/521	884.6/519

Table 5.4: *Results of the* `Band` *and* `Band`*+PL spectral fits to GBM+LAT (Pass 8) data during the time interval b [3.3 s, 9.8 s] of GRB 090926A.*

In the time interval d, I searched for the presence of a spectral break, which was marginally detected ($N_\sigma \sim 4$) in [Ackermann et al., 2011] with $E_f = 2.2^{+0.9}_{-0.7}$GeV. The marginal significance of the spectral break is confirmed by the LAT Pass 7 data analysis with $N_\sigma = 4.3$ (see Tab.5.6). However, interestingly the significance of the spectral break increased to $N_\sigma = 5.8$ using Pass 8 data above 30 MeV (Tab.5.6 and Fig.5.3, bottom panel). This analysis yielded a similar photon index to the one found in the time interval c ($\gamma = -1.75^{+0.02}_{-0.03}$), with a folding energy above 1 GeV ($E_f = 1.61^{+0.38}_{-0.31}$GeV). These results show, for the first time, a temporal evolution of the spectral attenuation up to the GeV domain. This temporal evolution, which has been made possible thanks to the increased event statistics in the LAT Pass 8 data set, may help to understand the characteristics of the emission of GRB 090926A as we will see further in this chapter.

In all of the following sections, the `Band`+CUTPL model will be used as a reference model for comparison purposes. Unless otherwise stated, I will always use the whole GBM (10 keV-40 MeV) and LAT (>30 MeV) Pass 8 data sets in the joint analyses presented further in this chapter.

5.3.3 Thermal emission

Fermi observations have revealed deviations of some GRB prompt spectra from the commonly used `Band` function, requiring an additional component either as a thermal black-body (BB) component [Axelsson et al., 2012; Guiriec et al., 2013]. Such a thermal radiation was actually expected from theoretical models that consider the jet emission at the photospheric radius [Rees and Mészáros, 2005; Thompson et al., 2007] (see Eq.5.8). According to a recent work made by Guiriec et al. [2015a], a BB component is found to contribute to the prompt emission of GRB 090926A at early times. The main differences between this analysis and mine are the following:

- The joint GBM/LAT data analysis was performed using the LLE data selection instead of the `TRANSIENT100` class data used in my analysis.

LAT data set	Pass 7	Pass 8	
LAT energy range	100 MeV-100 GeV	100 MeV-100 GeV	30 MeV-100 GeV
Number of events	45	65	152
$A_{\texttt{Band}}$ ($\times 10^{-2}$ keV^{-1} cm^{-2} s^{-1})	33^{+3}_{-2}	33^{+4}_{-2}	34^{+2}_{-2}
`Band` $E_{\rm peak}$ (keV)	190^{+10}_{-7}	190^{+9}_{-8}	189^{+8}_{-9}
`Band` photon index α	$-0.63^{+0.08}_{-0.15}$	$-0.62^{+0.11}_{-0.12}$	$-0.60^{+0.13}_{-0.14}$
`Band` photon index β	$-3.8^{+0.4}_{-1.1}$	$-3.6^{+0.3}_{-1.1}$	$-3.7^{+0.5}_{-1.6}$
A_{cutpl} ($\times 10^{-4}$ keV^{-1} cm^{-2} s^{-1})	$8.0^{+1.1}_{-1.5}$	$8.4^{+1.1}_{-1.6}$	$8.9^{+0.6}_{-1.4}$
CUTPL photon index γ	$-1.66^{+0.05}_{-0.03}$	$-1.68^{+0.04}_{-0.03}$	$-1.68^{+0.04}_{-0.03}$
CUTPL folding energy E_f (GeV)	$0.31^{+0.08}_{-0.06}$	$0.38^{+0.07}_{-0.06}$	$0.37^{+0.06}_{-0.05}$
Break significance N_σ	5.9	6.3	7.7

Table 5.5: *Results of the* `Band`*+CUTPL spectral fits to GBM+LAT data during the time interval c (from 9.8 s to 10.5 s post-trigger) of GRB 090926A. The reference energy E_0 in Eq.3.12 has been fixed to 1 MeV as in [Ackermann et al., 2011].*

LAT data set	Pass 7	Pass 8	
LAT energy range	100 MeV-100 GeV	100 MeV-100 GeV	30 MeV-100 GeV
Number of events	107	154	321
$A_{\texttt{Band}}$ ($\times 10^{-2}$ keV^{-1} cm^{-2} s^{-1})	$9.9^{+0.4}_{-0.6}$	$10.0^{+0.5}_{-0.5}$	$10.1^{+0.4}_{-0.2}$
`Band` $E_{\rm peak}$ (keV)	183^{+7}_{-7}	182^{+6}_{-6}	180^{+5}_{-6}
`Band` photon index α	$-0.70^{+0.07}_{-0.08}$	$-0.68^{+0.07}_{-0.08}$	$-0.65^{+0.05}_{-0.04}$
`Band` photon index β	$-2.9^{+0.1}_{-0.2}$	$-2.9^{+0.1}_{-0.2}$	$-2.9^{+0.1}_{-0.3}$
A_{cutpl} ($\times 10^{-10}$ keV^{-1} cm^{-2} s^{-1})	$4.9^{+0.8}_{-0.6}$	$6.1^{+0.8}_{-0.8}$	$6.4^{+0.2}_{-0.3}$
CUTPL photon index γ	$-1.76^{+0.04}_{-0.03}$	$-1.77^{+0.05}_{-0.01}$	$-1.75^{+0.02}_{-0.03}$
CUTPL folding energy E_f (GeV)	$2.02^{+0.80}_{-0.48}$	$1.63^{+0.53}_{-0.35}$	$1.61^{+0.38}_{-0.31}$
Break significance N_σ	4.3	5.6	5.8

Table 5.6: *Results of the* `Band`*+CUTPL spectral fits to GBM+LAT data during the time interval d (from 10.5 s to 21.6 s post-trigger) of GRB 090926A. The reference energy E_0 in Eq.3.12 has been fixed to 1 GeV as in [Ackermann et al., 2011].*

- The detectors used in [Guiriec et al., 2015a] (N6, N7, N3, B0, B1) are different from those used in [Ackermann et al., 2011].
- A good consistency of the NaI and BGO detectors was assumed i.e. a normalization factor f_{eff}=1, versus 0.83 in my analysis (see Sect.5.3)
- The time intervals used in [Guiriec et al., 2015a] are different than the b, c, d intervals used in my work.

In this section, a joint analysis of this burst including a BB component is presented. The contribution of a black-body component was tested as an additional component

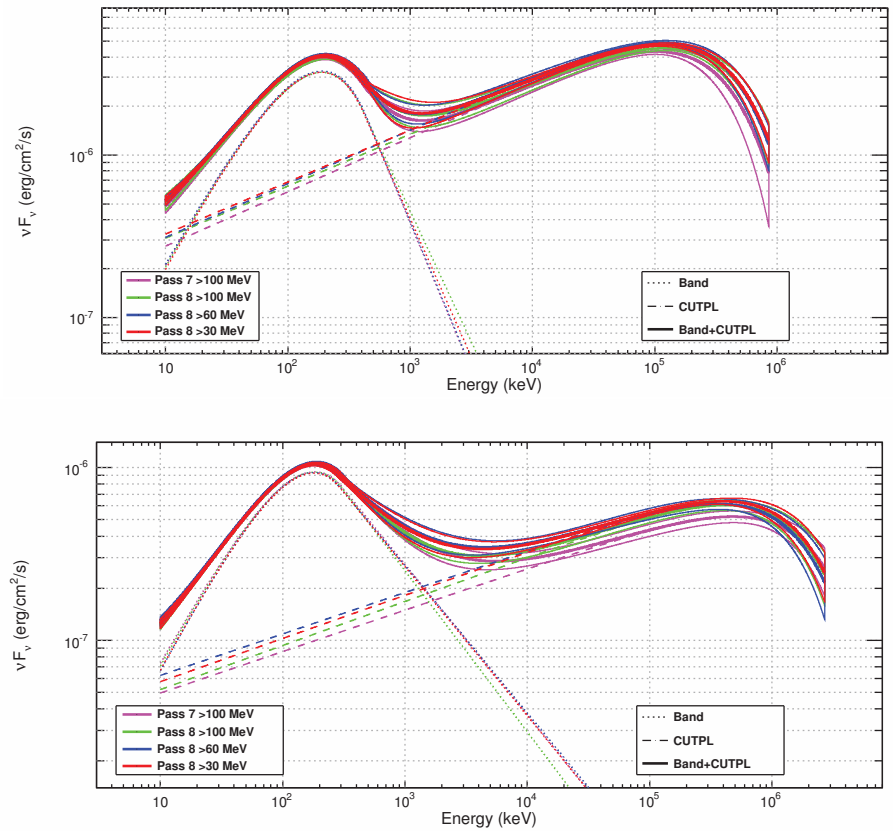

Figure 5.3: *GRB 090926A νFν spectra in the time interval c (top) and in the time interval d (bottom). Each solid curve represents the fitted spectral shape (Band+CUTPL), within a 68% confidence level contour derived from the errors on the fit parameters.*

Time interval		**time interval b**	**time interval c**	**time interval d**
Preferred Model		Band	Band + CUTPL	Band + CUTPL
Castor STAT	**dof**			
Band	521	892.1	-	-
Band + **BB**	519	851.1	-	-
Band + **CUTPL**	518	-	588.7	640.6
Band + **CUTPL** + **BB**	516	-	589.1	628.7

Table 5.7: *Castor statistic results for the best fits to GBM+LAT data during the time intervals b, c and d with and without a black-body contribution.*

of the best fit model in each of the three time intervals b (Band), c and d (Band + CUTPL). The corresponding C-stat values are presented in Tab.5.7. This table

shows a Δ C-stat equal to 1 and 12 for time intervals c and d, respectively with respect to their corresponding best fit model. This analysis, hence, did not show any detection of a BB component in any of the two time intervals. On the contrary, the result in the time interval b shows a strong contribution of the BB component with a temperature kT= $92.5^{+3.3}_{-3.2}$ keV and a $\sim 6\sigma$ significance (Δ C-stat = 41 for 2 d.o.f.). This detection was confirmed using the *XSPEC* software with a Δ C-stat of 31 (N$\sigma \sim 5.2$) at the temperature 88.2 ± 6.1 keV. Guiriec et al. [2015a] estimated the BB temperature at kT=49$\pm$ 2.1 (Δ C-stat=37, i.e. $\sim 5\sigma$) for the time interval (5 s , 9 s). The difference with my result is likely explained by the different analysis configurations. Nevertheless, both analyses show that the BB component is detectable only at the beginning of the burst prompt emission, and can be ignored at later times (intervals c and d).

5.4 Spectrum representation

The spectral break detected at high energy in the prompt spectrum of GRB 090926A can result from the gamma-ray opacity to pair creation, or it can reflect the nature shape of the inverse Compton spectrum. Assessing the shape of the curvature of the high-energy spectrum is, therefore, crucial to be able to distinguish between the two scenarios.

5.4.1 High-energy power-law component with a sharp break

In order to assess the shape of the high-energy spectrum in the time interval c, I examined different models that could be representative of some theoretical predictions. A detailed study of the $\gamma\gamma$ opacity to pair creation in GRB jets has been published by [Hascoët et al., 2012]. Due to the evolution of $\gamma\gamma$ opacity with time, the time integrated high-energy spectrum can be considered as a superposition of a set of elementary spectra with an exponential cutoff. The evolution of these cutoffs in time is different between a case of a single pulse light curve and the case of a more complex light curve [Hascoët et al., 2012] (see the left panel of Fig.5.4). In the former case, the attenuation causes an initial steep break in the local photon index (i.e. a broken power law), followed by an exponential cutoff at the highest energies (see the top right panel of Fig.5.4). In the latter case, the effect of the spectral attenuation is smoother and more difficult to parameterize (see the bottom right panel of Fig.5.4).

Since the light curve of GRB 090926A consists of a single pulse in the time interval c, I fitted the high-energy spectrum using the previous `Band`+CUTPL model and adding a Multiplicative Broken Power Law (MBPL, Eq.3.15), in order to approximate the spectral shape of the $\gamma\gamma$ attenuation as described above. The resulting model, `Band`+MBPL$\times$CUTPL, has two extra parameters, the break energy E_b and the change β in the spectral index. The second column of Tab.5.8 shows the re-

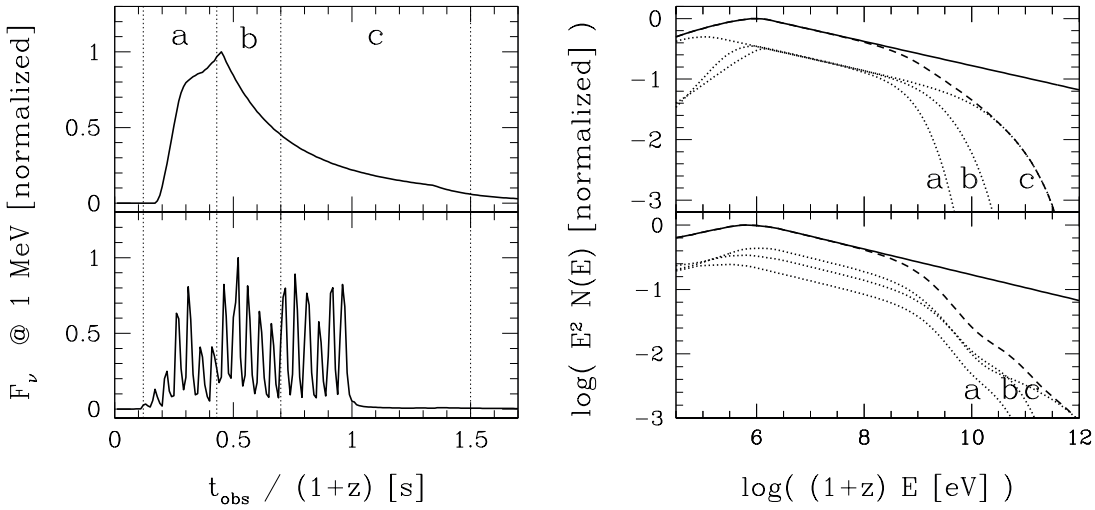

Figure 5.4: *Temporal and spectral evolution of the $\gamma\gamma$ opacity. The upper panels of the two figures show the case of a monopulse GRB, while the bottom panels show the case of a complex multiple-pulse GRB. Left-hand panels: the gamma-ray light curve at 1MeV (source frame) as a function of the source rest-frame time. The dotted lines define the boundaries of the time intervals a, b, c. Right-hand panels: $\nu F\nu$ spectra in the time intervals a, b, c (dotted line) and a+b+c (dashed line). The solid line shows the whole time-integrated spectrum (a+b+c) without $\gamma\gamma$ absorption. These figures are taken from the figure 6 of Hascoët et al. [2012].*

sults of this fit. Comparing the C-stat value with the one reported in Tab.5.7 for the reference model, it can be seen that both models fit the data similarly (with similar C-stat values). However, the spectral parameter E_b of the MBPL model is not well constrained, therefore, this spectrum does not exhibit any power-law break as the one predicted in [Hascoët et al., 2012]. The complexity of the model certainly explains the difficulty to constrain all parameters, as shown for instance by the large correlation between the β parameter of MBPL and each of the extra PL index γ and folding energy E_f ($\rho_{\beta,\gamma}$=-0.87, ρ_{β,E_f}=-0.45). Therefore, I repeated the analysis after simplifying the model, using a `Band`+PL×MBPL to fit the data. The results are presented in Tab.5.8 (right column) and shown in Fig.5.5. The change in the fit statistic, Δ C-stat=5.2, shows that this model fits the data as well as the `Band`+CUTPL model. The Δ C-stat between the `Band`+PL×MBPL and `Band`+PL models shows that the break energy is detected with 7.4σ, similar to the significance of the spectral break detected by the `Band`+CUTPL model. However, due to the large correlation between the MBPL parameters ($\rho_{\beta,Eb}$= -0.73), and since the `Band`+PL×MBPL model has one more parameter than the `Band`+CUTPL model, I preferred to keep the latter for the following.

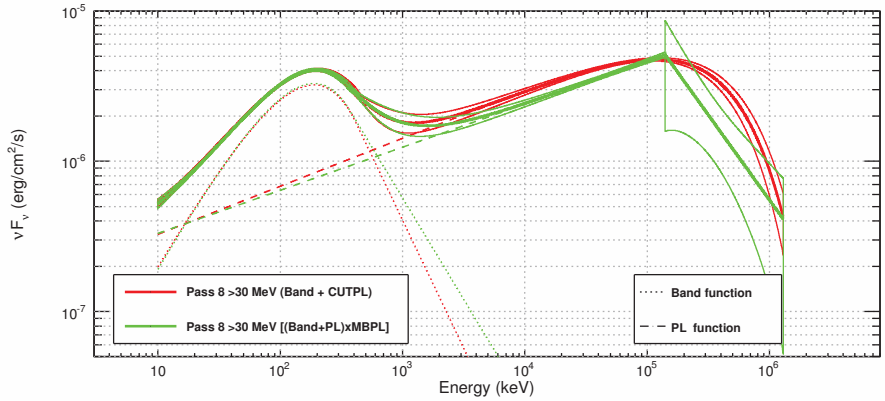

Figure 5.5: *GRB 090926A $\nu F\nu$ spectra in the time interval c. The red (resp. green) solid curve represents the fitted spectral shape* **Band**+*CUTPL (resp.* (**Band**+*PL)×MBPL), within a 68% confidence level contour derived from the errors on the fit parameters.*

Parameters	Band + **CUTPL×MBPL**	Band + **PL×MBPL**
Band		
α	$-0.58^{+0.08}_{-0.11}$	$-0.57^{+0.14}_{-0.11}$
β	$-4.1^{+0.7}_{-1.1}$	$-3.35^{+0.34}_{-0.72}$
E_{peak} (keV)	$181.0^{+7.0}_{-2.5}$	$188.5^{+8.2}_{-8.5}$
CUTPL		
Index	$-1.69^{+0.01}_{-0.05}$	$-1.71^{+0.03}_{-0.02}$
Folding energy E_f (MeV)	520^{+90}_{-100}	-
MBPL		
β	$-0.15^{+0.05}_{-0.05}$	$-1.42^{+0.52}_{-0.63}$
E_b (MeV)	100^{+85}_{-68}	140^{+60}_{-80}
C-stat / dof	589.4 / 516	593.9 / 517
Δ C-stat w.r.t Band + CUTPL	0.6	5.2

Table 5.8: *Results of the* **Band**+*CUTPL×MBPL (second column) and* **Band** *+ PL×MBPL (third column) spectral fits to GBM+LAT (Pass 8) data during the time interval c [9.8 s, 10.5 s] of GRB 090926A.*

5.4.2 High-energy power-law component with a smooth curvature

The inverse Compton (IC) process is a possible explanation for the extra PL detected in some GRB spectra [Daigne et al., 2011]. Since the IC component has a smoother curvature than the CUTPL component, I tried to fit the high-energy spec-

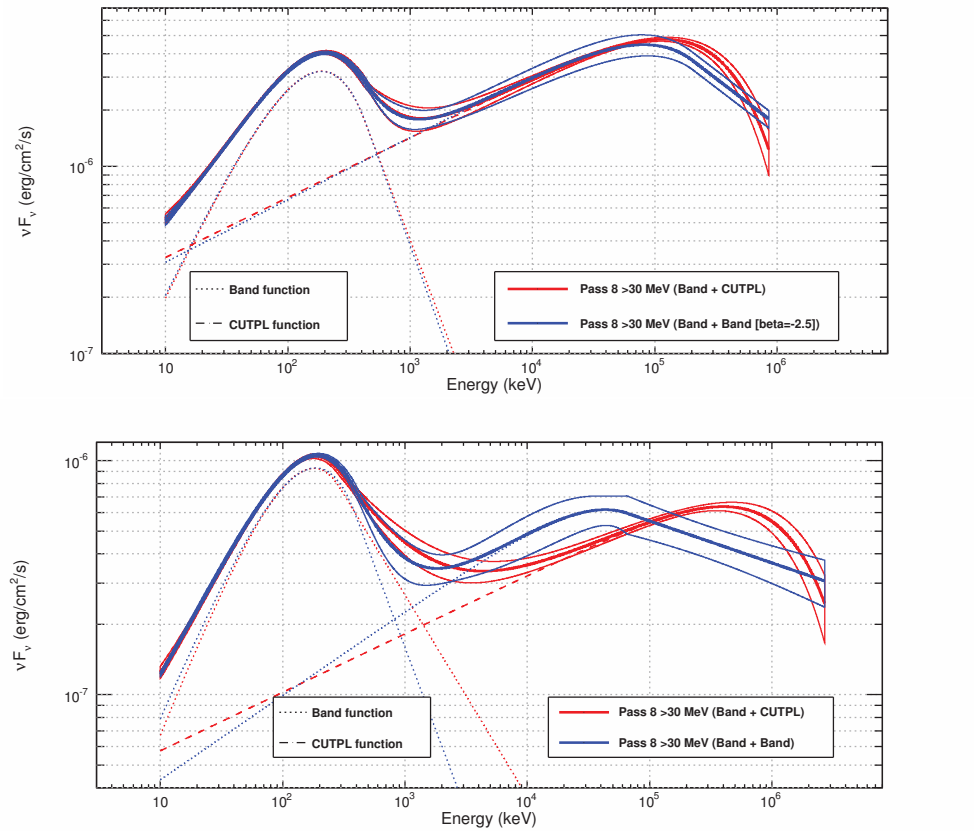

Figure 5.6: *Spectral energy distributions in the time interval c top) and time interval d (bottom) for the joint GBM-LAT analysis using LAT Pass 8 data above 30 MeV. The solid curves represent the spectral models* `Band`*+CUTPL (red) and* `Band`*+*`Band` *(blue), within a 68% confidence level contour derived from the errors on the fit parameters.*

tral break of GRB 090926A with a `Band` function, i.e. I used a `Band`+`Band` model in the following.

In the time interval c, the β parameter of the second `Band` function is under-constrained. In addition to the fact that the `Band`+`Band` model has one more parameter than the `Band` + CUTPL model, this may due to the insufficient statistics at high energy in this time interval. Using the likelihood profile of this parameter, I found an upper limit of β at -2.5 (68% C.L.), which I held fixed for constraining the other parameters. In this case, the `Band`+`Band` model and the `Band` + CUTPL model have the same number of parameters. The results of the `Band`+`Band` model for the time intervals c and d are summarized in Tab.5.9. The SEDs for the time interval c of the two models are represented in the top panel of Fig.5.6. The `Band`+`Band`

model has a similar fit quality as the Band+CUTPL model with a smaller folding energy $8.2^{+1.1}_{-1.3}\times10^4$ MeV and an increase of 4 in C-stat compared with the C-stat value reported in Tab.5.7.

In the time interval d, all the model parameters were left free. It can be seen from Fig.5.6, bottom panel that the second Band component is ill-defined, with a peak energy that is smaller and not well constrained $(4.4^{+4.3}_{-1.6})\times10^4$) MeV. The decrease in fit statistic, ΔC-stat=17, is insufficient to distinguish between the two fit models. Therefore, the Band+CUTPL model remains the preferred one, since it has one less parameter.

Parameters	Time interval c	Time interval d
First Band		
A_{Band} ($keV^{-1}\,cm^{-2}\,s^{-1}$)	$0.33^{+0.03}_{-0.02}$	$0.094^{+0.005}_{-0.006}$
α	$-0.62^{+0.14}_{-0.13}$	$-0.75^{+0.08}_{-0.09}$
β	$-3.8^{+0.54}_{-1.2}$	$-3.4^{+0.3}_{-0.9}$
E_{peak} (keV)	189^{+9}_{-7}	186^{+7}_{-7}
Second Band		
A_{Band} ($keV^{-1}\,cm^{-2}\,s^{-1}$)	$0.041^{+0.007}_{-0.009}$	$0.006^{+0.001}_{-0.001}$
α	$-1.67^{+0.05}_{-0.03}$	$-1.64^{+0.09}_{-0.05}$
β	fixed -2.5	$-2.18^{+0.06}_{-0.08}$
E_0 ($\times1^4$ keV)	240^{+5}_{-5}	12^{+13}_{-6}
C-stat / dof	592.5 / 518	622.9 / 517

Table 5.9: *Results of the Band+Band spectral fits to GBM+LAT (Pass 8) data during the time interval c [9.8 s, 10.5 s] and d [10.5 s, 21.6 s] of GRB 090926A. E_0 of the second Band function is equal to $E_{peak}/(2+\alpha)$.*

5.4.3 Zoom on the low-energy spectrum

Assuming that the inverse Compton emission process is responsible for the additional power-law component observed in the LAT energy domain, one does not expect this emission to contribute significantly to the low-energy flux. However, one can see from the SEDs portrayed in Fig.5.7 that the extra PL overshoots (or has a similar flux as) the Band function below a few tens of keV. In order to check the necessity for an extension of this PL down to very low energies, I repeated the analyses presented in Sect.5.3.2 using the Band+CUTPL model yet excluding the GBM low-energy data. For the time intervals c and d, I performed new spectral analyses starting at 20 keV and 40 keV, respectively. Tables 5.10 and 5.11 show the main results of these analyses.

In the time interval c, it is worth noting that both the spectral index and the spectral break are similar to the fit values reported previously, showing that the

Parameters	10 keV - 100 GeV	20 keV - 100 GeV	40 keV - 100 GeV
Band			
α	$-0.60^{+0.13}_{-0.14}$	$-0.44^{+0.21}_{-0.22}$	$-0.3^{+0.22}_{-0.23}$
CUTPL			
Index	$-1.68^{+0.04}_{-0.03}$	$-1.71^{+0.05}_{-0.04}$	$-1.63^{+0.08}_{-0.12}$
Folding energy E_f (10^5 keV)	$3.7^{+0.6}_{-0.5}$	$3.8^{+1.0}_{-0.5}$	$3.7^{+1.0}_{-0.4}$
Significance of the cutoff	7.7	7.0	6.7

Table 5.10: *Results of the* `Band`*+CUTPL spectral fit to GBM+LAT (Pass 8) data during the time interval c [9.8 s, 10.5 s] of GRB 090926A in the three energy ranges [10 keV - 100 GeV], [20 keV - 100 GeV] and [40 keV - 100 GeV].*

Parameters	10 keV - 100 GeV	20 keV - 100 GeV	40 keV - 100 GeV
Band			
α	$-0.65^{+0.05}_{-0.04}$	$-0.56^{+0.09}_{-0.09}$	$-0.35^{+0.25}_{-0.17}$
CUTPL			
Index	$-1.75^{+0.02}_{-0.03}$	$-1.79^{+0.02}_{-0.02}$	$-1.84^{+0.03}_{-0.04}$
Folding energy E_f (10^6 keV)	$1.6^{+0.4}_{-0.3}$	$1.6^{+0.5}_{-0.3}$	$1.9^{+1.2}_{-0.3}$
Significance of the cutoff	5.8	5.3	4.1

Table 5.11: *Results of the* `Band`*+CUTPL spectral fit to GBM+LAT (Pass 8) data during the time interval d [10.5 s, 21.6 s] of GRB 090926A in the three energy ranges [10 keV - 100 GeV], [20 keV - 100 GeV] and [40 keV - 100 GeV].*

high-energy spectrum is not necessarily correlated to the keV spectrum. The significance of the spectral break decreases slightly from 7.7σ in the energy range starting at 10 keV to 6.7σ in the energy range starting at 40 keV. This decrease is due to the smaller lever arm in energy, i.e. to the fact that the additional power-law is less anchored to the low-energy data. As expected also, the `Band` α photon index is the most affected parameter, with harder values and slightly larger uncertainties as the analysis energy threshold increases (see Fig.5.7, top panel).

In the time interval d, the values obtained for the folding energy E_f remain unchanged in the three analyses. Like in the time interval c, the `Band` α slope is also the most affected parameter (Tab.5.11 and Fig.5.7). However, the low-energy spectral index is affected by large uncertainties especially for the highest analysis threshold.

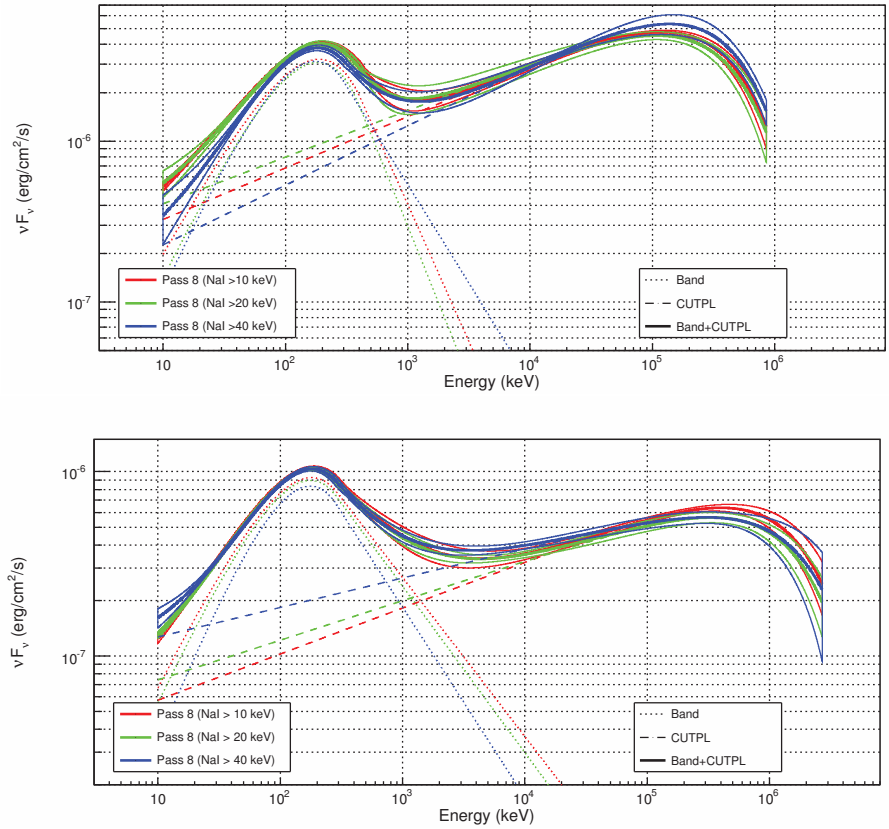

Figure 5.7: *GRB 090926A νF_ν spectra in the time interval c (top) and in the time interval d (bottom) in the three energy ranges [10 keV - 100 GeV], [20 keV - 100 GeV] and [40 keV - 100 GeV]. Each solid curve represents the fitted spectral shape (`Band`+CUTPL), within a 68% confidence level contour derived from the errors on the fit parameters.*

5.4.4 A physically-motivated phenomenological model

As discussed above, the inverse Compton process might be a viable interpretation for the additional power-law component at GeV energies. In addition, and according to the analyses presented in the previous section, the CUTPL component is not necessarily anchored to the low-energy data. Therefore, I investigate a new model in this section, where the flux of the CUTPL component in the keV-MeV domain is negligible with respect to the flux of the `Band` component. Suppressing the low-energy extension of the CUTPL component provides a new phenomenological model that I will assume to be representative of an underlying emission spectrum which consists of a synchrotron component in the keV-MeV domain, and of an inverse Compton component emerging at higher energies. In practice, in addition to the `Band` function at low energy, the high-energy spectrum is fitted with the CUTBPL component,

which consists of a broken power law with an exponential cutoff (Eq.3.13). In a first step, I fixed the photon spectral index below the break energy (γ_0 in Eq.3.13) at +4 in order to suppress the power-law contribution at low energies. This analysis gave a break energy at 197 ± 6 keV. In the subsequent analyses, the break energy Eb was always fixed at 200 keV. Moreover, I fixed the reference energy E_0 at 10 MeV and 100 MeV for the time intervals c and d, respectively.

The analysis results are reported in Tab.5.14 and presented in App.B. In both time intervals, the `Band` + CUTBPL model fits the data similarly to the `Band`+CUTPL model with a slightly larger Δ C-stat than the ones reported in Tab.5.7 (Δ C-stat= 15.9 and 12.1 in time intervals c and d respectively). As expected, the `Band` low-energy index becomes softer ($\alpha\sim$-0.9) with the `Band`+CUTBPL model (instead of -0.6 with the `Band`+CUTPL model). Interestingly, the value of α is in better agreement with the theoretical predictions of the synchrotron theory in the electron fast cooling regime, which is the most suitable in the GRB case due to their extreme variability and luminosity. While an index of -3/2 is expected in this regime [Sari et al., 1998] , this value can indeed increase up to $\sim$-1 when the IC losses of the electrons in the Klein-Nishina regime are accounted for [Daigne et al., 2011]. The folding energies obtained with the `Band`+CUTBPL model and their significance in time intervals c and d are close to the ones obtained with the `Band`+CUTPL model, with a slight harder power law spectral indices, especially in the time interval c. This analysis yields a spectral index $\gamma = -1.48^{+0.09}_{-0.08}$ (resp. $-1.71^{+0.05}_{-0.05}$) in the time interval c (resp. d) instead of $-1.68^{+0.04}_{-0.03}$ (resp. $-1.75^{+0.02}_{-0.03}$) with the `Band`+CUTPL model. It is worth to mention that the PL index for each of the two time intervals ($\gamma \sim -1.6$), is also compatible with the prediction of the fast-cooling electron synchrotron emission model of [Daigne et al., 2011].

5.5 Time evolution of the high-energy spectral break

The analysis reported in Sect.5.4.4, showed a temporal evolution of the spectral break between the two time intervals c and d. It is encouraging, then, to check the temporal evolution of the break within each time interval. To do so, the time interval c was split in two sub-intervals, either of equal statistics or depending on the rise and decay parts of the pulse. I performed a spectral analysis of each sub-interval using the `Band`+CUTBPL model. The results of this analysis are reported in Tab.5.12. From this table, one can notice that no time evolution was found within the time interval c, where the high-energy spectral break is detected in the two sub-intervals with the same significance particularly in the case of equal statistics. This result might be due to the small number of events in each sub-interval, hence, we can not exclude a possible time evolution within this time interval.

However, in the time interval d, the results reported in Tab.5.13 show a significant

Time intervals (same statistics)	[9.80-9.98] s	[9.98-10.50] s
Number of events	76	76
CUTBPL folding energy E_f (GeV)	$0.40^{+0.10}_{-0.08}$	$0.32^{+0.09}_{-0.06}$
Break significance N_σ	5.0	5.5
Time intervals (rise & decay)	[9.80-9.94] s	[9.94-10.50] s
Number of events	49	103
CUTBPL folding energy E_f (GeV)	$0.42^{+0.16}_{-0.10}$	$0.35^{+0.08}_{-0.07}$
Break significance N_σ	3.8	6.3

Table 5.12: *Results of the* **Band***+CUTBPL fits to GBM+LAT data in the sub-intervals (c_1 and c_2) of time interval c. The top part of this table shows the results for the intervals splitted in statistics, and the bottom for the intervals splitted as the light-curve evolution.*

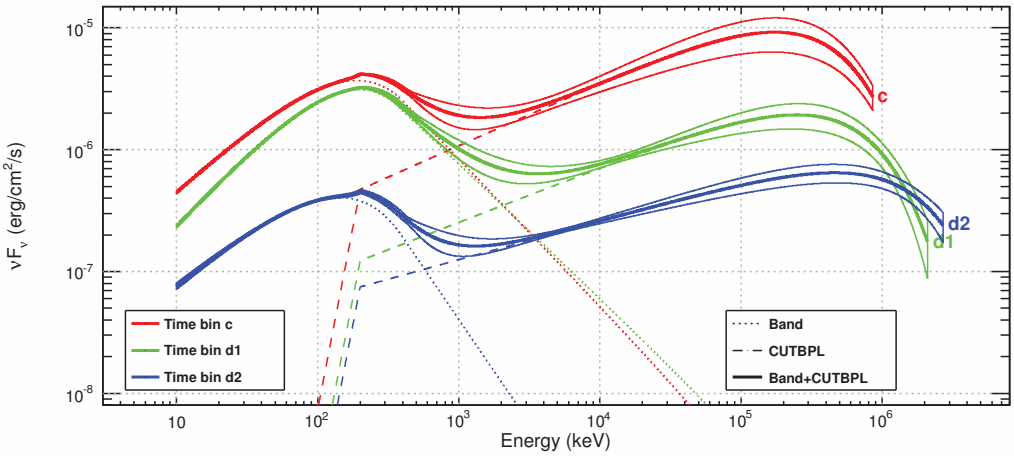

Figure 5.8: *Spectral energy distributions as measured by the Fermi GBM and LAT in the time interval c (red curves), d_1 (green curves) and d_2 (blue curves) using LAT Pass 8 data above 30 MeV. The solid curve in each SED represents the best fit model (*Band*+CUTBPL), within a 68% confidence level contour derived from the errors on the fit parameters.*

evolution of the folding energy between the two sub-intervals whatever the splitting method. Tab.5.14 summarizes the results of the joint analyses in the sub-intervals (d_1 and d_2) of equal statistics. It reveals that the folding energy evolves with time from $0.55^{+0.13}_{-0.10}$ GeV (with a significance $N_\sigma = 4.3$) in the time interval d_1 to $1.43^{+0.49}_{-0.25}$ GeV ($N_\sigma = 5.1$) in the time interval d_2. Fig.5.8 presents the SED of the three time intervals c, d_1 and d_2, showing clearly the increase of the spectral break with time.

Time intervals (same statistics)	[10.50-12.90] s	[12.90-21.60] s
Number of events	161	160
CUTBPL folding energy E_f (GeV)	$0.55^{+0.13}_{-0.10}$	$1.43^{+0.49}_{-0.25}$
Break significance N_σ	4.3	5.1
Time intervals (rise & decay)	[10.50-11.73] s	[11.73-21.60] s
Number of events	81	240
CUTBPL folding energy E_f (GeV)	$0.45^{+0.17}_{-0.10}$	$1.85^{+0.75}_{-0.30}$
Break significance N_σ	5.1	4.4

Table 5.13: *Results of the* **Band***+CUTBPL fits to GBM+LAT data in the sub-intervals (d_1 and d_2) of time interval d. The top part of this table shows the results for the intervals splitted in statistics, and the bottom for the intervals splitted as the light-curve evolution.*

Time interval	c	d	d_1	d_2
Time interval boundaries from T_0 (s)	9.8-10.5	10.5-21.6	10.5-12.9	12.9-21.6
A_{Band} ($\times 10^{-2}$ keV^{-1} cm^{-2} s^{-1})	34^{+2}_{-1}	$10.1^{+0.2}_{-0.3}$	29^{+1}_{-1}	$4.7^{+0.1}_{-0.2}$
Band $E_{\rm peak}$ (keV)	190^{+9}_{-9}	177^{+7}_{-3}	198^{+6}_{-10}	143^{+4}_{-7}
Band photon index α	$-0.94^{+0.03}_{-0.02}$	$-0.86^{+0.01}_{-0.03}$	$-0.73^{+0.01}_{-0.04}$	$-1.03^{+0.05}_{-0.02}$
Band photon index β	$-3.2^{+0.2}_{-0.9}$	$-3.1^{+0.2}_{-0.5}$	$-3.1^{+0.2}_{-0.4}$	$-3.7^{+0.3}_{-1.5}$
A_{cutbpl} ($\times 10^4$ keV^{-1} cm^{-2} s^{-1})	$4.6^{+0.9}_{-0.9}$	$(9.4^{+0.5}_{-0.1}) \times 10^3$	$(12^{+7}_{-4}) \times 10^3$	$(7^{+1}_{-1}) \times 10^3$
CUTBPL photon index γ	$-1.48^{+0.09}_{-0.08}$ (-1.68 ± 0.22)	$-1.71^{+0.05}_{-0.05}$	$-1.55^{+0.12}_{-0.10}$	$-1.68^{+0.05}_{-0.05}$
CUTBPL folding energy E_f (GeV)	$0.34^{+0.07}_{-0.05}$ $(0.41^{+0.27}_{-0.14})$	$1.20^{+0.22}_{-0.18}$	$0.55^{+0.13}_{-0.10}$	$1.43^{+0.49}_{-0.25}$
Break significance N_σ	7.6	6.1	4.3	5.1
$C_{\rm stat}$ / dof	604.7 / 518	652.7 / 518	559.0 / 518	603.2 / 518
Δ C-stat	15.9	12.1	6.1	15.1

Table 5.14: *Results of the* **Band***+CUTBPL fits to GBM-LAT data during the time intervals c, d, d_1 and d_2. The reference energy E_0 in equation 3.13 has been fixed to 10 MeV for interval c and 100 MeV for intervals d, d_1 and d_2.*

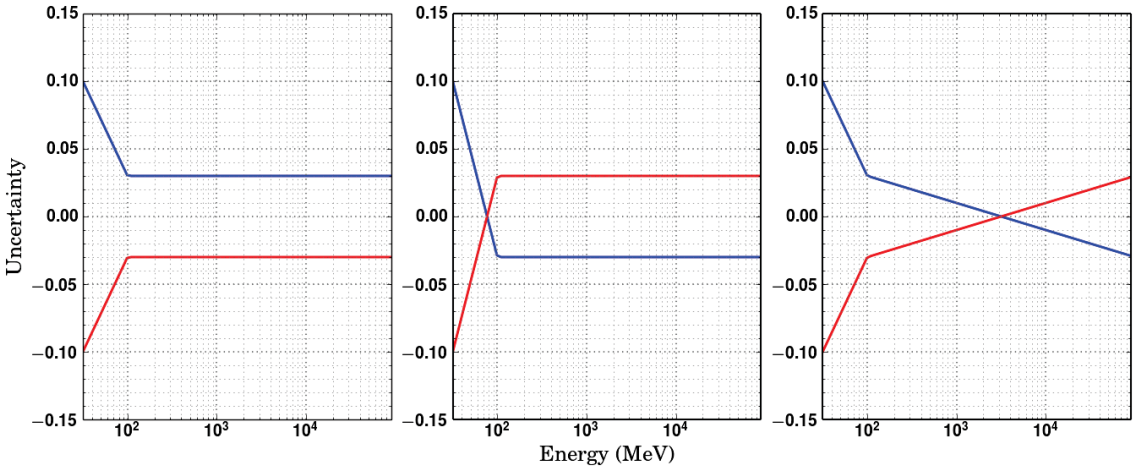

Figure 5.9: *Possible containment intervals of the relative systematic uncertainty $\epsilon(E)$ on the LAT effective area as a function of the photon energy E. The blue and red lines correspond to the values 1 and -1, respectively, of the bracketing factor B(E) (see Fig.2.12).*

5.6 Systematic effects

The measurements of the high-energy spectral break of GRB 090926A can be affected by systematic uncertainties due to the incomplete knowledge of the LAT IRFs. As has been shown in Sect.2.5, the systematic uncertainty on the effective area is the dominant source of uncertainties for spectral analyses. This uncertainty should be taken into account especially below 100 MeV, where the LAT energy dispersion is the widest.

In order to estimate the systematic errors on my results, I repeated the spectral analyses in the time intervals c, d_1 and d_2, taking account of the A_{eff} systematic defined by the LAT collaboration, as shown in the left panel of Fig.5.9 (see the FSSC[1] web site for more details). I also modified the ϵ(E) term of Eq.2.5 in two ways, shown in the middle and right panels of Fig.5.9, in order to find the one that has the biggest effect on the results. I found that the systematic uncertainties presented in the right panel of this figure caused the largest spectral distortion. This configuration is, therefore, used for the following analysis. The break energies obtained with and without including the systematic uncertainties for the three time intervals c, d_1 and d_2 are shown in Fig.5.10. This figure clearly shows that the systematic uncertainty on the LAT effective area does not significantly affect the

[1] `http://fermi.gsfc.nasa.gov/ssc/data/analysis/LAT_caveats.html`

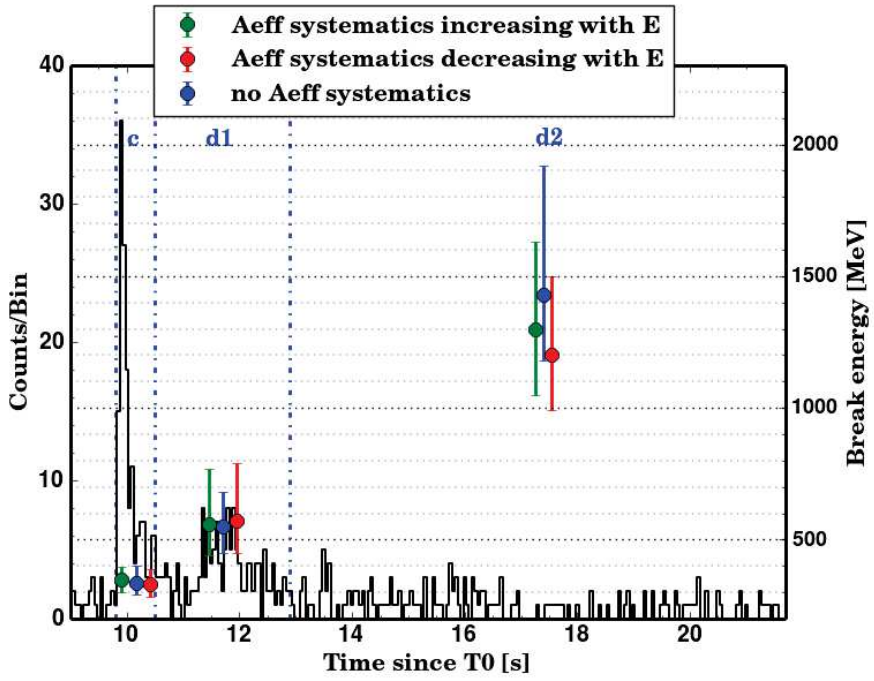

Figure 5.10: *Folding energies for the time intervals c, d_1 and d_2, obtained with or without considering the systematic uncertainties on the LAT effective area. The results have been superimposed to the LAT counts light curve above 30 MeV.*

results. Moreover, it can be seen that the confidence intervals on the folding energy in the three time intervals exclude each other, especially between the time intervals d_1 and d_2.

5.7 Estimation of the variability timescale

The detection of a spectral break at high energy is an interesting characteristic that can be used to estimate the relativistic jet Lorentz factor Γ [Baring and Harding, 1997; Granot et al., 2008; Hascoët et al., 2012]. The estimation of this latter requires a good estimation of the variability timescale in the light curve. For this aim, I built the light curve in each time interval c, d_1 and d_2 in four energy ranges using the summed data of the three NaI detectors (14 keV-260 keV), the BGO data (260 keV-5 MeV), and the LAT data starting at 30 MeV and 100 MeV. I fitted each pulse in the light curves with a temporal profile using the prescription from [Norris et al., 2005]:

$$I(t) = \begin{cases} 0, & t < t_s \\ A\, e^{-\frac{\tau_1}{(t-t_s)} - \frac{(t-t_s)}{\tau_2}} + B, & t > t_s \end{cases} \tag{5.1}$$

Time interval	Energy Range	τ_1	τ_2	t_p	t_v
c (9.8-10.5)	NaI	9.87 ± 0.88	10.05 ± 0.93	9.92 ± 0.01	0.09 ± 0.01
	BGO	9.84 ± 5.73	10.06 ± 5.97	9.93 ± 0.02	0.11 ± 0.01
	LAT ($>$ 30 MeV)	9.88 ± 0.63	9.99 ± 0.63	9.92 ± 0.01	0.05 ± 0.01
	LAT ($>$ 100 MeV)	9.89 ± 0.84	10.01 ± 0.84	9.93 ± 0.01	0.06 ± 0.01
d_1 (10.5-21.6)	NaI	10.25 ± 0.16	12.50 ± 0.90	11.11 ± 0.03	1.13 ± 0.04
	BGO	10.68 ± 0.07	11.90 ± 0.35	11.06 ± 0.07	0.63 ± 0.12
	LAT ($>$ 30 MeV)	11.31 ± 0.82	12.18 ± 1.46	11.60 ± 0.11	0.44 ± 0.12
	LAT ($>$ 100 MeV)	11.38 ± 1.50	12.20 ± 2.69	11.65 ± 0.20	0.41 ± 0.34

Table 5.15: *Pulse parameters τ_1 and τ_2, peak time t_p and variability timescale t_v for the time intervals c and d_1 in the NaI, BGO and two LAT energy ranges.*

where A is a normalization factor, t_s is the starting time as defined in [Norris et al., 2005], τ_1 and τ_2 are related to the peak time $t_p = t_s + \sqrt{\tau_1 \tau_2}$, and the constant parameter B accounts for the background in each detector. The variability timescale is computed as the half width at half maximum of the pulse:

$$t_v = \frac{\tau_2}{2} \sqrt{\left(\ln(2) + 2\sqrt{\frac{\tau_1}{\tau_2}} \right)^2 - 4\frac{\tau_1}{\tau_2}}. \tag{5.2}$$

This analysis was performed by minimizing a χ^2 statistic.

The fit parameters are shown in Tab.5.15. Fig.5.12 presents the peak time t_p and the variability timescale t_v in time intervals c and d_1. Not surprisingly, the synchronization which has been detected in all detectors during the time interval c is confirmed by this analysis, as shown by the red curve in the top panel of Fig.5.12. The red curve of the bottom panel of this figure shows comparable variability timescales for this time interval between the NaI, BGO (with $t_v = 0.10 \pm 0.01$ s) and the LAT energy ranges (with $t_v = 0.06 \pm 0.01$ s). However, in the time interval d_1, t_v decreases from 1.13 ± 0.04 s in the NaI light curve to reach similar timescales between the BGO (0.6 ± 0.1 s) and the LAT (0.4 ± 0.2 s) energy ranges. It is worth then to notice, for both time intervals, the compatibility of the measured GeV variability timescale to the ones in the MeV energy range. This result strongly suggests a common origin of both GeV and MeV emissions.

In the time interval d_2, the unstructured LAT light curve was difficult to fit. The NaI light curve in this time interval consists of two different pulses, which cannot be fitted by a single temporal profile. Therefore, I used the fit of the single pulse found in the BGO light curve which peaked at $t_p = 13 \pm 0.1$ s, with a $t_v = 0.5 \pm 0.1$ s.

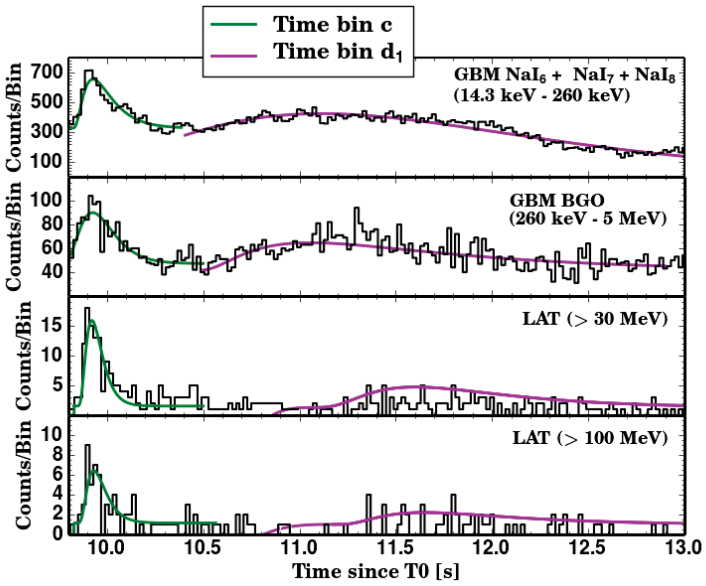

Figure 5.11: *GRB 090926A light curves as seen by the GBM and LAT instruments with a 0.02 s time bin. The data from the GBM NaI and BGO detectors were selected from the two energy bands 14.3-260 keV and 260 keV-5 MeV, respectively. The last two panels show the LAT light curves above 30 MeV and 100 MeV, respectively*

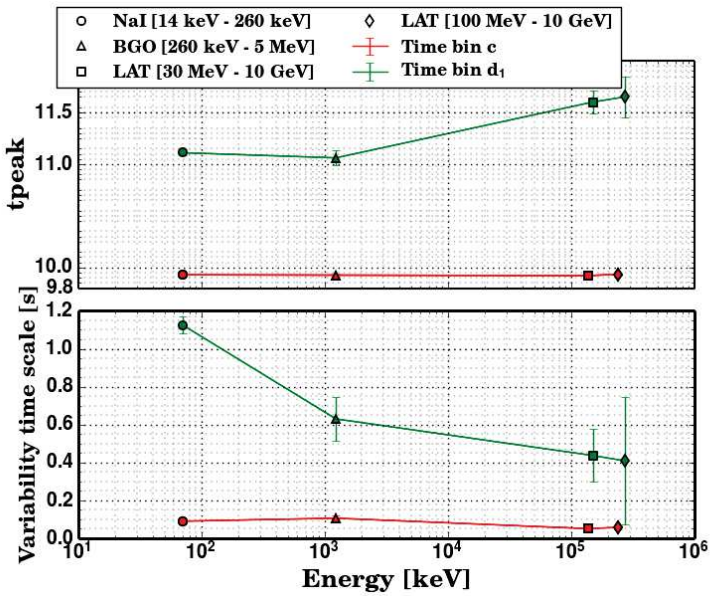

Figure 5.12: *Peak time t_p and variability timescale t_v measured for the time intervals c (red) and d_1 (green) in the NaI, BGO and two LAT energy ranges.*

5.8 Interpretation of the high-energy spectral break

In collaboration with R. Mochkovitch and F. Daigne from the "Institut d'Astrophysique de Paris" (IAP), we published my analysis results and their interpretation in [Yassine et al., 2017] (reproduced at the end of this chapter). We interpreted the spectral attenuation under two possible scenarios, either $\gamma\gamma$ attenuation, which is independent of the radiative processes, or the natural behavior of the inverse Compton spectrum. In this section, both scenarios are investigated by assuming that the prompt emissions are produced above the photosphere. The case of a prompt emission produced at the phosphere is discussed very briefly in our article [Yassine et al., 2017].

Assuming that the prompt emission is produced in the optically thin regime above the photosphere, the radius where the MeV photons are produced reads as:

$$R_{\rm MeV} \simeq 2c\,\Gamma^2 \frac{t_{\rm v}}{1+z}\,. \tag{5.3}$$

This expression corresponds to the radius used in the internal shock scenario [Daigne and Mochkovitch, 1998] and also it is similar to the radius in some magnetic reconnection models such as ICMART (Internal-collision-induced Magnetic Reconnection and Turbulence) [Zhang and Yan, 2011].

5.8.1 Scenario 1: γ-ray opacity to pair creation

If the high-energy spectral cutoff is due to pair creation, then the jet Lorentz factor can be estimated from the burst parameters. Following [Hascoët et al., 2012], the Lorentz factor can be expressed as:

$$\begin{aligned}\Gamma_{\gamma\gamma} &= \frac{K\,\Phi(s)}{\left[\frac{1}{2}\left(1+\frac{R_{\rm GeV}}{R_{\rm MeV}}\right)\left(\frac{R_{\rm GeV}}{R_{\rm MeV}}\right)\right]^{1/2}}\,(1+z)^{-(1+s)/(1-s)} \\ &\times \left\{\sigma_{\rm T}\left[\frac{D_{\rm L}(z)}{ct_{\rm v}}\right]^2 E_* F(E_*)\right\}^{1/2(1-s)}\,\left[\frac{E_*\,E_{\rm cut}}{(m_e c^2)^2}\right]^{(s+1)/2(s-1)}\,.\end{aligned} \tag{5.4}$$

where $t_{\rm v}$ is the observed variability timescale in the considered time interval, $E_{\rm cut}$ is the cutoff energy which is equal to the folding energy $E_{\rm f}$ of the detected spectral break, E_* is the typical energy of the seed photons interacting with those at $E_{\rm cut}$. $\sigma_{\rm T}$ is the Thomson cross-section ($\sigma_{\rm T}$= 6.65×10^{-29}m^2 for an electron of radius r$_e$), z is the redshift of the GRB (z=2.1062, Rau et al. [2010]) and $D_{\rm L}(z)$ is the luminosity distance which is equal to 5.1×10^{28} cm for a Hubble constant H_0=72 km.s^{-1} and the cosmological parameters (Ω_Λ=0.73, Ω_M=0.27) used in [Ackermann et al., 2011]. The parameter s is the photon index of the seed spectrum close to E_*, the seed spectrum can be approximated by $F(E) = F(E_*)\,(E/E_*)^s$ (cm^{-2} MeV^{-1}). The energy E_* is given by:

$$E_* \simeq \frac{(2\Gamma\, m_{\rm e}c^2)^2}{(1+z)^2 E_{\rm cut}} \simeq 1.1\,{\rm MeV}\left(\frac{\Gamma}{100}\right)^2\left(\frac{E_{\rm cut}}{1\,{\rm GeV}}\right)^{-1} \tag{5.5}$$

For Γ^2 is required to account for the relativistic motion of the jet. E_* appears in Eq.5.4 in two factors with opposite scaling: $(E_* F(E_*))^{1/2(1-s)} \propto E_*^{(s+1)/2(1-s)}$ and $E_*^{(s+1)/2(s-1)}$, thus the Lorentz factor does not depend on its exact value. For the time interval c we chose E_* at 10 MeV as the seed photons clearly belong to the power-law segment of the CUTBPL spectral component. For the time intervals d_1 and d_2 we chose the values 2.5 MeV and 1 MeV, respectively as their seed photons belong to the plateau between the low and high energy components (see Fig.5.8).

The function $\Phi(s)$ of Eq.5.4 is defined as:

$$\Phi(s) = \left[2^{1+2s}\mathcal{I}(s)\right]^{\frac{1}{2(1-s)}} , \tag{5.6}$$

where $\mathcal{I}(s)$ depends on the photon index s only [Hascoët et al., 2012]:

$$\mathcal{I}(s) = \int_0^1 \frac{y}{(1-y^2)^{2+s}}\, g(s)\, \mathrm{d}s \tag{5.7}$$

with $g(y) = \frac{3}{16}(1-y^2)\left[(3-y^4)\ln\frac{1+y}{1-y} - 2y(2-y^2)\right]$ which reflects the dependence of the $\gamma\gamma$ cross section on the energy. The constant K of Eq.5.4 is a calibration factor determined by [Hascoët et al., 2012] from a detailed calculation of the $\gamma\gamma$ opacity taking into account the temporal and spatial dependence of the target photon field in the comoving frame. If the Lorentz factor in the ejecta varies between $\Gamma_{\rm min}$ and $\Gamma_{\rm max}$= (2 to 5) $\Gamma_{\rm min}$, the values of K cluster around $0.4 - 0.5$ [Hascoët et al., 2012]. In this case, Eq.5.4 corresponds to the lowest Lorentz factor $\Gamma_{\rm min}$ in the outflow [Hascoët et al., 2012].

All the observed parameters of Eq.5.4, except the index s, have been calculated or estimated in Sect.5.5 and 5.7. In addition, I estimated the index s of the seed spectrum close to E_* by performing Monte-Carlo simulations using the results and the covariance matrix of the spectral fit of the `Band`+CUTBPL model. I assumed that the 7 parameters of this model follow a multi-dimensional Gaussian distribution. I created 10^4 simulated spectra for each time interval and I built the distribution of s in each of them. The value of s that I used in Eq.5.4 was chosen as the value which has the maximum probability (MPV) of the final distribution. The errors on this parameter were derived from the 68% confidence level symmetric interval that is centered on the MPV (Fig.5.13). Tab.5.16 summarizes all the observed quantities required for Eq.5.4 in time intervals c, d_1 and d_2 as well as the resulting Lorentz factor, assuming equal MeV and GeV radii ($R_{\rm GeV} = R_{\rm MeV}$). With this assumption, we obtained the lowest Lorentz factor in the outflow $\Gamma_{\rm min} = \Gamma_{\gamma\gamma}(E_f)$= 233 ± 18, 100 ± 8 and 98 ± 9 for time intervals c, d_1 and d_2, respectively. The result in the time interval c is similar to the $\Gamma_{\rm min} \simeq 220$ reported in [Ackermann et al., 2011]. We also derived the emission radius for each time interval, which was found to be of few 10^{14} cm (see Tab.5.16). The evolution of the jet Lorentz factor with respect

to the ratio of GeV over MeV radii is presented in Fig.5.14 (solid line) for the three time intervals. As expected from Eq.5.4, this figure shows that the Lorentz factor decreases with an increasing ratio of the radii.

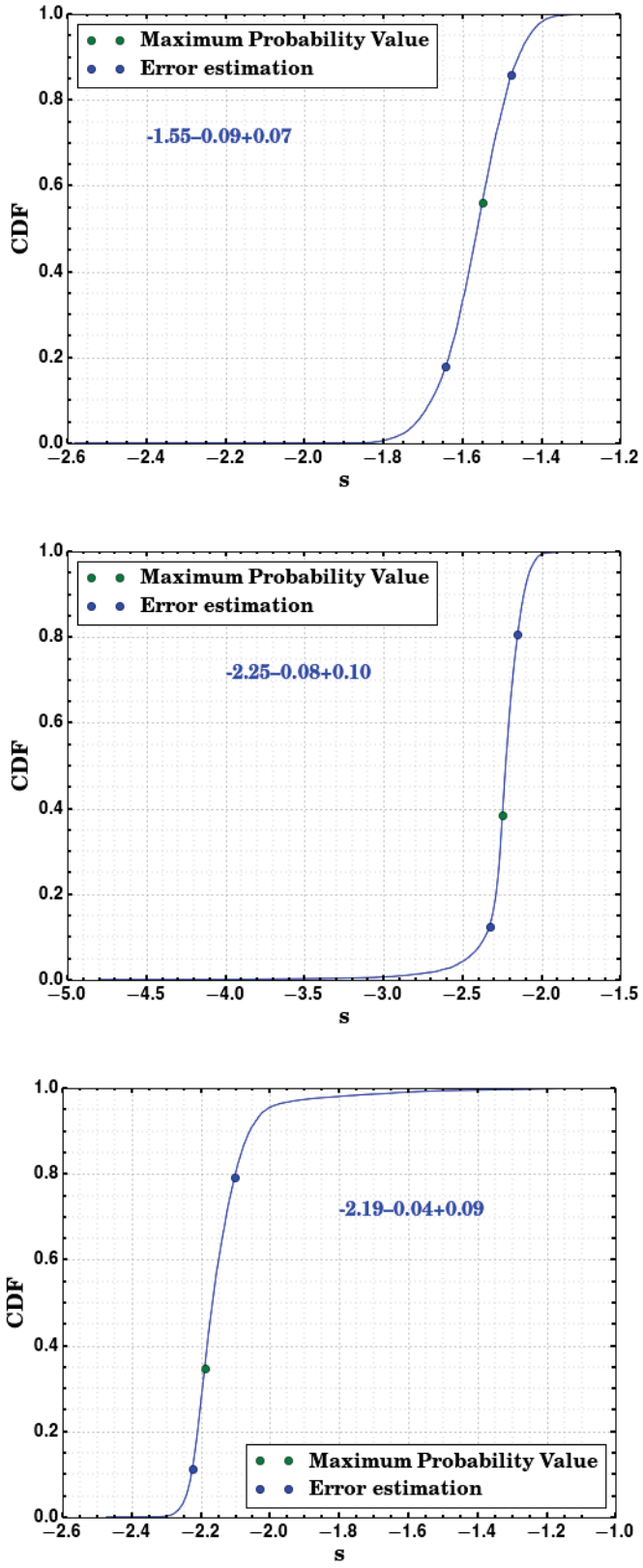

Figure 5.13: *Cumulative distribution functions of the seed photon index s with errors at 68% containement in the time interval c (top, left), d_1 (top, right) and d_2 (bottom panel).*

Time interval	c	d_1	d_2
Burst parameters			
t_v (s)	0.1 ± 0.01	0.6 ± 0.1	0.5 ± 0.1
s	$-1.55^{+0.07}_{-0.09}$	$-2.25^{+0.10}_{-0.08}$	$-2.19^{+0.09}_{-0.04}$
$\Phi(s)$	0.511 ± 0.009	0.463 ± 0.004	0.465 ± 0.003
E_f (GeV)	$0.34^{+0.07}_{-0.05}$	$0.55^{+0.13}_{-0.10}$	$1.43^{+0.49}_{-0.25}$
$E_{\rm max}$ (GeV)	0.85	2.04	2.66
E_* (MeV)	10	2.5	1.0
$F(E_*)$ (10^{-2} cm^{-2} MeV^{-1})	0.22 ± 0.03	4.0 ± 0.8	5 ± 1
Luminosity (10^{53} erg s^{-1})	16.9 ± 3.1	1.73 ± 0.14	1.85 ± 0.15
Constraints if the break at E_f is due to gamma-ray opacity to pair creation (assuming $R_{\rm GeV} = R_{\rm MeV}$)			
Lorentz factor $\Gamma_{\gamma\gamma(E_f)}$	233 ± 18	100 ± 8	98 ± 9
Emission radius $R = R_{\rm MeV} = R_{\rm GeV}$ (10^{14} cm)	1.1 ± 0.1	1.2 ± 0.2	1.0 ± 0.1
Photospheric radius $R_{\rm ph}$ (10^{14} cm)	0.5 ± 0.2	0.7 ± 0.2	0.8 ± 0.2
Constraints if the break at E_f is a natural break (assuming $R_{\rm GeV} = R_{\rm MeV}$)			
Lower limit on the Lorentz factor Γ	257 ± 17	129 ± 8	110 ± 8

Table 5.16: *The burst parameters and the spectral fit results for the three time intervals c, d_1 and d_2 using the* `Band` *+ CUTBPL model. Assuming that the high-energy spectral break at E_f detected is due to gamma-ray opacity to pair creation, we derived the corresponding Lorentz factors $\Gamma_{\gamma\gamma(E_f)}$. Assuming that the break reflects the natural curvature of the IC spectrum, we derived a lower limit $\Gamma_{\gamma\gamma(E_{max})}$.*

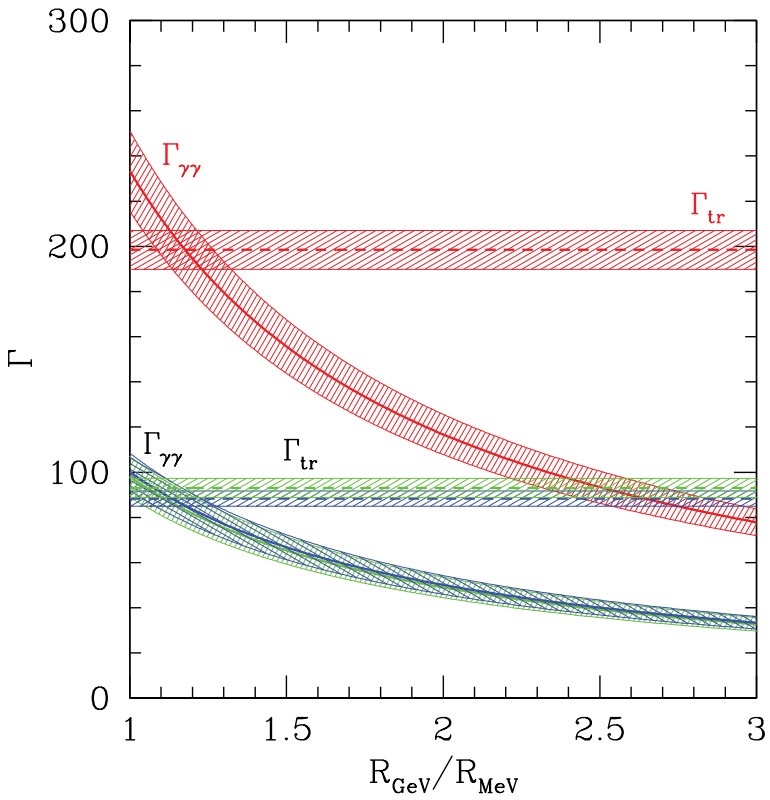

Figure 5.14: *The evolution of the Lorentz factor $\Gamma_{\gamma\gamma}$ for the time intervals c (red), d_1 (blue) and d_2 (green) as a function of the ratio of the GeV and MeV emission radii. These results are obtained assuming that the high-energy spectral break comes from photon opacity to pair creation. The dashed horizontal lines represent the lower limit of the Lorentz factor for transparency, $\Gamma_{\rm tr}$ (Eq.5.9). Each of these lines is enclosed by a 68% uncertainty contour which was obtained by propagating the errors on the measured values listed in Tab.5.16. Figure taken from Yassine et al. [2017]*

5.8.2 Comparison with the photosperic radius

In Sect.5.8.1 we assumed that the prompt emission is produced above the photosphere. In order to check whether this condition is fulfilled, the MeV and GeV emission radii must be compared with the photospheric radius $R_{\rm ph}$, which is defined as [Beloborodov, 2013]:

$$R_{\rm ph} \simeq \frac{\sigma_{\rm T}(1+f_{\pm})\,\dot{E}}{8\pi c^3 m_p \bar{\Gamma}^3(1+\sigma)}\,, \tag{5.8}$$

where $\bar{\Gamma}$ is the average Lorentz factor in the outflow, which we approximated as $\bar{\Gamma} = (\Gamma_{\rm min}+\Gamma_{\rm max})/2$; $f_{\pm}$ the ratio of the number of pairs to primary electrons, $\dot{E}$ the total power injected into the flow and σ its magnetization at large radius, where the prompt emission is produced. Since the optical depth for pair creation is less than unity at $R_{\rm MeV}$, as can be checked using the parameters in Tab.5.16, the number of

pairs can be neglected, i.e. $f_{\pm} = 0$. Adopting an internal shock model to explain the GRB emission, we also used a magnetization $\sigma \ll 1$. The power $\dot{E}$ is expressed as $\dot{E} = L/\epsilon_{\rm rad}$, where L is the gamma-ray luminosity (listed in Tab.5.16) and $\epsilon_{\rm rad}$ is the prompt emission efficiency fixed at $\epsilon_{\rm rad} = 0.1$ for this work. The photospheric radius is shown in Fig 5.15 along with the MeV and GeV emission radii as functions of the Lorentz factor Γ. From these figures it can be seen that the MeV and GeV emission radii are close to each other ($R_{MeV} \simeq R_{GeV} \simeq 10^{14}$ cm, for a photospheric radius $R_{ph} \simeq 10^{13}$ cm). As already suggested by the comparable variability timescales in the LAT and the GBM ranges, this figure clearly shows that both the MeV and GeV photons have the same origin.

Equivalently, the transparency condition can be expressed by comparing the MeV emission radius with the photospheric radius, i.e. requiring $R_{\rm MeV} > R_{\rm ph}$. Replacing these quantities by their expressions in Eqs.5.3 and 5.8 yields a minimum Lorentz factor $\bar{\Gamma}_{\rm tr}$:

$$\bar{\Gamma}_{\rm tr} \simeq \left[\frac{\sigma_{\rm T}(1+f_{\pm})\,\dot{E}}{8\pi c^4 m_p\,(1+\sigma)\,t_{\rm v}} \right]^{1/5} . \tag{5.9}$$

where the transparency condition now becomes $\Gamma > \bar{\Gamma}_{\rm tr}$. The value of the $\bar{\Gamma}_{\rm tr}$ is reported in Fig.5.14 as horizontal dashed lines for the three time intervals. This figure confirms that the transparency condition is fulfilled for an $R_{\rm GeV}/R_{\rm MeV}$ ratio close to 1. This defined $\bar{\Gamma}_{\rm tr}$ parameter is plotted in Fig.5.14 in horizontal dashed lines for the three time intervals. This figure shows that this condition is satisfied at radii ratios close to 1. This result confirms the conclusion found above.

5.8.3 Scenario 2: inverse Compton scattering in Klein-Nishina regime

The second possible scenario to explain the detected spectral breaks, still assuming that the prompt emission is produced above the photosphere, is the natural curvature of the inverse Compton spectrum. In this case the spectrum attenuation caused by the γ-ray opacity to pair creation is assumed to start at an energy which is beyond the observed energy range, i.e. we can use the energy E_{max} of the most energetic photon to derive a lower limit on the jet Lorentz factor Γ. To satisfy the transparency condition described above, Γ must therefore exceed the following lower limit:

$$\Gamma_{\rm inf} = \max(\Gamma_{\gamma\gamma}, \Gamma_{\rm tr})\,, \tag{5.10}$$

where $\Gamma_{\gamma\gamma}$ is the Lorentz factor calculated at E_{max} instead of E_{cut} in Eq.5.4. The results are presented in Fig.5.16 for each of the three time intervals. This figure shows that the transparency condition is now satisfied for a ratio of the emission radii ($R_{\rm GeV}/R_{\rm MeV} < 1.3$, 1.5 and 1.2 for the time interval c, d_1 and d_2) that can be

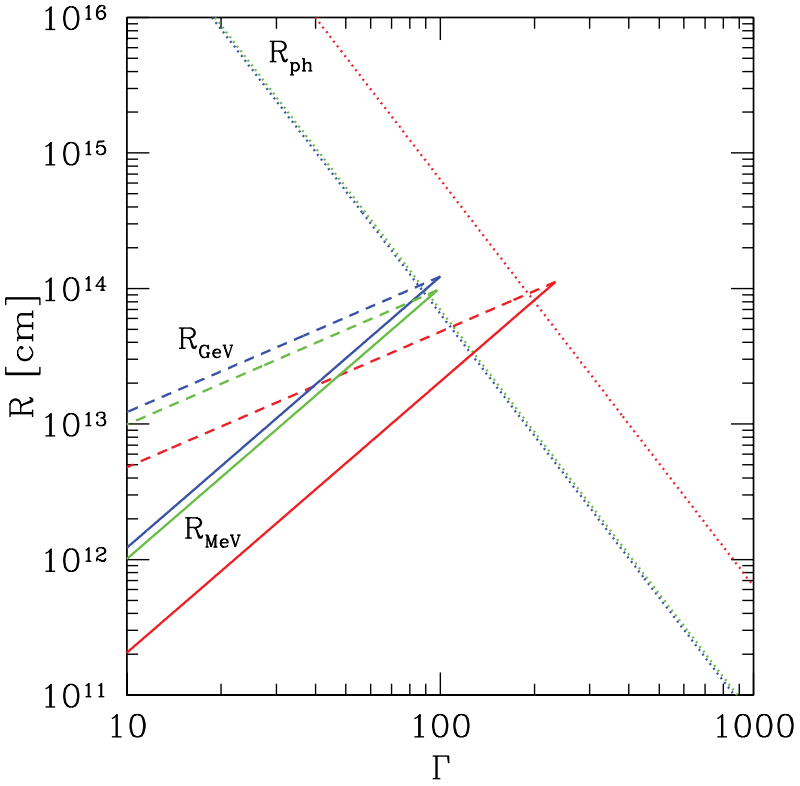

Figure 5.15: *MeV (full lines) and GeV (dashed lines) emission radii for the time intervals c (red), d_1 (blue) and d_2 (green) as function of the jet Lorentz factor* Γ. *The dotted lines correspond to the photospheric radius* $R_{\rm ph}$ *in each time interval.*

larger than the one required in the scenario 1 discussed previously. The values of the lower limit $\Gamma_{\rm inf}$ are also larger than the estimates of the Lorentz factor in the previous scenario : for $R_{\rm GeV}$=$R_{\rm MeV}$, $\Gamma_{\rm inf}$=257 ± 17, 129 ± 8 and 110 ± 8 for time intervals c, d_1 and d_2 respectively.

5.9 Summary and discussion

This chapter was devoted to detail time-resolved analysis of the remarkable GRB 090926A. Thanks to the LAT improved sensitivity with Pass 8 data, it was possible to study the high-energy spectral break of this burst with better precision. More importantly, I showed that this spectral break is significantly detected until the end of the prompt emission phase, and I revealed the temporal increase of the break energy from 0.3 to 1.4 GeV. I proved the stability of my results against the systematic uncertainties of the LAT instrument. In collaboration with theoreticians from the IAP laboratory, I interpreted the spectral breaks either as $\gamma\gamma$ attenuation (scenario 1) or as the natural curvature of the inverse Compton spectrum (scenario 2). Both

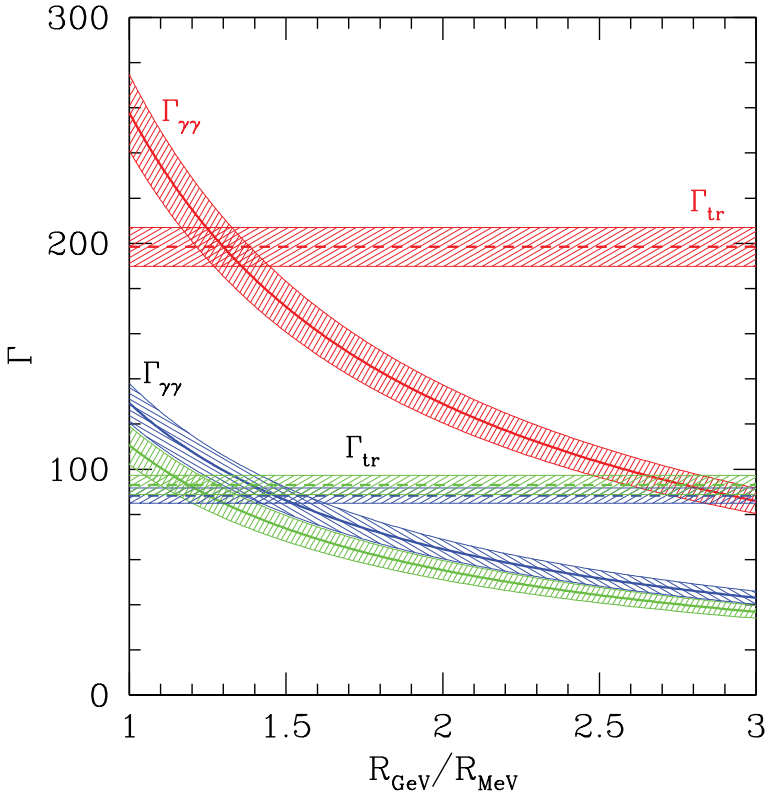

Figure 5.16: *Same as Fig.5.14, assuming that the observed cutoff is a natural break. The Lorentz factor* $\Gamma_{\gamma\gamma}$ *in this case is a lower limit obtained from the highest photon energy* E_{max} *in each time interval.*

interpretations require an accurate estimate of the variability timescales, which I provided by fitting the light curves appropriately. In the first scenario, we derived the Lorentz factor of the outflow, which was found to decrease from 230 in the first time interval to 100 at the end of the prompt phase. The compatible variability timescales between the MeV and the GeV energy ranges, as well as the theoretical interpretation strongly favor a common origin for both the low and high-energy emissions. In the second scenario, we derived lower limits on the Lorentz factor which are larger than the values obtained in the first scenario.

These novel results are the first observational proof of a temporal evolution of a spectral break up to GeV energies. Similar in-depth analyses would help to investigate whether this behavior is common to other bright GRBs detected by the LAT (e.g. the long GRB 090902B and the short GRB 090510). It is worth mentioning here the work by [Vianello et al., 2017], who performed time-resolved analyses of two GRBs that are bright in the GBM and faint above 100 MeV. These analyses revealed spectral breaks at energies less than 150 MeV, which have been interpreted as $\gamma\gamma$ attenuation or within the framework of a photospheric emission model. Both

hypotheses led to estimate the Lorentz factor of the GRB jets ($\Gamma \sim$100-400).

On the theoretical side, the results reported in this chapter call for the development of theoretical models that can account in detail for the characteristics of the GRB prompt spectra from keV to GeV energies. In this respect, it is interesting to note that in the case of GRB 090926A, the low-energy spectral index ($\sim$-0.9) and the spectral index of the extra PL ($\sim$-1.6) that are returned by the fits of the `Band`+CUTBPL function are reproduced by the IAP internal shock model [Bošnjak and Daigne, 2014; Daigne et al., 2011]. I will present a first exploration of this model in the next chapter.

5.10 Publication: Time evolution of the spectral break in the high-energy extra component of GRB 090926A, M. Yassine, F. Piron, R. Mochkovitch, and F. Daigne, 2017AA...606A..93Y, 2017

A&A 606, A93 (2017)
DOI: 10.1051/0004-6361/201630353
© ESO 2017

Astronomy & Astrophysics

Time evolution of the spectral break in the high-energy extra component of GRB 090926A

M. Yassine[1], F. Piron[1], R. Mochkovitch[2], and F. Daigne[2]

[1] Laboratoire Univers et Particules de Montpellier, Université de Montpellier, CNRS/IN2P3, 34095 Montpellier, France
e-mail: manal.yassine@lupm.in2p3.fr; piron@in2p3.fr
[2] UPMC-CNRS, UMR 7095, Institut d'Astrophysique de Paris, 75014 Paris, France
e-mail: mochko@iap.fr

Received 24 December 2016 / Accepted 24 April 2017

ABSTRACT

Aims. The prompt light curve of the long GRB 090926A reveals a short pulse ∼10 s after the beginning of the burst emission, which has been observed by the *Fermi* observatory from the keV to the GeV energy domain. During this bright spike, the high-energy emission from GRB 090926A underwent a sudden hardening above 10 MeV in the form of an additional power-law component exhibiting a spectral attenuation at a few hundreds of MeV. This high-energy break has been previously interpreted in terms of gamma-ray opacity to pair creation and has been used to estimate the bulk Lorentz factor of the outflow. In this article, we report on a new time-resolved analysis of the GRB 090926A broadband spectrum during its prompt phase and on its interpretation in the framework of prompt emission models.

Methods. We characterized the emission from GRB 090926A at the highest energies with Pass 8 data from the *Fermi* Large Area Telescope (LAT), which offer a greater sensitivity than any data set used in previous studies of this burst, particularly in the 30−100 MeV energy band. Then, we combined the LAT data with the *Fermi* Gamma-ray Burst Monitor (GBM) in joint spectral fits to characterize the time evolution of the broadband spectrum from keV to GeV energies. We paid careful attention to the systematic effects that arise from the uncertainties on the LAT response. Finally, we performed a temporal analysis of the light curves and we computed the variability timescales from keV to GeV energies during and after the bright spike.

Results. Our analysis confirms and better constrains the spectral break, which has been previously reported during the bright spike. Furthermore, it reveals that the spectral attenuation persists at later times with an increase of the break characteristic energy up to the GeV domain until the end of the prompt phase. We discuss these results in terms of keV−MeV synchroton radiation of electrons accelerated during the dissipation of the jet energy and inverse Compton emission at higher energies. We interpret the high-energy spectral break as caused by photon opacity to pair creation. Requiring that all emissions are produced above the photosphere of GRB 090926A, we compute the bulk Lorentz factor of the outflow, Γ. The latter decreases from 230 during the spike to 100 at the end of the prompt emission. Assuming, instead, that the spectral break reflects the natural curvature of the inverse Compton spectrum, lower limits corresponding to larger values of Γ are also derived. Combined with the extreme temporal variability of GRB 090926A, these Lorentz factors lead to emission radii $R \sim 10^{14}$ cm, which are consistent with an internal origin of both the keV−MeV and GeV prompt emissions.

Key words. gamma-ray burst: individual: GRB 090926A – radiation mechanisms: non-thermal

1. Introduction

To a large extent, the physical mechanims at work in gamma-ray bursts (GRBs) remain elusive more than 40 years after their discovery. The current paradigm (see, e.g., Piran 2004) associates these powerful flashes of hard X-rays and gamma rays with explosions of massive stars (the so-called long GRBs) or with the merging of neutron stars or black hole-neutron star binaries (short GRBs). These events can be detected from galaxies at cosmological distances owing to their huge luminosity, which is caused by an ultra-relativistic outflow moving toward the observer. The phenomenology distinguishes two consecutive phases of nonthermal emissions, with different temporal properties, independent of the GRB progenitor. The prompt phase of short GRBs lasts typically less than 2 s and it can continue for several minutes in some long GRBs. The prompt gamma-ray emission is the most intense and often highly variable with light curves that generally exhibit multiple pulses at different timescales. This contrasts with the smoother evolution of the afterglow phase that is observed at later times, where the maximum of the emission cools down to the X-ray and radio domains on a daily timescale as the overall intensity decreases.

The physical mechanisms that are responsible for the GRB prompt emission are still highly debated. In the internal shock scenario, the fast variability observed at early times is caused by shocks taking place within the jet, which accelerate the particles in the outflow and produce nonthermal radiations (Rees & Meszaros 1994; Kobayashi et al. 1997; Daigne & Mochkovitch 1998). Magnetic reconnection has been also discussed as an alternative to internal shocks in the case of outflows that are still highly magnetized at large distances (McKinney & Uzdensky 2012; Zhang & Zhang 2014; Beniamini & Granot 2016). In these models, the prompt emission is produced above the photosphere as suggested by the nonthermal spectrum. However, it has been shown that nonthermal emission can also be produced at the photosphere

if a subphotospheric dissipation mechanism is at work (Rees & Mészáros 2005; Pe'er et al. 2005; Ryde et al. 2011; Giannios 2012; Beloborodov 2013). After the prompt phase, the afterglow is produced at larger distances and is due to the interaction of the jet with the ambient medium, which creates a strong external shock.

Since the launch of the *Fermi* observatory in June 2008, the Large Area Telescope (LAT) has detected more than 100 GRBs above 20 MeV[1] (Vianello et al. 2015). The second instrument on board *Fermi*, the Gamma-ray Burst Monitor (GBM), has detected 1400 GRBs in the sub-MeV range during the first six years (Narayana Bhat et al. 2016) and more than 2000 as of today. Together, the GBM and LAT have provided a wealth of new information on the temporal and spectral properties of GRBs over a wide energy range. The properties of GRBs at high energies have been investigated in detail in the first LAT GRB catalog (Ackermann et al. 2013a). In general, their emission above 100 MeV starts significantly later than their keV−MeV prompt emission recorded by the GBM, and it continues over a much longer timescale. When sufficient photon statistics were available, their GeV emission was also found to be harder than the extrapolation of their keV−MeV emission spectrum and was generally well described by a power-law spectral component with a photon index $\gtrsim -2$. After the end of the keV−MeV prompt emission, this additional power-law component persists during hundreds of seconds, up to 19 h in the case of GRB 130427A (Ackermann et al. 2014). Specifically, Ackermann et al. (2013a) showed that the luminosity above 100 MeV decreases simply as $L(t) \propto t^{\lambda}$, with $\lambda \simeq -1$ at late times.

A possible interpretation of these results – for example, delayed onset of the GeV emission and power-law temporal decay of the long-lived GeV emission – considers the synchrotron emission from electrons accelerated at the external shock to explain the entire signal detected by the LAT (Razzaque 2010; Kumar & Barniol Duran 2010; Ghisellini et al. 2010; De Pasquale et al. 2010; Ackermann et al. 2013b; Lemoine et al. 2013; Wang et al. 2013). There is however a theoretical argument against this interpretation, as emphasized by Beloborodov et al. (2014); the LAT flux usually starts to decrease well before the end of the prompt emission in the GBM, which is too early to correspond to the self-similar stage of the afterglow evolution, expected on theoretical grounds at somewhat later times. Alternative models are based on the interaction of prompt photons with the shocked and/or unshocked ambient medium (see, e.g., Beloborodov et al. 2014) or imply a contribution of internal dissipation mechanisms to the LAT flux at early times. As discussed below, such an internal contribution seems unavoidable when variability is observed in the LAT.

Indeed, despite its ability to account for several observed high-energy properties of GRBs, the interpretation presented above has proven to be insufficient to explain all of the LAT GRB observations. The study of GRBs 090510, 090926A and 090902B by Ackermann et al. (2013a) revealed a flattening in the power-law temporal decay of the luminosity above 100 MeV well after the end of the keV−MeV prompt emission. For instance, the decay index λ of GRB 090926A increased from ~ -2.7 to ~ -0.9 at ~40 s post-trigger, while the prompt emission lasted only ~22 s in the GBM (Ackermann et al. 2011). Ackermann et al. (2013a) interpreted this flattening as a possible evolution from a phase where internal and external emissions combine at GeV energies to a phase where the afterglow emission prevails. Actually, an internal origin of the high-energy emission has to be favored during highly variable episodes, as observed in the prompt light curve of GRB 090926A. The additional power-law component in the spectrum of this burst was detected at the time of a short and bright pulse that was observed synchronously by the GBM and the LAT at ~10 s post-trigger. The attenuation of this spectral component at a few hundreds of MeV has been previously interpreted in terms of gamma-ray opacity to pair creation and used to estimate the bulk Lorentz factor of the outflow (Ackermann et al. 2011).

In this article, we reanalyze the broadband prompt emission spectrum of GRB 090926A with LAT Pass 8 data, which offer a greater sensitivity than any LAT data selection used in previous studies of this burst, particularly in the 30−100 MeV energy band. In Sect. 2, we present the *Fermi*/GBM and LAT data samples and our spectral analysis methods. In Sect. 3, we combine the GBM and LAT data in joint spectral fits to characterize the time evolution of the spectrum from keV to GeV energies. Careful attention is paid to the systematic effects arising from the uncertainties on the LAT response. Finally, we perform a temporal analysis of the light curves and we compute the variability timescales from keV to GeV energies during and after the bright spike. We discuss these results in Sect. 4 in terms of keV−MeV synchroton radiation of electrons accelerated during the dissipation of the jet energy and inverse Compton emission at higher energies. We interpret the high-energy spectral break as caused by photon opacity to pair creation. Requiring that all emissions are produced above the photosphere of GRB 090926A, we estimate the bulk Lorentz factor of the outflow and its time evolution. Our conclusions are given in Sect. 5.

2. Data preparation and spectral analysis methods

2.1. Observations and data selection

GRB 090926A has been observed over a broad energy range by the two instruments on board the *Fermi* observatory, the GBM and LAT. The GBM (Meegan et al. 2009) is a set of 12 NaI and 2 BGO scintillators installed around the spacecraft to cover a large portion of the sky. While the onboard trigger is based on the signal recorded by the NaI detectors only, both NaI (8−1000 keV) and BGO (0.15−40 MeV) detectors are used for spectral analyses on the ground. The LAT (Atwood et al. 2009) is the main instrument of *Fermi*. This pair-conversion telescope can cover the high-energy part of GRB spectra, from 20 MeV up to more than 300 GeV. GRB 090926A triggered the GBM on 2009 September 26, at T_0 = 04:20:26.99 UT and it occurred at an off-axis angle of 48° in the LAT field of view. The GBM and LAT response remained essentially constant during the prompt emission phase of the burst. Later follow-up observations of the optical afterglow of GRB 090026A placed this burst at a redshift $z = 2.1062$. Adopting a Hubble constant of $H_0 = 72\ \mathrm{km\,s^{-1}\,Mpc^{-1}}$ and cosmological parameters of $\Omega_\Lambda = 0.73$ and $\Omega_\mathrm{M} = 0.27$ as in Ackermann et al. (2011), this corresponds to a luminosity distance $D_\mathrm{L}(z) = 5.1 \times 10^{28}$ cm.

Following the analysis reported in Ackermann et al. (2011), we selected the GBM time-tagged event (TTE) data from three NaI detectors (N6, N7, and N8) and one BGO detector (B1). The GBM TTE data are unbinned in time and have the finest time (2 μs) and energy resolution that can be reached by the GBM. Since the launch of *Fermi*, the LAT event classes have been publicly released as different versions of the data, called passes, which correspond to different instrument responses. The

[1] http://fermi.gsfc.nasa.gov/ssc/observations/types/grbs/lat_grbs/table.php

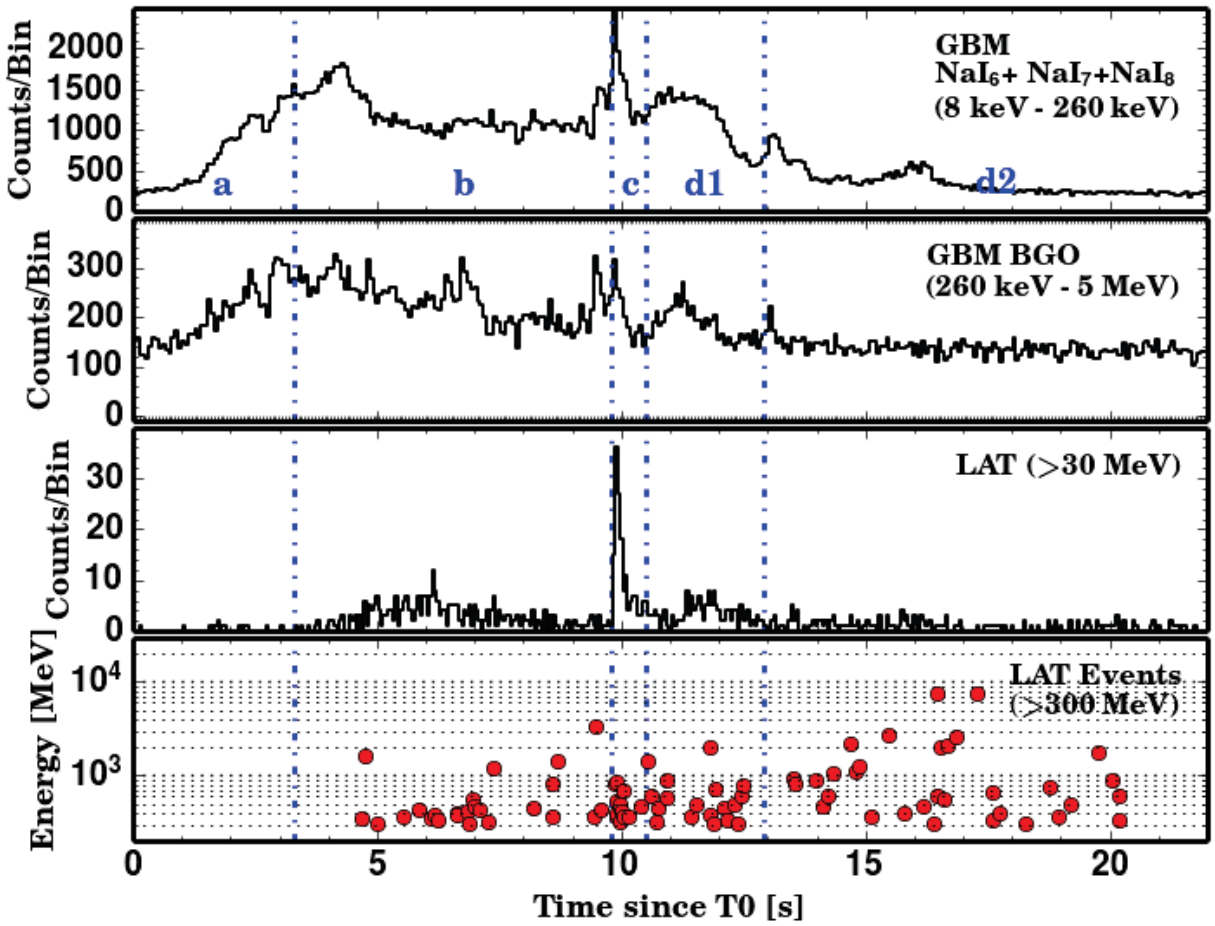

Fig. 1. GRB 090926A counts light curves as measured by the GBM and LAT, from lowest to highest energies. The sum of the counts in the GBM NaI detectors (*first panel*), in the GBM BGO detector facing the burst (*second panel*), and using the LAT Pass 8 transient-class events above 30 MeV within a 12° region of interest (*third panel*). The *last panel* shows the energies of the events from this sample, which have been detected above 300 MeV. The dashed blue vertical lines indicate the time intervals that are used for the joint GBM and LAT spectral analyses.

results reported in Ackermann et al. (2011) and in the first LAT GRB catalog (Ackermann et al. 2013a) are based on Pass 6 data. In this work, we used the Pass 8 data that were released in June 2015 at the *Fermi* Science Support Center[2] (FSSC hereafter). These data were processed with more elaborate reconstruction and classification algorithms. Most importantly for the purpose of GRB analyses, the LAT effective area was greatly improved and the spectral reach of the instrument was extended with the possibility of including photons with energies lower than 100 MeV, where the gain in effective area is the largest. Specifically, our analysis of GRB 090926A is based on the P8R2_TRANSIENT100_V6 event class, corresponding to event selection cuts that were optimized for the study of short gamma-ray transients. In order to show how Pass 8 data improves the LAT sensitivity to GRB spectral features, we repeated part of our analysis above 100 MeV using Pass 7 data (P7REP_TRANSIENT_V15), since the event reconstruction between Pass 6 and Pass 7 remained essentially unchanged. In all of our analyses, we selected the transient class events which fall in a region of interest (RoI) with fixed radius of 12°. In order to avoid any residual contamination from the Earth's limb, i.e., from γ-rays produced by the interactions of cosmic rays in the upper atmosphere, we also excluded all time intervals with a RoI zenith angle larger than 105°.

The GRB 090926A counts light curves based on the selections of the GBM and LAT data described above are shown in Fig. 1. For the joint GBM and LAT spectral analyses presented later in this article, we used the three time intervals (*b*, *c*, and *d*) that have been defined in Ackermann et al. (2011) with boundaries at T_0 + (3.3, 9.8, 10.5, 21.6) s, as shown in Fig. 1. We ignored the data taken during the 3.3 s post-trigger (time interval *a* in Fig. 1) since GRB 090926A was not detected by the LAT during this period (Ackermann et al. 2011). We also performed spectral analyses using LAT-only data over the whole duration of the burst. The corresponding time interval ($T_{90}^{\rm LAT}$ hereafter) that we adopted runs from T_0 + 5.5 s to T_0 + 225 s in accordance with the duration of the LAT emission reported in Ackermann et al. (2013a); this interval is much longer than the duration of ~15 s measured by the GBM. Table 1 shows the Pass 7 and Pass 8 event statistics collected by the LAT during the $T_{90}^{\rm LAT}$ time interval. About 2.4 times more events enter the Pass 8 selection and the gain in statistics is the largest below 100 MeV with an increase of event numbers by a factor of 4 to 7 depending on the energy range.

2.2. LAT-only spectral analysis

The LAT spectral analyses were performed with the suite of standard analysis tools (Science Tools version 10-00-02) available at

[2] http://fermi.gsfc.nasa.gov/ssc

Table 1. Event statistics in Pass 7 and Pass 8 data during the $T_{90}^{\rm LAT}$ of GRB 090926A (from 5.5 s to 225 s post-trigger).

Energy range	Number of Pass 7 events	Number of Pass 8 events	Pass 8/Pass 7
30–50 MeV	33	243	7.4
50–0.1 GeV	95	381	4.0
0.1–0.5 GeV	257	391	1.5
0.5–1 GeV	29	40	1.4
1–10 GeV	32	32	1.0
10–100 GeV	1	1	1.0
Total	447	1088	2.4

the FSSC[3]. The maximum likelihood (ML) method implemented in the *gtlike* tool can be applied in two different ways, either on a photon basis (unbinned ML hereafter) or binning the data in energy and sky position (binned ML). In this so-called forward-folding spectral reconstruction method, the LAT effective area and point spread function are folded with a source model to compute the number of predicted counts in the RoI (or the photon density for the unbinned case). The model includes the spectrum of GRB 090926A and of the background, whose parameters are fitted by comparing the expected and observed numbers through the maximization of the likelihood function. The background in the transient class events selected in Sect. 2.1 is mainly composed of charged cosmic rays that were misclassified as gamma rays. It includes also astrophysical gamma rays coming from galactic and extragalactic diffuse and point sources. In the case of GRB 090926A, the galactic emission could be neglected owing to its high galactic latitude ($b = -49.4°$). For these reasons, we simply used a power law to describe the spectrum of the background with an amplitude and a spectral index left free to vary. The spectrum of the GRB was fitted using either a power law or adding a spectral cutoff at high energy (see Sect. 2.4).

For the binned ML case, the *gtlike* tool offers the possibility of accounting for energy dispersion, at the cost of a slight increase in computing time. This allowed us to extend our analyses to Pass 8 events with energies below 100 MeV, i.e., to an energy domain where the LAT energy redistribution function is the widest and can affect the spectral reconstruction if not taken into account. Therefore, all of our analyses that include Pass 8 data below 100 MeV were performed with the binned ML method and correcting for the energy dispersion effect. As reported in Sect. 3, spectral analyses above 100 MeV were also performed using the binned and unbinned versions of the ML method to illustrate the gain in LAT sensitivity from Pass 7 to Pass 8 data and the consistency between all of these analyses.

2.3. Joint GBM-LAT spectral analysis

The joint GBM-LAT spectral analyses were performed with the *rmfit* tool (version 3.2) available at the FSSC[4], using the Castor fit statistic to account for the low counts in the LAT data. In these analyses, we prepared the LAT data using the aforementioned science tools. We binned the LAT data in energy with the *gtbin* tool, and we used the *gtbkg* tool to provide *rmfit* with a count spectrum of the background based on the best model parameters obtained from the fitting procedure described in Sect. 2.2.

The count spectrum of the background in the GBM was obtained by fitting background regions of the light curve before and after the burst, using the same time intervals as in Ackermann et al. (2011). In addition, we followed the methodology described in Ackermann et al. (2011) regarding the global effective area correction to be applied to the BGO data owing to the relative uncertainties in the NaI and BGO detectors responses. In order to match the flux given by the NaI detectors, a normalization factor $f_{\rm eff}$ between the two types of detectors (NaI and BGO) was introduced in the fit. We left $f_{\rm eff}$ free to vary and we estimated it by fitting the whole prompt emission spectrum (i.e., from $T_0 + 3.3$ s to $T_0 + 21.6$ s). The fitted value $f_{\rm eff} = 0.825 \pm 0.013$ is marginally compatible with the value of 0.79 reported in Ackermann et al. (2011). We also checked that this slight difference did not affect our results. In all of our joint analyses presented in Sect. 3, $f_{\rm eff}$ was held fixed at 0.83.

2.4. Spectral models

GRB 090926A was analyzed with different spectral models, which are chosen among the functions described below or as combinations of these functions. All functions are normalized by a free amplitude parameter A in units of cm^{-2} s^{-1} keV^{-1}. Following Ackermann et al. (2011), the spectra are always represented by the phenomenological Band function (Band et al. 1993) in the keV−MeV domain. This function is composed of two smoothly connected power laws with four free parameters ($A_{\rm B}$, $E_{\rm p}$, α, and β), i.e.,

$$\frac{{\rm d}N}{{\rm d}E}(E\,|\,A_{\rm B}, E_{\rm p}, \alpha, \beta) = A_{\rm B} \begin{cases} \left(\frac{E}{100\,{\rm keV}}\right)^{\alpha} \exp\left(-\frac{E\,(2+\alpha)}{E_{\rm p}}\right), & E \le E_{\rm p}\frac{\alpha-\beta}{2+\alpha} \\ \left(\frac{E}{100\,{\rm keV}}\right)^{\beta} \left(\frac{E_{\rm p}}{100\,{\rm keV}}\frac{\alpha-\beta}{2+\alpha}\right)^{\alpha-\beta} \exp\left(\beta-\alpha\right), & E > E_{\rm p}\frac{\alpha-\beta}{2+\alpha}, \end{cases} \quad (1)$$

where α and β are the respective photon indices, and $E_{\rm p}$ is the peak energy of the spectral energy distribution (SED), $\nu F_\nu = E^2 \frac{{\rm d}N}{{\rm d}E}$.

In the LAT energy range, we adopted either a power law (hereafter PL), a power law with exponential cutoff (CUTPL), or a broken power law with exponential cutoff (CUTBPL). The CUTBPL function has three free parameters ($A_{\rm C}$, γ and $E_{\rm f}$) and is defined as

$$\frac{{\rm d}N}{{\rm d}E}(E\,|\,A_{\rm C}, \gamma, E_{\rm f}) = A_{\rm C} \begin{cases} \left(\frac{E}{E_{\rm piv}}\right)^{\gamma_0} \exp\left(-\frac{E}{E_{\rm f}}\right), & E \le E_{\rm b} \\ \left(\frac{E_{\rm b}}{E_{\rm piv}}\right)^{\gamma_0} \left(\frac{E}{E_{\rm b}}\right)^{\gamma} \exp\left(-\frac{E}{E_{\rm f}}\right), & E > E_{\rm b}, \end{cases} \quad (2)$$

[3] http://fermi.gsfc.nasa.gov/ssc/data/analysis/software

[4] http://fermi.gsfc.nasa.gov/ssc/data/analysis/rmfit

where γ is the photon index and E_f is the folding energy of the exponential cutoff that characterizes the high-energy spectral break. At low energies, the break at $E_b = 200$ keV and the photon spectral index $\gamma_0 = +4$ have been fixed to ensure that the flux in the keV−MeV domain is negligible with respect to the flux from the Band spectral component, as expected from an emission spectrum that consists of a synchrotron component in the keV−MeV domain and an inverse Compton component at higher energies (see Sect. 3.2). Specifically, the break energy E_b was fixed to the value that is obtained when this parameter is left free to vary. In order to minimize the correlation between the fitted parameters, the pivot energy E_{piv} was chosen close to the decorrelation energy. This was fixed to a value between 200 MeV and 500 MeV in the LAT-only spectral analyses and to 10 MeV (time interval *c*) or 100 MeV (time interval *d*) in the GBM-LAT joint spectral fits.

The general formulation in Eq. (2) defines the PL and CUTPL functions as subsets of the CUTBPL function. The CUTPL function is obtained in the limit $E_b \to 0$ and the amplitude parameter is redefined as $A_C \to A' = A_C(E_b/E_{piv})^{\gamma_0}$. It has three free parameters (A', γ, and E_f) as follows:

$$\frac{dN}{dE}(E\,|\,A', \gamma, E_f) = A'\left(\frac{E}{E_{piv}}\right)^{\gamma} \exp\left(-\frac{E}{E_f}\right). \quad (3)$$

The PL function is obtained by further imposing $E_f \to +\infty$ (1 TeV in practice), leaving two free parameters (A' and γ) as follows:

$$\frac{dN}{dE}(E\,|\,A', \gamma) = A'\left(\frac{E}{E_{piv}}\right)^{\gamma}. \quad (4)$$

In the analyses presented in Sect. 3, we estimated the significance of the high-energy spectral break by fitting models with and without an exponential cutoff at the highest energies. For the LAT-only spectral analysis (Sect. 2.2), we computed the test statistic $TS = 2\,(\ln \mathcal{L}_1 - \ln \mathcal{L}_0)$, where $\mathcal{L}_0$ and $\mathcal{L}_1$ are the maximum values of the likelihood functions obtained with the PL and CUTPL models, respectively. For the joint GBM-LAT spectral analysis (Sect. 2.3), TS is simply given by the decrease in Castor fit statistic ΔC_{stat} when an exponential cutoff (i.e., the E_f parameter) is added to the high-energy power-law component of the spectral model. In the large sample limit, TS is equal to the square of the spectral break significance, thus we approximated the latter as $N_\sigma \simeq \sqrt{TS}$.

3. Results

This section presents the results of our spectral analyses. More information on the spectral fits are given in Tables A.1−A.6. Firstly, we performed a spectral analysis of GRB 090926A using LAT-only data over the burst duration at high energy and focusing on the time interval *c* (Sect. 3.1). Then, we performed a time-resolved spectral analysis of GRB 090926A through joint fits to the GBM and LAT data during the time intervals *c* and *d*, revealing the time evolution of the high-energy spectral break (Sects. 3.2.1 and 3.2.2). We carefully studied the stability of these results with respect to the systematic uncertainty on the LAT response (Sect. 3.2.3). Finally, we estimated the variability timescales in time intervals *c* and *d* and for the GBM and LAT energy ranges (Sect. 3.3), which are needed for the theoretical interpretation presented in the next section.

3.1. LAT-only spectral analysis

We first characterized the time-averaged spectrum of GRB 090926A using LAT Pass 7 and Pass 8 data above 100 MeV during the T_{90}^{LAT} time interval. We fitted the spectrum with a PL model using the unbinned ML method with Pass 7 data and the unbinned and binned ML methods with Pass 8 data. As shown in Table A.1, all of the three fits gave consistent results in terms of photon index and integrated flux above 100 MeV. Using Pass 8 data yielded spectral parameters that are slightly more constrained. A better accuracy was reached by applying the binned ML analysis to Pass 8 data including events with energies down to 30 MeV (see the last column of Table A.1). The number of events was ∼2.3 times higher in this configuration, yielding a photon index $\gamma = -2.20 \pm 0.03$ and an integrated flux of $(48 \pm 1.5) \times 10^{-5}$cm^{-2} s^{-1}. Figure 2 shows the SED of GRB 090926A for the four analyses described above and their excellent agreement. The narrowest confidence level contour, shown as a filled butterfly in the figure, is obtained for the last fit, which clearly illustrates the improvement of the spectral reconstruction with Pass 8 data above 30 MeV.

Then, we focused our analysis on the time interval *c*, where the high-energy spectral break of GRB 090926A was initially found (Ackermann et al. 2011). We fitted the spectrum with PL and CUTPL models using the same ML methods and data sets as for the analyses of the T_{90}^{LAT} time interval described above. As shown in Table A.2, the precision on the fitted photon index is poor owing to the low event statistics above 100 MeV. Moreover, no significant spectral break was found in these analyses. However, the binned ML analysis of Pass 8 data above 30 MeV yields a marginal detection ($N_\sigma = 4.4$) with a folding energy $E_f = 0.41^{+0.27}_{-0.14}$ GeV and a photon index $\gamma = -1.68 \pm 0.22$. These values are affected by large errors and they are fully compatible with the more accurate measurements reported in Ackermann et al. (2011), which were obtained using GBM and LAT data in a joint spectral fit.

3.2. Joint GBM-LAT spectral analysis

3.2.1. Spectrum representation

The results presented in Sect. 3.1 indicate that the high-energy spectral break of GRB 090926A is hard to detect with LAT-only data. Therefore, we considered GBM and LAT data in a joint spectral fit to bring in additional constraints on the photon index of the high-energy component and to increase the sensitivity to any possible spectral break. Starting with a single Band component in the spectral model, we reanalyzed the three time intervals *b*, *c*, and *d* with GBM and LAT Pass 7 or Pass 8 data. Then, we increased the complexity of the model by adding an extra high-energy PL component or a CUTPL component to search for the presence of a spectral break. As was found by Ackermann et al. (2011), the extra PL component was determined to be very significant in the time intervals *c* and *d* only. Nevertheless, we searched for a possible spectral break in the time interval *b*, i.e., we added an exponential attenuation to the high-energy power-law branch of the Band component. We found that a spectral break is not required by the data and that the Band model is enough to reproduce the spectrum of GRB 090926A in this time interval.

In time interval *c*, the comparison of the Band+PL and Band+CUTPL joint fits confirmed the presence of a high-energy spectral break in the extra PL. Not surprisingly, the evidence for this break was found to be the highest using LAT Pass 8 data

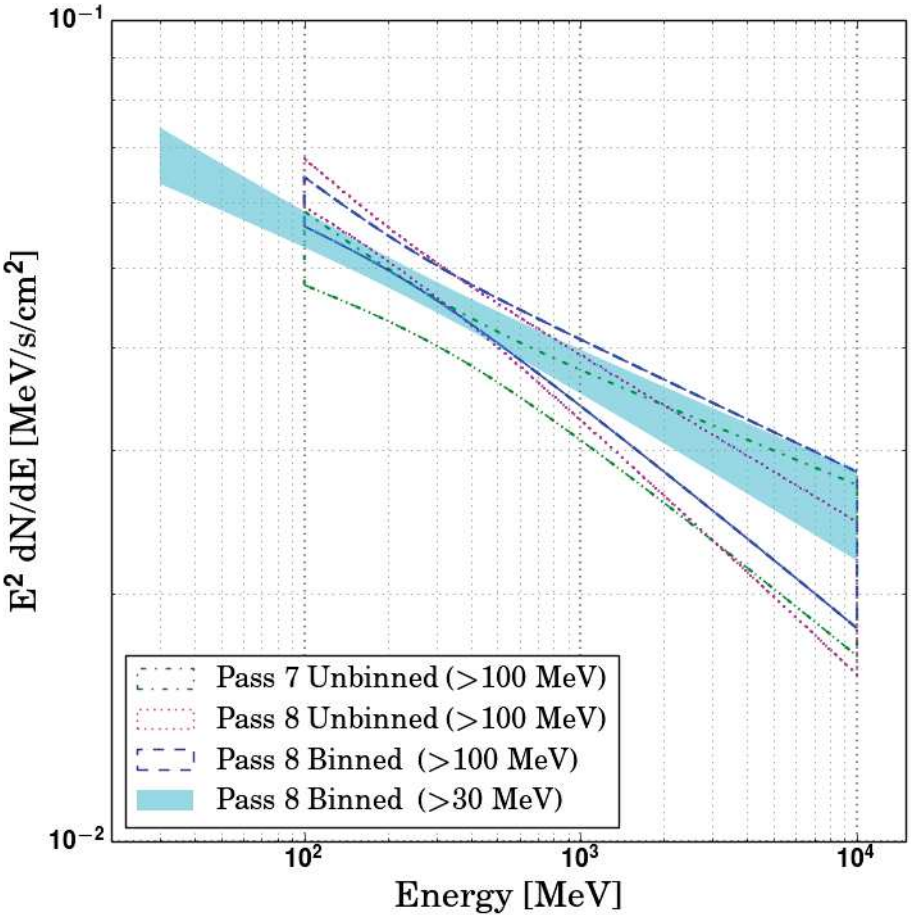

Fig. 2. GRB 090926A time-averaged spectral energy distribution as measured by the *Fermi*/LAT, using Pass 7 data above 100 MeV (dot-dashed butterfly) and Pass 8 data above 30 MeV (filled butterfly) or 100 MeV (dotted and dashed butterflies). Each spectrum is represented by a 68% confidence level contour derived from the errors on the parameters of the fitted power-law function.

above 30 MeV in the spectral fit, i.e., the best LAT data set with the widest spectral coverage. As shown in Table A.3 and Fig. A.1 (top panel), the break significance increased from $N_\sigma = 5.9$ with Pass 7 data above 100 MeV to $N_\sigma = 7.7$ with Pass 8 data above 30 MeV. Moreover, both the photon index $\gamma = -1.68^{+0.04}_{-0.03}$ and the folding energy $E_\mathrm{f} = 0.37^{+0.06}_{-0.05}$ GeV of the CUTPL component were very well constrained in the latter case. These values are compatible with the results reported in Ackermann et al. (2011), $\gamma = -1.71^{+0.02}_{-0.05}$ and $E_\mathrm{f} = 0.40^{+0.13}_{-0.06}$ GeV.

In time interval *d*, a marginal detection of a spectral break ($N_\sigma \sim 4$) was reported in Ackermann et al. (2011) with $E_\mathrm{f} = 2.2^{+0.9}_{-0.7}$ GeV. As shown in Table A.4 and in Fig. A.1 (bottom panel), we found a similar significance of $N_\sigma = 4.3$ when using LAT Pass 7 data above 100 MeV in the joint spectral fit. Using instead Pass 8 data above 30 MeV, the significance increased to $N_\sigma = 5.8$. This Band+CUTPL fit yielded a photon index, $\gamma = -1.75^{+0.02}_{-0.03}$, which is similar to the photon index found in the time interval *c*, and a folding energy $E_\mathrm{f} = 1.61^{+0.38}_{-0.31}$ GeV, which is significantly higher. These results reveal, for the first time, that the spectral attenuation persists at later times, with an increase of the break characteristic energy up to the GeV domain, and until the end of the keV−MeV prompt emission phase of GRB 090926A, as measured by the GBM.

In Sect. 4, we discuss our results in terms of keV−MeV synchroton radiation of electrons accelerated during the dissipation of the jet energy and inverse Compton emission at higher energies. In this theoretical framework, the inverse Compton component is not expected to contribute significantly to the flux at the lowest energies. The Band+CUTPL representation of GRB 090926A spectra, which we used in the aforementioned analyses, does not meet this requirement, since the extrapolation of the CUTPL component down to ∼10 keV yields a flux that is comparable to the flux of the Band component (see Fig. A.1 in this paper and Fig. 5 in Ackermann et al. 2011). Conversely, the CUTBPL component (see Sect. 2.4) is more physically motived. For these reasons, we repeated the joint spectral fits in the time intervals *c* and *d*, using LAT Pass 8 data above 30 MeV and adopting the Band+CUTBPL model.

As shown in the last two rows of Table 2, the choice of the Band+CUTBPL model as the best representation of GRB 090926A spectra is justified by its ability to reproduce the data adequately in the time intervals *c* and *d*. We investigated different representations of the spectral break, for example, trying to reproduce the more complex shape predicted in Fig. 6 of Hascoët et al. (2012), which consists of a broken power law with an exponential attenuation at higher energies. However, and similar to the analysis reported in Ackermann et al. (2011), the limited photon statistics prevented us from characterizing the shape of this spectral attenuation better than with the Band+CUTBPL model. The Castor fit statistics obtained with the Band+CUTBPL model are only slightly larger that those obtained with the Band+CUTPL model ($\Delta C_\mathrm{stat} = 15.9$ and 12.1 for time intervals *c* and *d*, respectively). In addition, the spectral parameters remained essentially unchanged, the main difference being observed for the Band photon index α, as expected from the different contributions of the CUTPL and CUTBPL components to the low-energy flux. This parameter decreased from $\alpha \sim -0.6$ (Band+CUTPL model; see Tables A.3 and A.4)

Table 2. Results of the Band+CUTBPL fits to GBM and LAT data during the time intervals c, d, d_1, and d_2.

Time interval	c	d	d_1	d_2
Time interval boundaries from T_0 (s)	9.8–10.5	10.5–21.6	10.5–12.9	12.9–21.6
Band amplitude A_B ($\times 10^{-2}$ cm^{-2} s^{-1} keV^{-1})	34^{+2}_{-1}	$10.1^{+0.2}_{-0.3}$	29^{+1}_{-1}	$4.7^{+0.1}_{-0.2}$
Band E_{peak} (keV)	190^{+9}_{-9}	177^{+7}_{-3}	198^{+6}_{-10}	143^{+4}_{-7}
Band photon index α	$-0.94^{+0.03}_{-0.02}$	$-0.86^{+0.01}_{-0.03}$	$-0.73^{+0.01}_{-0.04}$	$-1.03^{+0.05}_{-0.02}$
Band photon index β	$-3.2^{+0.2}_{-0.9}$	$-3.1^{+0.2}_{-0.5}$	$-3.1^{+0.2}_{-0.4}$	$-3.7^{+0.3}_{-1.5}$
CUTBPL amplitude A_C ($\times 10^4$ cm^{-2} s^{-1} keV^{-1})	$4.6^{+0.9}_{-0.9}$	$(9.4^{+0.5}_{-0.1}) \times 10^3$	$(12^{+7}_{-4}) \times 10^3$	$(7^{+1}_{-1}) \times 10^3$
CUTBPL photon index γ	$-1.48^{+0.09}_{-0.08}$ (-1.68 ± 0.22)	$-1.71^{+0.05}_{-0.05}$	$-1.55^{+0.12}_{-0.10}$	$-1.68^{+0.05}_{-0.05}$
CUTBPL folding energy E_f (GeV)	$0.34^{+0.07}_{-0.05}$ ($0.41^{+0.27}_{-0.14}$)	$1.20^{+0.22}_{-0.18}$	$0.55^{+0.13}_{-0.10}$	$1.43^{+0.49}_{-0.25}$
Break significance N_σ	7.6	6.1	4.3	5.1
C_{stat}/d.o.f.	604.7 / 518	652.7 / 518	559.0 / 518	603.2 / 518
ΔC_{stat}	15.9	12.1	6.1	15.1

Notes. The pivot energy E_{piv} in Eq. (2) was chosen close to the decorrelation energy. It was fixed to 10 MeV for interval c and 100 MeV for intervals d, d_1, and d_2. The last row shows the increase in C_{stat} with respect to fits with a Band+CUTPL model. In order to facilitate the comparison with the results from the LAT-only spectral analysis, we also indicated the values of the photon index γ and of the folding energy E_f found in Sect. 3.1 for the time interval c.

to $\alpha \sim -0.9$ (Band+CUBTPL model). Both values are higher than the theoretical prediction $\alpha = -3/2$ for pure fast-cooling synchrotron (Sari et al. 1998), whereas this regime is required to explain the high temporal variability and to reach a high radiative efficiency that is compatible with the huge observed luminosities. The value $\alpha \sim -0.6$ is difficult to reconcile with synchrotron radiation, except by invoking the marginally fast-cooling regime (Daigne et al. 2011; Beniamini & Piran 2013). The value $\alpha \sim -0.9$ found in the Band+CUTBPL model is in better agreement, as it is well below the synchrotron death line, $\alpha = -2/3$, and very close to the limit $\alpha \sim -1$ that is expected in the fast-cooling regime affected by inverse Compton scatterings in the Klein Nishina regime (Daigne et al. 2011). At high energy, the CUTBPL component is slightly harder than the CUTPL component with a fitted photon index $\gamma = -1.48^{+0.09}_{-0.08}$ (resp. $-1.71^{+0.05}_{-0.05}$) in the time interval c (resp. d), whereas the folding energy $E_f = 0.34^{+0.07}_{-0.05}$ GeV (resp. $1.20^{+0.22}_{-0.18}$ GeV) and its significance $N_\sigma = 7.6$ (resp. 6.1) are close to those previously obtained from the Band+CUTPL fit to the data.

3.2.2. Time evolution of the high-energy spectral break

The time evolution of the spectral break characteristic energy in the extra power-law component of GRB 090926A is a novel result that has been made possible thanks to the improved event statistics in the LAT Pass 8 data set. We further investigated this spectral evolution by splitting the time intervals c and d, either by dividing them into two subintervals of equal statistics or by isolating the rising and decaying parts in the corresponding light curves. Then, we performed a Band+CUTBPL fit using the same procedure as in Sect. 3.2.1.

The results of these four fits are reported in Tables A.5 and A.6. No time evolution was found within the interval c, in particular between the two subintervals of equal statistics, in which the high-energy spectral break was detected with high significance ($N_\sigma \geq 5$). Conversely, the high-energy spectral break was found to evolve within the time interval d with a significance between 4.1 and 5.3 depending on the splitting method. In the following, we retained the pair of subintervals with equal statistics, d_1 (from 10.5 s to 12.9 s post-trigger) and d_2 (from 12.9 s to 21.6 s post-trigger). The results of the Band+CUTBPL fits to GBM and LAT data during these time intervals are summarized in Table 2. As for the time intervals c and d, the Band+CUTBPL model was found to reproduce the data adequately. Between d_1 and d_2, the folding energy E_f increased from $0.55^{+0.13}_{-0.10}$ GeV (with a significance $N_\sigma = 4.3$) to $1.43^{+0.49}_{-0.25}$ GeV ($N_\sigma = 5.1$). The final SEDs for the time intervals c, d_1, and d_2, are represented in Fig. 3, where the increase of the high-energy spectral break from 0.34 GeV (interval c) to 1.43 GeV (interval d_2) is clearly visible.

3.2.3. Systematic effects

The measurements of the high-energy spectral break of GRB 090926A can be affected by systematic uncertainties due to the incomplete knowlege of the LAT instrument response functions (IRFs), namely the LAT effective area, point spread function and energy redistribution function. As explained in the FSSC documentation[5], the LAT collaboration has estimated the precision of the instrument simulation by performing several consistency checks between IRF predictions and data taken from bright gamma-ray sources (the Vela pulsar, bright active galactic nuclei, and the Earth's limb). The systematic uncertainty on the effective area is dominant for spectral analyses that account for energy dispersion, especially below 100 MeV. The maximum amplitude of this systematic effect has been parameterized as a function of the photon energy E, as represented by the blue curves in the left panel of Fig. 4. Therefore, we assessed the impact of the systematic effect on the effective area $A_{eff}(E)$ by replacing it with $A_{eff}(E)\,[1 + \epsilon(E)]$ in the joint spectral fits, where the chosen uncertainty amplitude $\epsilon(E)$ was constrained within this containment interval. The two ϵ(E) functions shown in red

[5] http://fermi.gsfc.nasa.gov/ssc/data/analysis/LAT_caveats.html

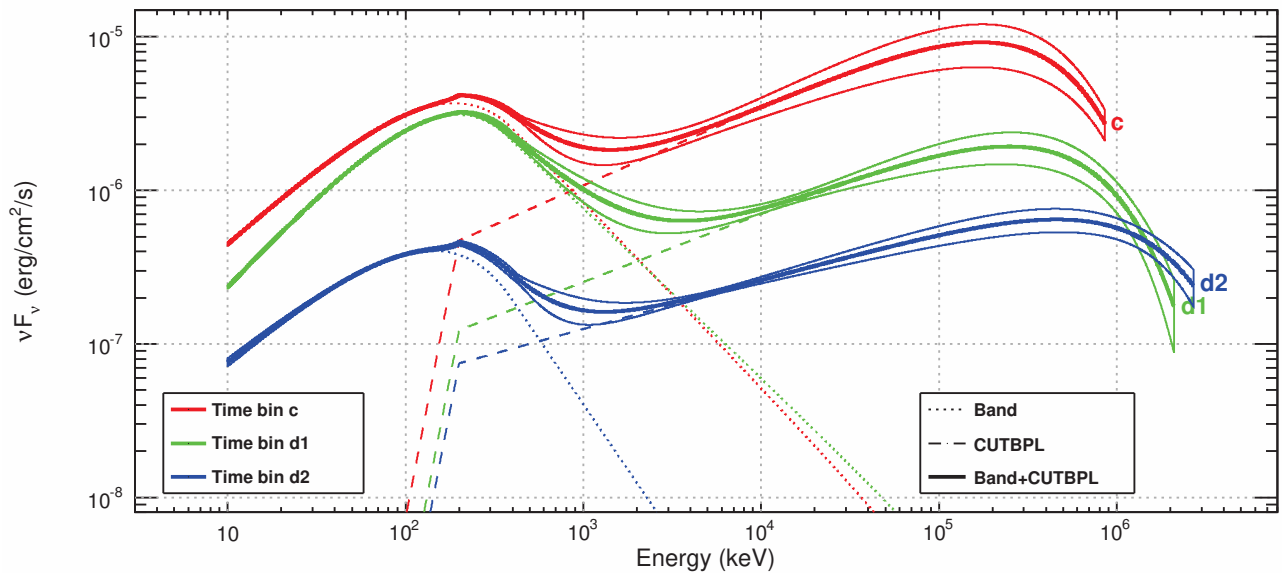

Fig. 3. GRB 090926A spectral energy distributions as measured by the *Fermi* GBM and LAT in time intervals c (red curves), d_1 (green curves), and d_2 (blue curves) with LAT Pass 8 data above 30 MeV. Each solid curve represents the best-fitted spectral shape (Band+CUTBPL) within a 68% confidence level contour derived from the errors on the fit parameters.

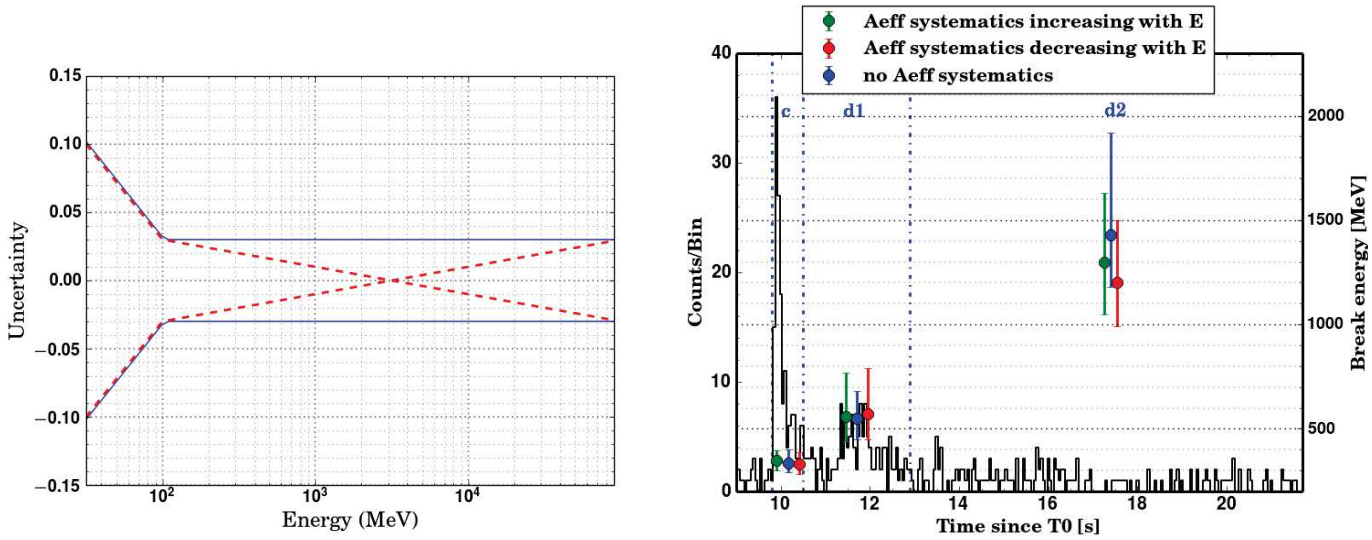

Fig. 4. *Left*: containment interval of the relative systematic uncertainty on the LAT effective area (blue curves) as a function of the photon energy E, and the two ϵ(E) functions used to estimate the corresponding distortion effect on our spectral analysis (red curves). *Right*: folding energies for the time intervals c, d_1, and d_2, obtained with or without considering the systematic uncertainties on the LAT effective area. The results were superimposed onto the LAT counts light curve above 30 MeV.

in the left panel of Fig. 4 were found to cause the largest spectral distortion. The folding energies E_f for the time intervals c, d_1, and d_2, obtained with or without twisting the effective area, are shown in the right panel of Fig. 4. As can be seen from this figure, the systematic uncertainty on the LAT effective area does not significantly affect the results because the observed changes in E_f are negligible with respect to their statistical errors. In particular, it is worth noting that the confidence intervals on E_f in the different time intervals still exclude each other after modifying the effective area.

3.3. Estimation of the variability timescale

The determination of the bulk Lorentz factor of GRB 090926A is performed in Sect. 4 through the computation of the photon opacity to pair creation, which requires a good estimate of the variability timescale, t_v, in all time intervals. For this purpose, we built the light curves for each time interval and in four energy bands with the summed NaI data (14–260 keV), the BGO data (260 keV–5 MeV), and the LAT data (30 MeV–10 GeV and 100 MeV–10 GeV). The first two energy ranges were chosen as in Ackermann et al. (2011). Following Norris et al. (2005), we then fitted each light curve with a temporal profile that is defined as the product of two exponentials, i.e.,

$$I(t) = \begin{cases} 0, & t < t_s \\ A\, e^{-\frac{\tau_1}{(t-t_s)} - \frac{(t-t_s)}{\tau_2}} + B, & t > t_s, \end{cases} \quad (5)$$

where A is a normalization factor, t_s is the starting time, τ_1 and τ_2 are related to the peak time $t_{peak} = \sqrt{\tau_1 \tau_2}$, and the constant

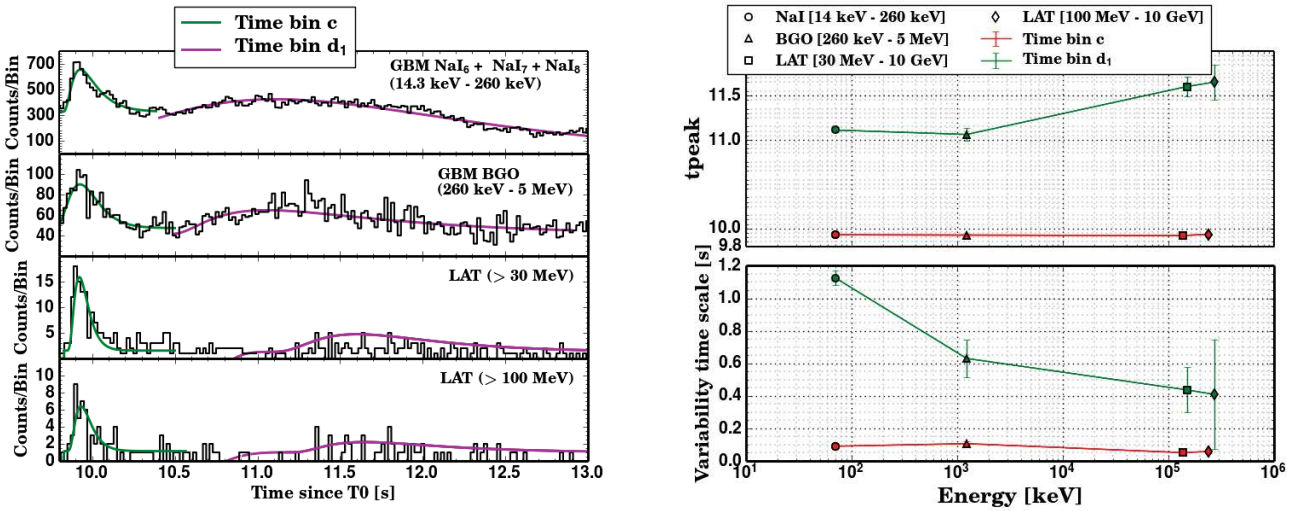

Fig. 5. *Left*: GBM and LAT light curves for GRB 090926A with a 0.02 s time binning. The data from the GBM NaI and BGO detectors were selected from two energy bands, 14.3−260 keV and 260 keV−5 MeV, respectively. The *last two panels* show the LAT light curves above 30 MeV and 100 MeV, respectively. *Right*: peak time $t_{\rm peak}$ and variability timescale $t_{\rm v}$ measured for the time intervals c (red) and d_1 (green) in the NaI, BGO, and LAT energy bands.

parameter B accounts for the background in each detector. We used a simple χ^2 statistic to check the quality of the fits, and we computed the variability timescale as the half width at half maximum,

$$t_{\rm v} = \frac{\tau_2}{2}\sqrt{\left(\log(2) + 2\sqrt{\frac{\tau_1}{\tau_2}}\right)^2 - 4\frac{\tau_1}{\tau_2}}.$$

The left panel of Fig. 5 shows the light curves from the beginning of the time interval c to the end of the time interval d_1, along with their temporal fits. The corresponding values of $t_{\rm peak}$ and $t_{\rm v}$ are reported in the right panel of the same figure. In the time interval c, our results confirm the remarkable synchronization of the bright spike across the whole spectrum with $t_{\rm peak} = 9.93 \pm 0.01$ s in all detectors. The variability timescales for this time interval is $t_{\rm v} = 0.10 \pm 0.01$ s in the NaI and BGO energy ranges and $t_{\rm v} = 0.06 \pm 0.01$ s in the two LAT energy ranges. In the time interval d_1, the timescale decreases from 1.13 ± 0.04 s (NaI) to 0.6 ± 0.1 s (BGO) and 0.4 ± 0.2 s (LAT). In both cases, the measured GeV variability timescales thus appear to be similar to those in the MeV energy range. The LAT light curve for the time interval d_2 was not structured enough and was too difficult to fit. Conversely, the NaI light curve consists of two different pulses that we fitted with two temporal profiles. Only the BGO light curve contains a single pulse at $t_{\rm peak} = 13 \pm 0.1$ s with a variability timescale $t_{\rm v} = 0.5 \pm 0.1$ s.

4. Interpretation and discussion

4.1. Context

If the high-energy spectral break observed in the time intervals c, d_1, and d_2 is an actual cutoff resulting from pair production $\gamma\gamma \rightarrow e^+e^-$, it can be used to estimate the value of the Lorentz factor Γ of the emitting material (Krolik & Pier 1991; Baring & Harding 1997; Lithwick & Sari 2001; Granot et al. 2008; Hascoët et al. 2012). However, the possibility that this spectral break could correspond to a natural curvature in the spectrum of the inverse Compton process in the Klein-Nishina regime (natural break hereafter) cannot be entirely excluded, and only a lower limit on Γ can be obtained in this case. We consider below these two possibilities in two different scenarios: (*i*) the GRB prompt emission in the GBM range is produced in the optically thin regime above the photosphere or (*ii*) this prompt emission is produced at the photosphere, as proposed in the dissipative photosphere model (Eichler & Levinson 2000; Rees & Mészáros 2005; Pe'er et al. 2006; Beloborodov 2010, 2013). In case (*i*), the radius at which the MeV photons are produced is given by

$$R_{\rm MeV} \simeq 2c\,\Gamma^2\,\frac{t_{\rm v}}{1+z}. \quad (6)$$

This estimate corresponds to the internal shock scenario (Rees & Mészáros 2005; Kobayashi et al. 1997; Daigne & Mochkovitch 1998) but a comparable radius is expected in some magnetic reconnection models such as ICMART (Zhang & Yan 2011). In both scenarios (*i*) and (*ii*) the GeV photons can be emitted from the same location as the MeV photons, $R_{\rm GeV} \simeq R_{\rm MeV}$, which is expected if the variability of the GeV and MeV emissions is comparable (as suggested by our analysis in Sect. 3.3), or from a larger radius $R_{\rm GeV} > R_{\rm MeV}$ if they come from the further reprocessing of the MeV photons (Beloborodov et al. 2014) or have an afterglow origin (Ando et al. 2008; Kumar & Barniol Duran 2009, 2010; Ghisellini et al. 2010; Piran & Nakar 2010).

4.2. Case (i): prompt emission produced above the photosphere

4.2.1. Constraints on the Lorentz factor if the high-energy spectral break is due to gamma-ray opacity to pair creation

In this case the radius of the MeV emission is given by Eq. (6) above. If the high-energy spectral break is an actual cutoff resulting from photon opacity to pair creation, the Lorentz factor can be directly estimated from the burst parameters (Eq. (59) in Hascoët et al. 2012) as follows:

$$\Gamma_{\gamma\gamma} = \frac{K\,\Phi(s)}{\left[\frac{1}{2}\left(1+\frac{R_{\rm GeV}}{R_{\rm MeV}}\right)\left(\frac{R_{\rm GeV}}{R_{\rm MeV}}\right)\right]^{1/2}}\,(1+z)^{-(1+s)/(1-s)} \times \{\sigma_{\rm T}\left[\frac{D_{\rm L}(z)}{ct_{\rm v}}\right]^2 E_* F(E_*)\}^{1/2(1-s)}\left[\frac{E_*\,E_{\rm cut}}{(m_e c^2)^2}\right]^{(s+1)/2(s-1)}. \quad (7)$$

Table 3. Burst parameters (variability timescale, spectral parameters and luminosity) for the three considered time intervals.

Time interval	c	d_1	d_2
t_v (s)	0.1 ± 0.01	0.6 ± 0.1	0.5 ± 0.1
s	$-1.55^{+0.07}_{-0.09}$	$-2.25^{+0.10}_{-0.08}$	$-2.19^{+0.09}_{-0.04}$
$\Phi(s)$	0.511 ± 0.009	0.463 ± 0.004	0.465 ± 0.003
E_f (GeV)	$0.34^{+0.07}_{-0.05}$	$0.55^{+0.13}_{-0.10}$	$1.43^{+0.49}_{-0.25}$
E_{max} (GeV)	0.85	2.04	2.66
E_* (MeV)	10	2.5	1.0
$F(E_*)$ (10^{-2} cm^{-2} MeV^{-1})	0.22 ± 0.03	4.0 ± 0.8	5 ± 1
Luminosity (10^{53} erg s^{-1})	16.9 ± 3.1	1.73 ± 0.14	1.85 ± 0.15
Lorentz factor $\Gamma_{\gamma\gamma}$ (E_f)	233 ± 18	100 ± 8	98 ± 9
Emission radius $R = R_{MeV} = R_{GeV}$ (10^{14} cm)	1.1 ± 0.1	1.2 ± 0.2	1.0 ± 0.1
Photospheric radius R_{ph} (10^{14} cm)	0.5 ± 0.2	0.7 ± 0.2	0.8 ± 0.2
Lower limit on the Lorentz factor $\Gamma_{\gamma\gamma}$ (E_{max})	257 ± 17	129 ± 8	110 ± 8

Notes. The last four lines give the obtained constraints for the two cases considered in Sect. 4.2: either the observed high-energy spectral break E_f is due to gamma-ray opacity to pair creation, which leads to a measurement of the Lorentz factor, or it is a natural break (last line). In this second case only a lower limit on the Lorentz factor can be obtained from the maximum energy E_{max} of the observed photons. In both cases, the results listed in the table corresponds to the assumption $R_{GeV} = R_{MeV}$, favored by the observed similar variability at low and high energy. The impact of $R_{GeV} > R_{MeV}$ on these results is illustrated in Fig. 6.

The various observed quantities appearing in Eq. (7) are listed in Table 3 for time intervals c, d_1, and d_2: t_v is the observed variability timescale in the considered time interval, estimated in Sect. 3.3; E_{cut} is the cutoff energy, which we assume here to be equal to the folding energy E_f that characterizes the spectral break (Sect. 3.2), also listed in Table 3; E_* is the typical energy of the seed photons interacting with those at the cutoff energy E_{cut}, s is the photon index of the seed spectrum close to E_*, and $F(E_*)$ is the photon fluence at E_* integrated over a duration t_v, so that the seed photon spectrum can be approximated by $F(E) = F(E_*)\,(E/E_*)^s$ (cm^{-2} MeV^{-1}). The energy E_* is given by

$$E_* \simeq \frac{\left(2\Gamma\, m_e c^2\right)^2}{(1+z)^2 E_{cut}} \simeq 1.1\,\mathrm{MeV} \left(\frac{\Gamma}{100}\right)^2 \left(\frac{E_{cut}}{1\,\mathrm{GeV}}\right)^{-1}, \quad (8)$$

where E_* and E_{cut} are the observed values. As the seed photon spectrum is approximated locally by a power law, a precise value of E_* is not required, as long as the correct region of the spectrum has been identified. It can be seen that the Lorentz factor $\Gamma_{\gamma\gamma}$ does not depend on a specific choice of E_* as long as this energy remains in a region where the spectrum keeps a fixed spectral index s. Indeed E_* appears in two factors in Eq. (7) with opposite scaling, $(E_* F(E_*))^{1/2(1-s)} \propto E_*^{-(s+1)/2(s-1)}$. For the time interval c, the seed photons belong clearly to the CUTBPL component (see Fig. 3 at ∼10 MeV), whereas for the time intervals d_1 and d_2, E_* is in the flat transition region of the spectrum where the Band and the CUTBPL components overlap (see Fig. 3). In order to quantify the photon index s, we built its distribution using the results of the spectral fits. Specifically, we assumed that the seven parameters of the Band+CUTBPL spectral model follow a multidimensional Gaussian distribution. Using their covariance matrix provided by the spectral fit, we generated 1000 sets of values for these parameters. For each generated spectrum, we computed numerically the photon index at E_*. The index s was chosen as the most probable value of the final distribution and its errors were derived from the 68% confidence interval around this value. The corresponding values of $F(E_*)$ in the table are deduced from the spectral fits presented in Sect. 3.2; the function $\Phi(s)$ is defined by

$$\Phi(s) = \left[2^{1+2s}\mathcal{I}(s)\right]^{\frac{1}{2(1-s)}}, \quad (9)$$

where $\mathcal{I}(s)$ depends on s only and equals (Hascoët et al. 2012)

$$\mathcal{I}(s) = \int_0^1 \frac{y}{(1-y^2)^{2+s}}\, g(s)\,\mathrm{d}s\,, \quad (10)$$

with $g(y) = \frac{3}{16}(1-y^2)\left[(3-y^4)\ln\frac{1+y}{1-y} - 2y(2-y^2)\right]$ coming directly from the dependence of the $\gamma\gamma$ cross section on the energy.

Finally, the constant K appearing in front of Eq. (7) has been calibrated by Hascoët et al. (2012) from a detailed time-dependent calculation of the $\gamma\gamma$ opacity taking into account a realistic geometry for the radiation field, i.e., a time-, space- and direction-dependent photon field in the comoving frame, as expected in an outflow with several emitting zones that are moving relativistically. This calculation, first carried out analytically by Granot et al. (2008) and then extended numerically by Hascoët et al. (2012), is much more realistic than the simple one-zone model that is used, for instance, by Lithwick & Sari (2001). The detailed calculation assumes that the Lorentz factor in the outflow varies between a lowest value Γ_{min} and a highest value $\kappa\Gamma_{min}$. If the contrast is on the order of $\kappa \sim 2$–5, the calibration factor remains in the interval $K \sim 0.4$–0.5. In such a variable outflow, the value of $\Gamma_{\gamma\gamma}$ obtained from Eq. (7) corresponds to the lowest Lorentz factor Γ_{min} in the outflow (Hascoët et al. 2012).

Table 3 provides the resulting Lorentz factor assuming an equal radius for GeV and MeV emissions. If the GeV photons are produced at $R_{GeV} > R_{MeV}$, the Lorentz factor is lower, as can be seen from Eq. (7). The result for each time interval is plotted in Fig. 6 (left panel). For $R_{GeV} = R_{MeV}$ (as suggested by the comparable variability timescales in the LAT and the MeV range, see Sect. 3.3), we find $\Gamma_{min} = \Gamma_{\gamma\gamma} = 233 \pm 18$, 100 ± 8 and 98 ± 9

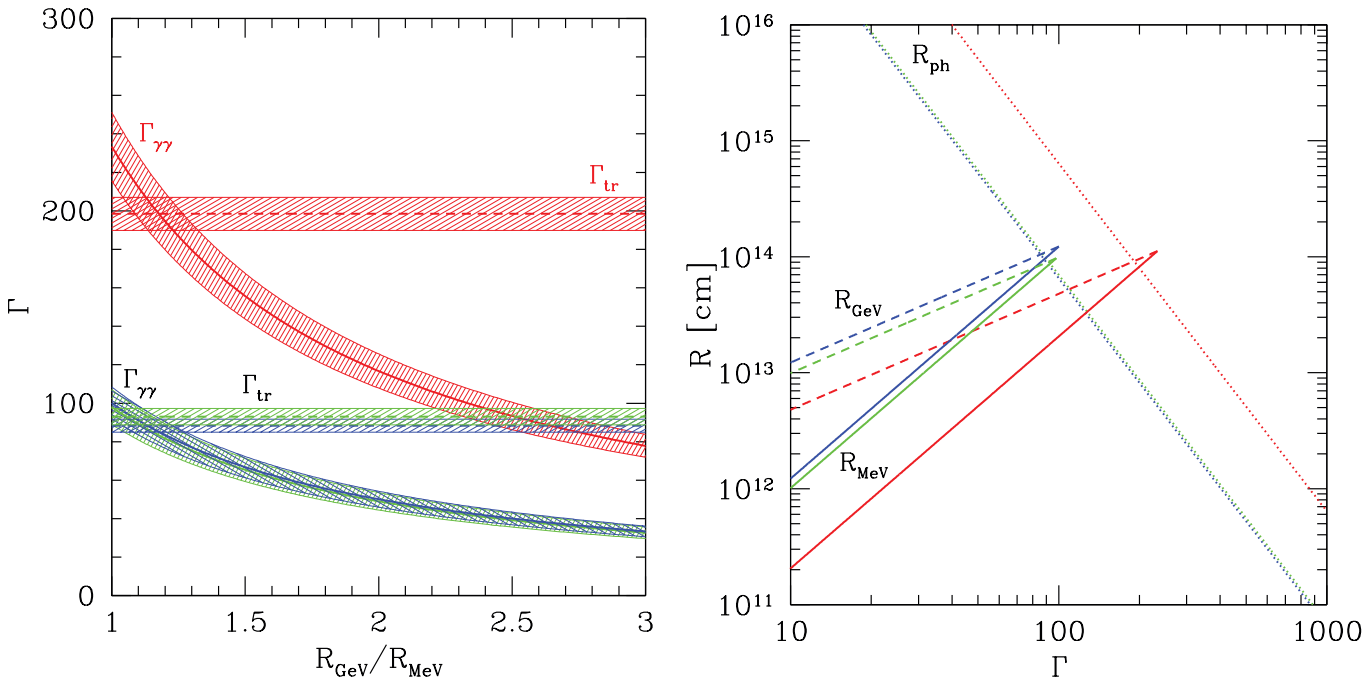

Fig. 6. *Left*: Lorentz factor $\Gamma_{\gamma\gamma}$ for the time intervals c (red), d_1 (blue), and d_2 (green) as a function of the ratio of the emission radii of the GeV and MeV photons, assuming that the high-energy spectral break comes from photon opacity to pair creation (Eq. (7)). The dashed lines represent the lower limit of the Lorentz factor for transparency, $\Gamma_{\rm tr}$ (Eq. (12)). The shaded strips indicate the typical uncertainty on these quantities, obtained by propagating the errors on the measured values listed in Table 3. *Right*: MeV (full lines) and GeV (dashed lines) emission radii as a function of the Lorentz factor. The dotted lines correspond to the photospheric radius $R_{\rm ph}$ in the different time intervals. The deceleration radius is not plotted, but we checked that it is always well above $R_{\rm ph}$, $R_{\rm MeV}$, and $R_{\rm GeV}$ for normal densities in the external medium (assuming either a wind or a uniform medium).

for time intervals c, d_1, and d_2, respectively. In the time interval c, our value is very close to the result of Ackermann et al. (2011), $\Gamma \simeq 220$, obtained from a similar analysis based on the detailed analytical approach developed in Granot et al. (2008). Table 3 also provides the resulting emission radius $R_{\rm MeV}$, which is on the order of 10^{14} cm.

These values for the lowest Lorentz factor in the outflow $\Gamma_{\rm min}$ have to be compared with the lower limits on the Lorentz factor for transparency to Thomson scattering on primary electrons and pair-produced leptons, which corresponds to the assumed condition that the prompt emission is produced above the photosphere. This condition reads $R_{\rm MeV} \geq R_{\rm ph}$, with the photospheric radius given by (Beloborodov 2013)

$$R_{\rm ph} \simeq \frac{\sigma_{\rm T}(1+f\pm)\,\dot{E}}{8\pi c^3 m_{\rm p} \bar{\Gamma}^3 (1+\sigma)}\,, \tag{11}$$

where $\bar{\Gamma}$ is the average Lorentz factor in the flow, which we approximate by $\bar{\Gamma} = \frac{1+\kappa}{2}\Gamma_{\rm min}$, where κ is the contrast defined above; $\sigma_{\rm T}$ is the Thomson cross section; $f\pm$ the ratio of the number of pairs to primary electrons; $\dot{E}$ the total power injected in the flow; and σ its magnetization at large radius, where the prompt emission is produced, so that $\dot{E}/(1+\sigma)$ is the kinetic power. We checked that for the values of the parameters in Table 3 the optical depth for pair creation is less than unity at $R_{\rm MeV}$. Therefore we adopt $f\pm = 0$ in Eqs. (11) and (12). We also assume $\sigma \ll 1$, which is expected for internal shocks. In magnetic reconnection models, if σ is large, $R_{\rm ph}$ is lower and the transparency condition is more easily satisfied. The power $\dot{E}$ is estimated from the gamma-ray luminosity L listed in Table 3 by $\dot{E} = L/\epsilon_{\rm rad}$ assuming a prompt emission efficiency $\epsilon_{\rm rad} = 0.1$. Table 3 provides the photospheric radius $R_{\rm ph}$ using the measurement of the Lorentz factor obtained from the $\gamma\gamma$ constraint. It can be seen that for $R_{\rm GeV} \simeq R_{\rm MeV}$ (as suggested by the comparable variability timescales in the LAT and the MeV range, see Sect. 3.3), the transparency condition is satisfied in all time intervals c, d_1, and d_2. We obtain an emission radius $\sim 10^{14}$ cm and a photospheric radius of a few 10^{13} cm in all time intervals. For $R_{\rm MeV}$ given by Eq. (6), the transparency condition $R_{\rm MeV} \geq R_{\rm ph}$ yields

$$\bar{\Gamma} > \bar{\Gamma}_{\rm tr} \simeq \left[\frac{\sigma_{\rm T}(1+f\pm)\,\dot{E}}{8\pi c^4 m_p\,(1+\sigma)\,t_{\rm v}}\right]^{1/5}. \tag{12}$$

The resulting $\Gamma_{\rm tr}$ is plotted in Fig. 6 (left panel, horizontal dashed lines). It appears clearly that the transparency condition can be fulfilled only if $R_{\rm GeV}/R_{\rm MeV} \leq 1.2$–$1.3$. As already mentioned, the comparable variability timescales at low and high energy indeed suggest that $R_{\rm GeV} \simeq R_{\rm MeV}$. When comparing $R_{\rm MeV}$ and $R_{\rm ph}$, the emission radius deduced from the variability timescale is the typical radius where the emission starts. However, the emission continues at larger radii as variations on larger timescales are also observed in the light curves. We conclude from this analysis that GRB 090926A seems fully compatible with the most standard model where the prompt emission is produced by shocks (or reconnection) above the photosphere.

The right panel of Fig. 6, which shows the photospheric and emission (MeV/GeV) radii as a function of the Lorentz factor, basically contains the same information, presented in a different way. Again, the figure clearly shows that observations in the three time intervals are compatible with an emission above the photosphere, as long as the emission radii of the MeV and GeV photons are close to each other. This is consistent with an internal origin for the high-energy component during the prompt phase suggested by the observed variability. We stress

that this analysis is largely independent of the precise radiative mechanisms. However, as mentioned in Sect. 3.2.1, a natural candidate is fast-cooling synchrotron radiation for the Band component and inverse Compton scatterings for the CUTBPL component. Therefore, we discuss below the possibility that the observed spectral break is due to the natural curvature of the latter component.

4.2.2. Constraints on the Lorentz factor if the high-energy spectral break is a natural break

If the high-energy spectral break reflects the natural curvature of the inverse Compton spectrum – namely it does not correspond to photon opacity to pair creation but simply results from the spectral shape of the radiative process – then only a lower limit on the Lorentz factor can be obtained. It is given, in each time interval, by

$$\Gamma_{\rm inf} = \max(\Gamma_{\gamma\gamma}, \Gamma_{\rm tr}), \quad (13)$$

where $\Gamma_{\gamma\gamma}$ is computed by the same Eq. (7) as above, using the maximum energy $E_{\rm max}$ of the observed photons in the time interval (listed in Table 3) in place of the folding energy $E_{\rm f}$. The resulting lower limit on the Lorentz factor is plotted in Fig. 7. It shows that, as soon as $R_{\rm GeV}/R_{\rm MeV} > 1.3$ in the time interval c (resp. 1.5 and 1.2 in the intervals d_1 and d_2), the transparency limit (Eq. (12)) becomes more constraining than the limit on the pair-creation opacity. However, it has already been mentioned that the variability analysis presented in Sect. 3.3 rather suggests $R_{\rm GeV} \simeq R_{\rm MeV}$. In this case, we find lower limits for the Lorentz factor equal to 257 ± 17, 129 ± 8, and 110 ± 8 in time intervals c, d_1, and d_2.

4.3. Case (ii): prompt emission produced at the photosphere

In the case where the prompt emission is produced at the photosphere, the radius of the MeV emission is $R_{\rm MeV} = R_{\rm ph}$, given by Eq. (11) above. The constraints derived from the observed spectral break become more difficult to obtain. Indeed, contrary to the previous case, increasing the Lorentz factor drives the emitting surface inward, contributing to increasing the optical depth for the GeV photons. However pair creation is now expected below and at the photosphere with values of several tens for $f\pm$ (Beloborodov 2013), which, on the contrary, would contribute to push the photosphere outward. Moreover, since prompt emission at the photosphere corresponds to lower emission radii $R_{\rm MeV}$ than in the optically thin scenario, most of the GeV photons could be produced above the photosphere (e.g., at a few $R_{\rm ph}$) and still show a short variability timescale ($t_{\rm v}$ value of a few $R_{\rm ph}/2c\Gamma^2$). In photospheric models, constraining the Lorentz factor from the high-energy spectral break therefore would require a detailed modeling of the radiative transfer from below to above the photosphere, which is beyond the scope of this paper.

4.4. Discussion

It is widely believed that very bright GRBs should have large Lorentz factors. This assumption is based on the pair creation constraint combined with the *Fermi*/LAT observations of the first bright GRBs (GRBs 080916C, 090510, and 090902B), whose spectrum do not exhibit any attenuation at GeV energies (Abdo et al. 2009b,a; Ackermann et al. 2010). However, later studies (Granot et al. 2008; Hascoët et al. 2012) pointed out that the single-zone model used in these early studies was not accurate enough. Large Lorentz factors are also required in models that assume that the GeV emission is produced at the external shock in order to ensure an early deceleration (Kumar & Barniol Duran 2009; Ghisellini et al. 2010). In the present study of GRB 090926A, we disfavor the external origin scenario because of the observed fast variability of the high-energy emission and find values of the Lorentz factor in the three time intervals reported in Table 3 that are not especially high. From Eq. (7), a lower Lorentz factor and a short variability timescale make the detection of a cutoff due to pair-creation opacity easier since (see, e.g., Dermer et al. 1999)

$$E_{\rm cut} \propto \Gamma^{2(s-1)/(s+1)}\, t_{\rm v}^{-2/(s+1)}, \quad (14)$$

giving $E_{\rm cut} \propto \Gamma^{10}\, t_{\rm v}^4$ and $E_{\rm cut} \propto \Gamma^{5.3}\, t_{\rm v}^{1.7}$ for $s = -1.5$ and -2.2, respectively. This could explain why the cutoff in the time interval c with $t_{\rm v} = 0.1$ s, $\Gamma \sim 230$ and a very large luminosity was the most easily accessible. With a larger Lorentz factor the cutoff would have been shifted to a much higher energy and would have been difficult to characterize. More generally, the very steep dependence of $E_{\rm cut}$ with the Lorentz factor means that, for a given burst, a cutoff can be observed in the LAT range for a very small interval in Γ only. This may explain why bursts like GRB 090926A are not common in the LAT catalog.

As mentioned in Sect. 4.2.1, the Lorentz factor that we find in the time interval c is very close to the value obtained by Ackermann et al. (2011) with the time dependent model of Granot et al. (2008). Another way to estimate the Lorentz factor consists in assuming that the peak flux time in the LAT or visible range is a good proxy for the deceleration time of the relativistic ejecta (see, however, Hascoët et al. 2014). With this method Ackermann et al. (2013a) found $\Gamma \simeq 600$ (resp. 400) for a uniform external medium of density $n = 1$ cm^{-3} (resp. a stellar wind with a parameter $A_* = 0.1$), assuming a deceleration time $t_{\rm dec} \simeq 10$ s and a gamma-ray efficiency $f_\gamma = 0.25$. The obtained result depends on these parameters as

$$\Gamma \propto \begin{cases} (f_\gamma n)^{-1/8}\, t_{\rm dec}^{-3/8} & \text{uniform external medium} \\ (f_\gamma A_*)^{-1/4}\, t_{\rm dec}^{-1/4} & \text{stellar wind,} \end{cases} \quad (15)$$

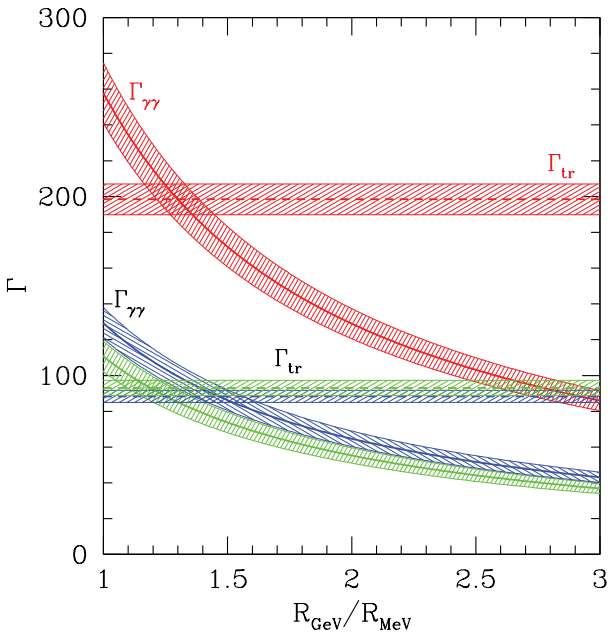

Fig. 7. Same as left panel of Fig. 6, but assuming that the observed cutoff is a natural break. The Lorentz factor $\Gamma_{\gamma\gamma}$ is now a lower limit obtained from the photon of highest energy in each time interval.

which shows that an external medium denser than what was assumed by Ackermann et al. (2013a) (e.g., with $n = 1000$ cm^{-3} or $A_* = 1$) or a deceleration time larger than 10 s could reconcile the two approaches. A value of $t_{\rm dec}$ larger than 10 s is actually very likely, since the peak flux time in the LAT light curve coincides with the spike in time interval c, which probably results from internal dissipation as indicated by its extreme variability.

The evolution of the Lorentz factor from the time interval c to intervals d_1 and d_2 is moderate, showing a decrease by a factor of 2, while the luminosity in the time interval c is 8 times larger and the variability timescale is 5−6 times smaller. The Lorentz factor follows approximately a trend $\Gamma \propto L^{0.3}$ but clearly, with only three time intervals (and two with very similar temporal and spectral parameters) more data will be needed to check whether this expected behavior (see, e.g., Baring 2006) is also found in other bursts and over large parts of their temporal evolution.

5. Conclusions

We presented a new time-resolved analysis of GRB 090926A broadband spectrum during its prompt phase. We combined the *Fermi*/GBM and LAT data in joint spectral fits to characterize the time evolution of its spectrum from keV to GeV energies, using a Band+CUTBPL spectral model in view of discussing our results in terms of keV−MeV synchroton radiation of accelerated electrons and inverse Compton emission at higher energies. In this analysis, we made use of the LAT Pass 8 data publicly released in June 2015, which offer a greater sensitivity than any LAT data selection used in previous studies of this burst. Using a Band+CUTBPL model to account for the broadband spectral energy distribution of GRB 090926A, we confirmed and better constrained the spectral break at the time of the bright spike, which is observed at ∼10 s post-trigger across the whole spectrum. Our analysis revealed that the spectral attenuation persists at later times, with an increase of the break characteristic energy until the end of the prompt phase, from 0.34 GeV (interval c) to 1.43 GeV (interval d_2). We paid careful attention to the systematic effects arising from the uncertainties on the LAT response, and we showed that this time evolution of the spectral break in the high-energy power-law component of GRB 090926A spectrum is solid and well established.

After computing the variability timescales from keV to GeV energies during and after the bright spike, we discussed our results in the framework of prompt emission models. We interpret the high-energy spectral break as caused by photon opacity to pair creation. Requiring that all emissions are produced above the photosphere of GRB 090926A, we computed the bulk Lorentz factor of the outflow, Γ. The latter decreases from 230 during the spike to 100 at the end of the prompt emission, a novel result that improves upon early publications on this burst (Ackermann et al. 2011). Assuming, instead, that the spectral break reflects the natural curvature of the inverse Compton spectrum, lower limits corresponding to larger values for Γ were also derived. Despite the increased photon statistics provided in LAT Pass 8 data, we could not favor any of these possible scenarios. In both scenarios, the extreme temporal variability of GRB 090926A and the Lorentz factors lead to emission radii $R \sim 10^{14}$ cm and to a photospheric radius of a few 10^{13} cm in all time intervals. This strongly suggests an internal origin of both the keV−MeV and GeV prompt emissions associated with internal jet dissipation above the photosphere. This interpretation is reinforced by the flattening of the gamma-ray light curve decay, which occurs well after the end of the keV−MeV prompt emission (Ackermann et al. 2013a), as mentioned in Sect. 1.

In the future, further progress toward the understanding of the GRB GeV emission that coincides with the emergence of an additional power-law component will be possible by using LAT Pass 8 data in broadband analyses of other LAT bright bursts with similar temporal and spectral properties to GRB 090926A, such as the short GRB 090510 (Ackermann et al. 2013a). On the theoretical side, the results obtained in our study and, in general, the complex time evolution of GRB emission spectrum during their prompt phase, also call for the development of detailed broadband physical models to pinpoint which processes dominate during the first instants of the GRB emission and to assess the contribution of internal emission to the GeV spectrum. For instance, our results regarding the photon spectral indices at low energies ($\alpha \sim -0.9$) and at high energies ($\gamma \sim -1.6$) are promising, since they show good agreement with prompt emission models based on fast-cooling electron synchrotron emission with inverse Compton scatterings in the Klein Nishina regime (Bošnjak & Daigne 2014). Dedicated simulations aimed at reproducing GRB 090926A spectral evolution in detail constitute the next step in this direction.

Acknowledgements. The *Fermi* LAT Collaboration acknowledges generous ongoing support from a number of agencies and institutes that have supported both the development and operation of the LAT as well as scientific data analysis. These include the National Aeronautics and Space Administration and the Department of Energy in the United States, the Commissariat à l'Énergie Atomique and the Centre National de la Recherche Scientifique/Institut National de Physique Nucléaire et de Physique des Particules in France, the Agenzia Spaziale Italiana and the Istituto Nazionale di Fisica Nucleare in Italy, the Ministry of Education, Culture, Sports, Science and Technology (MEXT), High Energy Accelerator Research Organization (KEK) and Japan Aerospace Exploration Agency (JAXA) in Japan, and the K. A. Wallenberg Foundation, the Swedish Research Council and the Swedish National Space Board in Sweden. Additional support for science analysis during the operations phase is gratefully acknowledged from the Istituto Nazionale di Astrofisica in Italy and the Centre National d'Études Spatiales in France. The authors would like to thank the Programme National Hautes Énergies for their financial support (PNHE, funded by CNRS/INSU-IN2P3, CEA and CNES, France). They also thank J. Palmerio for his careful reading of the manuscript.

References

Abdo, A. A., Ackermann, M., Ajello, M., et al. 2009a, ApJ, 706, L138
Abdo, A. A., Ackermann, M., Arimoto, M., et al. 2009b, Science, 323, 1688
Ackermann, M., Asano, K., Atwood, W. B., et al. 2010, ApJ, 716, 1178
Ackermann, M., Ajello, M., Asano, K., et al. 2011, ApJ, 729, 114
Ackermann, M., Ajello, M., Asano, K., et al. 2013a, ApJS, 209, 11
Ackermann, M., Ajello, M., Asano, K., et al. 2013b, ApJ, 763, 71
Ackermann, M., Ajello, M., Asano, K., et al. 2014, Science, 343, 42
Ando, S., Nakar, E., & Sari, R. 2008, ApJ, 689, 1150
Atwood, W. B., Abdo, A. A., Ackermann, M., et al. 2009, ApJ, 697, 1071
Band, D., Matteson, J., Ford, L., et al. 1993, ApJ, 413, 281
Baring, M. G. 2006, ApJ, 650, 1004
Baring, M. G., & Harding, A. K. 1997, ApJ, 491, 663
Beloborodov, A. M. 2010, MNRAS, 407, 1033
Beloborodov, A. M. 2013, ApJ, 764, 157
Beloborodov, A. M., Hascoët, R., & Vurm, I. 2014, ApJ, 788, 36
Beniamini, P., & Granot, J. 2016, MNRAS, 459, 3635
Beniamini, P., & Piran, T. 2013, ApJ, 769, 69
Bošnjak, Ž., & Daigne, F. 2014, A&A, 568, A45
Daigne, F., & Mochkovitch, R. 1998, MNRAS, 296, 275
Daigne, F., Bošnjak, Ž., & Dubus, G. 2011, A&A, 526, A110
De Pasquale, M., Schady, P., Kuin, N. P. M., et al. 2010, ApJ, 709, L146
Dermer, C. D., Chiang, J., & Böttcher, M. 1999, ApJ, 513, 656
Eichler, D., & Levinson, A. 2000, ApJ, 529, 146
Ghisellini, G., Ghirlanda, G., Nava, L., & Celotti, A. 2010, MNRAS, 403, 926
Giannios, D. 2012, MNRAS, 422, 3092
Granot, J., Cohen-Tanugi, J., & Silva, E. d. C. e. 2008, ApJ, 677, 92
Hascoët, R., Daigne, F., Mochkovitch, R., & Vennin, V. 2012, MNRAS, 421, 525

Hascoët, R., Beloborodov, A. M., Daigne, F., & Mochkovitch, R. 2014, ApJ, 782, 5
Kobayashi, S., Piran, T., & Sari, R. 1997, ApJ, 490, 92
Krolik, J. H., & Pier, E. A. 1991, ApJ, 373, 277
Kumar, P., & Barniol Duran, R. 2009, MNRAS, 400, L75
Kumar, P., & Barniol Duran, R. 2010, MNRAS, 409, 226
Lemoine, M., Li, Z., & Wang, X.-Y. 2013, MNRAS, 435, 3009
Lithwick, Y., & Sari, R. 2001, ApJ, 555, 540
McKinney, J. C., & Uzdensky, D. A. 2012, MNRAS, 419, 573
Meegan, C., Lichti, G., Bhat, P. N., et al. 2009, ApJ, 702, 791
Narayana Bhat, P., Meegan, C. A., von Kienlin, A., et al. 2016, ApJS, 223, 28
Norris, J. P., Bonnell, J. T., Kazanas, D., et al. 2005, ApJ, 627, 324
Pe'er, A., Mészáros, P., & Rees, M. J. 2005, ApJ, 635, 476
Pe'er, A., Mészáros, P., & Rees, M. J. 2006, ApJ, 642, 995
Piran, T. 2004, Rev. Mod. Phys., 76, 1143
Piran, T., & Nakar, E. 2010, ApJ, 718, L63
Razzaque, S. 2010, ApJ, 724, L109
Rees, M. J., & Meszaros, P. 1994, ApJ, 430, L93
Rees, M. J., & Mészáros, P. 2005, ApJ, 628, 847
Ryde, F., Pe'er, A., Nymark, T., et al. 2011, MNRAS, 415, 3693
Sari, R., Piran, T., & Narayan, R. 1998, ApJ, 497, L17
Vianello, G., Omodei, N., & Fermi/LAT Collaboration. 2015, ArXiv e-prints [arXiv:1502.03122]
Wang, X.-Y., Liu, R.-Y., & Lemoine, M. 2013, ApJ, 771, L33
Zhang, B., & Yan, H. 2011, ApJ, 726, 90
Zhang, B., & Zhang, B. 2014, ApJ, 782, 92

Appendix A: Spectral analysis results

In this section we give more information on the spectral analyses reported in Sect. 3.

Table A.1. Results of the PL fits to LAT data during the $T_{90}^{\rm LAT}$ time interval (from 5.5 s to 225 s post-trigger).

Analysis method	Unbinned ML		Binned ML	
LAT data set	Pass 7	Pass 8	Pass 8	Pass 8
LAT energy range	100 MeV–100 GeV	100 MeV–100 GeV	100 MeV–100 GeV	30 MeV–100 GeV
Number of events	319	464	464	1088
PL amplitude A' ($\times 10^{-4}$ cm^{-2} s^{-1} keV^{-1})	3.8 ± 0.3	8.7 ± 0.4	8.5 ± 0.4	8.1 ± 0.3
PL photon index γ	-2.19 ± 0.07	-2.25 ± 0.06	-2.21 ± 0.06	-2.20 ± 0.03
>100 MeV flux (10^{-5} cm^{-2} s^{-1})	45 ± 3.1	51 ± 2.4	50 ± 2.4	48 ± 1.5

Notes. The pivot energy $E_{\rm piv}$ in Eq. (4) was fixed to 330 MeV for Pass 7 and 240 MeV for Pass 8, close to the decorrelation energies.

Table A.2. Results of the CUTPL fits to LAT data during the time interval *c* (from 9.8 s to 10.5 s post-trigger).

Analysis method	Unbinned ML		Binned ML	
LAT data set	Pass 7	Pass 8	Pass 8	Pass 8
LAT energy range	100 MeV–100 GeV	100 MeV–100 GeV	100 MeV–100 GeV	30 MeV–100 GeV
Number of events	45	65	65	152
CUTPL amplitude A' ($\times 10^{-4}$ cm^{-2} s^{-1} keV^{-1})	3.4 ± 0.9	3.3 ± 0.7	1.0 ± 0.6	3.2 ± 0.6
CUTPL photon index γ	-1.21 ± 0.82	-1.13 ± 0.68	-1.11 ± 0.72	-1.68 ± 0.22
CUTPL folding energy $E_{\rm f}$ (GeV)	$0.23^{+0.30}_{-0.10}$	$0.24^{+0.22}_{-0.09}$	$0.26^{+0.25}_{-0.09}$	$0.41^{+0.27}_{-0.14}$
Break significance N_σ	2.3	2.7	2.5	4.4

Notes. The pivot energy $E_{\rm piv}$ in Eq. (3) was fixed to 500 MeV, close to the decorrelation energy.

Table A.3. Results of the Band+CUTPL fits to GBM+LAT data during the time interval *c* (from 9.8 s to 10.5 s post-trigger).

LAT data set	Pass 7	Pass 8	
LAT energy range	100 MeV–100 GeV	100 MeV–100 GeV	30 MeV–100 GeV
Number of events	45	65	152
Band amplitude A_B ($\times 10^{-2}$ cm^{-2} s^{-1} keV^{-1})	33^{+3}_{-2}	33^{+4}_{-2}	34^{+2}_{-2}
Band $E_{\rm peak}$ (keV)	190^{+10}_{-7}	190^{+9}_{-8}	189^{+8}_{-9}
Band photon index α	$-0.63^{+0.08}_{-0.15}$	$-0.62^{+0.11}_{-0.12}$	$-0.60^{+0.13}_{-0.14}$
Band photon index β	$-3.8^{+0.4}_{-1.1}$	$-3.6^{+0.3}_{-1.1}$	$-3.7^{+0.5}_{-1.6}$
CUTPL amplitude A' ($\times 10^{-4}$ cm^{-2} s^{-1} keV^{-1})	$8.0^{+1.1}_{-1.5}$	$8.4^{+1.1}_{-1.6}$	$8.9^{+0.6}_{-1.4}$
CUTPL photon index γ	$-1.66^{+0.05}_{-0.03}$	$-1.68^{+0.04}_{-0.03}$	$-1.68^{+0.04}_{-0.03}$
CUTPL folding energy $E_{\rm f}$ (GeV)	$0.31^{+0.08}_{-0.06}$	$0.38^{+0.07}_{-0.06}$	$0.37^{+0.06}_{-0.05}$
Break significance N_σ	5.9	6.3	7.7

Notes. The pivot energy $E_{\rm piv}$ in Eq. (3) was fixed to 1 MeV as in Ackermann et al. (2011).

Table A.4. Results of the Band+CUTPL fits to GBM+LAT data during the time interval *d* (from 10.5 s to 21.6 s post-trigger).

LAT data set	Pass 7	Pass 8	
LAT energy range	100 MeV–100 GeV	100 MeV–100 GeV	30 MeV–100 GeV
Number of events	107	154	321
Band amplitude A_B ($\times 10^{-2}$ cm^{-2} s^{-1} keV^{-1})	$9.9^{+0.4}_{-0.6}$	$10.0^{+0.5}_{-0.5}$	$10.1^{+0.4}_{-0.2}$
Band $E_{\rm peak}$ (keV)	183^{+7}_{-7}	182^{+6}_{-6}	180^{+5}_{-6}
Band photon index α	$-0.70^{+0.07}_{-0.08}$	$-0.68^{+0.07}_{-0.08}$	$-0.65^{+0.05}_{-0.04}$
Band photon index β	$-2.9^{+0.1}_{-0.2}$	$-2.9^{+0.1}_{-0.2}$	$-2.9^{+0.1}_{-0.3}$
CUTPL amplitude A' ($\times 10^{-10}$ cm^{-2} s^{-1} keV^{-1})	$4.9^{+0.8}_{-0.6}$	$6.1^{+0.8}_{-0.8}$	$6.4^{+0.2}_{-0.3}$
CUTPL photon index γ	$-1.76^{+0.04}_{-0.03}$	$-1.77^{+0.05}_{-0.01}$	$-1.75^{+0.02}_{-0.03}$
CUTPL folding energy $E_{\rm f}$ (GeV)	$2.02^{+0.80}_{-0.48}$	$1.63^{+0.53}_{-0.35}$	$1.61^{+0.38}_{-0.31}$
Break significance N_σ	4.3	5.6	5.8

Notes. The pivot energy $E_{\rm piv}$ in Eq. (3) was fixed to 1 GeV as in Ackermann et al. (2011).

Table A.5. Results of the Band+CUTBPL fits to GBM+LAT data for time subintervals in *c*.

Time intervals (same statistics)	[9.80–9.98] s	[9.98–10.50] s
Number of events	76	76
CUTBPL folding energy $E_{\rm f}$ (GeV)	$0.40^{+0.10}_{-0.08}$	$0.32^{+0.09}_{-0.06}$
Break significance N_σ	5.0	5.5
Time intervals (rise & decay)	[9.80–9.94] s	[9.94–10.50] s
Number of events	49	103
CUTBPL folding energy $E_{\rm f}$ (GeV)	$0.42^{+0.16}_{-0.10}$	$0.35^{+0.08}_{-0.07}$
Break significance N_σ	3.8	6.3

Table A.6. Results of the Band+CUTBPL fits to GBM+LAT data for time subintervals in *d*.

Time intervals (same statistics)	[10.50–12.90] s	[12.90–21.60] s
Number of events	161	160
CUTBPL folding energy $E_{\rm f}$ (GeV)	$0.55^{+0.13}_{-0.10}$	$1.43^{+0.49}_{-0.25}$
Break significance N_σ	4.3	5.1
Time intervals (rise & decay)	[10.50–11.73] s	[11.73–21.60] s
Number of events	81	240
CUTBPL folding energy $E_{\rm f}$ (GeV)	$0.45^{+0.17}_{-0.10}$	$1.85^{+0.75}_{-0.30}$
Break significance N_σ	5.1	4.4

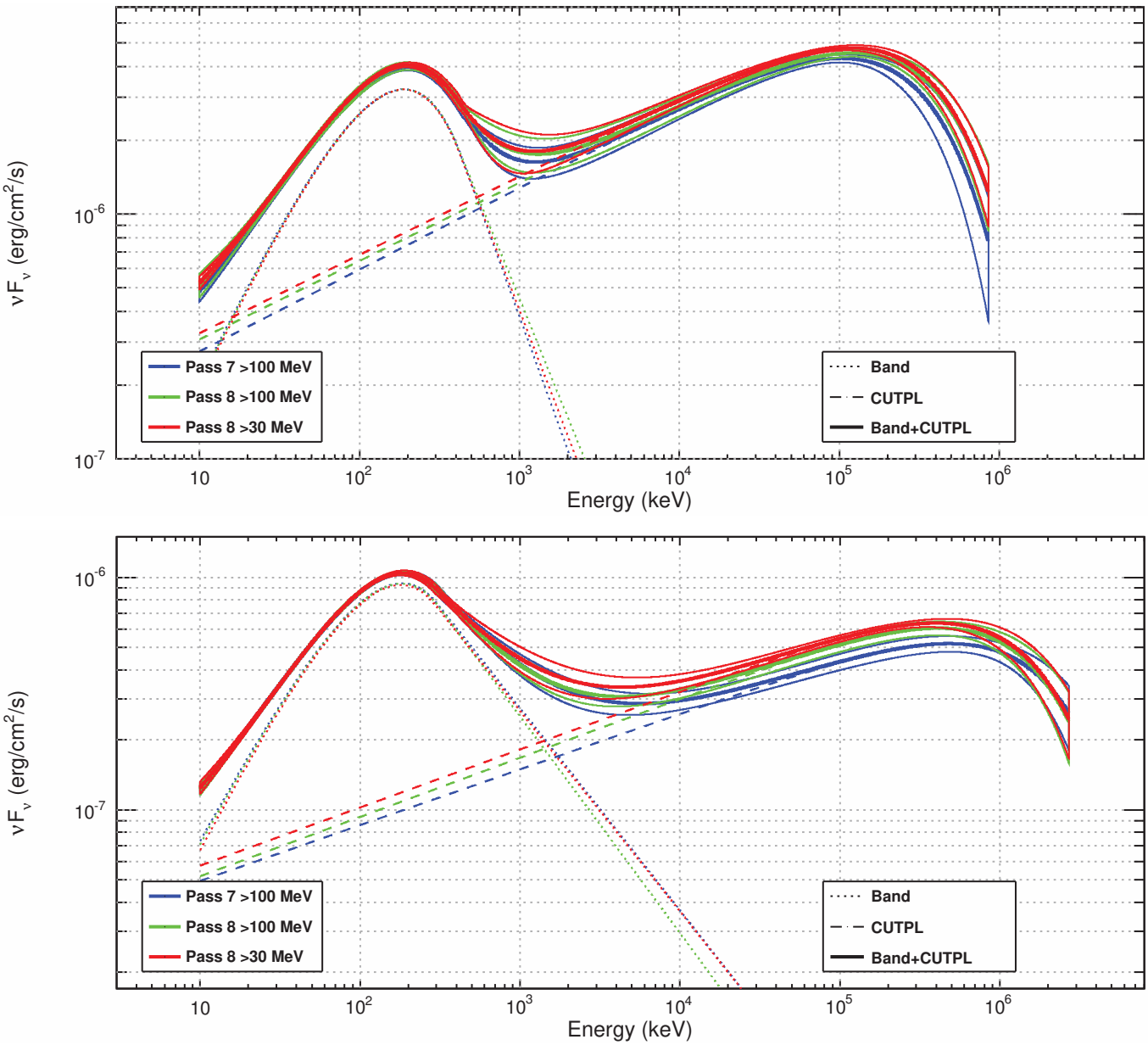

Fig. A.1. GRB 090926A spectral energy distributions as measured by the *Fermi* GBM and LAT in time intervals *c* (*top panel*) and *d* (*bottom panel*), using LAT Pass7 above 100 MeV, and Pass 8 data above 30 MeV and 100 MeV (see Tables A.3 and A.4 for more details). Each solid curve represents the best-fitted spectral shape (Band+CUTBPL), within a 68% confidence level contour derived from the errors on the fit parameters.

CHAPTER 6

Exploration of an internal shock model

Contents

The physical origin of the GRB prompt emission is still a matter of debate, despite great advances in the GRB domain. In this chapter, I present my investigation of the internal shock model in the context of *Fermi*. Although this model suffers from some limitations, it has been explored in detail and often confronted with success to the observations, unlike many other theoretical models for the prompt emission that are available in the literature. In Sect.6.1, I introduce the version of the internal shock model that was developed by my collaborators at the IAP. Then, I characterize the theoretical spectra and simulate them as they would be observed by *Fermi* (Sect.6.2). The analysis of the simulated spectra is presented in Sect.6.3. In Sect.6.4, I introduce a new fitting function in order to compare the model with a large sample of real GRBs. Sect.6.5 presents the study of a sample of 64 GBM GRBs. In Sect.6.6 I apply also the model to the bright GRB 090926A, which was studied in Chap.5. Finally Sect.6.7 summarizes the main results of this chapter.

6.1 The IAP internal shock model

The internal shock (IS) model is one of the most popular models owing to its ability to reproduce many observed properties of the GRB prompt emission. In particular, the extreme variability seen in most of the GRB light curves is a natural consequence of the IS model. In this model, a highly relativistic and collimated outflow converts a fraction of its kinetic energy into internal energy through internal shocks, which occur when the distribution of the Lorentz factor is not uniform in the jet. Part of the energy that is dissipated in the shocks is transferred to a fraction of the electrons, which eventually emit non-thermal radiation.

A version of the IS model has been implemented by F. Daigne, R. Mochkovitch and their collaborators at IAP since 1998, and improved at various occasions. In their model, internal shock waves are produced by multiple collisions between solid layers moving at different velocities in the jet. This discrete numerical approach is able to reproduce most of the GRB properties, in particular the shape of the observed gamma-ray pulses and the variability timescales [Daigne and Mochkovitch, 1998]. This approach has been also validated by the comparison with more realistic hydrodynamical simulations, which are more time consuming [Daigne and Mochkovitch, 2000]. Although the shock microphysics is not fully treated, realistic prescriptions are used to describe the electron acceleration mechanism. The main inputs and parameters of the IAP model are the following:

- the burst duration and its redshift
- the jet kinetic energy, E_k
- the distribution of the jet Lorentz factor

- the fraction of the dissipated energy that is transferred to the magnetic field, ϵ_B
- the fraction of the dissipated energy that is transferred to the electrons, ϵ_e (ϵ_e=ϵ_B=1/3 for an equipartition between the electrons, the magnetic field and the protons)
- the fraction ζ of accelerated electrons
- the spectral index p of the power-law distribution of the accelerated electrons.

The IAP model assumes that the prompt emission of GRBs is produced by shock-accelerated electrons above the photosphere. The numerical code that simulates the shock dynamics has been coupled to a radiative code, which follows the evolution of the electron and photon distributions in order to produce realistic light curves and spectra from keV to GeV energies in the observer frame. The radiative processes include the synchrotron emission from the accelerated electrons and the inverse Compton (IC) scatterings in the Klein-Nishina regime. Synchrotron self-absorption at low energy and photon-photon annihilation at high energy are also accounted for [Bošnjak et al., 2009].

6.2 Simulation of the IAP synthetic burst

As explained in Chap.3, the comparison of theoretical models with observations must be performed after convolution of the models with the instrument responses. Sect.6.2.1 presents the characteristics of the synthetic burst provided by the IAP team. The convolution of this simulated burst with the instrument responses is presented in Sect.6.2.2.

6.2.1 Characteristics of the burst

In the context of this work, I used a synthetic burst provided by the IAP team. This simulation was performed assuming a simple profile of the Lorentz factors along the jet, which produces a unique pulse in the light curve. In order to boost the observed flux, the burst was simulated at a low redshift, z=0.07, and it has an isotropic equivalent kinetic energy $E_k = 10^{54}$ erg. It is a long burst with a duration of 15 s, and it is bright during the first 6 seconds only. It has an isotropic equivalent energy $E_{\gamma,iso}$= 1.35×10^{52} erg with 1.26×10^{52} erg in the synchrotron component and 0.09×10^{52} erg in the IC component.

The intrinsic properties of this burst are described in [Bošnjak and Daigne, 2014]. It corresponds to the case B discussed in this article, with the following parameters: ϵ_B =10^{-3} (i.e., a low magnetic field to enhance the IC flux), ϵ_e=1/3, a varying ζ parameter, and an electron spectral index p=2.7. The output of this simulation is

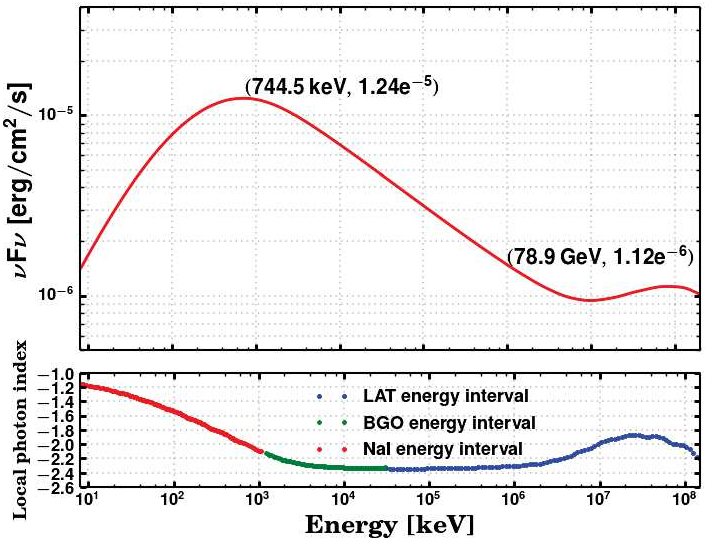

Figure 6.1: *Spectral energy distribution of the synthetic burst (top panel) and its local photon index with respect to the energy (bottom panel).*

a file containing the flux at different energies and times. Fig.6.1 shows the spectral energy distribution of the synthetic burst during 15 s, in the top panel, and the evolution with energy of the local photon index Γ, in the bottom panel. I calculated the local photon index numerically as the derivative of the photon differential spectrum F=dN/dE with respect to the energy, $\Gamma = \partial \ln(F)/\partial \ln(E)$.

Based on the output file of the simulation, I calculated the fluence of the synthetic burst, which is 5.4×10^{-4} erg cm^{-2}in the energy range [10 keV - 1 MeV] during the first 6 s. From the fluence distribution of the bursts detected by the GBM and the LAT until 2013 (Fig.1.16, left), it can be seen that this synthetic burst would be a very rare event. In order to consider more realistic situations, I created two other bursts by dividing the initial flux of the synthetic burst by 10 and 100. In the following, the three synthetic bursts ($\times1$, $\times0.1$, $\times0.01$) will be denoted GRB_B001, GRB_B010 and GRB_B100. The light curve of each of these bursts is split in three time intervals [0 s, 1 s], [1 s, 3 s] and [3 s, 6 s]. The corresponding SFDs and local photon indices are shown in Fig.6.2. This figure shows a temporal evolution of the spectral shape. It is, therefore, interesting to study the synthetic burst in a detailed time-resolved analysis in order to understand its spectral properties.

6.2.2 Simulation procedure

Following Eq.3.5, the mean numbers of counts in the GBM and LAT that are expected from the synthetic GRBs can be obtained from the convolution of the GRB

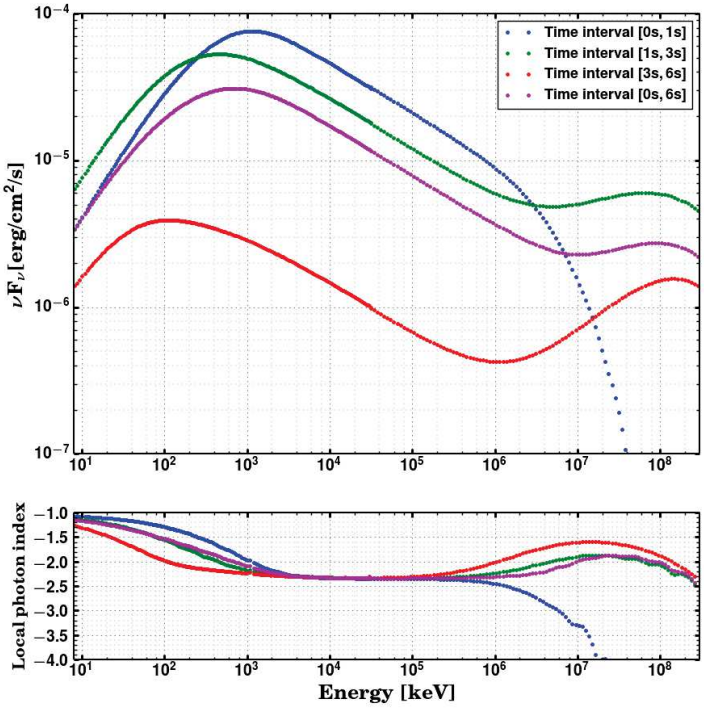

Figure 6.2: *Specral energy distributions and their local photon index distributions in the four time intervals [0 s, 1 s], [1 s, 3 s], [3 s, 6 s] and [0 s, 6 s].*

differential spectra with the detector response matrices (DRM). In this numerical calculation, I used the DRMs of the four GBM detectors (N6, N7, N8, B1) that have seen GRB 090926A (see Sect.5.3.1), and the DRM of the LAT produced by ***gtrspgen*** (see Sect.3.4.3) for the same burst. The mean count light curves and count spectra are shown in Fig.6.3.

Then, I used the *XSPEC* software to create realizations of the three bursts as they would be observed by the *Fermi* instruments. The input spectrum of each synthetic burst was defined by the *atable* option of the *XSPEC model* command, and the Poisson counts were generated with the *fakeit* command. The fit results for such fluent bursts should not be affected by the background contribution, therefore, this simulation was performed without any background.

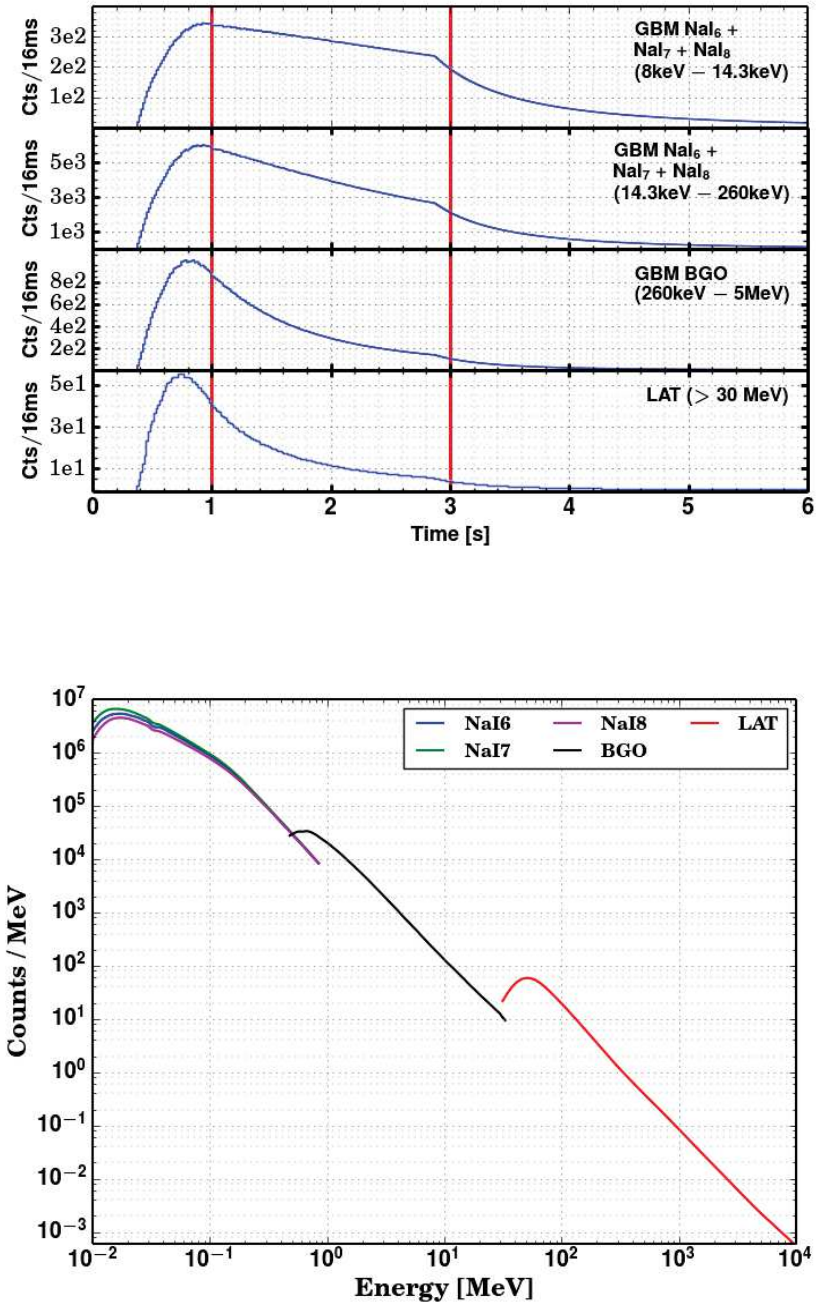

Figure 6.3: ***Top:*** *Multi-detector light curve of the synthetic burst: summed counts in two energy ranges of GBM/NaI detectors (first 2 panels), in the GBM/BGO energy range (third panel) and using the largest LAT energy range (bottom panel). The red solid lines show the boundaries of the three time intervals [0 s, 1 s], [1 s, 3 s] and [3 s, 6 s].* ***Bottom:*** *Count spectrum of the synthetic burst.*

6.3 Spectral analyses of the simulated bursts

6.3.1 Spectral models

To fit the spectrum of the synthetic burst provided by the IS model, I considered some of the spectral models that are commonly used to fit GRB spectra, and I also created my own parametric model. I estimated the ability of these models to reproduce the simulated spectra, looking also at the energy dependence of their local photon index for a more accurate comparison.

The `Band` function (Eq.1.2) is often used to fit the keV-MeV spectrum of GRBs The local photon index of this function reads:

$$\Gamma_{\texttt{Band}}(E) = \begin{cases} \alpha - \frac{(2+\alpha)}{E_p}E, & E \leq E_p \frac{\alpha-\beta}{2+\alpha} \\ \beta, & E > E_p \frac{\alpha-\beta}{2+\alpha} \end{cases} \tag{6.1}$$

where α, β and E_p are the parameters defined in Eq.1.2.

The smoothly broken power law model (SBPL) is suggested by [Gruber et al., 2014] to fit the GRB spectra, however, using a large sample of GBM GRBs, they showed that the SBPL is the best fit model for only 6.6% of this sample. For this reason, this model is not used in this study.

The simpler the model used to fit a spectrum, the better the constraints on the parameters. With one parameter less than the `Band` function, the log-parabola model (`logpar` hereafter) was suggested by [Massaro et al., 2010] to fit the spectra of GRBs. This model is expressed as:

$$\frac{dN_{log}}{dE} = A_{log}\left(\frac{E}{E_0}\right)^{-\gamma-\beta\log(E/E0))} \tag{6.2}$$

where A_{log} is the amplitude parameter in $\mathrm{keV}^{-1}\,\mathrm{cm}^{-2}\,\mathrm{s}^{-1}$and E_0 is a fixed reference energy. The local photon index is a function of the spectral parameters γ and β:

$$\Gamma_{log}(E) = -\gamma - 2\beta\log\left(\frac{E}{E_0}\right) \tag{6.3}$$

and the peak energy E_p of the `logpar` function reads:

$$E_p = E_0 \times 10^{\frac{2-\gamma}{2\beta}} \tag{6.4}$$

The `logpar` function has a continuous curvature unlike the `Band` function, especially around the peak energy. Its main drawback lies in its symmetric shape. Since most of the photons are detected at low energies because of the steepness of the GRB spectra, this symmetry implies that the spectral parameters are essentially

constrained by the low-energy data. In order to gain some latitude at high energies, I modified the function to freeze the local photon index above a break energy E_b. The new function, `modiflog`, has 4 parameters:

$$\frac{dN_{modif}}{dE} = A_{modif} \begin{cases} \left(\frac{E}{E_0}\right)^{-\gamma-\beta\,\log(E/E_0)}, & E \leq E_b \\ \left(\frac{E_b}{E_0}\right)^{-\gamma-\beta\,\log(E_b/E_0)} \times \left(\frac{E}{E_b}\right)^{-\gamma-2\,\beta\,\log(E_b/E_0)}, & E > E_b \end{cases} \tag{6.5}$$

As can be seen from this equation, the spectral index above E_b is equal to -γ - $2\,\beta\log(E_b/E_0)$. Finally, I introduced the symmetric modification at low energies, which make the spectral fit around the peak energy less dependent on the low-energy data. The new function, `doublemodif`, has 5 parameters:

$$\frac{dN_{double}}{dE} = A_{double} \begin{cases} \left(\frac{E'_b}{E_0}\right)^{-\gamma-\beta\,\log(E'_b/E_0)} \times \left(\frac{E}{E'_b}\right)^{-\gamma-2\,\beta\,\log(E'_b/E_0)}, & E \leq E'_b \\ \left(\frac{E}{E_0}\right)^{-\gamma-\beta\,\log(E/E_0)}, & E'_b \leq E \leq E_b \\ \left(\frac{E_b}{E_0}\right)^{-\gamma-\beta\,\log(E_b/E_0)} \times \left(\frac{E}{E_b}\right)^{-\gamma-2\,\beta\,\log(E_b/E_0)}, & E > E_b \end{cases} \tag{6.6}$$

6.3.2 Spectral analyses

The four functions defined in the previous section were used to fit the spectra of the synthetic bursts in the four time intervals [0 s, 1 s], [1 s, 3 s], [3 s, 6 s] and [0 s, 6 s]. This work was performed in the GBM energy range [8 keV - 40 MeV]. The reference energy E_0 in Eqs.6.2, 6.5 and 6.6 is fixed to 500 keV. Most of the figures presented in this chapter correspond to the analysis in the time interval [1 s - 3 s] for each of the three bursts. The fit results for the other time intervals are reported in summary tables and their figures are presented in App.C.1. Fig.6.4 shows the spectral fits of the GRB_B010 burst in the time interval [1 s - 3 s] with the four aforementioned functions. The top left panel of this figure shows clearly that the local photon index is not reproduced by the `Band` function fit, in particular around the peak energy and above.

By definition, the local photon index of the `logpar` function decreases linearly with the logarithm of the energy. For this reason, this function can not reproduce the spectrum of the synthetic bursts, especially at low and high energies. The modifications applied to this function yield better fits, especially at high energy with the `modiflog` function and at low energy with the `doublemodif` function. However, the last two models do not well reproduce the spectrum either. As a result, none of the studied functions is able to represent the IS model spectra.

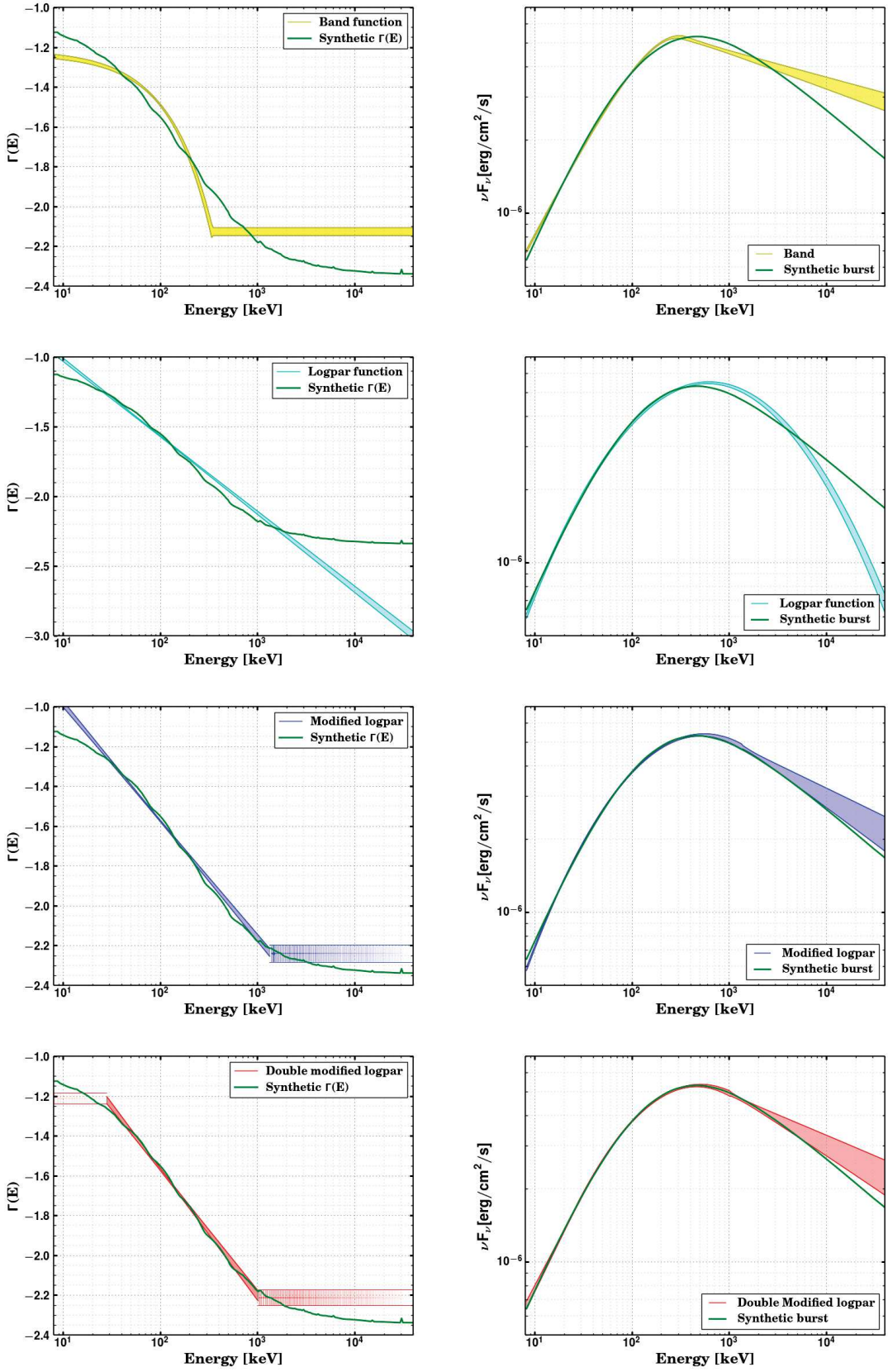

Figure 6.4: *Local photon index (left) and SED (right) of the* GRB_B010 *burst in the time interval [1 s, 3 s], from a fit with the* `Band`, `logpar`, `modiflog` *and* `doublemodif` *functions (from top to bottom).*

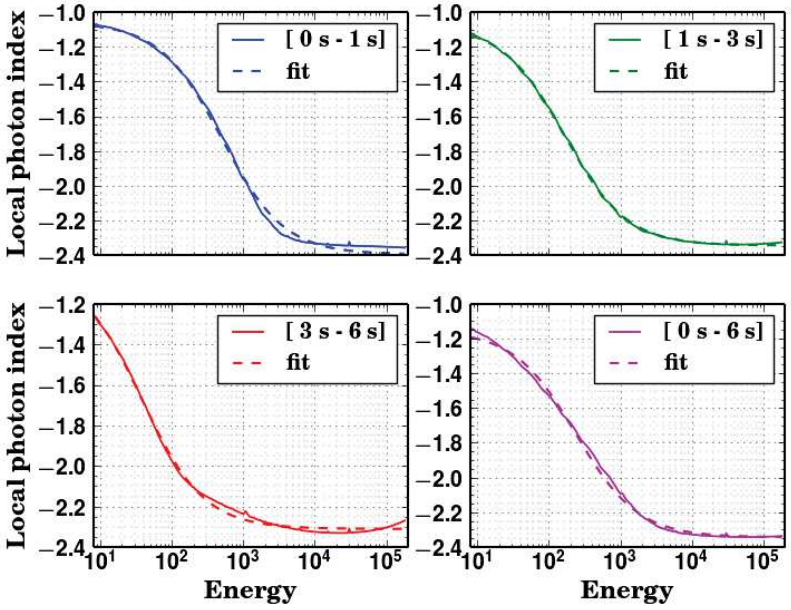

Figure 6.5: *Fit of Eq.6.7 to the local photon index in the MeV range for the four time intervals of the* GRB_B001 *synthetic burst.*

6.4 A new fitting function for GRB spectra

6.4.1 Parameterization of the MeV spectrum

In order to build a function that is representative of the IAP model spectra, I fitted their local photon index as a function of energy with the following parameterization:

$$\Gamma_{MeV}(E) = -a + \frac{b}{(E + X_0)} = \frac{\partial \ln(F_{MeV})}{\partial \ln(E)} \tag{6.7}$$

where a, b, X_0 are the parameters of this ad-hoc function and F_{MeV} is the photon flux spectrum to be determined. The Γ_{MeV} function fits adequately the local photon index in the four time intervals as shown in Fig.6.5. Integrating Eq.6.7, one gets:

$$F_{MeV}(E) = F(E_r) \exp\left(-a \ln\left[\frac{E}{E_r}\right]\right) \exp\left(\frac{b}{X_0} \ln\left[\frac{E}{E_r}\frac{(X_0 + E_r)}{(X_0 + E)}\right]\right) \tag{6.8}$$

with a reference energy E_r (see more details in App.C.1). To give a physical meaning of this integrated function, I defined the parameters α and β as the asymptotic indices. When E $\to$ 0, $F_{MeV}(E)$ becomes proportional to $E^{\frac{b}{X_0}-a}$, and $F_{MeV}(E) \propto E^{-a}$ when E $\to +\infty$. Therefore, I defined the asymptotic spectral slopes $\alpha = \frac{b}{X_0} - a$ and $\beta = -a$.

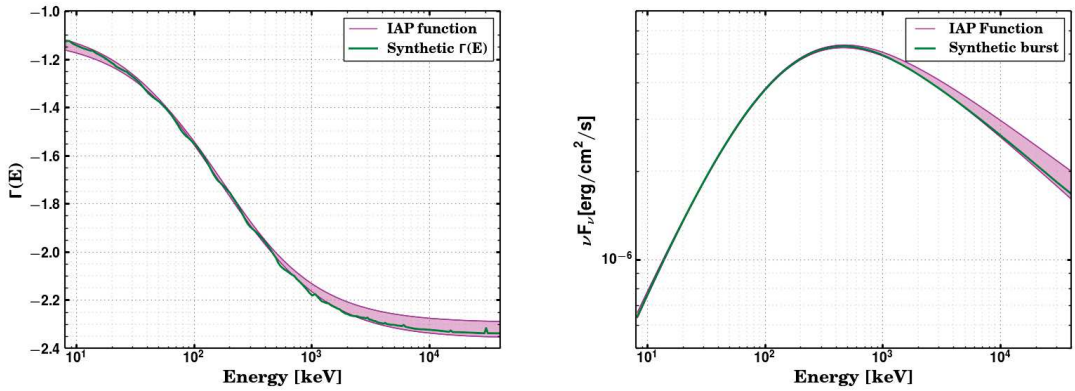

Figure 6.6: *Local photon index (left) and SED (right) of the* GRB_B010 *burst from a fit with the* `IAP` *function in the time interval [1 s, 3 s].*

The peak energy E_p is defined as the solution of $\partial \ln E^2F(E)/\partial(E/E_r) = 0$. At the end, I built a new function, called `IAP` hereafter, with four parameters α, β, E_p, the amplitude A_{IAP} and a fixed parameter E_r:

$$\boxed{\frac{dN_{IAP}}{dE} = A_{IAP}\left(\frac{E}{E_r}\right)^{\alpha} \times \left[\frac{E - E_p(2+\beta)/(2+\alpha)}{E_r - E_p(2+\beta)/(2+\alpha)}\right]^{\beta-\alpha}} \tag{6.9}$$

The local photon index of the `IAP` function reads:

$$\Gamma_{IAP}(E) = \alpha + (\beta - \alpha)\frac{E}{E - E\left(\frac{2+\beta}{2+\alpha}\right)} \tag{6.10}$$

I applied this new spectral function to the three synthetic spectra in the four time intervals. It is worth to mention that the value of the reference energy E_r in Eq.6.9 can change only the amplitude of the SED, therefore, it is only a scale factor and is not expected to affect the analysis results. This parameter was fixed in the four time intervals to the expected peak energy of the synthetic spectra: E_r= 1150, 478, 114 and 745 keV for the time intervals [0 s, 1 s], [1 s, 3 s], [3 s, 6 s] and [0 s, 6 s], respectively. Fig.6.6 shows the local photon index and the SED of the GRB_B010 burst from a fit with the `IAP` function in the time interval [1 s, 3s]. This figure shows that the `IAP` function reproduces perfectly the synthetic spectrum in this interval.

The analyses results of the three bursts GRB_B001, GRB_B010 and GRB_B100 in the four time intervals are presented in Tab.6.1. Figs.6.7, 6.8 and 6.9 show the results in the time interval [1 s - 3 s]. The bottom panels of these figures show the ratio of the difference between the local photon index of each of the five fitted functions (noted as "fit") and the true index of the synthetic spectrum (noted as "model") over

		C-stat value			
Class	**Time intervals**	**0 s, 1 s**	**1 s, 3 s**	**3 s, 6 s**	**0 s, 6 s**
GRB_B001	`Band`	602.5	906.4	485.5	1403.2
	`logpar`	767.7	676.8	614.9	630.6
	`modiflog`	767.7	568.9	614.9	589.0
	`doublemodif`	526.1	540.0	2370.2	**570.1**
	`IAP`	**486.0**	**498.3**	**451.6**	638.2
GRB_B010	`Band`	457.6	538.6	447.1	577.7
	`logpar`	469.7	558.5	454.9	469.3
	`modiflog`	469.7	533.9	454.9	468.8
	`doublemodif`	**438.6**	525.2	455.3	**466.4**
	`IAP`	441.2	**522.9**	**442.5**	483.6
GRB_B100	`Band`	464.8	446.4	359.3	461.4
	`logpar`	464.4	445.0	363.9	446.7
	`modiflog`	464.4	445.0	363.9	446.7
	`doublemodif`	462.3	441.9	376.4	446.8
	`IAP`	462.5	443.5	359.9	448.5

Table 6.1: *C-stat values of the spectral fits of the three synthetic bursts from top to bottom. The spectral fits of each burst were performed with the functions studied in this section:* `Band`*,* `logpar`*,* `modiflog`*,*`doublemodif` *and* `IAP`*. The C-stat minimum value is reported in blue for the first two bursts. For the third burst, all functions yield similar C-stat values.*

the "fit" error that is obtained from the fit results by the error propagation method. In order to compare the fit quality of the different functions, I define the quotient:

$$Q = \frac{\sum_{i=0}^{n} \left(\frac{fit_i - model_i}{error_i} \right)^2}{n - n_{par}} \tag{6.11}$$

where the index i runs over all energy channels, and n_{par} is the number of parameters of the fitted function. Q is an approximate reduced χ^2, and its value is displayed in the bottom panel of Figs.6.7, 6.8 and 6.9. These figures show that the `IAP` function has the lowest Q value with respect to the other four functions. The large flux of GRB_B001 resulted in small uncertainties on the fitted parameters, and in larger Q values than for the other two synthetic bursts (Fig.6.7). These figures also show that the `logpar` function yields the largest Q value for the three bursts. In particular, it does not reproduce the spectra at low and high energies, as expected. The `modiflog` and `doublemodif` functions yield better fits, but their parameters are not constrained for the three bursts in all the time intervals. For the case of GRB_B100 shown in Fig.6.9, the `modiflog` function behaved as a `logpar` function, with a break energy above the analyzed energy range.

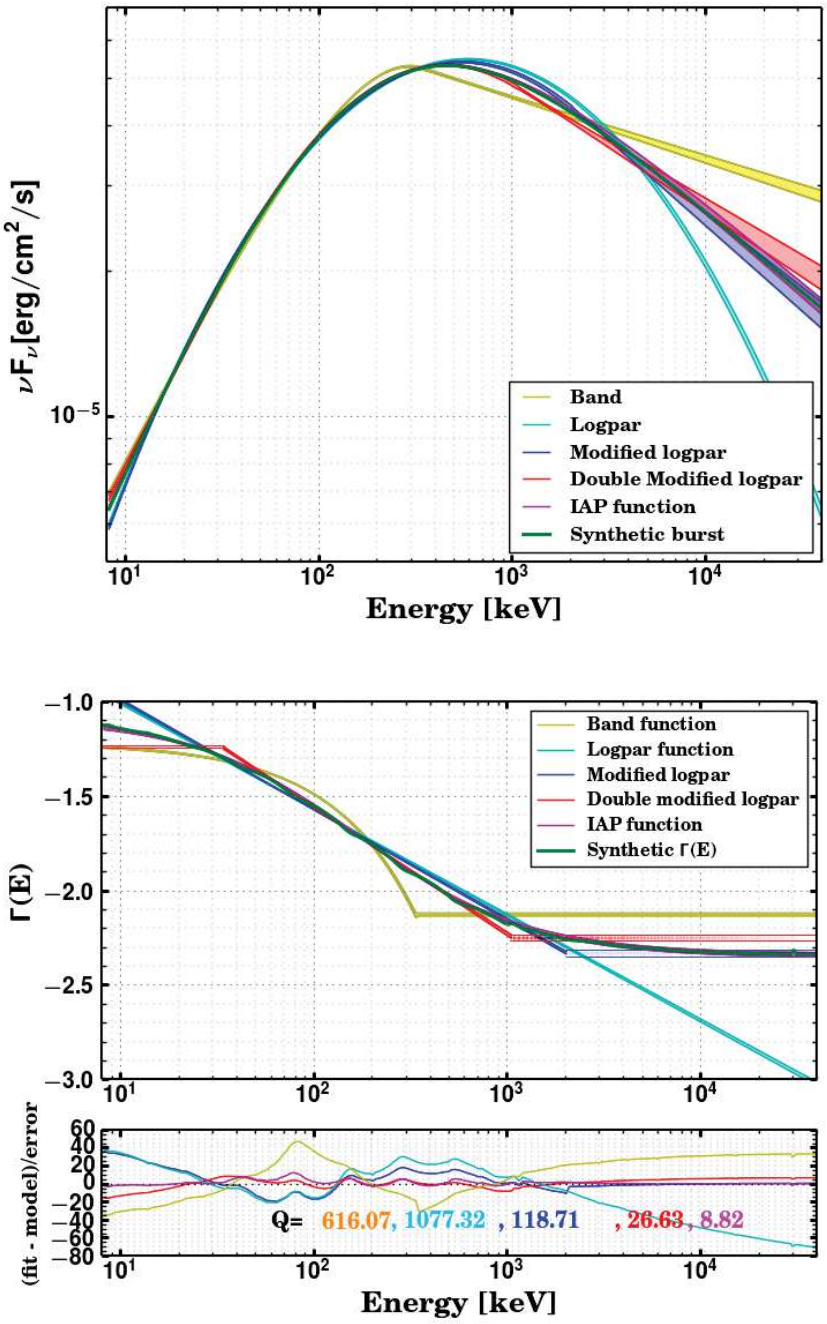

Figure 6.7: ***Top:*** *SEDs of the* GRB_B001 *burst in the time interval [1 s, 3 s], from a fit with five spectral functions.* ***Bottom:*** *Local photon index as function of the photon energy. The quotient Q is a* χ^2*-like (see Sect.6.4.1 for details).*

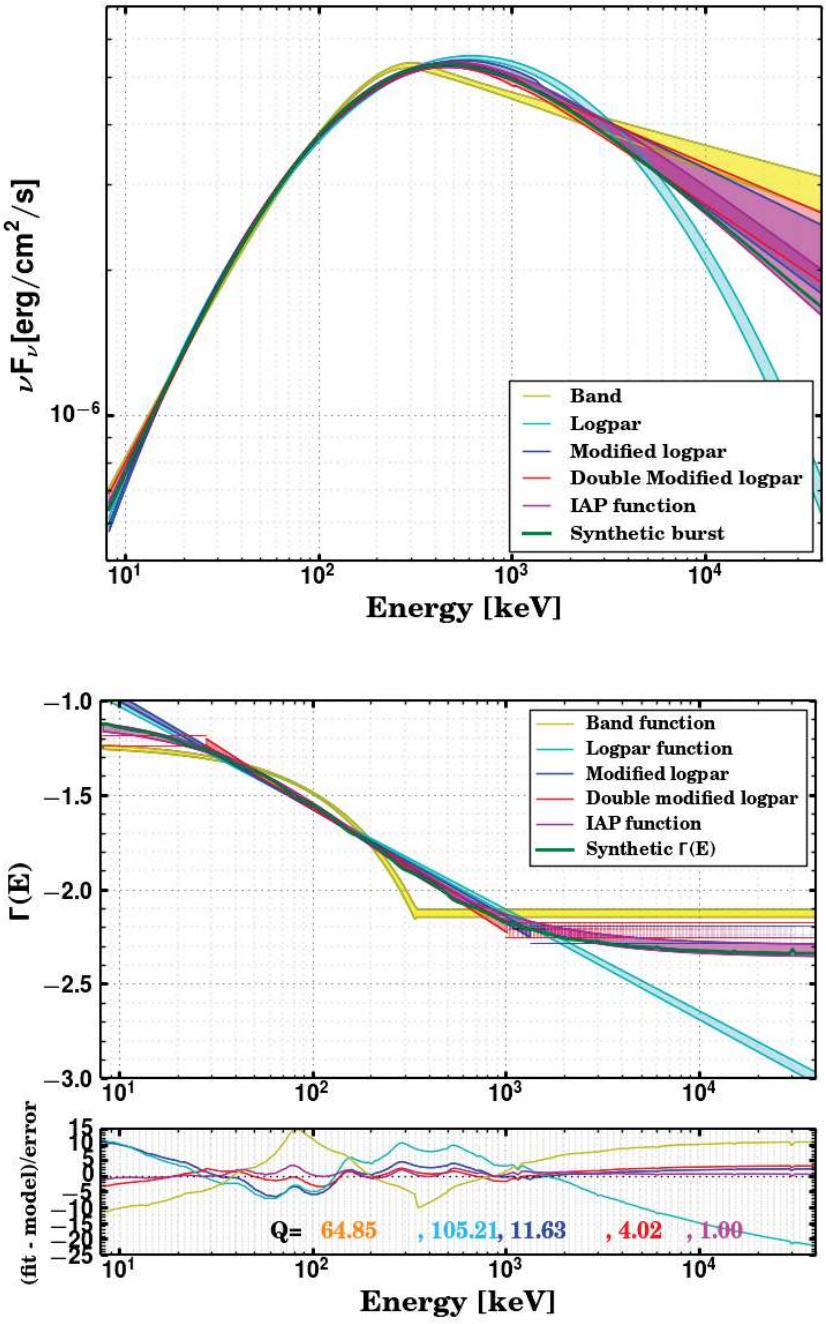

Figure 6.8: ***Top:*** *SEDs of the* GRB_B010 *burst in the time interval [1 s, 3 s], from a fit with five spectral functions.* ***Bottom:*** *Local photon index as function of the photon energy. The quotient Q is a* χ^2*-like.*

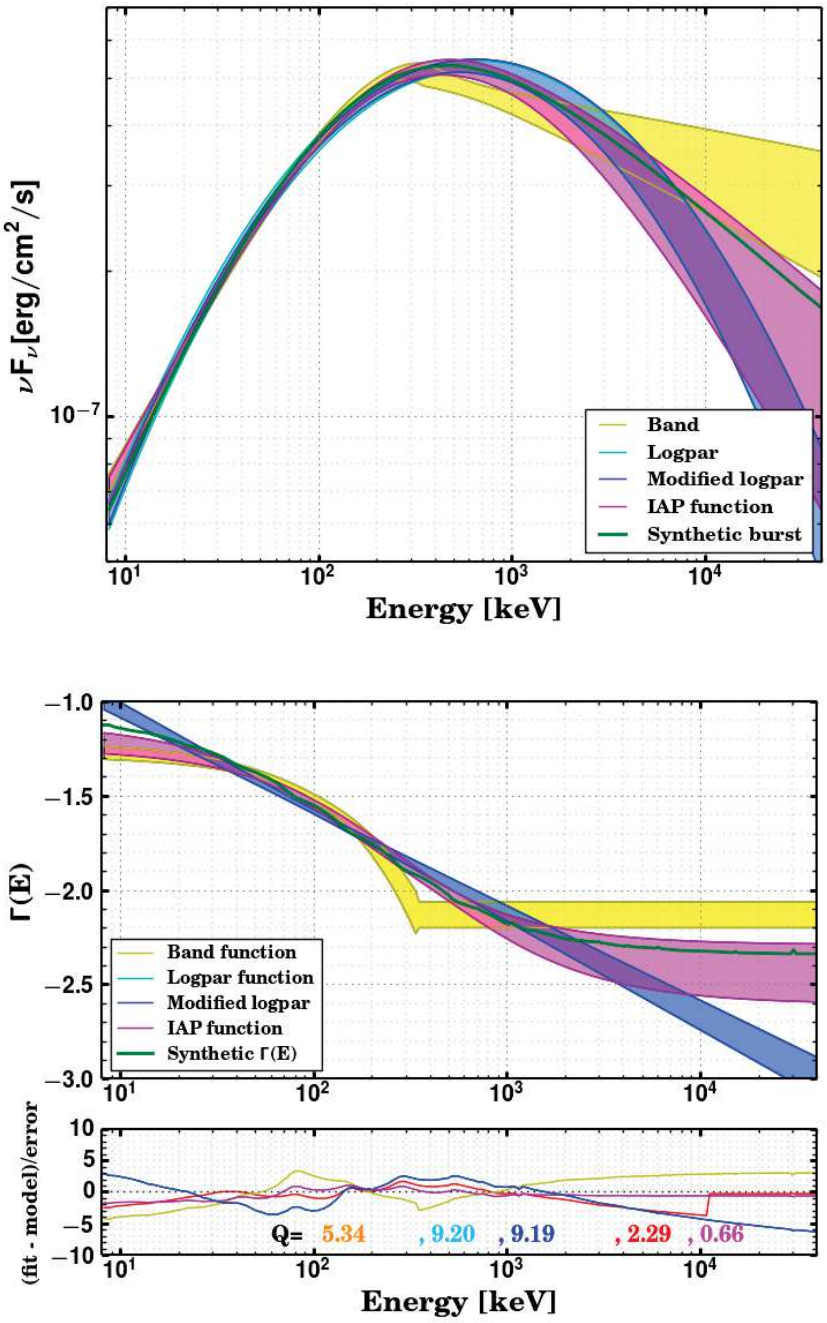

Figure 6.9: ***Top:*** *SEDs of the* GRB_B100 *burst in the time interval [1 s, 3 s], from a fit with five spectral functions.* ***Bottom:*** *Local photon index as function of the photon energy. The quotient Q is a* χ^2*-like. The* `modiflog` *model overlaps the* `logpar` *model. The parameters of the doublemodif model are badly constrained (with large uncertainties), therefore the model is not shown on the figure.*

Time interval	model	E_p	α	β	Amplitude
[0 s, 1 s]	Band	761.3 ± 13.9	-1.141 ± 0.004	-2.163 ± 0.014	1.9621 ± 0.0102
	IAP	1215.7 ± 25.3	-1.071 ± 0.007	-2.445 ± 0.024	0.0364 ± 0.0003
[1 s, 3 s]	Band	294.9 ± 3.4	-1.221 ± 0.004	-2.128 ± 0.006	3.1003 ± 0.0186
	IAP	458.7 ± 5.5	-1.085 ± 0.008	-2.346 ± 0.011	0.1450 ± 0.0005
[3 s, 6 s]	Band	99.1 ± 2.9	-1.373 ± 0.016	-2.157 ± 0.010	0.4766 ± 0.0151
	IAP	118.5 ± 2.9	-0.948 ± 0.076	-2.290 ± 0.017	0.1915 ± 0.0010
[0 s, 6 s]	Band	377.5 ± 4.0	-1.270 ± 0.003	-2.088 ± 0.005	1.4650 ± 0.0061
	IAP	658.9 ± 8.9	-1.163 ± 0.006	-2.277 ± 0.009	0.0342 ± 0.0001

Table 6.2: *Results of the* `Band` *and* `IAP` *fits for* GRB_B001 *in the four time intervals. The reference energy E_r in Eq.6.9 has been fixed to the true peak energy in each time interval: E_p= 1150, 478.38, 113.5 and 744.5 keV for the time intervals [0 s, 1 s], [1 s, 3 s], [3 s, 6 s] and [0 s, 6 s] respectively.*

According to Tab.6.1, the `IAP` function has the lowest C-stat values in most of the time intervals of GRB_B001 and GRB_B010. For the faint GRB_B100, the five functions gave comparable C-stat values. This means that the five functions provide equivalent fits of faint bursts. Therefore, distinguishing between the different functions requires bright or very bright GRB fluences.

6.4.2 Comparison of the `IAP` and `Band` functions

The results of the previous section show that the `IAP` function gives the best fits, as expected from a spectral model that has been built directly from the synthetic spectra. This function, therefore can be considered as representative of the IAP IS model. Interestingly, this function has the same number of parameters as the `Band` function. It is thus important to compare it with the `Band` function which is the most used function to fit the prompt MeV spectra.

Time interval	model	E_p	α	β	Amplitude
[0 s, 1 s]	Band	677.4 ± 39.7	-1.13 ± 0.01	-2.11 ± 0.04	0.20084 ± 0.00366
	IAP	1178.0 ± 81.6	-1.06 ± 0.02	-2.41 ± 0.07	0.00351 ± 0.00008
[1 s, 3 s]	Band	298.0 ± 11.0	-1.23 ± 0.01	-2.13 ± 0.02	0.30773 ± 0.00578
	IAP	469.9 ± 18.4	-1.08 ± 0.03	-2.33 ± 0.03	0.01448 ± 0.00016
[3 s, 6 s]	Band	104.0 ± 11.1	-1.44 ± 0.05	-2.13 ± 0.03	0.04237 ± 0.00409
	IAP	127.4 ± 11.1	-1.02 ± 0.27	-2.23 ± 0.05	0.01873 ± 0.00032
[0 s, 6 s]	Band	377.0 ± 13.1	-1.27 ± 0.01	-2.07 ± 0.02	0.14558 ± 0.00195
	IAP	684.7 ± 32.1	-1.16 ± 0.02	-2.26 ± 0.03	0.00342 ± 0.00003

Table 6.3: *Same as Tab.6.2 for* GRB_B010.

Time interval	model	E_p	α	β	Amplitude
[0 s, 1 s]	Band	708.5 ± 134.8	-1.09 ± 0.05	-2.07 ± 0.12	0.01927 ± 0.00113
	IAP	1333.3 ± 323.5	-1.03 ± 0.08	-2.40 ± 0.24	0.00037 ± 0.00003
[1 s, 3 s]	Band	297.35 ± 36.5	-1.25 ± 0.04	-2.13 ± 0.07	0.03006 ± 0.00182
	IAP	457.2 ± 49.8	-1.18 ± 0.07	-2.45 ± 0.16	0.00144 ± 0.00005
[3 s, 6 s]	Band	55.4 ± 16.5	-0.90 ± 0.38	-2.00 ± 0.06	0.01362 ± 0.01206
	IAP	129.8 ± 34.2	-2.e-11 ± 3.24	-2.18 ± 0.13	0.00194 ± 0.00011
[0 s, 6 s]	Band	444.5 ± 49.6	-1.31 ± 0.03	-2.13 ± 0.07	0.01373 ± 0.00051
	IAP	677.8 ± 77.7	-1.24 ± 0.04	-2.38 ± 0.12	0.00035 ± 0.00001

Table 6.4: *Same as Tab.6.2 for* GRB_B100.

In Fig.6.10, I present the IAP and the Band functions using the same set of parameters. The top panel of this figure shows the spectra of the two models using different values of α, while fixing the other three parameters of both models at the same values. The bottom panel shows the two models using different E_p values. It can be seen that the IAP function is wider than the Band function in both cases. However, no conclusion can be drawn at this stage since both functions would have different parameters when fitted to the same data, as was seen in the previous sections. In particular, the greater smoothness of the IAP function (that can be seen, e.g., on the red curves in the top panel of Fig.6.10) implies that the asymptotic slopes α and β are reached less rapidly.

Tabs.6.2, 6.3, and 6.4 show the parameters of the Band and IAP fits to GRB_B001, GRB_B010 and GRB_B100, respectively. The asymptotic slopes α and β of the Band function are different from those of the IAP function. Specifically, α is harder and β is softer for the IAP function, as expected from the results presented in Figs.6.4 and 6.6. In addition, the peak energies are much better reproduced with the IAP function, and the Band function fit excludes the true Epeak value at more than 5 standard deviations.

A recent work of [Yu et al., 2015] shows that the spectrum that is expected in the electron synchrotron model is wider than the Band fits of most GRBs detected by the GBM. These authors conclude that other radiation processes are required to explain the GRB prompt emission. However, the synchrotron spectrum used in [Yu et al., 2015] was simply derived from a Maxwellian electron distribution, and did not account for the jet dynamics and for the evolution of the electron and photon distributions. For instance, we saw in Sect.5.4.4 that the IC losses of the electrons in the Klein-Nishina regime increase the observed spectral index at low energies and can make the spectrum narrow. Besides, [Yu et al., 2015] discuss the difference between the Band fits and the expectation from their synchrotron model without fitting this model to the data as well. The comparison might thus be uncertain, or biased by

instrumental effects. It is therefore interesting to revisit their conclusions and to confront the more complete model developed by the IAP team to the observations. I will present such an analysis further in this chapter. In the rest of this section, I compare the spectral sharpness of the `IAP` function, which is based on a physical model, with that of the phenomenological `Band` function.

To compare the width of both functions, I followed [Yu et al., 2015] who proposed a method to calculate the sharpness of the fit spectra. I calculated the spectral sharpness from the triangle that is defined by the vertices at $E_p/10$, E_p and $3E_p$. In order to compute accurately the sharpness angle and its errors, I performed Monte-Carlo simulations using the fit parameters and their covariance matrix, and assuming a multi-dimensional Gaussian distribution of the parameters. This process was repeated 1000 times for each time interval for each of the synthetic bursts GRB_B010 and GRB_B001. The sharpness angle was computed as the Maximum Probability Value (MPV) of the final angle distribution obtained from the 1000 spectra. The errors on the angle were calculated from the 68% confidence interval around the MPV value.

I checked that this method is safe and accurate. This was done by examining whether the 1000 created spectra are included within the error contours of the initial fit at a defined confidence level. Fig.6.11 shows the distribution of 1000 spectra in the time interval [1 s, 3 s] with the `IAP` and the `Band` functions. For the four time intervals, I found that almost all the randomly generated spectra are included within the 3σ error contours of both fits. In Fig.6.12 I show an example of the output of this simulation with the `IAP` function. The left panel of this figure shows the sharpness angle distribution that was built from the 1000 spectra. The right panel of this figure shows the Cumulative Distribution Function (CDF), which was used to derive 68% error interval around the MPV. The results of this analysis are reported in Tab.6.5 for the two bursts and shown in Figs.6.13 and 6.14 in the four time intervals of the GRB_B001 synthetic burst. These results confirm that the `IAP` function perfectly fits the synthetic spectra, and yields measured E_p and sharpness angles that are very close to their true values. On the contrary, the `Band` function is not suitable to fit the synthetic spectra, and it underestimates systematically their width, with sharpness angles that are always slightly smaller.

As a conclusion, the `IAP` function proposed in this section reproduces the shape and the parameters of the MeV spectra of the synthetic burst. To represent the whole spectrum of the synthetic burst, a parameterization at GeV energies is now required, as presented in the next section.

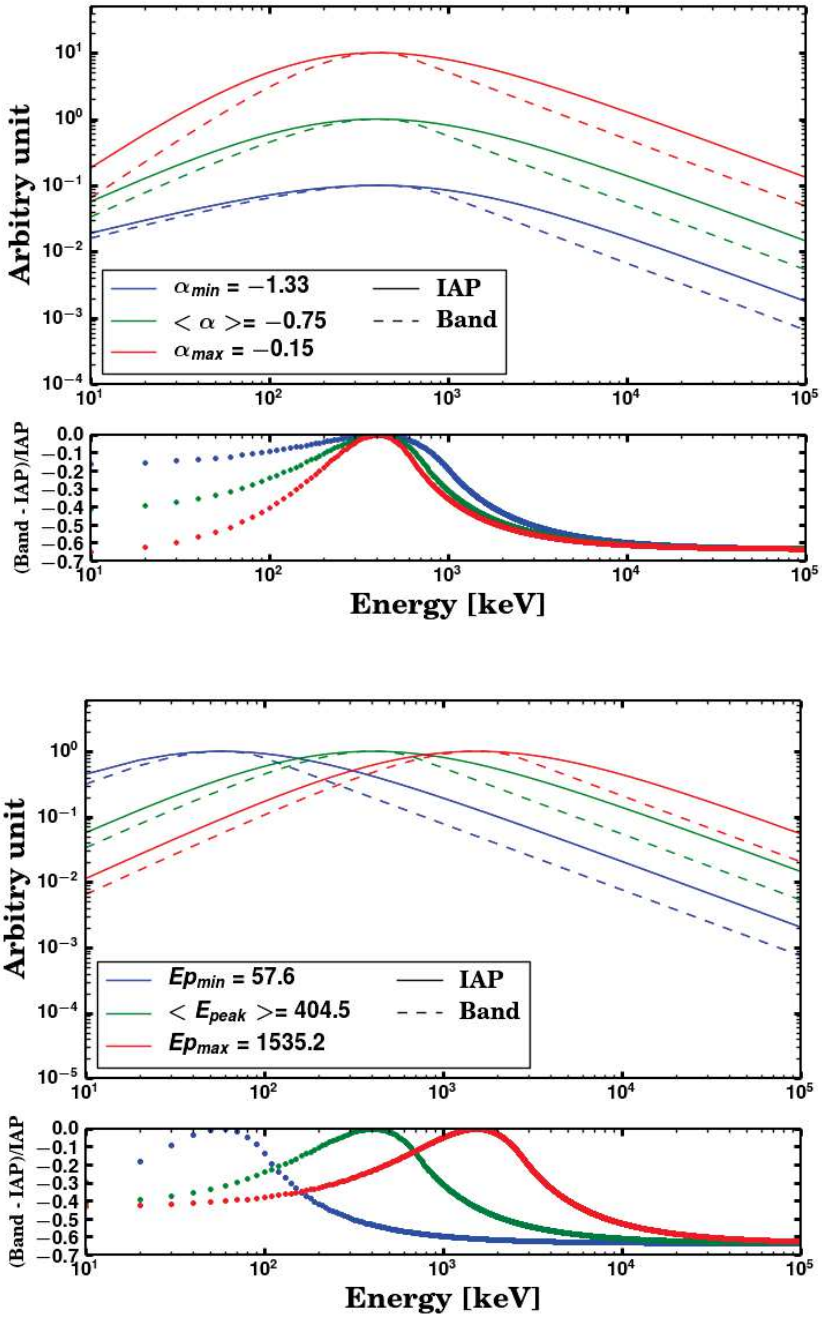

Figure 6.10: *Comparison of the* `IAP` *function with the* `Band` *function using the same set of parameters* α *and* E_p.

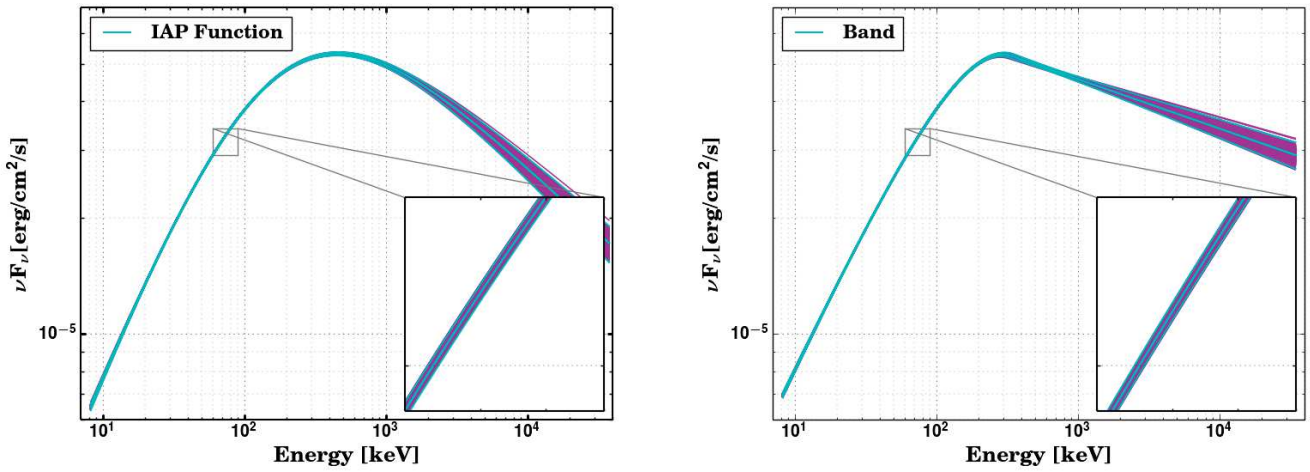

Figure 6.11: *SEDs of the 1000 simulated spectra (magenta lines) compared with the 3σ error contours (cyan lines) of the* `IAP` *fit (left) and* `Band` *fit (right).*

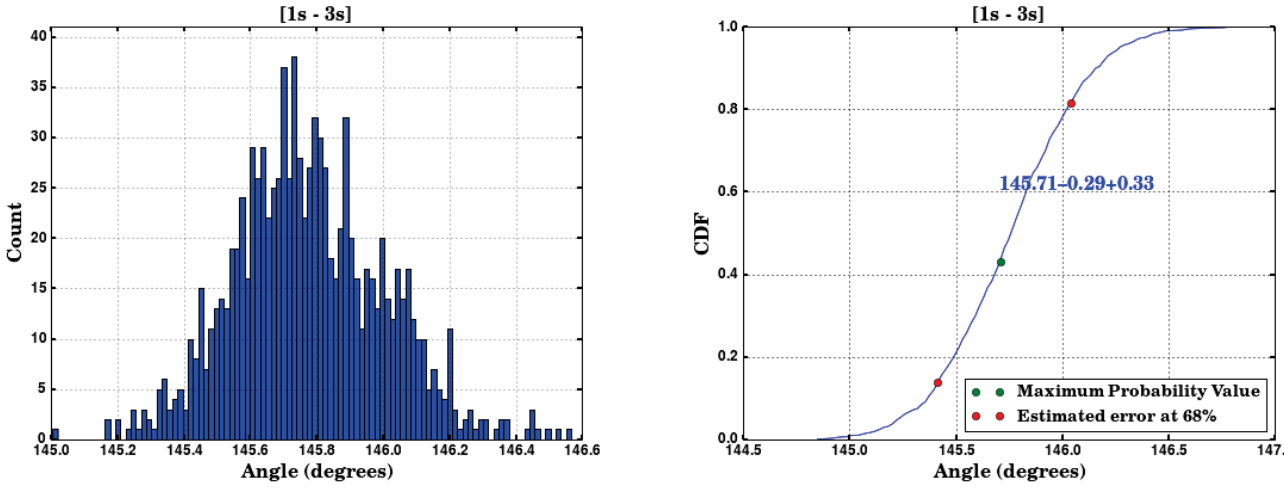

Figure 6.12: ***Left:*** *Angle distribution obtained from 1000 simulated spectra using the* `IAP` *function fit.* ***Right:*** *Cumulative distribution (CDF) with the MPV represented as a green point and the 68% errors as red points.*

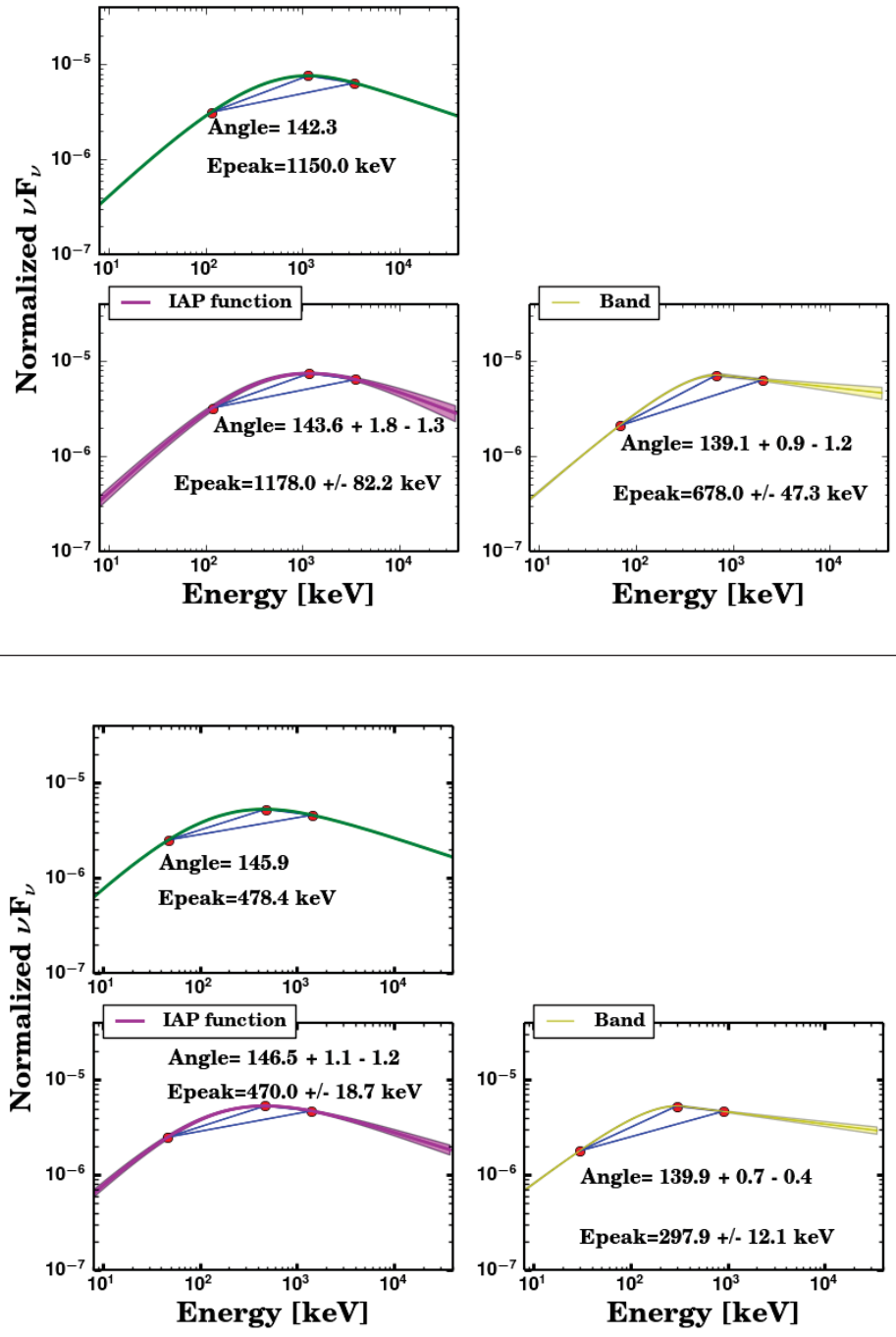

Figure 6.13: *SEDs of* GRB_B010 *for the time interval [0 s, 1 s] (top panel) and [1 s, 3 s] (bottom panel). Each panel contains three SEDs, one for the synthetic spectrum and the others obtained from the fits of the* `IAP` *(bottom left) and* `Band` *(bottom right) functions.*

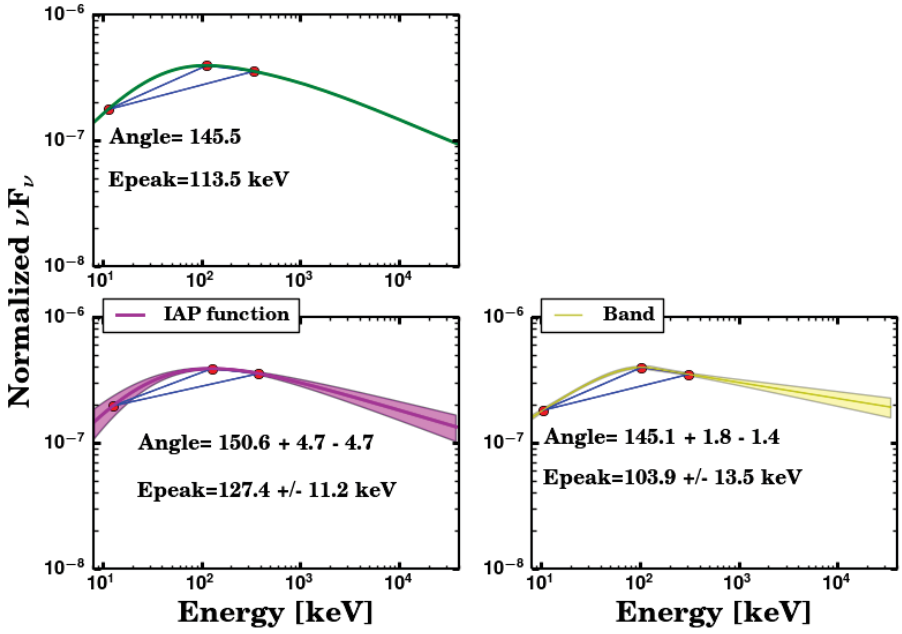

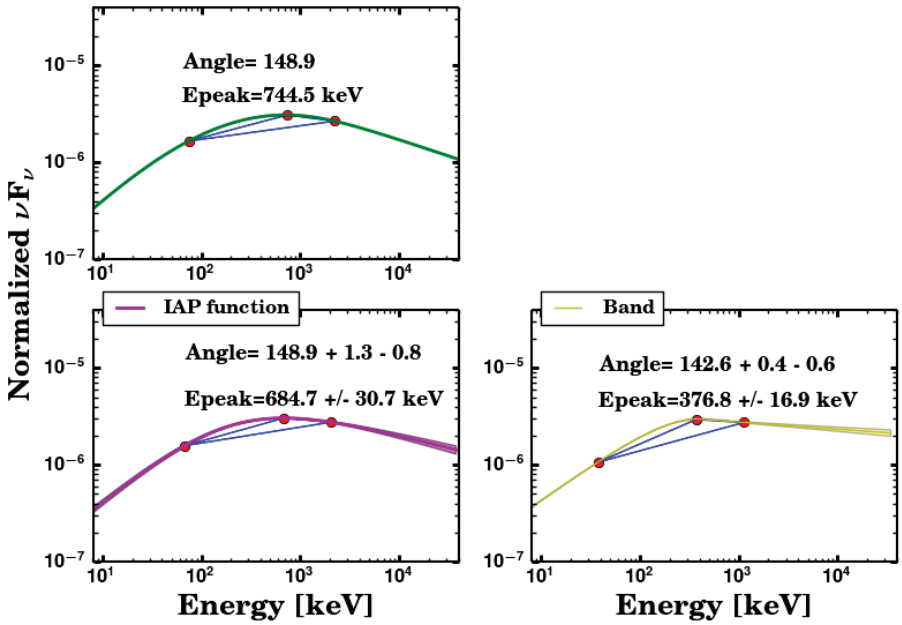

Figure 6.14: *SEDs of* GRB_B010 *for the time interval [3 s, 6 s] (top panel) and [0 s, 6 s] (bottom panel). Each panel contains three SEDs, one for the synthetic spectrum and the others obtained from the fits of the* `IAP` *(bottom left) and* `Band` *(bottom right) functions.*

		Angle			
Class	**Time intervals**	**0 s, 1 s**	**1 s, 3 s**	**3 s, 6 s**	**0 s, 6 s**
	Synthetic	142.3	145.9	145.5	148.9
	`Band`	$137.7^{+0.4}_{-0.2}$	$140.0^{+0.2}_{-0.1}$	$142.7^{+0.6}_{-0.3}$	$142.0^{+0.2}_{-0.1}$
GRB_B001	`IAP`	$143.5^{+0.5}_{-0.5}$	$145.7^{+0.3}_{-0.3}$	$145.8^{+1.3}_{-1.0}$	$148.6^{+0.4}_{-0.3}$
	Synthetic	142.3	145.9	145.5	148.9
	`Band`	$139.1^{+0.9}_{-1.2}$	$139.9^{+0.7}_{-0.4}$	$145.1^{+1.8}_{-1.4}$	$142.6^{+0.4}_{-0.6}$
GRB_B010	`IAP`	$143.6^{+1.8}_{-1.3}$	$146.5^{+1.1}_{-1.2}$	$150.6^{+4.7}_{-4.7}$	$148.9^{+1.3}_{-0.8}$

Table 6.5: *Sharpness angle of the* `Band` *and* `IAP` *spectra for the two bursts* GRB_B001 *and* GRB_B010.

6.4.3 Parameterization of the GeV spectrum

Using the same methodology as before, I started from the local index to build a function that describes the synthetic spectra at high energy. It can be seen from Fig.6.2 that the IC component is more pronounced in the two time intervals [1 s, 3 s] and [3 s, 6 s], with a peak energy at ∼100 GeV. To study the spectra in the high-energy range, I fitted the local photon index in these two time intervals above 100 GeV in order to avoid a possible excess of the MeV spectral component. I used the following function to fit the local photon index:

$$\Gamma_{GeV}(E) = \lambda - (\delta + 1) \times \left(\frac{E}{E_s}\right)^{\delta+1} = \frac{\partial \ln(F_{GeV})}{\partial \ln(E)} \tag{6.12}$$

As can be seen in Fig.6.15, this function fits the local photon index quite well, with λ=-1.82 ± 0.01 (resp. -1.53 ± 0.01), δ=-0.10 ± 0.07 (resp. -0.12 ± 0.03) and E_s = (3.8 ± 0.2)10^2 GeV (resp. (2.9 ± 0.1)10^2 GeV) for the time interval [1 s - 3 s] (resp.[3 s - 6 s]). Since the values of δ are much smaller than 1, I simplified the function by setting this parameter to 0. The integration of the new function simply gives a power law with an exponential cutoff of the form:

$$F_{GeV}(E) = A_{GeV} \left(\frac{E}{E_f}\right)^{\lambda} \exp\left(-\frac{E}{E_s}\right) \tag{6.13}$$

which is the same as the CUTPL model presented in Eq.3.12.

6.4.4 Broadband spectral analysis

As mentioned above, the IC component of the synthetic spectra peaks at ∼100 GeV, which is far above the GRB break energies that have been observed with the LAT. In the future, new synthetic spectra are required to simulate other situations, e.g. the high-energy break observed by the LAT in the spectrum of GRB 090926A (see Chap.5). For the time being, I multiplied the LAT effective detection area by 100 to increase the number of counts at high energy and to illustrate the performance

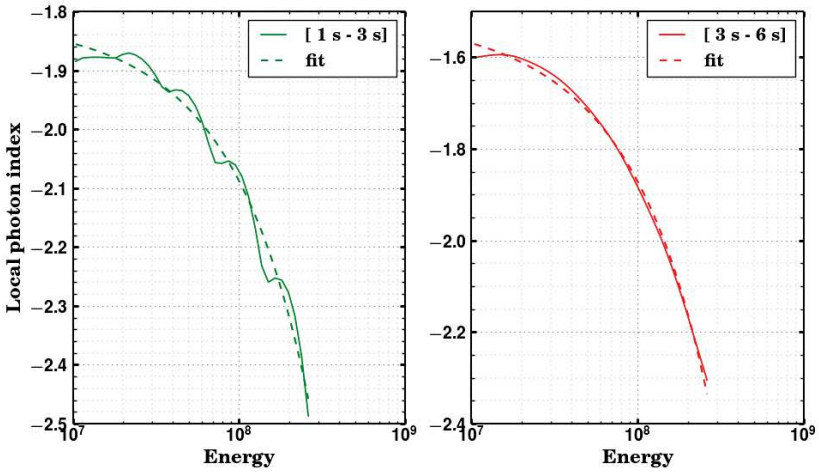

Figure 6.15: *Fit of the local photon index in the time intervals [1 s, 3 s] and [3 s, 6 s] above 10 GeV, using Eq.6.13.*

of the spectral parameterization found in the previous sections.

The broadband spectral analyses were performed for the two time intervals [1 s - 3 s] and [3 s- 6s]. In each time interval, I simulated GBM and LAT data for the synthetic burst with the full flux (GRB_B001). I used the `IAP` + CUTPL spectral model, with a reference energy E_0 of the CUTPL fixed at 10 GeV. Fig.6.16 shows the very good quality of the fits. This result shows that the `IAP` + CUTPL model can be used to fit the whole keV/MeV-GeV spectrum of the simulated burst. Hence, it is worth applying this complete model to real data. In the following sections, the `IAP` MeV function is applied to GBM GRBs, while the whole model is applied to the keV-GeV spectrum of GRB 090926A.

6.5 Application to GBM bursts

6.5.1 GRB sample and data selection

According to my simulation results, a large number of counts is required to compare the fit quality of the different spectral models. For this reason, I selected only the GBM GRBs detected up to 2016 whose energy fluences are larger than 10^{-5} erg cm^{-2}(i.e. comparable to those of the GRB_B001 and GRB_B010 synthetic bursts). I excluded the bursts that have additional components (BB, PL, cutoff) at low or high energies. These bursts are listed in Tab.6.7. I excluded as well the bursts which have the PL model as the best fit model in the GBM spectral

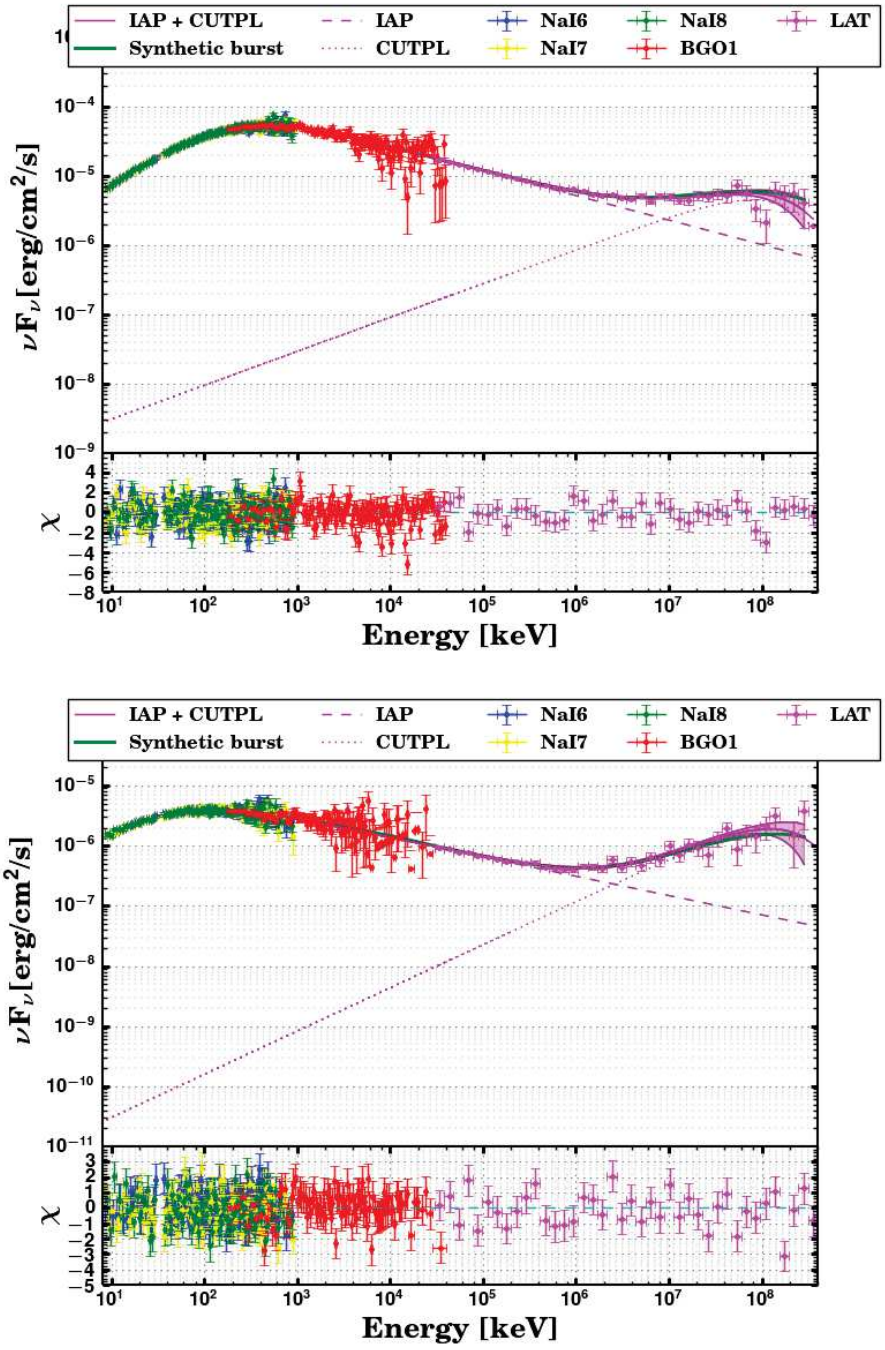

Figure 6.16: *Fits of the keV-GeV spectrum of the synthetic burst* GRB_B001 *in the time intervals [1 s - 3 s] (top) and [3 s - 6 s] (bottom). The points in color that are superimposed to the SED error contours are indicative only, since they were obtained from an approximate correction of the count spectra based on the instrument responses.*

Time interval	**[1 s, 3 s]**	**[3 s, 6 s]**
IAP		
E_p (keV)	457.66 ± 4.06	119.17 ± 2.88
α	-1.09 ± 0.01	-1.03 ± 0.05
β	-2.354 ± 0.003	-2.321 ± 0.004
$\mathbf{A}_{MeV}$ ($\mathbf{keV^{-1}\,cm^{-2}\,s^{-1}}$)	0.145 ± 0.001	0.193 ± 0.001
CUTPL		
λ	-1.51 ± 0.06	-1.28 ± 0.07
Folding energy $\mathbf{E}_f$ ($\times$ $\mathbf{10^2}$ GeV)	1.65 ± 0.71	1.72 ± 0.91
$\mathbf{A}_{GeV}$ ($\mathbf{keV^{-1}\,cm^{-2}\,s^{-1}}$)	$(167.4 \pm 11.5)\times10^{-13}$	$(39.03 \pm 3.53)\times10^{-13}$
C-stat/dof	532.61/510	501.58/510

Table 6.6: *Results of the IAP+CUTPL fits to the burst* GRB_B001 *during the time intervals [1 s - 3 s] and [3 s - 6 s].*

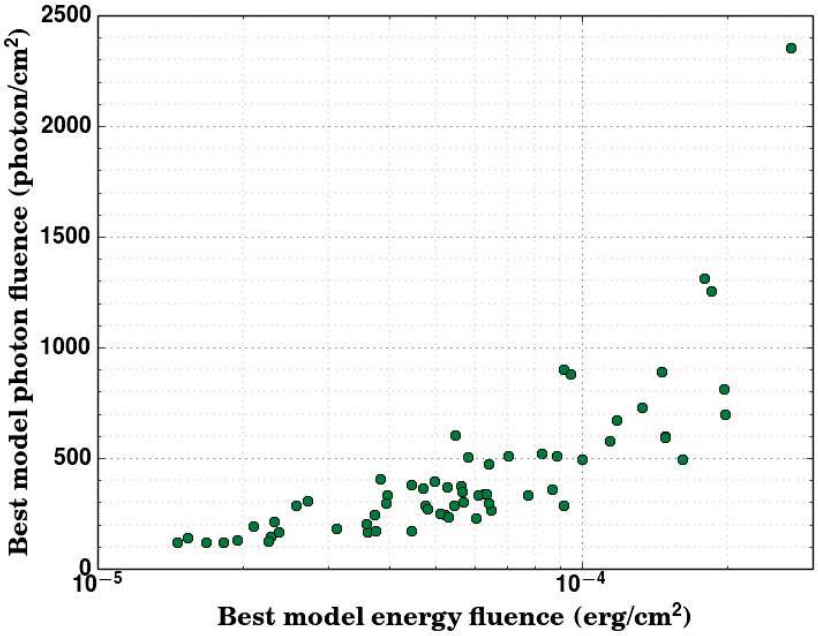

Figure 6.17: *Distribution of the photon and energy fluences of 64 selected GRBs. These fluences are obtained with the best fit model of each burst as reported in [Gruber et al., 2014].*

catalog[1][Gruber et al., 2014]. The bursts which have bad fit in the GBM catalog or in my analysis ($\chi^2 > 1.9$) are also excluded. As a result, my sample contained 64

[1]available on HEASARC webpage: `https://heasarc.gsfc.nasa.gov/W3Browse/fermi/fermigbrst.html`

Bursts	Spectral component	Reference
GRB 080916C	PL	[Ackermann et al., 2013b]
GRB 081215A	Strong spectral evolution	[Tierney et al., 2013]
GRB 090424	BB	[Tierney et al., 2013]
GRB 090820	BB	[Tierney et al., 2013]
GRB 090902B	BB, PL	[Abdo et al., 2009a]
GRB 090926A	BB, PL, Cutoff	[Ackermann et al., 2011; Guiriec et al., 2015a]
GRB 100724B	BB	[Guiriec et al., 2011]
GRB 110721	BB	[Axelsson et al., 2012]

Table 6.7: *List of the bright bursts excluded from the analysis.*

GBM GRBs, which are listed in Tab.C.3. More than half of the selected bursts (36 GRBs) are best fitted by the `Band` function in the GBM spectral catalog. The best fit model in this catalog is the Comptonized model for 22 of the remaining GRBs and the SBPL model for the last 6 GRBs. Fig.6.17 shows the photon and the energy fluences obtained with the best fit model of the selected GRBs in the GBM spectral catalog. These fluences are calculated as the integral of the energy flux over the burst duration in the energy range [10 - 1000] keV.

Our spectral analyses were performed with a maximum of 3 NaI detectors for each GRB with one BGO detector. I selected the detectors which have source angles $\leqslant 60°$ for NaI detectors and $< 90°$ for the BGO detectors. The background in each detector was determined manually before and after the prompt emission of each GRB, and it was fitted by a polynomial using the *GBMtoolkit* tool (see Sect.3.4.2). The Signal-to-Noise Ratio (SNR) of a given GRB in the N NaI detectors that have seen the burst is calculated as $\sum_i^N (c_i - b_i)/\sqrt{\sum_i^N b_i}$ where c_i and b_i are the number of counts and the background, respectively. The SNRs of the selected GRBs are presented in Fig.6.18. This figure shows that most of the selected GRBs have comparable SNRs except for GRB 120624B and GRB 150627A which have much lower and higher SNRs, respectively.

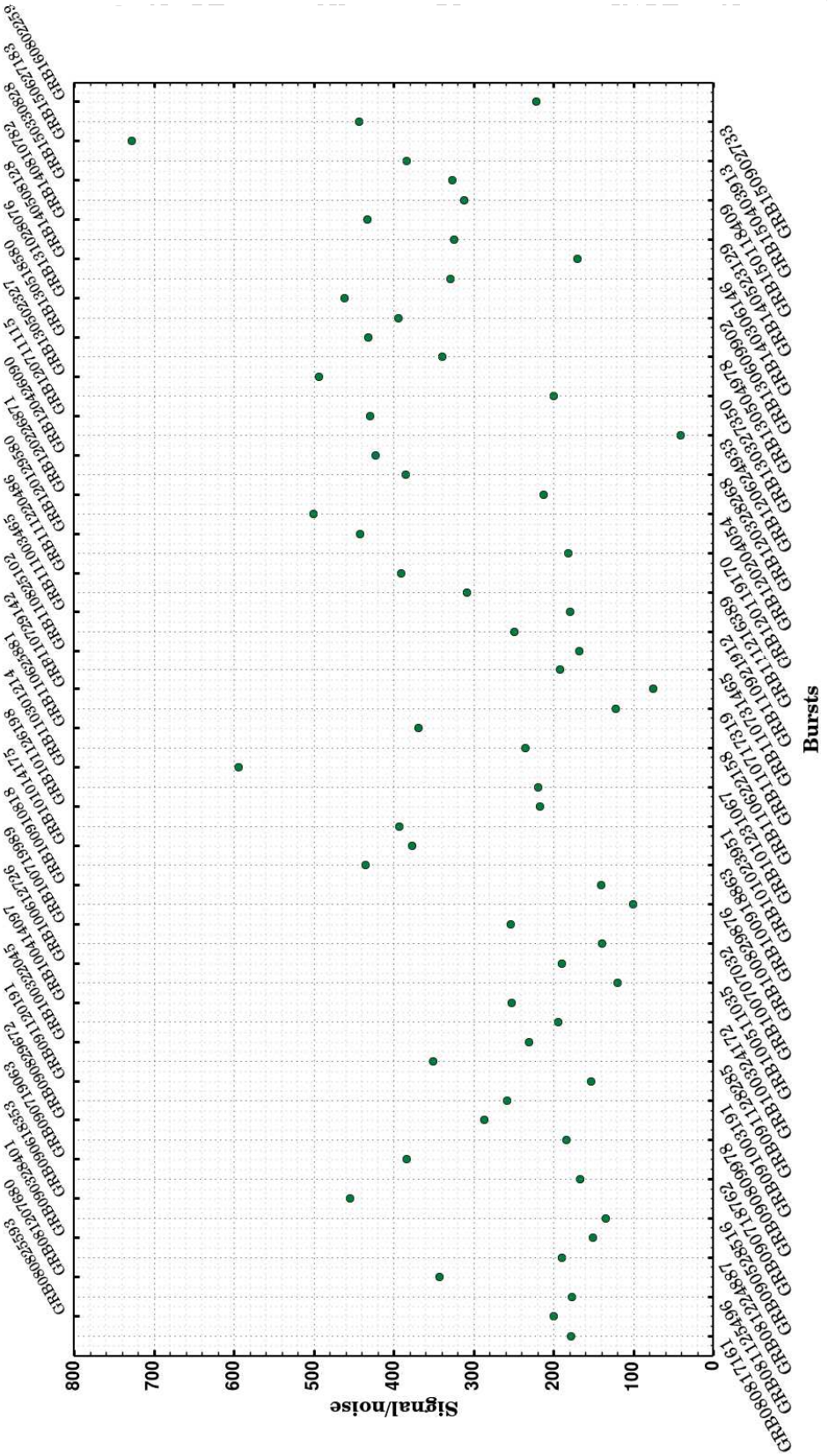

Figure 6.18: *Signal to noise ratio of the 64 selected GRBs.*

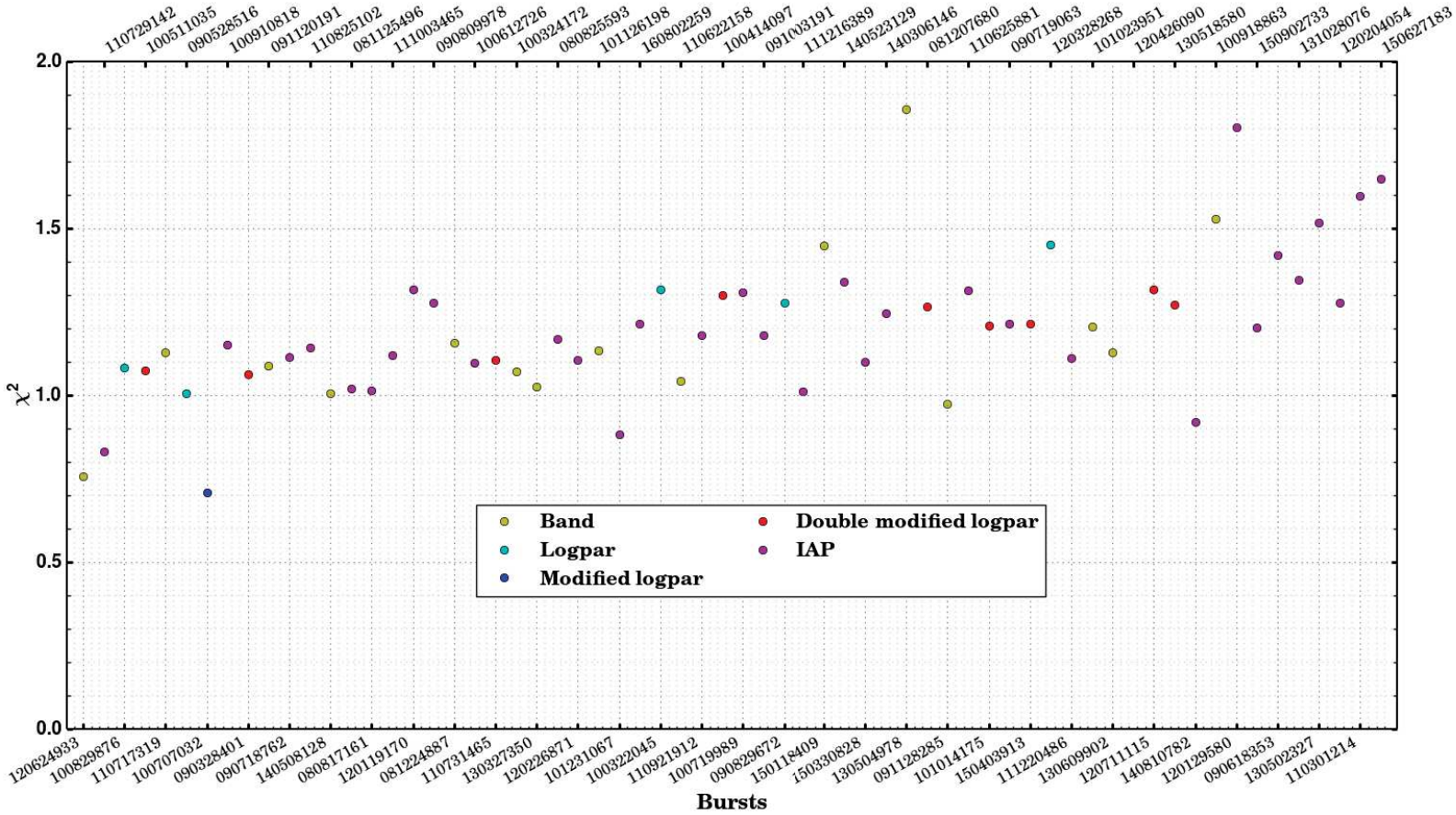

Figure 6.19: *Lowest χ^2 among the 5 fitted models for the 64 selected GRBs. The GRBs are arranged in SNR, increasing from the left to the right.*

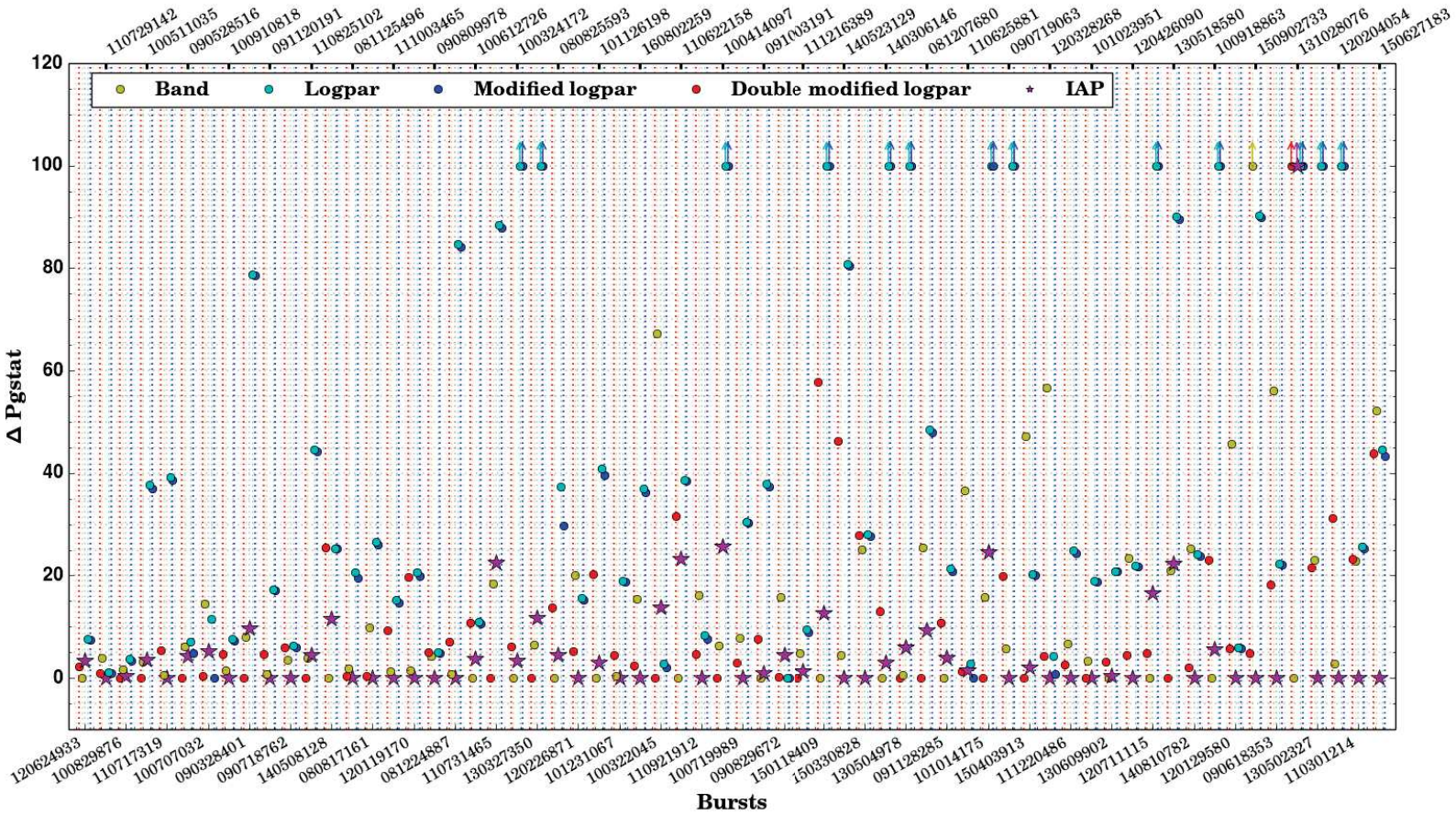

Figure 6.20: *Distribution of ΔPgstat values of four models with respect to the one which has the lowest Pgstat value. The latter is thus placed on the zero horizontal line for each GRB. The GRBs are arranged in SNR, increasing from the left to the right. For each GRB, five markers correponding to the five models are displayed within two vertical (red and blue) lines. Arrows at the top of the figure stand for models with a ΔPgstat larger than 100.*

6.5.2 Identification of the good models

The spectral analyses of the selected GRBs were performed with the *XSPEC* software using the five spectral models: `Band`, `logpar`, `modiflog`, `doublemodif` and `IAP`. The reference energy E_0 in equations 6.2, 6.5 and 6.6 of the `logpar`, `modiflog`, `doublemodif` models, is fixed to 500 keV. Likewise, the reference energy E_r of Eq.6.9 for the `IAP` model is fixed to 500 keV. In all of the plots presented in the following, the GRBs are displayed in SNR ascending order.

In a first step, I used the χ^2 statistic to quickly estimate the goodness of each fit. The lowest reduced χ^2 among the 5 fits is reported in Fig.6.19. This figure shows that the fits are relatively good, with χ^2 values clustered around 1.2. The χ^2 value increases very slowly with the SNR, probably because of the imperfections of the model and/or minor systematic uncertainties that become visible for the brightest GRBs only. The magenta points on this figure show that the `IAP` model has the lowest χ^2 for more than half of the GRBs (33/64), versus 15 GRBs only for the `Band` function (yellow points).

In a second step, I used the Pgstat statistic to get unbiased estimates of the spectral parameters. Moreover, this statistic is recommended to compare the spectral models between each other (hypothesis tests). Fig.6.20 shows the ΔPgstat of each model with respect to the model which has the lowest Pgstat (reference model hereafter). This calculation is done for all GRBs, which are displayed with increasing SNR on the figure. The first seven GRBs have comparable Pgstat values for the five spectral models (ΔPgstat$<$8). The `IAP` model has the lowest Pgstat for half of the selected GRBs. In most of the other cases, this model is often as good as the reference model. The differences in Pgstat increases with the SNR, indicating that the models can be more easily distinguished from each other when the event statistic is higher.

The statistical test that I used to decide whether two models are equivalent or not is based on the likelihood ratio test presented in Chap.3. The ΔPgstat between two models is a likelihood ratio, however its probability distribution function (PDF) under the null hypothesis (i.e., the reference model) can not be guessed from first principles. In particular, the Wilks theorem can not be invoked since many of the models are not nested. Therefore, one should compute the PDF by simulating a large number of spectra for each GRB and for each pair of models. Given the large number of cases, I focused on the `Band` and `IAP` models, in case of a low or a medium value of the SNR.

I performed Monte-Carlo simulations for two cases of the GRB sample, GRB 100910A (SNR=141) and GRB 110921A (SNR=249). For each GRB, I considered the `Band` model as the null hypothesis and simulated 10^5 `Band` spectra with fixed parameters

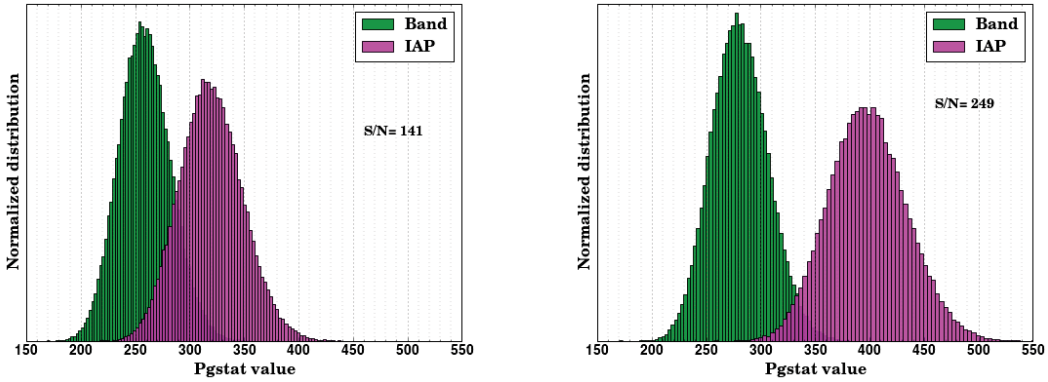

Figure 6.21: *Distributions of Pgstat from the fits of the* **Band** *and* **IAP** *models to simulated spectra with low (left) and medium (right) SNR. The number of degrees of freedom (237) is the same for all fits.*

α=-0.6, β=-2.6 and E_p= 350 keV. These simulations were performed using *XSPEC* for the duration of each GRB, using the DRM of the GBM detectors that have seen the burst. Each of the simulated spectra was then fitted with the `Band` and `IAP` models. The resulting distributions of Pgstat and ΔPgstat=Pgstat$_{Band}$-Pgstat$_{IAP}$ are shown in Figs.6.21 and 6.22, respectively. I fitted the two ΔPgstat distributions with an asymmetric Gaussian function and extrapolated the fit to compute the ΔPgstat limit that corresponds approximately to 5 standard deviations. As a result, the probability that a statistical fluctuation yields a better fit with the `IAP` model than with the `Band` model was found to be less than 10^{-6} ($\sim 5\sigma$) for a ΔPgstat greater than 20 (low SNR) and 3 (medium SNR). Beyond these limits, the null hypothesis (i.e., the `Band` model) must be rejected. Because these limits are not far from each other, and because it was complicated and time consuming to determine a limit for each GRB and each pair of models, it is reasonable to adopt a single limit of ΔPgstat=10 in all situations.

The `IAP` model is the reference model for 31/64 GRBs, 18 of which are equivalently fitted by the `Band` model according to the statistical test described above. Conversely, the `Band` model has the lowest Pgstat value for 15/64 GRBs, 10 of which are fitted by the `IAP` model as well. The `IAP` (resp. Band) model is the unique model to fit the data adequately for 5 (resp. 4) GRBs (Tab.6.8, left column) only. All in all, the `IAP` (resp. Band) model is a good model for 83% (resp. 66%) of the GRBs (Tab.6.8, right column). Concerning the other three models, only the `doublemodif` shows good performance. It is as good as the `Band` model, though with one more parameter.

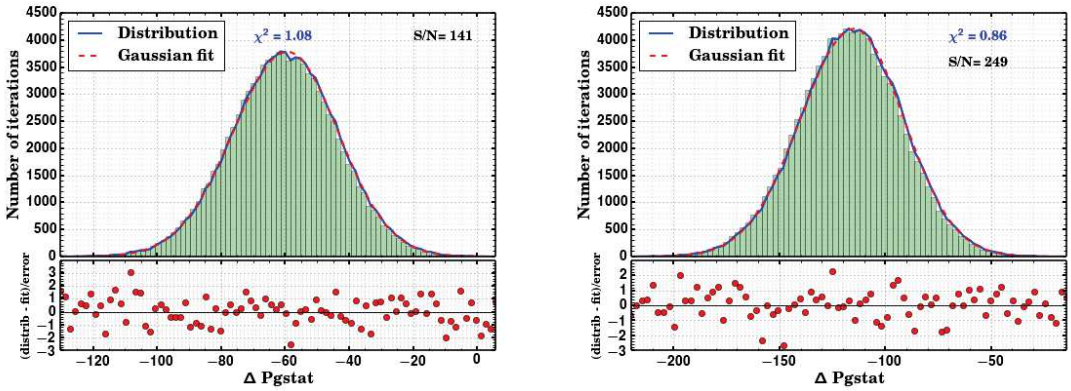

Figure 6.22: *Fit of an asymmetric Gaussian function to the distribution of $\Delta Pgstat$ between the* `Band` *and the* `IAP` *model for the low (left) and medium (right) SNR cases. The bottom panel of the two figures shows the ratio of the difference between the histogram and its fit over the error ($\sqrt{N}$ in each bin).*

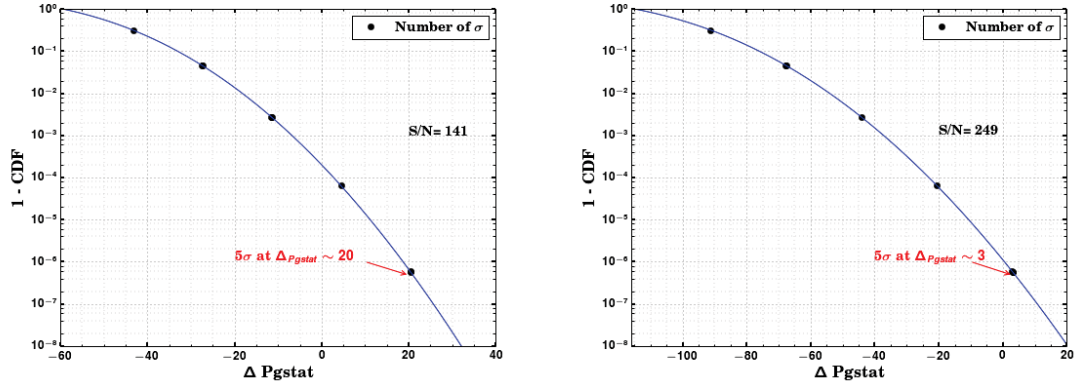

Figure 6.23: *$\Delta Pgstat$ limit at 5σ of the low (left) and medium (right) SNR cases.*

6.5.3 Parameters of the `Band` and `IAP` models

This section is dedicated to comparing the GRB spectral parameters obtained with the `Band` and the `IAP` models. The fit results of both models are reported in Tab.C.3. Fig.6.24 compares the E_p parameters obtained with both models. It can be seen that the E_p values of the `IAP` model are larger than the values obtained with the `Band` function for most of the GRBs. The E_p distributions are presented in Fig.6.26, and the values obtained for each GRB and each model are presented in Fig.6.25.

Fig.6.27 compares the α parameters obtained with both models. In this figure,

	Number of GRBs among 64	
Spectral models	The only model within ΔPgstat $\leqslant 10$	A good model within ΔPgstat $\leqslant 10$
`IAP`	5	53
`Band`	4	42
`doublemodif`	3	45
`modiflogpar`	0	15
`logpar`	0	14

Table 6.8: *Statistic of best and good fit models for the sample of GRBs*

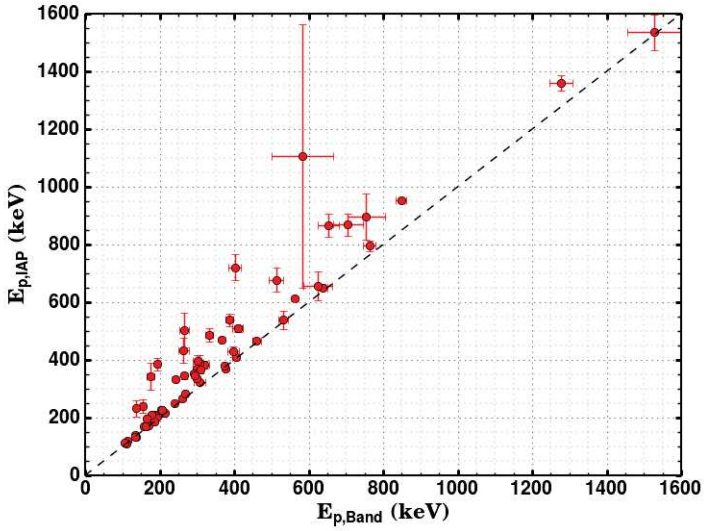

Figure 6.24: *Comparison of the E_p parameter between the* `Band` *and* `IAP` *models.*

the dashed lines indicate the upper limit (-2/3) of the low-energy spectral index that is expected from a synchrotron emission (slow cooling regime). Therefore, the GRB spectra that lie above these lines seem to be incompatible with the synchrotron theory. However, the α parameter is an asymptotic value that is often not reached by the local photon index within the GBM energy range, as noted by [Preece et al., 1998]. I computed the energy E_{lim} at which the local photon index $\Gamma(E)$ approaches the asymptotic value α within its error $\delta\alpha$. Namely, I solved the equation $\Gamma(E_{lim}) = \alpha - \delta\alpha$ using the definition of the local photon index of the `Band` and `IAP` models in Eqs.6.1 and 6.10, respectively. The E_{lim} energies are expressed as:

$$E_{lim,IAP} = \frac{\delta\alpha E_p}{(2+\alpha)} \frac{(2+\beta)}{(\beta - \alpha + \delta\alpha)} \tag{6.14}$$

$$E_{lim,Band} = \frac{\delta\alpha E_p}{2+\alpha} \tag{6.15}$$

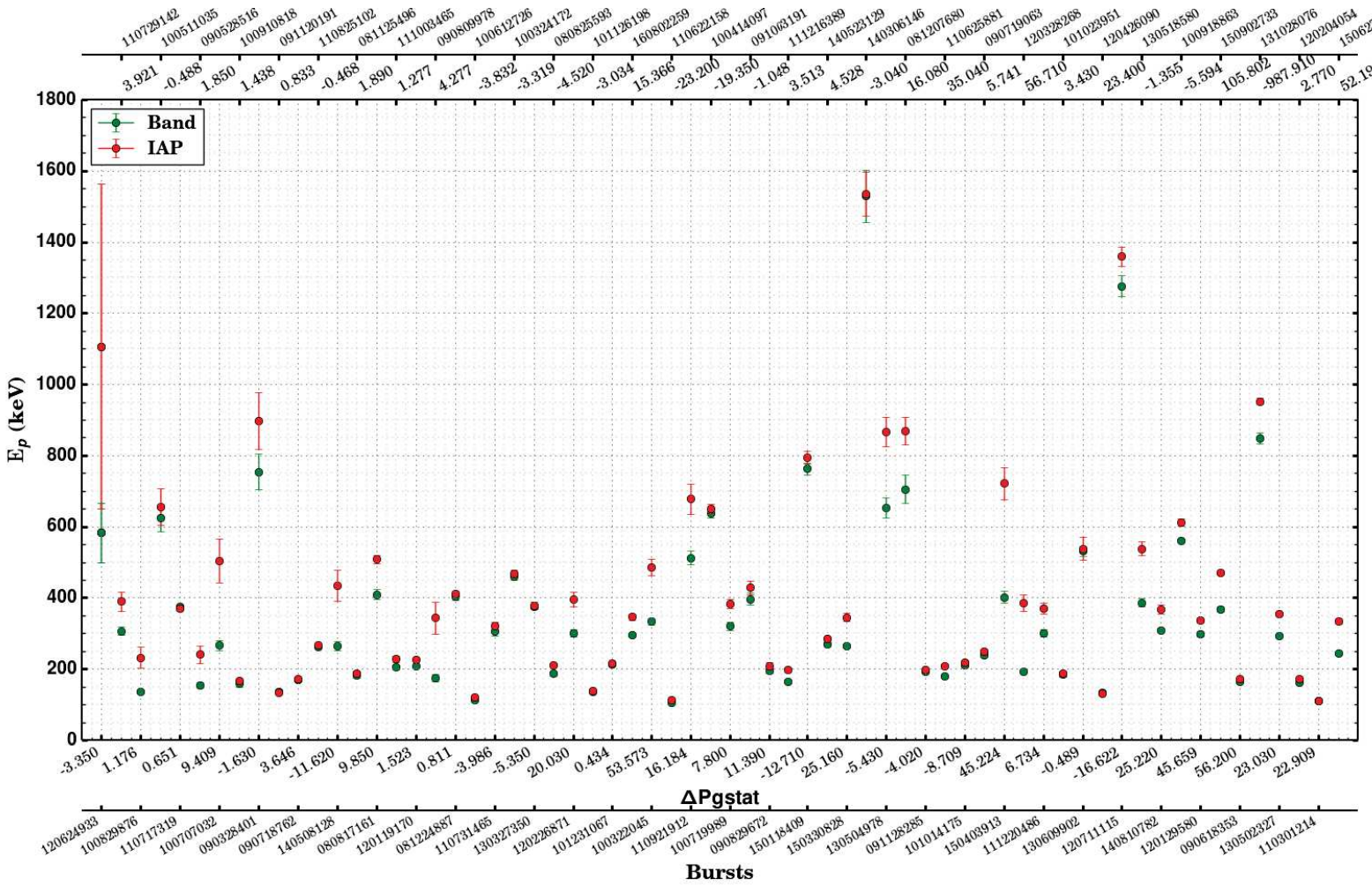

Figure 6.25: *E_p parameter values obtained with the* **Band** *and the* **IAP** *models for the GRB sample. The GRBs are arranged in SNR, increasing from the left to the right. Their corresponding $\Delta Pgstat$ values ($\Delta Pgstat$=$Pgstat_{Band}$ - $Pgstat_{IAP}$) are also indicated.*

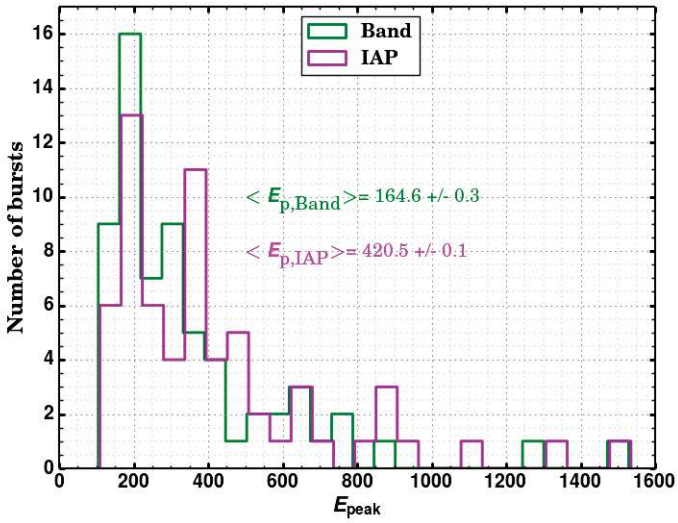

Figure 6.26: *Distributions of the E_p parameter of the* **Band** *and* **IAP** *models. The weighted means are displayed in the figure.*

The E_{lim} energy is presented in Fig.6.28 with respect to the E_p energy of the GRB spectra. This figure shows that most of the bursts have a limit energy below the lower limit of the GBM energy range. Hence, to have a fair comparison of the low-energy index between the two models, I computed the local photon index at 10 keV, i.e. right above the low-energy boundary of the GBM NaI detectors. This spectral slope α_{10} is shown in Fig.6.29 for the two models. The values of α_{10} for the `IAP` model are only slightly larger than those of the `Band` model. They are also less scattered than the values of the asymptotic α presented in Fig.6.27. More interestingly, this figure shows that most of the studied GRBs have spectral indices softer than the death line limit (-2/3). The α and α_{10} distributions of both models are presented in Fig.6.30. This figure shows that the weighted means for the `IAP` (resp. Band) model decreased from $\langle\alpha\rangle$=-0.75 (resp. -0.87) to $\langle\alpha_{10}\rangle$=-0.91 (resp. -0.98). A detailed comparison between α and α_{10} for each GRB is presented in Fig.6.31. Fig.6.32 shows the difference between α and α_{10} with respect to the peak energy E_p. Since the two spectral indices are correlated, the error on their difference is chosen as the largest of their errors. As expected, the asymptotic index is systematically larger than the index at 10 keV especially for the GRBs that have small peak energies. For these GRBs, the difference in α_{10} between the two models is also the strongest (Fig.6.33).

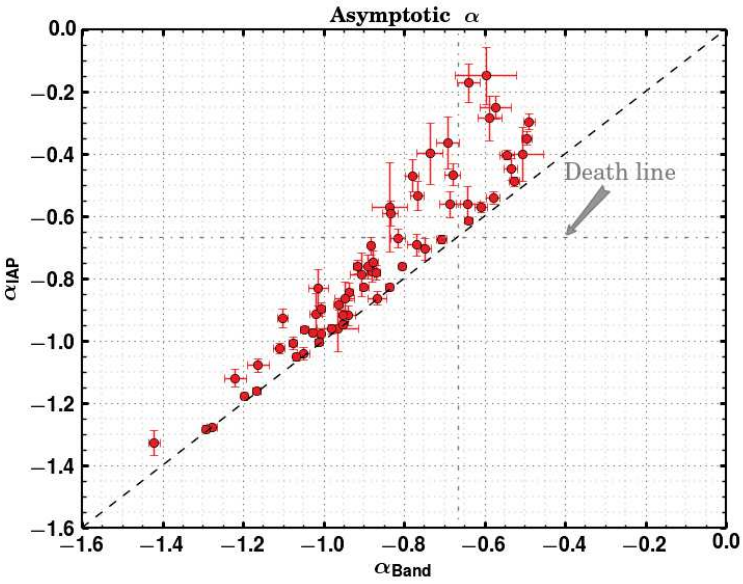

Figure 6.27: *Comparison of the asymptotic α parameter between the* `Band` *and* `IAP` *models. The gray dashed lines indicate the upper limit (-2/3) of the low-energy spectral index for synchrotron emission (slow cooling regime)*

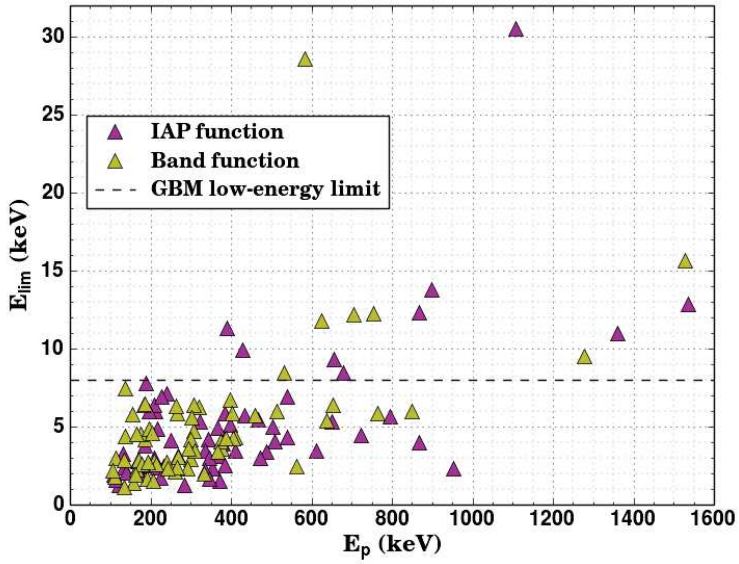

Figure 6.28: *Limit energies E_{lim} of the* `IAP` *and* `Band` *models compared with their peak energies E_p. The dashed line represents the lower limit of the GBM energy range.*

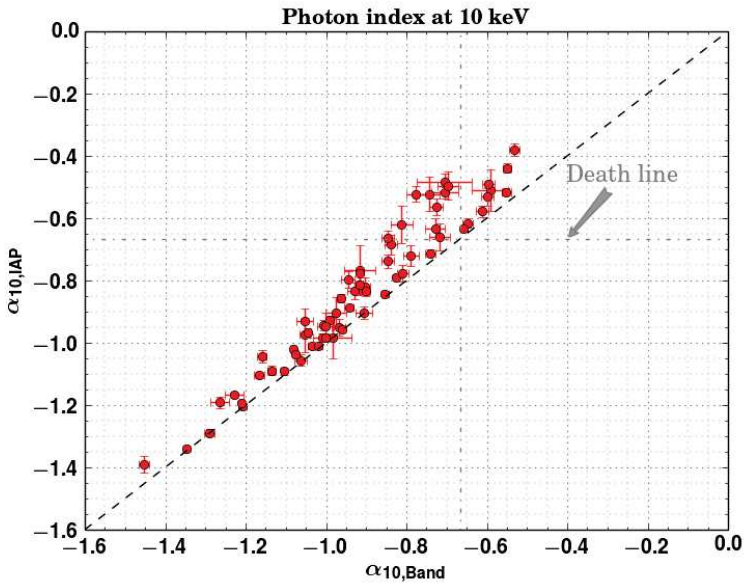

Figure 6.29: *Comparison of the local photon index at 10 keV α_{10} between the* **Band** *and* **IAP** *models. The gray dashed lines indicate the upper limit (-2/3) of the low-energy spectral index for synchrotron emission (slow cooling regime).*

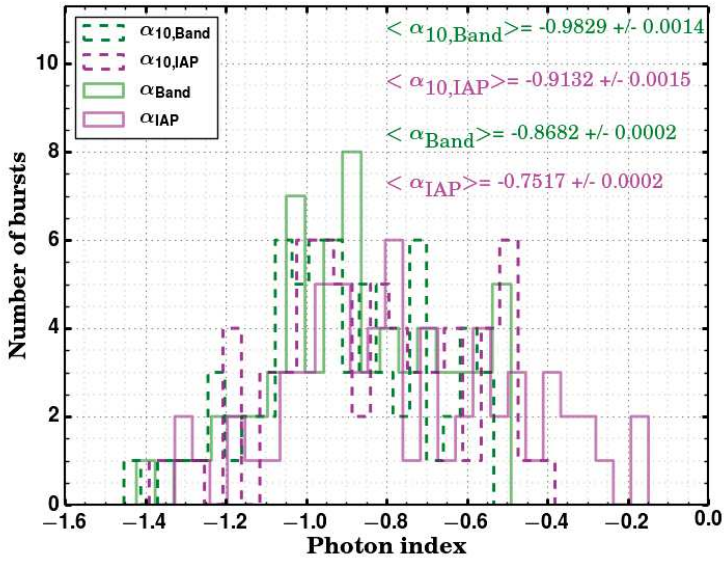

Figure 6.30: *Distributions of the α and α_{10} parameters of the* **Band** *and* **IAP** *models. The weighted means are displayed in the figure.*

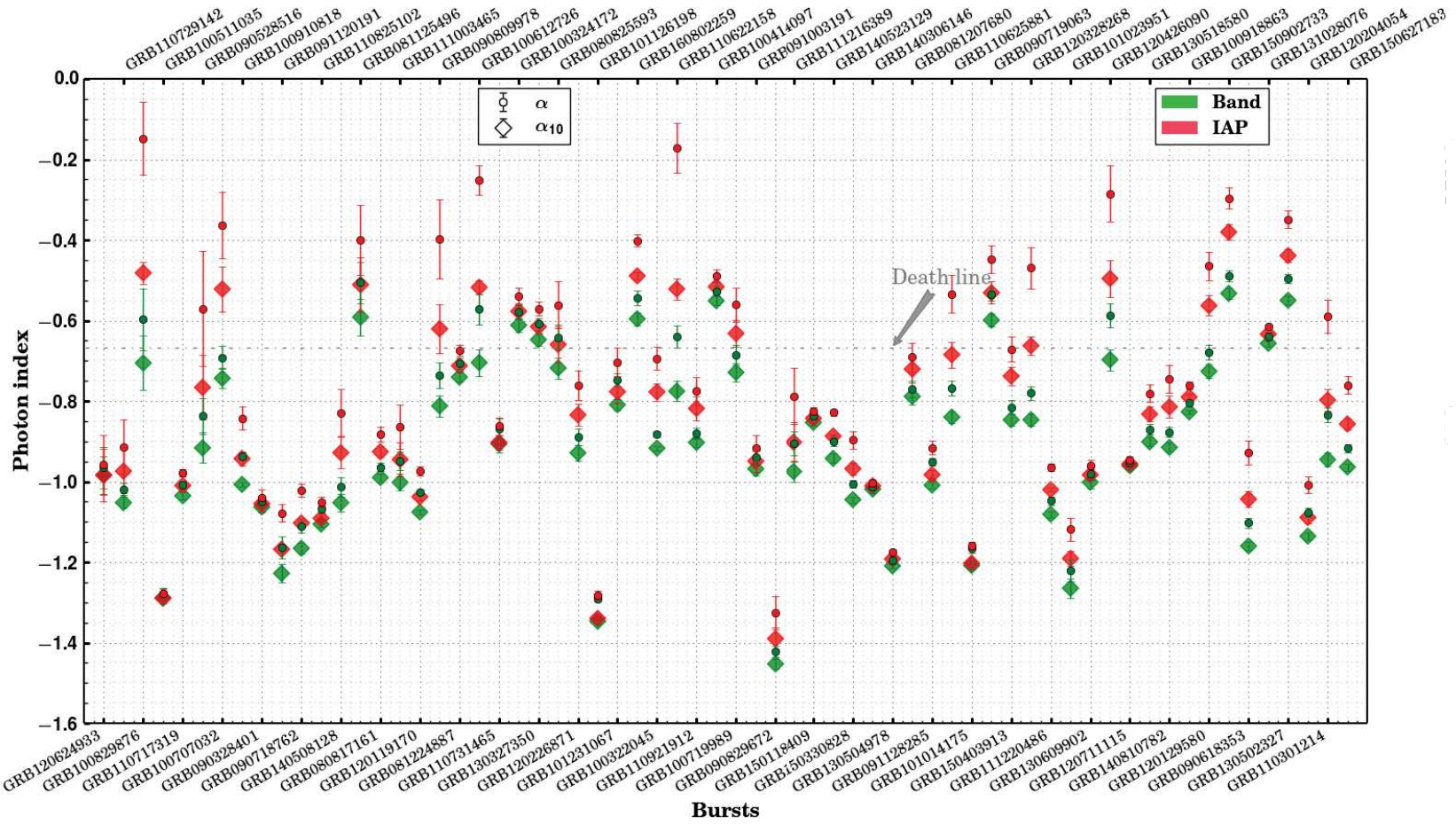

Figure 6.31: *α and α_{10} parameter values obtained with the* `Band` *and the* `IAP` *models for the GRB sample. The GRBs are arranged in SNR, increasing from the left to the right. The gray dashed line indicates the upper limit (-2/3) of the low-energy spectral index for synchrotron emission (slow cooling regime).*

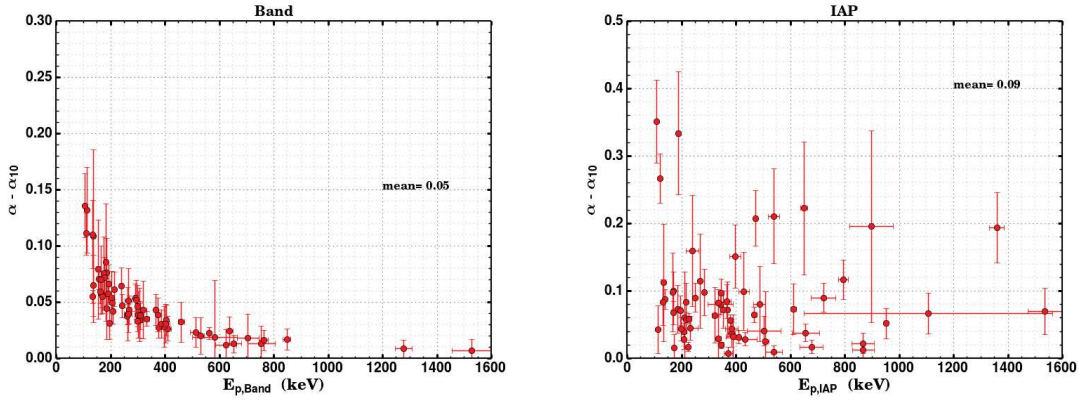

Figure 6.32: *Difference between α and α_{10} compared with the peak energy E_p for the* `Band` *model (left panel) and the* `IAP` *model (right panel). Each vertical error bar is chosen as the largest of the two parameter errors. The arithmetic mean of the values on the y-axis is also indicated.*

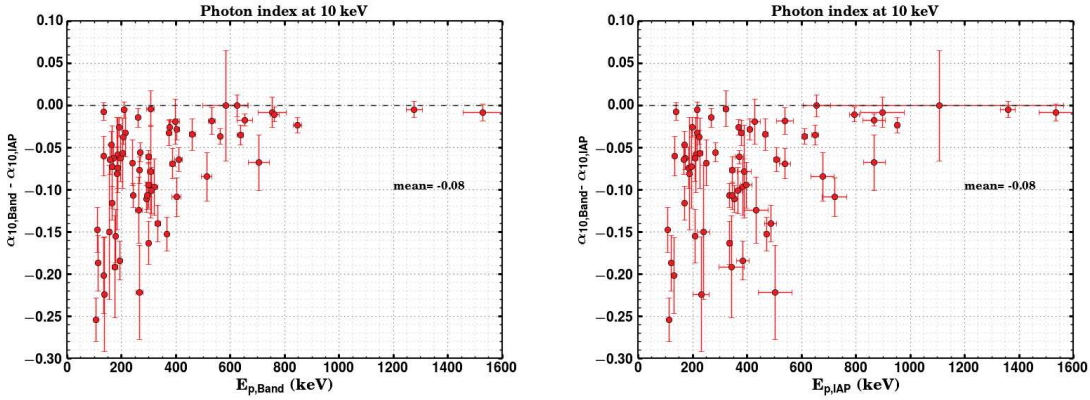

Figure 6.33: *Difference between $\alpha_{10,Band}$ and $\alpha_{10,IAP}$ compared with the peak energy E_p for the* `Band` *model (left panel) and the* `IAP` *model (right panel). Each vertical error bar is chosen as the largest of the two parameter errors. The arithmetic mean of the values on the y-axis is also indicated.*

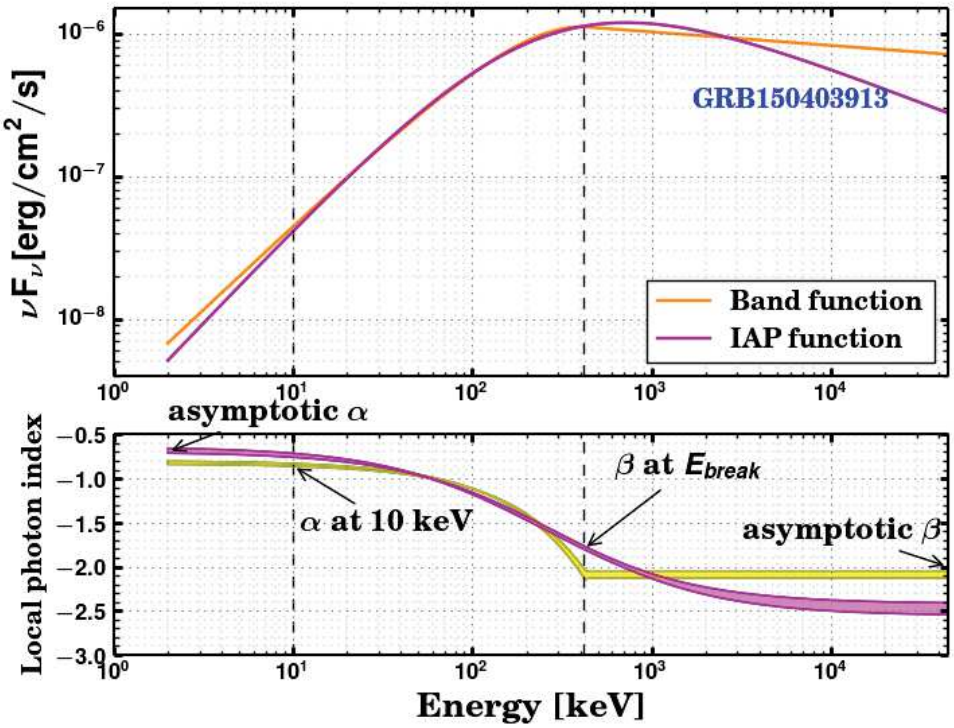

Figure 6.34: *Local photon index of a representative GRB with the* `Band` *and* `IAP` *models. The notations of* α *and* β *spectral indices displayed in this figure are used to compare the two model parameters.*

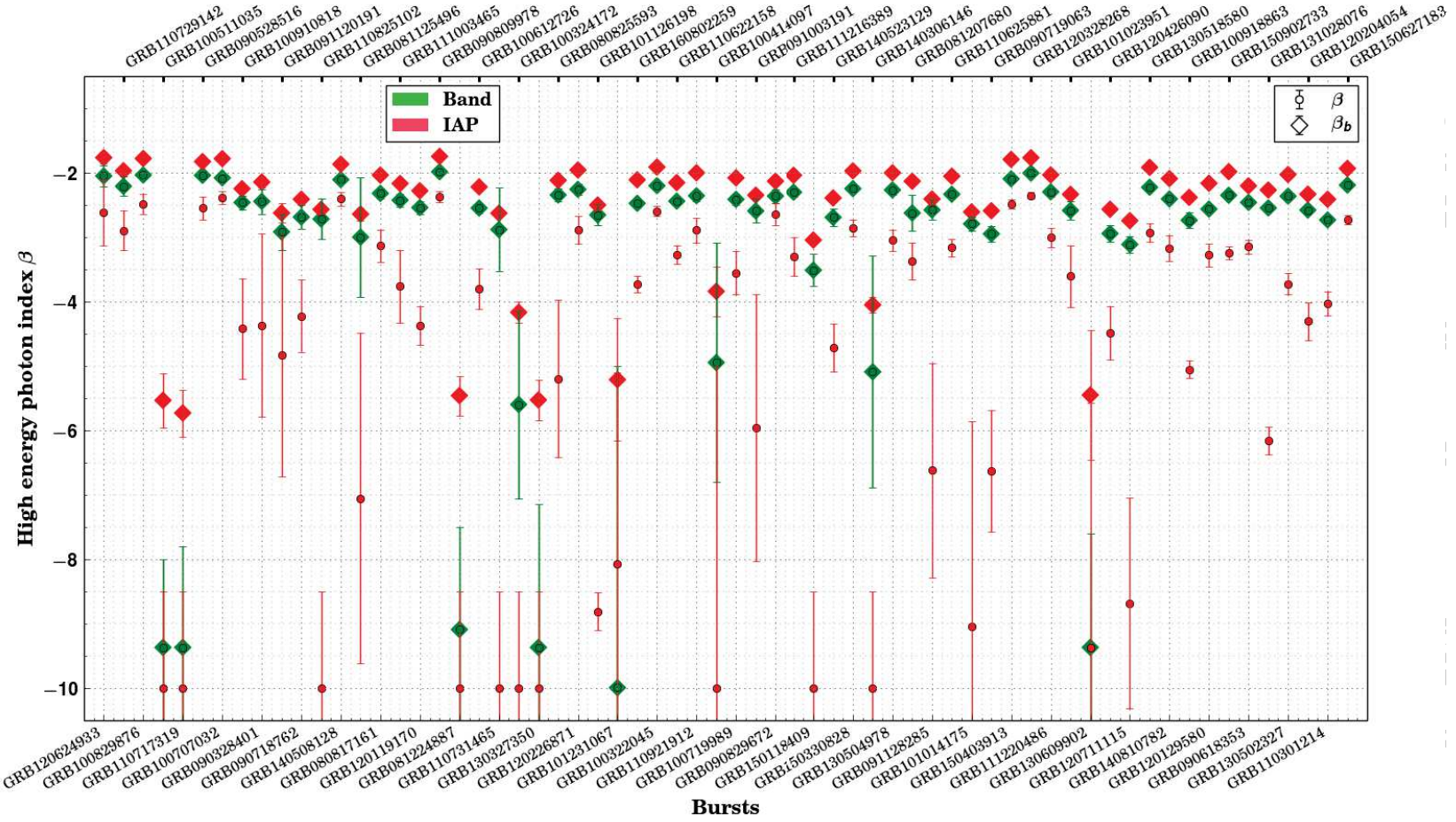

Figure 6.35: *β and β_b parameter values obtained with the* `Band` *and the* `IAP` *models for the GRB sample. The GRBs are arranged in SNR, increasing from the left to the right.*

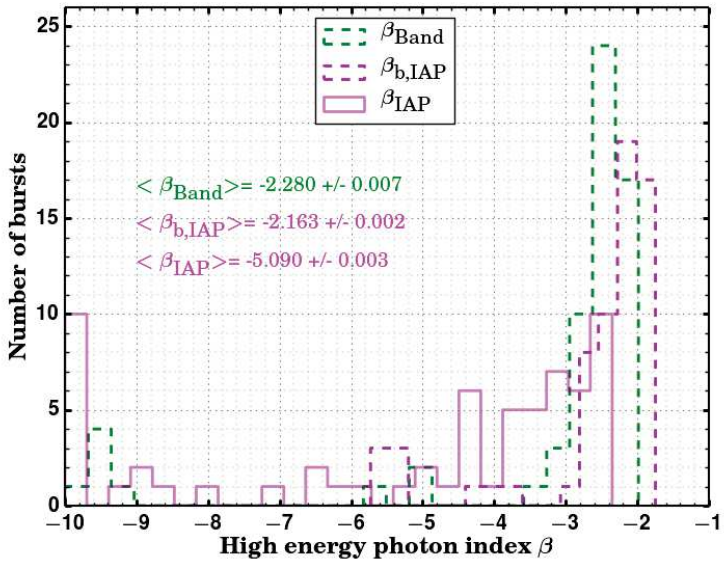

Figure 6.36: *Distributions of the β and β_b parameters of the* `Band` *and* `IAP` *models. The weighted means are displayed in the figure.*

As can be seen from Fig.6.35, the values of β are softer for the `IAP` model than for the `Band` model. For some GRBs, this parameter is poorly constrained because of low photon statistics above the break energy. The β parameter of the `IAP` model is an asymptotic value at high energy, which may not be reached by the local photon index within the GBM energy range. To compare both models in this energy domain, I thus defined β_b as the photon index at the break energy $E_b = E_p(\alpha-\beta)/(2+\alpha)$ of the `Band` function (see Fig.6.34). For the `Band` model, β_b is identical to β since the `Band` function is defined as a power law above E_b. Fig.6.35 presents the β and β_b parameters of both models for each GRB. As expected, the values of β_b for the `IAP` model are harder than β, because of the continuous curvature of the `IAP` function. As a result, $\beta_{IAP} < \beta_{Band} < \beta_{b,IAP}$ (see also Fig.6.36).

Fig.6.34 shows the results of the `Band` and `IAP` fits to the typical GRB 150403. This figure summarizes the results obtained in this section, and illustrates the trend observed for the vast majority of the GRBs in the sample. It shows how both spectral parameterizations differ and intersect each other when applied to real data. Interestingly, the same trend is observed for the GRB sample as for the synthetic bursts analyzed in Sect.6.4.2 (see Tabs.6.2, 6.3 and 6.4), i.e. the spectrum fitted with the `IAP` model is a bit wider around the peak energy than the spectrum fitted with the `Band` model, but narrower when observed over a wider energy range.

6.5.4 Spectral sharpness

Using the same methodology as in Sect.6.4.2, I compared the sharpness angle of the spectra obtained from the fits of the `Band` and `IAP` models. For each GRB of the sample and each model, I simulated 10^3 spectra using the fit parameters and their covariance matrix. As before, the sharpness angle is defined as the MPV of the resulting angle distribution, and its error is computed from the 68% confidence interval around the MPV. As shown in Fig.6.37, this work confirms the results obtained in the previous section, namely that the IAP spectra are slightly wider than the `Band` spectra. The sharpness angle is strongly dependent on the photon indices near the SED peak. As expected, this angle decreases when α increases (Fig.6.38) and/or when β decreases (Figs.6.39 and 6.40). Naturally, it is independent of the peak energy itself (Fig.6.41).

The results of this work are also in very good agreement with the analysis performed by [Yu et al., 2015]. Despite different choices of the time intervals (time-integrated spectra in this work vs. time-resolved spectra in [Yu et al., 2015]), the distributions of the sharpness angles are very similar between both analyses and they range from $\sim$115° to $\sim$140° (Fig.6.37, and blue solid curve in the left panel of figure 7 in [Yu et al., 2015]). The sharpness angle of the time-integrated spectrum of the synthetic burst from the IAP IS model ($\sim$149°, see Tab.6.5) is larger than for any GRB in the sample that I analyzed. This difference results mainly from the low-energy spectral index α, which is smaller ($\alpha \simeq$-1.2, see Tab.6.2) than for most of the GRBs in the sample (Figs.6.27 and 6.30). Conversely, the high-energy index of the synthetic burst ($\beta \simeq$-2.3) corresponds to the core of the sample distribution (Figs.6.35 and 6.36). Interestingly, an increase (resp. decrease) of 0.5 in α (resp. β) implies a decrease of $\sim$15° in sharpness (Fig.6.40) and would reincorporate the synthetic burst into the bulk of the GRB sample. In Sect.6.7, I will discuss possible solutions that could reconcile the observations with the IAP internal shock model.

6.6 Application to GRB 090926A

I revisited the broadband spectral analysis of GRB 090926A presented in Chap.5, using the new fitting function obtained in Sect.6.4.3. I focused my analysis on the time intervals c [9.8 s, 10.5 s] and d [10.5 s, 21.6 s] during which high-energy spectral breaks were detected. Interestingly, these breaks have similar shapes as the one of the synthetic spectrum, although the latter occurs at a much higher energy (see Sect.6.4.4). As before, the spectral analyses were performed using joint GBM/LAT Pass 8 data above 30 MeV.

In a first step, I used the `IAP`+ CUTPL model for the two time intervals. The reference energy of the CUTPL model (Eq.3.12) was fixed to 1 MeV and 1 GeV for

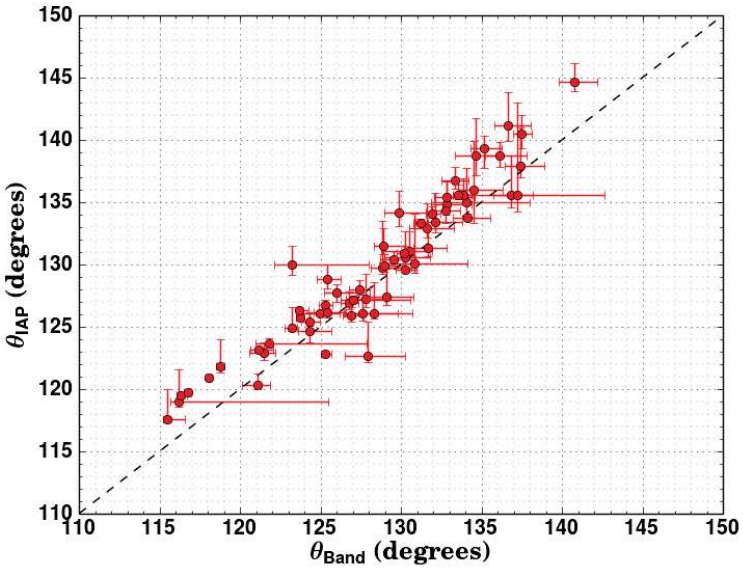

Figure 6.37: *Sharpness angles of the* `IAP` *fits versus the angles of the* `Band` *fits to the GRB spectra.*

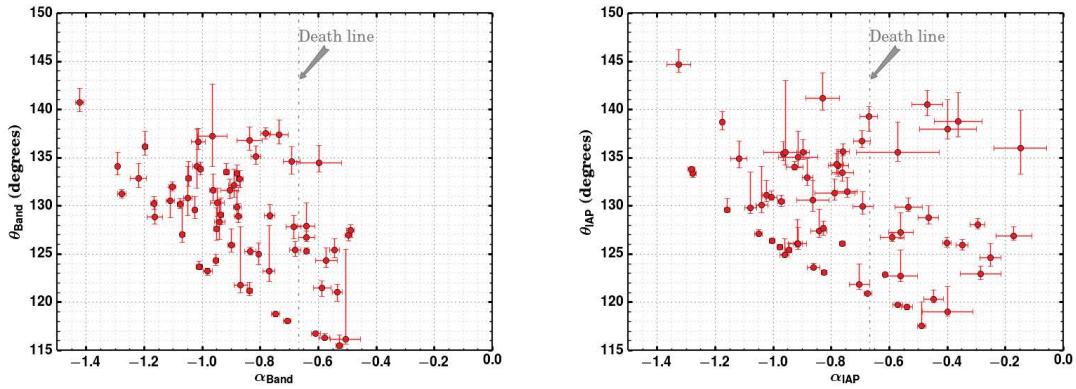

Figure 6.38: *Sharpness angle compared with the α parameter for the* `Band` *model (left panel) and the* `IAP` *model (right panel).*

time bins c and d, respectively, as in [Ackermann et al., 2011]. The fit results are presented in Tab.6.9 and shown in the top panels of Figs.6.42 and 6.43. The `IAP` + CUTPL model fits the data with a Pgtat of 560 for the time interval c and 582 for the time interval d with 510 d.o.f. This spectral analysis yielded a spectral index γ= -1.71$^{+0.03}_{-0.02}$ (resp. -1.80$^{+0.01}_{-0.02}$) and a folding energy E_f=0.38$^{+0.10}_{-0.08}$ GeV (resp. 1.34$^{+0.46}_{-0.27}$ GeV) for the time interval c (resp. d) versus -1.68$^{+0.04}_{-0.03}$ (resp. -1.75$^{+0.02}_{-0.03}$) and 0.37$^{+0.06}_{-0.05}$ GeV (resp.1.61$^{+0.38}_{-0.31}$ GeV) in Chap.5 [Yassine et al., 2017]. In other words, the

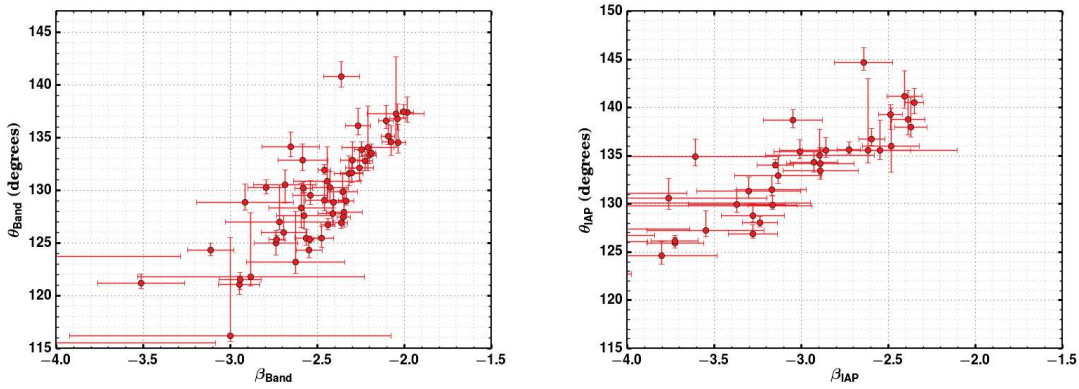

Figure 6.39: *Sharpness angle compared with the β parameter for the* ***Band*** *model (left panel) and the* ***IAP*** *model (right panel).*

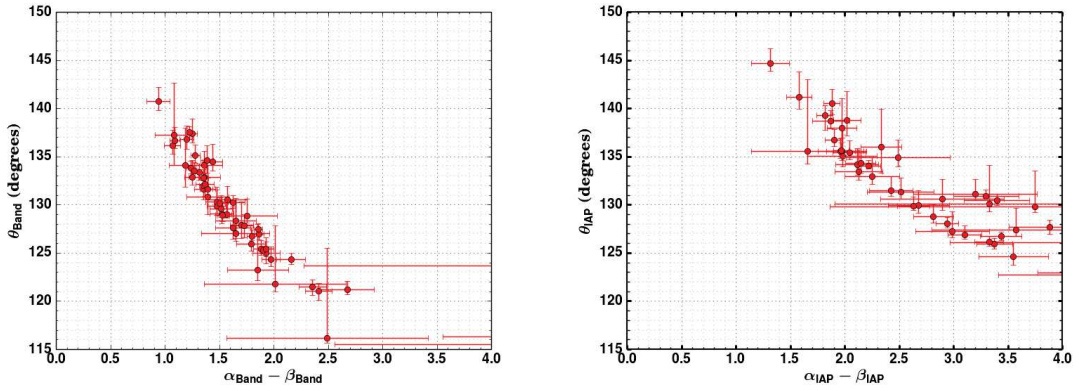

Figure 6.40: *Sharpness angle compared with α-β for the* ***Band*** *model (left panel) and the* ***IAP*** *model (right panel).*

IAP+CUTPL model fits well the data, and it yields high-energy spectral parameters that are close to those of the Band+CUTPL model. The fitted values of the α parameter ($\sim$-0.44) for the IAP+CUTPL model violate the synchrotron line of death (at -2/3) much more than those of the Band+CUTPL model. Therefore, I repeated the analysis after replacing the CUTPL component by a CUTBPL component, for the same reasons as those presented in Chap.5. Using this IAP+CUTBPL model that is more physically motivated, I obtained the results in Tab.6.9, which are presented in the bottom panels of Figs.6.42 and 6.43. These spectral fits yielded a spectral index $-1.52^{+0.02}_{-0.02}$ (resp. $-1.73^{+0.05}_{-0.04}$) and a folding energy Ef=$0.27^{+0.07}_{-0.05}$ GeV (resp. $1.12^{+0.32}_{-0.25}$ GeV). Again, these values are close to those obtained with the Band+CUTBPL model. Besides, the fitted values of the α parameter for the IAP+CUTBPL model

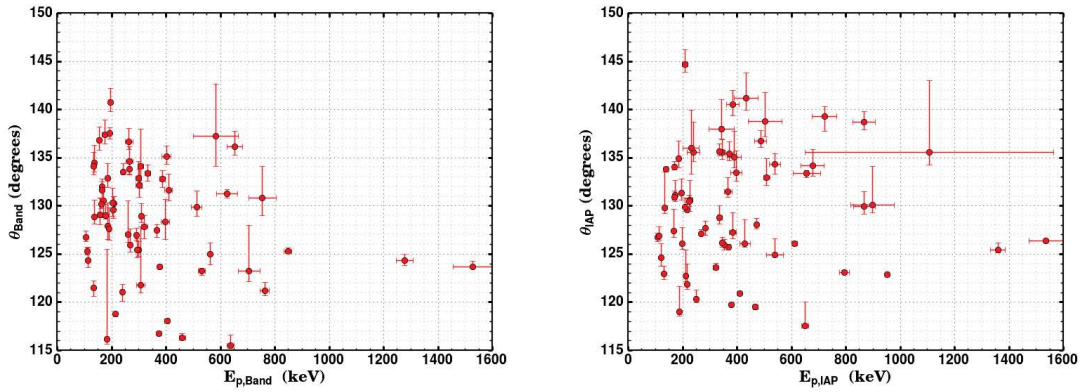

Figure 6.41: *Sharpness angle compared with the peak energy E_p for the* `Band` *model (left panel) and the* `IAP` *model (right panel).*

are now well below the synchrotron line of death (-0.97±0.02 and -0.86±0.02 for the time intervals c and d, respectively). However, the Pgstat increased by more than 100 between the `IAP`+CUTPL and `IAP`+CUTBPL fits (see Tab.6.9), indicating that the latter model should be taken with caution. For both models, the β parameter is very steep and not well constrained, which might explain the difference in goodness of fit. These very negative values of β translate also into very small sharpness angles ($\sim$110°). Harder and better constrained values of β would certainly improve the goodness of fit and increase the spectral sharpness. Naturally, no more data can be added to the [1 - 30] MeV energy range, i.e. in the valley of the SED where the GBM and LAT count rates are depleted (see Figs.6.42 and 6.43). However, the spectral model could be improved in this energy range in the future, e.g. adopting a more realistic representation of the inverse Compton component that would rise rapidly above $\sim$1 MeV, instead of the CUTBPL component that affects the fit of the synchrotron component down to $\sim$300 keV.

6.7 Summary and discussion

I studied the spectro-temporal evolution of the synthetic burst provided by the internal shock model of the IAP team. This model simulates the dynamics of the shocks that take place within GRB jets, as well as the synchrotron and inverse Compton radiations from a population of relativistic electrons. The acceleration of the electrons is treated through theoretical prescriptions of the shock microphysics.

In a first step, I simulated the synthetic burst as it would be observed by the GBM and the LAT, using their instrument response functions. I performed a detailed spectral analysis of the simulated synthetic spectra, and I built a new function

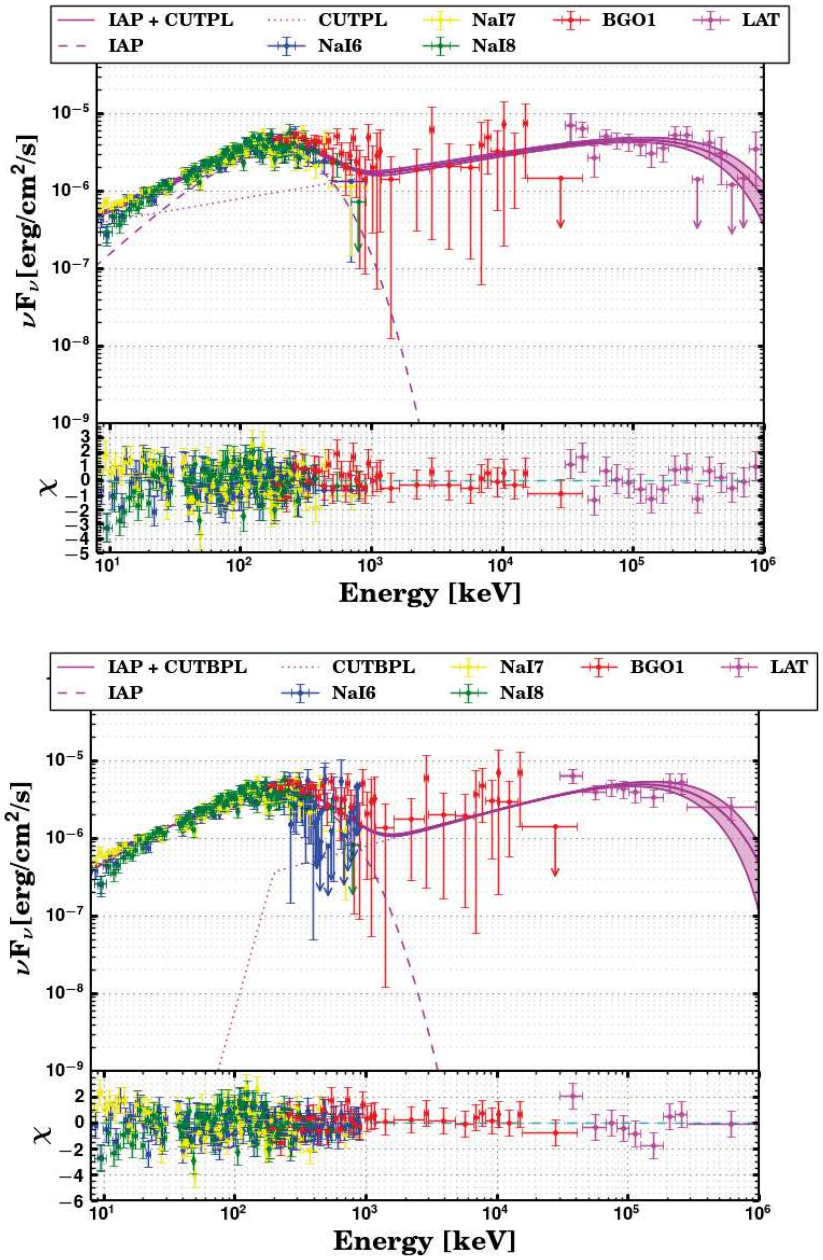

Figure 6.42: *Spectral energy distributions of GRB 090926A in time interval c for the joint GBM/LAT analysis using LAT Pass 8 above 30 MeV. The solid curve represents the* `IAP` *+ CUTPL model (top) and the* `IAP` *+ CUTBPL model (bottom), within a 68% confidence level contour derived from the errors on the fit parameters. The reference energy of the CUTPL and CUTBPL were fixed to 1 MeV and 10 MeV respectively as was done in Chap.5 [Yassine et al., 2017].*

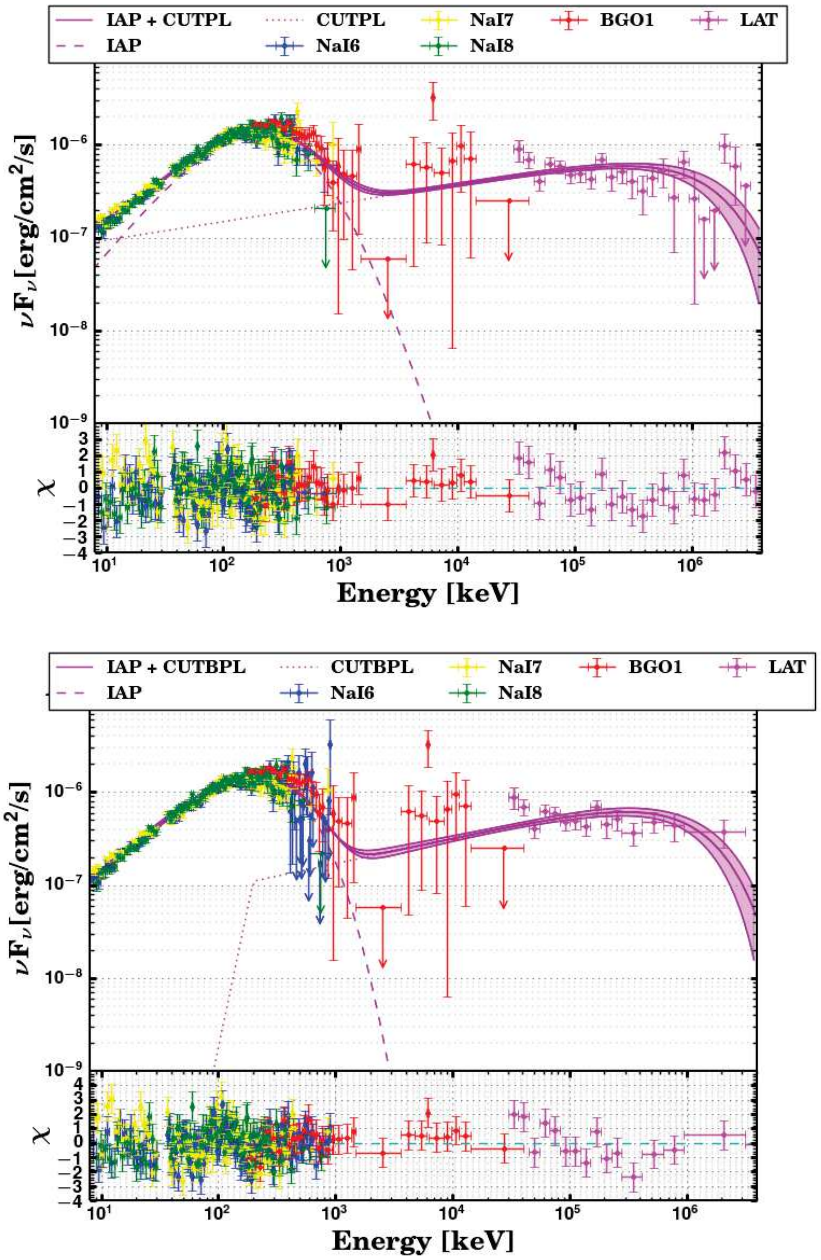

Figure 6.43: *Spectral energy distributions of GRB 090926A in time interval d for the joint GBM/LAT analysis using LAT Pass 8 above 30 MeV. The solid curve represents the* `IAP` *+ CUTPL model (top) and the* `IAP` *+ CUTBPL model (bottom), within a 68% confidence level contour derived from the errors on the fit parameters. The reference energy of the CUTPL and CUTBPL are fixed to 1 MeV and 10 MeV respectively as was done in Chap.5 [Yassine et al., 2017]*

	Models		
Time intervals	**Parameters**	**IAP + CUTPL**	**IAP + CUTBPL**
Interval c	IAP		
	$\mathbf{A_{MeV}}$ $(\times\mathbf{10^{-5}})$ $\mathbf{keV^{-1}\,cm^{-2}\,s^{-1}}$	327^{+59}_{-58}	576^{+5}_{-5}
	E_p **(keV)**	188^{+8}_{-10}	202^{+1}_{-1}
	α	$-0.44^{+0.21}_{-0.15}$	$-0.97^{+0.02}_{-0.02}$
	β	$-16.5^{+9.1}_{-1.0}$	$-15.0^{+4.1}_{-1.0}$
	CUT(PL/BPL)		
	$\mathbf{A_{GeV}}$ $\mathbf{keV^{-1}\,cm^{-2}\,s^{-1}}$	$96.7^{+9.3}_{-8.2}$ $(\times\,10^{-5})$	$35.9^{+2.1}_{-3.7}(\times 10^{3})$
	λ	$-1.71^{+0.03}_{-0.02}$	$-1.52^{+0.02}_{-0.02}$
	E_f **(GeV)**	$0.38^{+0.10}_{-0.08}$	$0.27^{+0.07}_{-0.05}$
	Pgstat/dof	560.3/510	675.9/510
Interval d	IAP		
	$\mathbf{A_{MeV}}$ $(\times\mathbf{10^{-5}})$ $\mathbf{keV^{-1}\,cm^{-2}\,s^{-1}}$	186^{+7}_{-9}	203^{+15}_{-11}
	E_p **(keV)**	201^{+4}_{-5}	204^{+7}_{-5}
	α	$-0.44^{+0.14}_{-0.08}$	$-0.86^{+0.02}_{-0.02}$
	β	$-6.12^{+0.93}_{-1.05}$	$-14.96^{+7.78}_{-1.00}$
	CUT(PL/BPL)		
	$\mathbf{A_{GeV}}$ $\mathbf{keV^{-1}\,cm^{-2}\,s^{-1}}$	$58.8^{+4.8}_{-5.4}(\times\,10^{-11})$	$10.7^{+1.7}_{-2.9}(\times\,10^{7})$
	λ	$-1.79^{+0.01}_{-0.02}$	$-1.73^{+0.05}_{-0.04}$
	E_f **(GeV)**	$1.34^{+0.46}_{-0.27}$	$1.12^{+0.32}_{-0.25}$
	Pgstat/dof	582.0/510	717.5/510

Table 6.9: *Results of the* `IAP`*+CUTPL and* `IAP`*+CUTBPL fits to GBM/LAT data in the intervals c and d of GRB 090926A.*

(called `IAP`) that is representative of their shape in the keV-MeV domain. Interestingly, the sharpness angle of this function is slightly larger than that of the `Band` function. At high energy, the spectrum of the synthetic burst can be simply represented by a power law with an exponential cutoff.

In a second step, I studied the spectral shape of 64 GRBs which are bright and fluent in the GBM. This analysis showed that the `IAP` function can fit adequately most (83%) of the MeV spectra in the sample, while the `Band` function is suitable for a smaller fraction (66%). The physical `IAP` function and the phenomenological `Band` function are good representations of GRB MeV spectra, but some differences were found between both parameterizations. A spectrum that is fitted with the `IAP` function appears a bit wider around its peak energy than with the `Band` function, yet it appears narrower when it is considered within a broader energy range. Besides, the fits with the `IAP` function return somewhat larger E_p values than with the `Band` function. As a result, the sharpness angle obtained from the `IAP` function fits is slightly larger, as already noted for the synthetic spectra. Finally, I

applied the IAP+CUTBPL model successfully to the prompt emission spectrum of GRB 090926A in the time intervals c and d where its high-energy break is detected. The quality of these fits would be obviously improved if more data were available at ∼10 MeV, or using a more realistic representation of the inverse Compton spectral component at these energies.

The sharpness angle of the synthetic spectrum is larger than that of any GRB in the GBM sample. The sharpness angle scales with the difference between the spectral indices, β-α. In the synchrotron fast-cooling regime, the high-energy spectral index β is equal to -(p/2+1), where p is the electron spectral index. For instance, p=2.7 and β=-2.3 for the synthetic burst. The value of p that is expected from the shock acceleration theory is not precisely known in the case of mildly-relativistic shocks such as internal shocks. However, typical values of p range from 2.3 to 2.9 as discussed in [Bošnjak and Daigne, 2014], thus the expected value of β is relatively constrained. Anyhow, the β value of -2.3 falls in the core of the distribution that is obtained from the GBM sample (Figs.6.35 and 6.36). Outside this distribution core, GRBs tend to have a softer and less constrained β, namely β seems to be underestimated because of the lack of signal in the BGO detectors above the peak energy. Therefore, these spectra would probably have a larger sharpness angle if they were measured more precisely around ∼1 MeV.

A second possibility to reconcile the theory with observations is given by the marginally fast-cooling regime that has been investigated in detail by [Daigne et al., 2011] and [Beniamini and Piran, 2013]. According to these authors, this regime can yield values of α up to -2/3, versus -1.2 for the synthetic burst used in my work. As mentioned in Sect.6.5.4, such an increase of 0.5 in α would reincorporate the synthetic burst into the bulk of the GBM sample. In the marginally fast-cooling regime, the electron energy losses are still dominated by radiative losses, but adiabatic losses become comparable. This regime could be reached in the case of internal shocks with a low contrast [Daigne et al., 2011]. Finally, specific choices of the microphysical parameters could alleviate the synchrotron line-of-death problem. In particular, more realistic configurations of the magnetic field in the shocked region should be investigated. Since the magnetic field is expected to decrease behind the shock and to be maximal at the shock where the more energetic electrons radiate, a varying magnetic field would harden the resulting synchrotron emission spectrum. In the future, it is thus essential to explore the parameter space of the IAP IS model and to improve its description of the shock microphysics in order to identify the physical configurations that best apply to the observations.

Conclusions and perspectives

Thanks to its large effective area and to the improved performance of the Pass 8 algorithms, the *Fermi*/LAT telescope detected more than 100 GRBs above few tens of MeV in 8 years of operation. The combined observations of GRBs with the *Fermi*/GBM and LAT instruments offer a unique opportunity to study their spectral and temporal properties over a broad energy range. In particular, the large number of *Fermi* GRBs allowed GRB population studies from keV to GeV energies for the first time, and investigations of their global properties. These observations provided new constraints for theoretical models of GRB high-energy emission. During my thesis, I had the opportunity to learn about these various aspects, from the observation of GRBs to their analysis and interpretation. Specifically, my work was devoted to the understanding of the prompt high-energy emission of GRBs. I focused on bright GRBs with well measured spectra in view of in-depth comparisons with the predictions of a theoretical model, which has been developed by collaborators at the "Institut d'Astrophysique de Paris" (IAP).

First of all, I acquired a strong expertise in the observation and analysis of GRBs during my thesis. I was on duty as Burst Advocate several times in three years, and I contributed to the analysis of GRB candidates in real time. I gained knowledge of the instruments (e.g., on-board and on-ground data processing algorithms, instrument performance) and I learnt the standard techniques to perform complete analyses of GRBs (detection, localization, spectral reconstruction).

An important part of my thesis work deals with the high-energy prompt emission of GRB 090926A. I performed a detailed time-resolved spectral analysis of this bright and highly variable burst with GBM and LAT Pass 8 data. Compared to past analyses of this burst, I extended the LAT spectral reach down to 30 MeV, which is now possible with Pass 8 data. I also paid a careful attention to the energy dispersion effect, which is the largest below 100 MeV. My results improve upon early

publications on this burst. Not only do they confirm with a greater significance the spectral break at ∼400 MeV that is observed during a short spike, but they also reveal the presence of a spectral attenuation throughout the GRB prompt emission, as well as an increase of the break energy up to the GeV domain. In collaboration with the IAP team, I interpreted the spectral break in terms of γ-ray absorption or as a natural curvature of the inverse Compton (IC) emission in the Klein-Nishina regime. Lower limits on the jet Lorentz factor were obtained in the latter hypothesis, while the former allowed a precise measurement of the jet velocity. The jet Lorentz factor was found to decrease from 230 to 100 at the end of the prompt emission. Combined with my estimates of the variability timescales from keV to GeV energies, these results lead to emission radii R $\sim 10^{14}$ cm, which are consistent with an internal origin of both the keV-MeV and GeV prompt emissions above the photosphere.

Understanding the physical processes at work in GRB jets requires the comparison of their spectral and temporal properties with dedicated theoretical models. However, most of the spectral models that are employed to characterize GRB prompt spectra are based on phenomenological or mathematical functions, like the `Band` function. For this reason, the second part of my thesis work is an exploration of the internal shock (IS) model that has been developed by the IAP team. This model simulates the GRB jet dynamics and the radiations (synchrotron and IC processes) from a population of shock-accelerated electrons. I simulated the response of the *Fermi* instruments to the synthetic GRB spectra provided by this numerical code. From these simulations, I built a new parametric function that is representative of the model and can be used as a proxy to fit the keV-MeV spectra of GRBs. I applied this function to a sample of 64 GBM bright GRBs and showed that it is able to reproduce most of their spectra. The spectral fits with the `IAP` physical function returns slightly larger peak energies and sharpness angles than the fits with the phenomenological `Band` function. Finally, I confronted the IAP model to the prompt emission spectrum of GRB 090926A. I obtained a relatively good agreement and I identified a couple of solutions that may improve it.

Many interesting studies should be considered to extend this work in the future. Firstly, it is worth trying to look for spectral breaks in the spectra of other LAT GRBs. Spectral analyses are now possible down to 30 MeV with LAT Pass 8 data, with a huge gain in event statistic below 100 MeV. Therefore, revisiting the time-resolved broadband spectral analyses of LAT bright GRBs is needed and could result in the detection of spectral breaks that were difficult to see in the past. Such a systematic re-analysis has not been performed yet, except for GRBs 100724B and 160509A [Vianello et al., 2017]. Besides, more spectral breaks will be certainly discovered with future GRB detections.

The detection of spectral breaks and/or very energetic photons can strongly constrain (or put limits on) the jet Lorentz factor when it is combined with accurate

estimates of the variability timescales. In the remarkable case of GRB 090926A, this allowed me also to demonstrate that the whole keV-to-GeV emission has an internal origin. This finding contrasts with the commonly-accepted scenario, which interprets (a fair fraction of) the GeV emission as the synchrotron radiation of electrons that are accelerated at the external shock. Unlike the prompt keV-MeV variable emission, the GeV emission evolves smoothly with time in this scenario. Therefore, the complete characterization of the variability is key to disentangle between both types of emission. Specifically, measuring the pulse shape and lags in the light curves, as well as their evolution with energy, would help to identify the respective contributions of the internal and external shocks to the emission that is detected by the LAT during the prompt keV-MeV emission. It would also help to better understand the transition to the long-lived emission detected at later times by the LAT. In practice, such an analysis could focus on the brightest LAT GRBs with high photon statistic above hundreds of MeV. The observed temporal properties would then be compared with the predictions of the IS model (e.g. [Bošnjak and Daigne, 2014]).

In the future, the IAP IS model should be further tested using other LAT GRBs that have an additional high-energy component (e.g. the short GRB 090510). As mentioned above, the model accounts for the spectrum of GRB 090926A quite well. However, the peak energy of the IC component in the model is much higher than the observed break energies of GRB 090926A. Simulations of realistic synthetic spectra are thus required on a case by case basis. More generally, the parameter space of the IAP IS model needs to be thoroughly explored to find the configurations that best apply to the observations. In particular, it is fundamental to identify which microphysical parameters (e.g., marginally fast-cooling regime, varying magnetic field) could improve the data-model agreement in terms of synchrotron indices and spectral sharpness. Once benchmark models are defined, one could try to perform non-parametric spectral fits to constrain directly the model parameters without using the `IAP` function as a proxy anymore. On the observational side, significant progress will be also possible with *Fermi* and with future GRB-dedicated missions like SVOM. SVOM will provide a large sample of GRBs with measured redshift and it will observe their emission in the prompt phase until the late aferglow phase. SVOM will measure the GRB prompt emission spectra with great precision, from very low energies thanks to the 4-keV threshold of its main instrument ECLAIRs up to MeV energies with the GRM, providing new and invaluable information on the underlying physical processes.

APPENDIX A

Maximum likelihood method

A.1 Unbinned likelihood analysis

The probability density of a photon arriving at time t, at the measured energy E′ and direction $\hat{p}'$ is given by:

$$M_l(E', \hat{p}', t) = \int_{SR} dE d\hat{p} R(E, \hat{p}; E', \hat{p}', t) S(E, \hat{p}, \Lambda) \tag{A.1}$$

where $\Lambda = \{\lambda\}$ represents the set of the model parameters, $\hat{p}'$ and E' are the measured direction and the energy. $S(E, \hat{p}, \Lambda)$ is the differential spectrum in units $photons/cm^2/s/keV/sr$, assuming that the flux is independent of time. $R(E, \hat{p}; E', \hat{p}')$ is the product of the LAT IRFs (Eq.2.3). The integral in Eq.A.1 is taken over the entire source region (SR), which contains the sources that may contribute to the observed signal (see Sect.3.2.2). Since the bins in this method are very small (of size $dE' \times d\hat{p}' \times dt$), the distribution of photons M in each bin can be characterized by a Poisson distribution. Thus, the probability to have no events in such a bin is given by:

$$\exp^{-M(E', \hat{p}', t) dE' d\hat{p}' dt} \tag{A.2}$$

This equation must be multiplied by the factor $M(E', \hat{p}', t) dE' d\hat{p}' dt$ to obtain the probability of having only one photon in the same 3D bin. Then the likelihood function is given by:

$$\mathcal{L}(\{x_i\}, \Lambda) = \prod_i M(E'_i, \hat{p}'_i, t_i) dE' d\hat{p}' dt \times \prod_{k=i,j} \exp^{-M(E'_k, \hat{p}'_k, t_k) dE'_k d\hat{p}' dt} \tag{A.3}$$

where the index i refers to the bins that contain one single event, and j to the empty bins. The likelihood in logarithmic scale becomes:

$$\ln \mathcal{L}(\{x_i\}, \Lambda) = \sum_i \ln M(E'_i, \hat{p}'_i, t_i) + \sum_i \ln(dE' d\hat{p}' dt) - \int M(E', \hat{p}', t) dE' d\hat{p}' dt \tag{A.4}$$

The second term in this equation is a fixed sum over the observed counts and is independent on the model parameters. It can thus be ignored in the comparison between different models. The third term of Eq.A.4 is the number of the photons predicted by the model (N_{pred}). Therefore, Eq.A.4 becomes:

$$\ln \mathcal{L}(\{x_i\}, \Lambda) = \sum_i \ln M(E'_i, \hat{p}'_i, t_i) - N_{pred} \tag{A.5}$$

A.2 Binned likelihood analysis

For data binned in (E',$\hat{p}'$), the number of photons predicted by the model for the combination of the point and diffuse sources indexed by l, in the energy bin k is:

$$H_k = \sum_l H_{lk} \tag{A.6}$$

where H_{lk} is expressed as:

$$H_{lk} = \int_k dE' d\hat{p}' \int dt \int_{ROI} dE d\hat{p} S_l(E, \hat{p}) R(E', \hat{p}'; E, \hat{p}, t) \tag{A.7}$$

The binned likelihood function reads:

$$\mathcal{L}(\{x_i\}, \Lambda) = \prod_{k=1}^{n_k} \frac{H_k^{n_k} \exp^{-H_k}}{n_k!} \tag{A.8}$$

Where n_k is the number of the observed counts in each bin. The logarithm of this likelihood gives an expression that is similar to Eq.A.5:

$$\ln \mathcal{L}(\{x_i\}, \Lambda) = \sum_k n_k \ln H_k - N_{pred} \tag{A.9}$$

APPENDIX B

Count spectra and fit residuals of of GRB 090926A

This section presents the count spectra and fit residuals obtained with the `Band` + CUTPL and `Band` + CUTBPL models for the time intervals c and d of GRB 090926A.

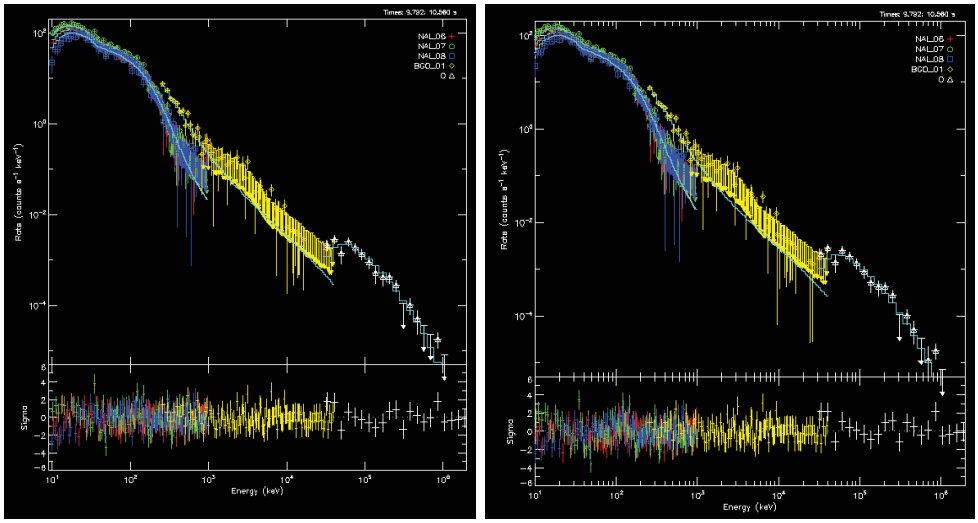

Figure B.1: *Count spectra (top panels) and fit residuals (bottom panels) of GRB 090926A during the time interval c [9.8 s, 10.5 s] with the* `Band` *+ CUTPL model (left) and the* `Band` *+ CUTBPL model (right).*

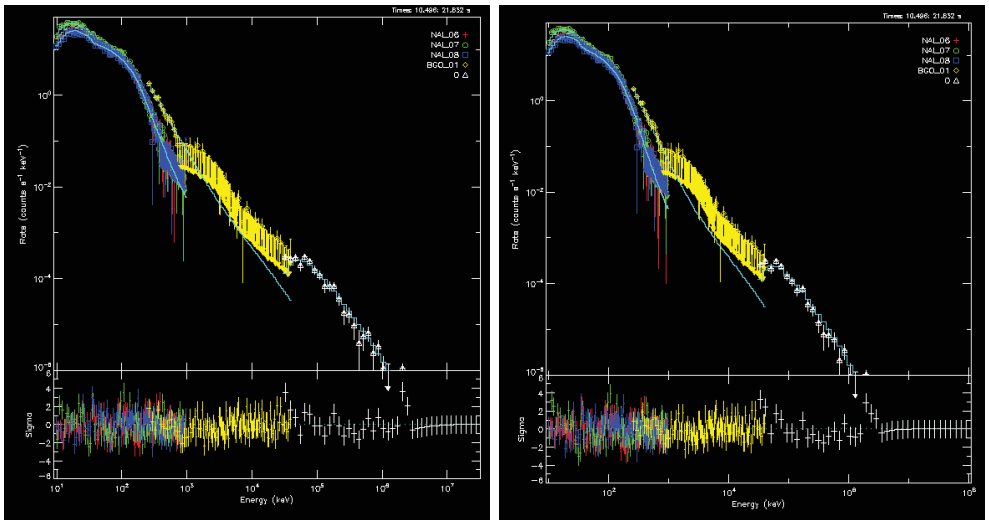

Figure B.2: *Count spectra (top panels) and fit residuals (bottom panels) of GRB 090926A duringg the time interval d [10.5 s, 21.6 s] with the* `Band` *+ CUTPL model (left) and the* `Band` *+ CUTBPL model (right).*

APPENDIX C

Derivation of the IAP function and fit results

This appendix describes how the mathematical formula of the `IAP` fit function has been derived. Then, the results of the fits of the synthetic and real (GBM) bursts are summarized.

C.1 Derivation of the `IAP` function

Starting from Eq.6.7, one can write

$$\frac{\partial \ln(F(E))}{\partial \ln(E)} = E \times \frac{\partial \ln(F(E))}{\partial E} = -a + \frac{b}{(E + X_0)} \tag{C.1}$$

The integration of this function with respect to E gives:

$$\begin{aligned} \ln(F(E)) &= \int \left(-\frac{a}{E} + \frac{b}{E(E+X_0)} \right) dE && \text{(C.2)} \\ &= -a \ln E + b \int \frac{dE}{E(E+X_0)} && \text{(C.3)} \\ &= -a \ln E + b \times \left(\int \frac{dE}{EX_0} - \int \frac{dE}{X_0(E+X_0)} \right) && \text{(C.4)} \\ &= -a \ln E + \frac{b}{X_0} \ln \left(\frac{E}{E+X_0} \right) + c && \text{(C.5)} \end{aligned}$$

with c the integration constant. At a given E_r, c is equal to:

$$c = \ln(F(E_r)) + a \ln E_r - \frac{b}{X_0} \ln \left(\frac{E_r}{E_r + X_0} \right) \tag{C.6}$$

The exponential of Eq.C.5, gives:

$$F(E) = F(E_r)exp\left(-a\ln\left[\frac{E}{E_r}\right]\right)exp\left(\frac{b}{X_0}\ln\left[\frac{E(E_r+X_0)}{E_r(E+X_0)}\right]\right) \quad (C.7)$$

$$= F(E_r)\left(\frac{E}{E_r}\right)^{-a+d}\times\left(\frac{E+X_0}{E_r+X_0}\right)^{-d} \quad (C.8)$$

with $d = b/X_0$. For E $\to$ 0, $F(E) \propto E^{d-a}$, and for E $\to \infty$, $F(E) \propto E^{-a}$. We thus define $\alpha = d - a$, $\beta = -a$, $\delta = \beta - \alpha = -d$, $b = -E_1$ such that $b/d = E_1/\delta = X_0$. Therefore, Eq.C.8 becomes:

$$F(E) = F(E_r)\left(\frac{E}{E_r}\right)^{\alpha}\left(\frac{E+E_1/\delta}{E_r+E_1/\delta}\right)^{\delta} \quad (C.9)$$

$$= F(E_r)U^{\alpha}\left(\frac{U+U_1/\delta}{1+U_1/\delta}\right)^{\delta} \quad (C.10)$$

with U= E/E_r and U_1= E_1/E_r.
The SED can be expressed as:

$$\nu F_\nu = E^2F(E) = F(E_r)U^{\alpha+2}\left(\frac{U+U_1/\delta}{1+U_1/\delta}\right)^{\delta} \quad (C.11)$$

The solution of:

$$\frac{\partial \ln E^2F(E)}{\partial(E/E_r)} = 0 \quad (C.12)$$

gives the peak energy of this function:

$$E_p = \frac{-E_1(\alpha+2)}{(\beta-\alpha)(\beta+2)} = \frac{-X_0(\alpha+2)}{(\beta+2)} \quad (C.13)$$

Replacing these terms in Eq.C.10, we get the `IAP` function:

$$F_{MeV}(E) = A_{IAP}\left(\frac{E}{E_r}\right)^{\alpha}\left(\frac{E-E_p(2+\beta)/(2+\alpha)}{E_r-E_p(2+\beta)/(2+\alpha)}\right)^{\delta} \quad (C.14)$$

$$(C.15)$$

C.2 Spectral analysis of synthetic bursts

We present the results of the spectral analyses of the three synthetic bursts caseBp27zetavar_z007, caseBp27zetavar_z007_10 and caseBp27zetavar_z007_100 in the time intervals [0 s, 1 s], [3 s, 6 s] and [0 s, 6 s]. These analyses are performed using the five spectral functions: `Band`, `logpar`, `modiflog`, `doublemodif` and `IAP`. Each figure represents the three bursts in a defined time interval.

C.3 Spectral analysis of GBM bursts

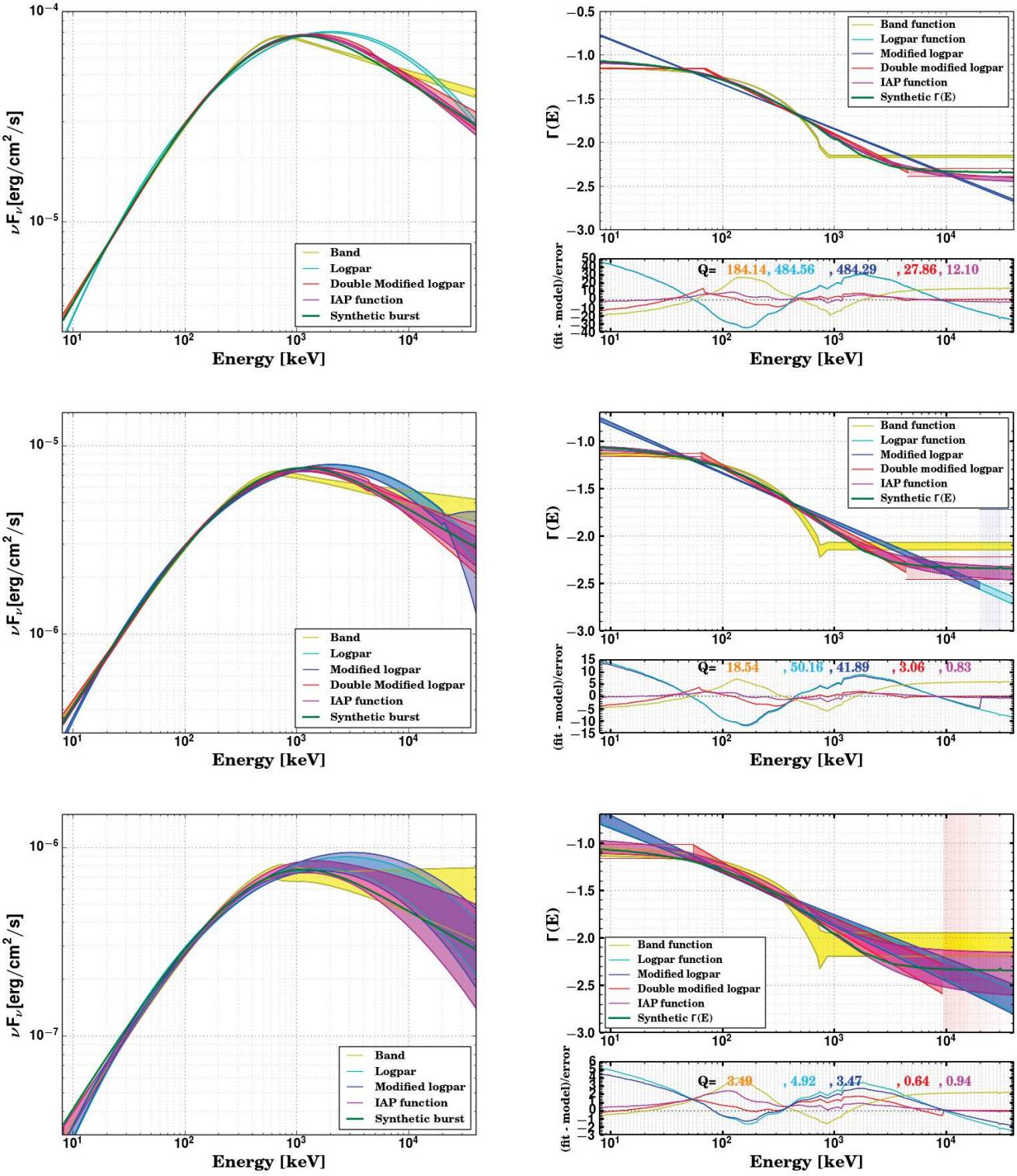

Figure C.1: *Results of the spectral fits for the* GRB_B001, GRB_B010 *and* GRB_B100 *synthetic bursts (from top to bottom) in the time interval [0 s, 1 s].*

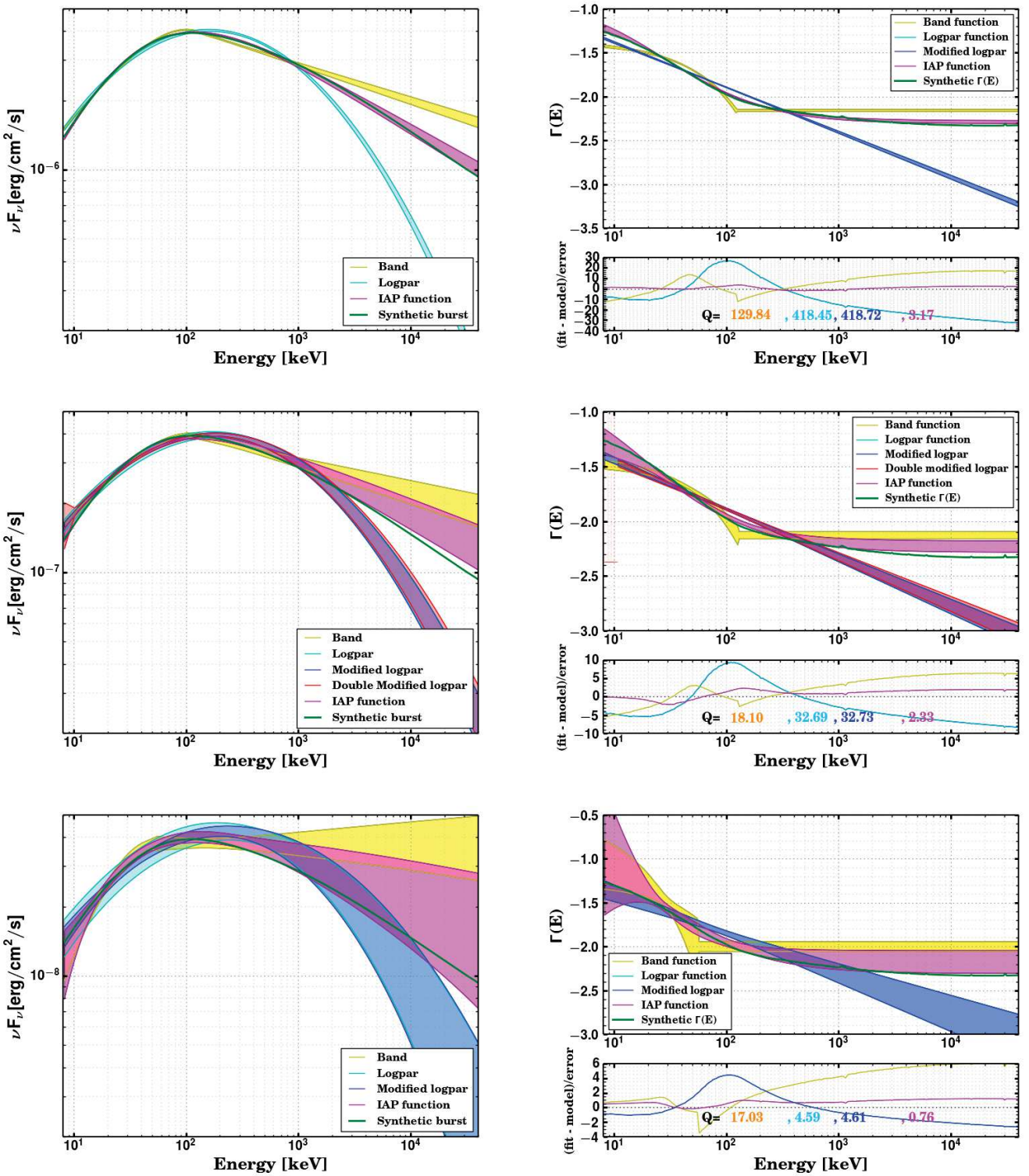

Figure C.2: *Results of the spectral fits for the* GRB_B001, GRB_B010 *and* GRB_B100 *synthetic bursts (from top to bottom) in the time interval [3 s, 6 s].*

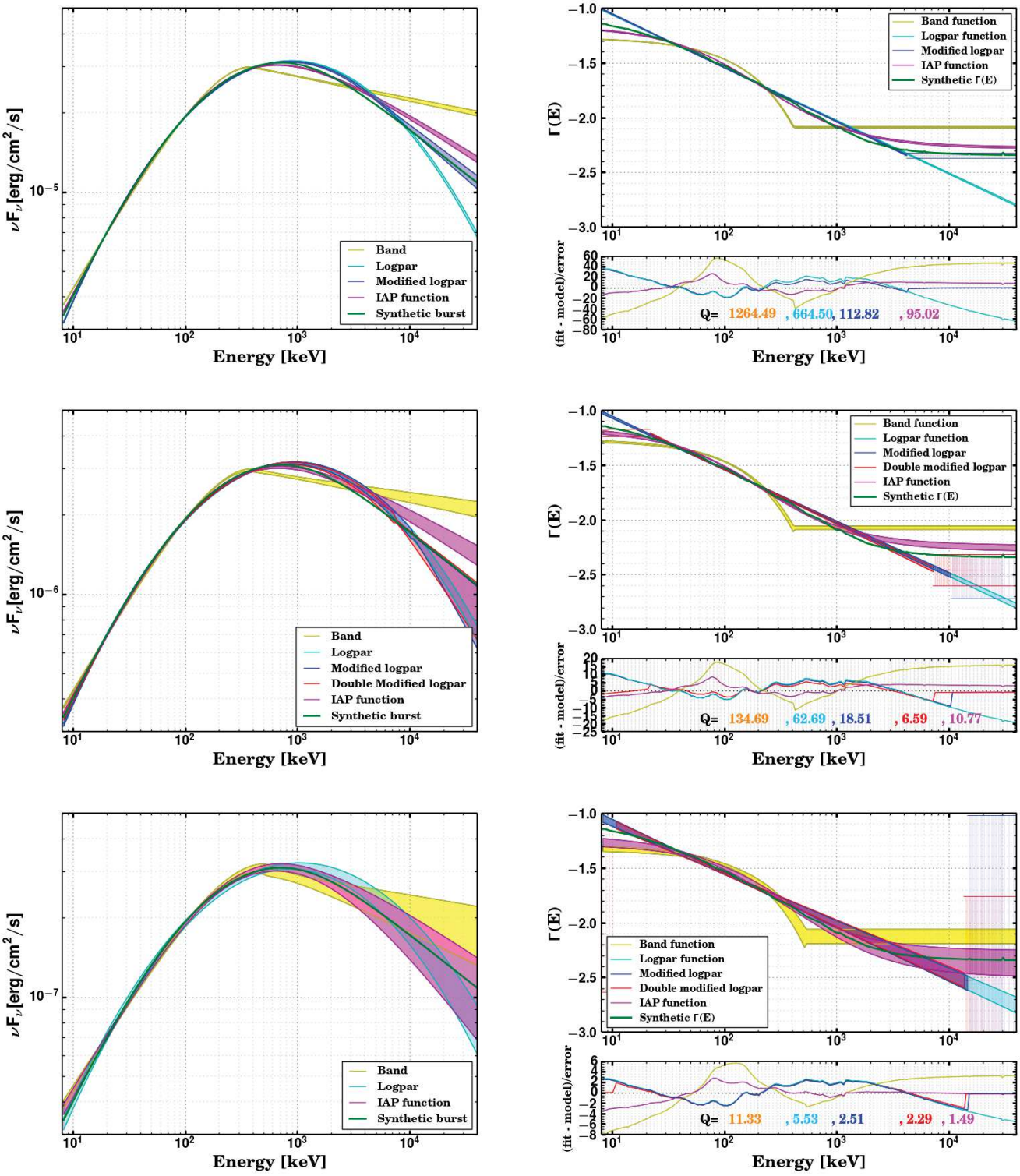

Figure C.3: *Results of the spectral fits for the* GRB_B001, GRB_B010 *and* GRB_B100 *synthetic bursts (from top to bottom) in the time interval [0 s, 6 s].*

Table C.1: *Results of the* `Band` *and* `IAP` *spectral fits to GBM data for the prompt emission of 64 GRBs.*

Bursts	**models**	$\mathbf{E}_{peak}$	α	α_{10}	β	β_b	**A** ($\times 10^{-4}$)
GRB080817161	`Band`	409.72 ± 14.01	-0.96 ± 0.01	-0.99 ± 0.01	-2.32 ± 0.08	-2.32 ± 0.08	145.36 ± 2.25
	`IAP`	508.57 ± 11.49	-0.88 ± 0.02	-0.93 ± 0.01	-3.13 ± 0.25	-2.04 ± 0.02	8.92 ± 0.16
GRB080825593	`Band`	186.87 ± 6.89	-0.64 ± 0.03	-0.72 ± 0.03	-2.35 ± 0.10	-2.35 ± 0.10	640.91 ± 29.67
	`IAP`	210.99 ± 5.01	-0.56 ± 0.06	-0.66 ± 0.04	-5.19 ± 1.22	-2.12 ± 0.03	10.59 ± 0.21
GRB081125496	`Band`	183.47 ± 8.49	-0.51 ± 0.05	-0.59 ± 0.05	-3.00 ± 0.92	-3.00 ± 0.92	913.02 ± 71.95
	`IAP`	187.31 ± 6.24	-0.40 ± 0.09	-0.51 ± 0.07	-7.06 ± 2.56	-2.64 ± 0.09	10.18 ± 0.73
GRB081207680	`Band`	704.92 ± 39.63	-0.77 ± 0.02	-0.79 ± 0.02	-2.62 ± 0.28	-2.62 ± 0.28	75.05 ± 1.40
	`IAP`	868.35 ± 38.90	-0.69 ± 0.04	-0.72 ± 0.03	-3.37 ± 0.28	-2.13 ± 0.04	8.64 ± 0.19
GRB081224887	`Band`	403.93 ± 9.99	-0.71 ± 0.01	-0.74 ± 0.01	-9.09 ± 1.58	-9.09 ± 1.58	371.54 ± 6.45
	`IAP`	410.61 ± 7.32	-0.67 ± 0.01	-0.71 ± 0.01	-10.00 ± 1.50	-5.46 ± 0.31	23.82 ± 0.27
GRB090328401	`Band`	754.28 ± 50.91	-1.05 ± 0.02	-1.06 ± 0.01	-2.44 ± 0.19	-2.44 ± 0.19	98.44 ± 1.74
	`IAP`	897.28 ± 80.08	-1.04 ± 0.02	-1.06 ± 0.02	-4.37 ± 1.42	-2.14 ± 0.08	9.59 ± 0.17
GRB090528516	`Band`	153.88 ± 7.43	-0.84 ± 0.04	-0.92 ± 0.04	-2.04 ± 0.05	-2.04 ± 0.05	197.09 ± 13.74
	`IAP`	240.55 ± 23.72	-0.57 ± 0.14	-0.77 ± 0.08	-2.55 ± 0.18	-1.83 ± 0.04	3.89 ± 0.18
GRB090618353	`Band`	164.47 ± 2.86	-1.10 ± 0.01	-1.16 ± 0.01	-2.46 ± 0.04	-2.46 ± 0.04	720.37 ± 15.11
	`IAP`	171.00 ± 2.48	-0.93 ± 0.03	-1.04 ± 0.02	-3.15 ± 0.11	-2.20 ± 0.01	13.04 ± 0.21
GRB090718762	`Band`	170.47 ± 4.91	-1.11 ± 0.01	-1.17 ± 0.01	-2.69 ± 0.18	-2.69 ± 0.18	311.84 ± 7.93
	`IAP`	172.66 ± 2.44	-1.02 ± 0.02	-1.10 ± 0.01	-4.22 ± 0.57	-2.41 ± 0.04	5.29 ± 0.25
GRB090719063	`Band`	239.91 ± 1.94	-0.54 ± 0.02	-0.60 ± 0.02	-2.95 ± 0.12	-2.95 ± 0.12	1281.06 ± 30.25
	`IAP`	249.80 ± 3.58	-0.45 ± 0.03	-0.53 ± 0.03	-6.62 ± 0.94	-2.59 ± 0.03	30.87 ± 0.61
GRB090809978	`Band`	175.19 ± 10.18	-0.74 ± 0.03	-0.81 ± 0.03	-1.98 ± 0.04	-1.98 ± 0.04	677.12 ± 35.31
	`IAP`	343.79 ± 45.78	-0.40 ± 0.10	-0.62 ± 0.06	-2.37 ± 0.09	-1.75 ± 0.02	16.66 ± 0.46
GRB090829672	`Band`	196.06 ± 8.82	-1.42 ± 0.01	-1.45 ± 0.01	-2.36 ± 0.10	-2.36 ± 0.10	280.38 ± 7.64
	`IAP`	208.34 ± 10.43	-1.33 ± 0.04	-1.39 ± 0.03	-2.64 ± 0.17	-2.13 ± 0.02	7.96 ± 0.19

Continued on next page

Table C.1 – *Continued from previous page*

Bursts	**models**	$\mathbf{E}_{peak}$	α	α_{10}	β	β_b	**A** ($\times 10^{-4}$)
GRB091003191	Band	396.88 ± 16.19	-0.94 ± 0.02	-0.97 ± 0.02	-2.59 ± 0.19	-2.59 ± 0.19	272.33 ± 6.84
	IAP	428.59 ± 19.34	-0.92 ± 0.03	-0.95 ± 0.03	-5.95 ± 2.07	-2.35 ± 0.06	16.14 ± 0.46
GRB091120191	Band	135.54 ± 4.86	-1.16 ± 0.03	-1.23 ± 0.02	-2.92 ± 0.28	-2.92 ± 0.28	193.47 ± 9.35
	IAP	134.24 ± 3.82	-1.08 ± 0.02	-1.17 ± 0.01	-4.83 ± 1.89	-2.62 ± 0.15	2.09 ± 0.25
GRB091128285	Band	192.18 ± 1.50	-0.95 ± 0.01	-1.01 ± 0.01	-2.58 ± 0.16	-2.58 ± 0.16	160.04 ± 1.41
	IAP	199.23 ± 1.63	-0.92 ± 0.02	-0.98 ± 0.01	-6.62 ± 1.66	-2.41 ± 0.04	2.84 ± 0.03
GRB100322045	Band	333.28 ± 9.65	-0.88 ± 0.01	-0.92 ± 0.01	-2.20 ± 0.04	-2.20 ± 0.04	306.74 ± 5.55
	IAP	486.50 ± 23.09	-0.69 ± 0.03	-0.78 ± 0.02	-2.60 ± 0.07	-1.91 ± 0.02	15.56 ± 0.20
GRB100324172	Band	460.55 ± 11.66	-0.58 ± 0.02	-0.61 ± 0.02	-5.60 ± 1.46	-5.60 ± 1.46	369.11 ± 6.44
	IAP	468.00 ± 9.16	-0.54 ± 0.02	-0.58 ± 0.02	-10.00 ± 1.50	-4.17 ± 0.17	30.46 ± 0.49
GRB100414097	Band	637.47 ± 11.74	-0.53 ± 0.01	-0.55 ± 0.01	-4.95 ± 1.86	-4.95 ± 1.86	349.27 ± 3.72
	IAP	651.08 ± 12.47	-0.49 ± 0.01	-0.52 ± 0.01	-10.00 ± 5.00	-3.84 ± 0.39	46.07 ± 0.32
GRB100511035	Band	624.56 ± 38.05	-1.28 ± 0.01	-1.29 ± 0.01	-9.37 ± 1.37	-9.37 ± 1.37	94.05 ± 1.52
	IAP	655.78 ± 50.56	-1.28 ± 0.01	-1.29 ± 0.01	-10.00 ± 1.50	-5.53 ± 0.42	6.75 ± 0.12
GRB100612726	Band	113.48 ± 1.98	-0.57 ± 0.04	-0.70 ± 0.03	-2.55 ± 0.07	-2.55 ± 0.07	1289.89 ± 79.25
	IAP	121.01 ± 1.64	-0.25 ± 0.04	-0.52 ± 0.02	-3.80 ± 0.32	-2.22 ± 0.02	6.29 ± 0.57
GRB100707032	Band	266.40 ± 13.58	-0.69 ± 0.03	-0.74 ± 0.03	-2.08 ± 0.05	-2.08 ± 0.05	236.12 ± 10.32
	IAP	503.71 ± 61.14	-0.36 ± 0.08	-0.52 ± 0.06	-2.39 ± 0.10	-1.78 ± 0.02	9.74 ± 0.18
GRB100719989	Band	320.94 ± 11.97	-0.69 ± 0.03	-0.73 ± 0.02	-2.41 ± 0.08	-2.41 ± 0.08	462.21 ± 14.61
	IAP	383.62 ± 12.76	-0.56 ± 0.04	-0.63 ± 0.03	-3.55 ± 0.34	-2.08 ± 0.03	22.35 ± 0.43
GRB100829876	Band	135.62 ± 4.88	-0.60 ± 0.08	-0.71 ± 0.07	-2.04 ± 0.04	-2.04 ± 0.04	945.71 ± 104.21
	IAP	231.85 ± 29.50	-0.15 ± 0.09	-0.48 ± 0.03	-2.49 ± 0.16	-1.78 ± 0.06	13.79 ± 0.84
GRB100910818	Band	158.62 ± 9.61	-0.94 ± 0.01	-1.01 ± 0.01	-2.46 ± 0.11	-2.46 ± 0.11	375.55 ± 8.33
	IAP	168.41 ± 1.89	-0.84 ± 0.03	-0.94 ± 0.02	-4.42 ± 0.78	-2.25 ± 0.03	5.08 ± 0.44
GRB100918863	Band	561.71 ± 2.73	-0.80 ± 0.01	-0.83 ± 0.01	-2.74 ± 0.12	-2.74 ± 0.12	204.65 ± 0.97
	IAP	611.84 ± 9.53	-0.76 ± 0.01	-0.79 ± 0.01	-5.05 ± 0.14	-2.38 ± 0.02	18.93 ± 0.25

Continued on next page

Table C.1 – *Continued from previous page*

Bursts	**models**	$\mathbf{E}_{peak}$	α	α_{10}	β	β_b	**A** ($\times 10^{-4}$)
GRB101014175	Band	210.13 ± 4.37	-1.17 ± 0.01	-1.21 ± 0.01	-2.79 ± 0.11	-2.79 ± 0.11	624.70 ± 11.51
	IAP	217.83 ± 5.06	-1.16 ± 0.01	-1.20 ± 0.01	-9.04 ± 3.19	-2.61 ± 0.03	14.63 ± 0.35
GRB101023951	Band	185.07 ± 7.23	-1.22 ± 0.03	-1.26 ± 0.02	-2.58 ± 0.14	-2.58 ± 0.14	219.54 ± 9.84
	IAP	186.53 ± 6.38	-1.12 ± 0.03	-1.19 ± 0.02	-3.61 ± 0.48	-2.33 ± 0.04	4.73 ± 0.19
GRB101126198	Band	135.21 ± 0.94	-1.29 ± 0.01	-1.35 ± 0.01	-2.65 ± 0.17	-2.65 ± 0.17	210.96 ± 1.26
	IAP	140.04 ± 1.40	-1.28 ± 0.01	-1.34 ± 0.01	-8.81 ± 0.29	-2.50 ± 0.01	2.48 ± 0.05
GRB101231067	Band	213.73 ± 1.57	-0.75 ± 0.02	-0.81 ± 0.01	-9.99 ± 4.99	-9.99 ± 4.99	251.19 ± 3.14
	IAP	215.74 ± 4.01	-0.70 ± 0.04	-0.78 ± 0.03	-8.07 ± 2.97	-5.21 ± 0.95	4.63 ± 0.15
GRB110301214	Band	110.11 ± 0.64	-0.83 ± 0.02	-0.95 ± 0.02	-2.73 ± 0.05	-2.73 ± 0.05	4242.40 ± 123.65
	IAP	109.54 ± 1.68	-0.59 ± 0.04	-0.80 ± 0.03	-4.03 ± 0.18	-2.41 ± 0.01	22.02 ± 0.85
GRB110622158	Band	105.22 ± 0.88	-0.64 ± 0.03	-0.78 ± 0.03	-2.44 ± 0.04	-2.44 ± 0.04	540.93 ± 24.73
	IAP	113.91 ± 1.96	-0.17 ± 0.06	-0.52 ± 0.03	-3.28 ± 0.14	-2.15 ± 0.01	2.87 ± 0.15
GRB110625881	Band	179.29 ± 4.30	-0.77 ± 0.02	-0.84 ± 0.02	-2.33 ± 0.04	-2.33 ± 0.04	929.25 ± 26.40
	IAP	209.56 ± 3.40	-0.53 ± 0.05	-0.68 ± 0.03	-3.16 ± 0.14	-2.05 ± 0.01	17.44 ± 0.33
GRB110717319	Band	375.83 ± 4.71	-1.01 ± 0.01	-1.04 ± 0.01	-9.37 ± 1.57	-9.37 ± 1.57	98.22 ± 0.76
	IAP	369.87 ± 6.63	-0.98 ± 0.01	-1.01 ± 0.01	-10.00 ± 1.50	-5.73 ± 0.36	5.08 ± 0.06
GRB110729142	Band	306.63 ± 11.10	-1.02 ± 0.02	-1.05 ± 0.01	-2.21 ± 0.15	-2.21 ± 0.15	34.97 ± 0.85
	IAP	389.85 ± 26.16	-0.91 ± 0.07	-0.97 ± 0.05	-2.89 ± 0.31	-1.97 ± 0.03	1.56 ± 0.04
GRB110731465	Band	306.78 ± 14.55	-0.87 ± 0.02	-0.91 ± 0.02	-2.88 ± 0.65	-2.88 ± 0.65	565.46 ± 14.37
	IAP	321.86 ± 9.17	-0.86 ± 0.02	-0.90 ± 0.02	-10.00 ± 1.50	-2.63 ± 0.05	23.34 ± 0.64
GRB110825102	Band	261.70 ± 1.83	-1.07 ± 0.01	-1.11 ± 0.01	-2.72 ± 0.31	-2.72 ± 0.31	176.75 ± 1.15
	IAP	267.34 ± 1.34	-1.05 ± 0.01	-1.09 ± 0.01	-10.00 ± 1.50	-2.57 ± 0.02	5.60 ± 0.04
GRB110921912	Band	512.93 ± 19.82	-0.88 ± 0.01	-0.90 ± 0.01	-2.36 ± 0.09	-2.36 ± 0.09	283.29 ± 5.40
	IAP	678.30 ± 42.91	-0.78 ± 0.04	-0.82 ± 0.03	-2.89 ± 0.19	-2.00 ± 0.03	22.38 ± 0.44
GRB111003465	Band	204.70 ± 7.26	-0.95 ± 0.02	-1.00 ± 0.02	-2.43 ± 0.10	-2.43 ± 0.10	393.96 ± 16.08
	IAP	227.99 ± 9.30	-0.86 ± 0.06	-0.95 ± 0.04	-3.76 ± 0.57	-2.17 ± 0.04	9.30 ± 0.44

Continued on next page

Table C.1 – *Continued from previous page*

Bursts	**models**	$\mathbf{E}_{peak}$	α	α_{10}	β	β_b	**A** ($\times 10^{-4}$)
GRB111216389	Band	164.83 ± 4.56	-0.91 ± 0.03	-0.98 ± 0.03	-2.30 ± 0.06	-2.30 ± 0.06	198.65 ± 9.45
	IAP	197.36 ± 6.96	-0.79 ± 0.07	-0.90 ± 0.05	-3.30 ± 0.30	-2.04 ± 0.02	3.54 ± 0.18
GRB111220486	Band	300.15 ± 9.89	-1.05 ± 0.01	-1.08 ± 0.01	-2.30 ± 0.07	-2.30 ± 0.07	308.09 ± 5.75
	IAP	371.11 ± 14.97	-0.96 ± 0.01	-1.02 ± 0.00	-3.01 ± 0.15	-2.03 ± 0.02	13.22 ± 0.22
GRB120119170	Band	207.70 ± 1.03	-1.03 ± 0.01	-1.08 ± 0.01	-2.54 ± 0.10	-2.54 ± 0.10	206.86 ± 1.32
	IAP	225.54 ± 2.80	-0.97 ± 0.01	-1.04 ± 0.01	-4.37 ± 0.30	-2.28 ± 0.02	4.96 ± 0.04
GRB120129580	Band	298.58 ± 7.01	-0.68 ± 0.02	-0.73 ± 0.02	-2.56 ± 0.07	-2.56 ± 0.07	3845.27 ± 99.62
	IAP	336.56 ± 8.02	-0.47 ± 0.03	-0.56 ± 0.03	-3.28 ± 0.18	-2.16 ± 0.02	157.28 ± 2.38
GRB120204054	Band	163.17 ± 1.63	-1.08 ± 0.01	-1.14 ± 0.01	-2.58 ± 0.05	-2.58 ± 0.05	612.23 ± 11.11
	IAP	171.31 ± 2.55	-1.01 ± 0.02	-1.09 ± 0.02	-4.31 ± 0.30	-2.33 ± 0.01	9.72 ± 0.20
GRB120226871	Band	300.69 ± 11.26	-0.89 ± 0.02	-0.93 ± 0.02	-2.26 ± 0.08	-2.26 ± 0.08	231.03 ± 7.50
	IAP	397.03 ± 20.65	-0.76 ± 0.04	-0.83 ± 0.03	-2.89 ± 0.22	-1.96 ± 0.02	10.27 ± 0.19
GRB120328268	Band	193.59 ± 3.98	-0.78 ± 0.02	-0.85 ± 0.01	-2.00 ± 0.02	-2.00 ± 0.02	798.83 ± 20.96
	IAP	385.30 ± 22.74	-0.47 ± 0.05	-0.66 ± 0.02	-2.35 ± 0.05	-1.77 ± 0.03	22.73 ± 0.29
GRB120426090	Band	134.55 ± 3.04	-0.59 ± 0.03	-0.70 ± 0.03	-2.94 ± 0.12	-2.94 ± 0.12	4721.45 ± 208.45
	IAP	132.16 ± 2.74	-0.28 ± 0.07	-0.50 ± 0.05	-4.49 ± 0.42	-2.57 ± 0.03	27.07 ± 1.56
GRB120624933	Band	582.53 ± 83.01	-0.97 ± 0.05	-0.98 ± 0.05	-2.05 ± 0.16	-2.05 ± 0.16	18.04 ± 0.93
	IAP	1106.56 ± 456.83	-0.96 ± 0.07	-0.98 ± 0.07	-2.62 ± 0.51	-1.77 ± 0.10	1.59 ± 0.07
GRB120711115	Band	1276.70 ± 30.55	-0.95 ± 0.01	-0.96 ± 0.01	-3.11 ± 0.13	-3.11 ± 0.13	384.84 ± 2.47
	IAP	1359.88 ± 27.18	-0.95 ± 0.01	-0.96 ± 0.01	-8.68 ± 1.64	-2.74 ± 0.04	54.75 ± 0.23
GRB130327350	Band	375.29 ± 7.72	-0.61 ± 0.02	-0.65 ± 0.01	-9.37 ± 2.22	-9.37 ± 2.22	287.50 ± 4.77
	IAP	379.19 ± 8.04	-0.57 ± 0.02	-0.62 ± 0.01	-10.00 ± 1.50	-5.53 ± 0.31	16.73 ± 0.29
GRB130502327	Band	292.55 ± 4.75	-0.50 ± 0.01	-0.55 ± 0.01	-2.36 ± 0.04	-2.36 ± 0.04	972.46 ± 16.00
	IAP	354.20 ± 5.16	-0.35 ± 0.02	-0.44 ± 0.02	-3.72 ± 0.16	-2.03 ± 0.01	41.59 ± 0.40
GRB130504978	Band	653.58 ± 28.97	-1.20 ± 0.01	-1.21 ± 0.01	-2.27 ± 0.07	-2.27 ± 0.07	232.01 ± 2.32
	IAP	866.88 ± 40.66	-1.18 ± 0.01	-1.19 ± 0.01	-3.05 ± 0.17	-2.00 ± 0.02	18.13 ± 0.18

Continued on next page

Table C.1 – *Continued from previous page*

Bursts	**models**	$\mathbf{E}_{peak}$	α	α_{10}	β	β_b	**A** ($\times 10^{-4}$)
GRB130518580	Band	386.97 ± 10.40	-0.87 ± 0.01	-0.90 ± 0.01	-2.22 ± 0.05	-2.22 ± 0.05	329.76 ± 5.71
	IAP	538.71 ± 20.38	-0.78 ± 0.02	-0.83 ± 0.02	-2.93 ± 0.14	-1.92 ± 0.02	20.30 ± 0.24
GRB130609902	Band	531.37 ± 13.31	-0.98 ± 0.02	-1.00 ± 0.02	-9.37 ± 1.77	-9.37 ± 1.77	46.99 ± 0.70
	IAP	538.60 ± 31.42	-0.96 ± 0.02	-0.98 ± 0.01	-9.37 ± 3.80	-5.45 ± 1.01	3.66 ± 0.08
GRB131028076	Band	847.78 ± 15.15	-0.64 ± 0.01	-0.66 ± 0.01	-2.55 ± 0.03	-2.55 ± 0.03	790.86 ± 5.71
	IAP	952.50 ± 8.64	-0.61 ± 0.00	-0.63 ± 0.00	-6.16 ± 0.22	-2.27 ± 0.01	125.00 ± 0.52
GRB140306146	Band	1528.75 ± 72.96	-1.01 ± 0.01	-1.02 ± 0.01	-5.09 ± 1.80	-5.09 ± 1.80	125.79 ± 1.27
	IAP	1535.17 ± 62.10	-1.00 ± 0.01	-1.01 ± 0.01	-10.00 ± 1.50	-4.05 ± 0.12	17.74 ± 0.20
GRB140508128	Band	264.42 ± 13.07	-1.01 ± 0.02	-1.05 ± 0.02	-2.11 ± 0.04	-2.11 ± 0.04	312.00 ± 11.08
	IAP	433.60 ± 43.55	-0.83 ± 0.06	-0.93 ± 0.04	-2.41 ± 0.10	-1.87 ± 0.02	12.43 ± 0.25
GRB140523129	Band	269.26 ± 7.07	-0.90 ± 0.01	-0.94 ± 0.01	-2.69 ± 0.13	-2.69 ± 0.13	632.36 ± 9.31
	IAP	284.58 ± 3.58	-0.83 ± 0.01	-0.89 ± 0.01	-4.71 ± 0.37	-2.39 ± 0.02	21.43 ± 0.27
GRB140810782	Band	308.85 ± 5.64	-0.88 ± 0.01	-0.92 ± 0.01	-2.41 ± 0.06	-2.41 ± 0.06	286.22 ± 5.28
	IAP	367.52 ± 13.91	-0.75 ± 0.03	-0.81 ± 0.03	-3.17 ± 0.20	-2.09 ± 0.03	12.65 ± 0.18
GRB150118409	Band	762.81 ± 16.81	-0.84 ± 0.01	-0.85 ± 0.01	-3.51 ± 0.25	-3.51 ± 0.25	331.94 ± 2.79
	IAP	795.46 ± 17.93	-0.83 ± 0.01	-0.84 ± 0.01	-10.00 ± 1.50	-3.04 ± 0.06	39.85 ± 0.25
GRB150330828	Band	264.82 ± 4.73	-1.01 ± 0.01	-1.04 ± 0.01	-2.25 ± 0.04	-2.25 ± 0.04	201.54 ± 3.48
	IAP	345.60 ± 10.96	-0.90 ± 0.02	-0.97 ± 0.02	-2.86 ± 0.13	-1.97 ± 0.01	7.68 ± 0.10
GRB150403913	Band	402.10 ± 16.38	-0.82 ± 0.02	-0.85 ± 0.02	-2.09 ± 0.04	-2.09 ± 0.04	436.64 ± 10.17
	IAP	721.32 ± 45.22	-0.67 ± 0.03	-0.74 ± 0.02	-2.49 ± 0.07	-1.79 ± 0.02	28.96 ± 0.37
GRB150627183	Band	243.45 ± 4.52	-0.92 ± 0.01	-0.96 ± 0.01	-2.19 ± 0.02	-2.19 ± 0.02	663.71 ± 10.69
	IAP	334.29 ± 7.75	-0.76 ± 0.02	-0.86 ± 0.01	-2.73 ± 0.07	-1.93 ± 0.01	23.02 ± 0.22
GRB150902733	Band	367.57 ± 6.92	-0.49 ± 0.01	-0.53 ± 0.01	-2.35 ± 0.04	-2.35 ± 0.04	1085.01 ± 17.21
	IAP	471.63 ± 6.91	-0.30 ± 0.03	-0.38 ± 0.02	-3.24 ± 0.10	-1.98 ± 0.01	68.32 ± 0.57
GRB160802259	Band	294.64 ± 5.05	-0.54 ± 0.02	-0.60 ± 0.02	-2.47 ± 0.07	-2.47 ± 0.07	862.92 ± 19.88
	IAP	346.49 ± 8.79	-0.40 ± 0.01	-0.49 ± 0.01	-3.73 ± 0.13	-2.11 ± 0.02	36.20 ± 0.70

Bibliography

Aartsen, M. G., Abbasi, R., Abdou, Y., Ackermann, M., and Adams, J., e. a. (2013). First Observation of PeV-Energy Neutrinos with IceCube. *Physical Review Letters*, 111(2):021103.

Aartsen, M. G., Ackermann, M., Adams, J., Aguilar, J. A., and Ahlers, M., e. a. (2017). Multiwavelength follow-up of a rare IceCube neutrino multiplet. *ArXiv e-prints*.

Abbott, B. P., Abbott, R., Abbott, T. D., Abernathy, M. R., and Acernese, F., e. a. (2016). GW150914: The Advanced LIGO Detectors in the Era of First Discoveries. *Physical Review Letters*, 116(13):131103.

Abbott, B. P., Abbott, R., Abbott, T. D., Acernese, F., Ackley, K., Adams, C., Adams, T., Addesso, P., and et al. (2017). GW170104: Observation of a 50-Solar-Mass Binary Black Hole Coalescence at Redshift 0.2. *ArXiv e-prints*.

Abbott, B. P., Abbott, R., Adhikari, R., Ajith, P., and Allen, B., e. a. (2009). LIGO: the Laser Interferometer Gravitational-Wave Observatory. *Reports on Progress in Physics*, 72(7):076901.

Abdo, A. A., Ackermann, M., Ajello, M., Asano, K., and Atwood, W. B., e. a. (2009a). Fermi Observations of GRB 090902B: A Distinct Spectral Component in the Prompt and Delayed Emission. *APJL*, 706:L138–L144.

Abdo, A. A., Ackermann, M., Ajello, M., Asano, K., and Atwood, W. B., e. a. (2010). Fermi Detection of Delayed GeV Emission from the Short Gamma-Ray Burst 081024B. *APJ*, 712:558–564.

Abdo, A. A., Ackermann, M., Arimoto, M., Asano, K., and Atwood, W. B., e. a. (2009b). Fermi Observations of High-Energy Gamma-Ray Emission from GRB 080916C. *Science*, 323:1688.

Abdo, A. A., Ackermann, M., Asano, K., Atwood, W. B., and Axelsson, M., e. a. (2009c). Fermi Observations of High-energy Gamma-ray Emission from GRB 080825C. *APJ*, 707:580–592.

Abraham, J., Abreu, P., Aglietta, M., Ahn, E. J., Allard, D., Allen, J., Alvarez-Muñiz, J., Ambrosio, M., Anchordoqui, L., Andringa, S., and et al. (2010). Measurement of the energy spectrum of cosmic rays above 10^{18} eV using the Pierre Auger Observatory. *Physics Letters B*, 685:239–246.

Abreu, P., Aglietta, M., Ahn, E. J., Albuquerque, I. F. M., Allard, D., Allekotte, I., Allen, J., Allison, P., Alvarez Castillo, J., and et al. (2011). Anisotropy and chemical composition of ultra-high energy cosmic rays using arrival directions measured by the Pierre Auger Observatory. *JCAP*, 6:022.

Accadia, T., Acernese, F., Alshourbagy, M., Amico, P., and Antonucci, F., e. a. (2012). Virgo: a laser interferometer to detect gravitational waves. *Journal of Instrumentation*, 7:3012.

Acero, F., Ackermann, M., Ajello, M., Albert, A., and Atwood, W. B., e. a. (2015). Fermi Large Area Telescope Third Source Catalog. *APJS*, 218:23.

Ackermann, M., Ajello, M., Albert, A., Allafort, A., and Antolini, E., e. a. (2013a). The Fermi All-sky Variability Analysis: A List of Flaring Gamma-Ray Sources and the Search for Transients in Our Galaxy. *APJ*, 771:57.

Ackermann, M., Ajello, M., Albert, A., Allafort, A., and Atwood, W. B., e. a. (2012a). The Fermi Large Area Telescope on Orbit: Event Classification, Instrument Response Functions, and Calibration. *APJS*, 203:4.

Ackermann, M., Ajello, M., Albert, A., Anderson, B., and Arimoto, M., e. a. (2016). Fermi-LAT Observations of the LIGO Event GW150914. *APJL*, 823:L2.

Ackermann, M., Ajello, M., Asano, K., Atwood, W. B., and Axelsson, M., e. a. (2014). Fermi-LAT Observations of the Gamma-Ray Burst GRB 130427A. *Science*, 343:42–47.

Ackermann, M., Ajello, M., Asano, K., Axelsson, M., and Baldini, L., e. a. (2011). Detection of a Spectral Break in the Extra Hard Component of GRB 090926A. *APJ*, 729:114.

Ackermann, M., Ajello, M., Asano, K., Axelsson, M., Baldini, L., and Ballet, J., e. a. (2013b). The First Fermi-LAT Gamma-Ray Burst Catalog. *APJS*, 209:11.

Ackermann, M., Ajello, M., Baldini, L., and Barbiellini, G., e. a. (2012b). Constraining the High-energy Emission from Gamma-Ray Bursts with Fermi. *APJ*, 754:121.

Ackermann, M., Asano, K., Atwood, W. B., Axelsson, M., Baldini, L., and Ballet, J., e. a. (2010). Fermi Observations of GRB 090510: A Short-Hard Gamma-ray Burst with an Additional, Hard Power-law Component from 10 keV TO GeV Energies. *APJ*, 716:1178–1190.

Actis, M., Agnetta, G., Aharonian, F., Akhperjanian, A., and Aleksić, J., e. a. (2011). Design concepts for the Cherenkov Telescope Array CTA: an advanced facility for ground-based high-energy gamma-ray astronomy. *Experimental Astronomy*, 32:193–316.

Agostinelli, S., Allison, J., Amako, K., Apostolakis, J., and Araujo, H., e. a. (2003). G EANT4a simulation toolkit. *Nuclear Instruments and Methods in Physics Research A*, 506:250–303.

Asano, K., Guiriec, S., and Mészáros, P. (2009). Hadronic Models for the Extra Spectral Component in the Short GRB 090510. *APJL*, 705:L191–L194.

Atteia, J.-L., Barat, C., Hurley, K., Niel, M., and Vedrenne, G., e. a. (1987). A second catalog of gamma-ray bursts - 1978-1980 localizations from the interplanetary network. *APJS*, 64:305–317.

Atwood, W. B., Abdo, A. A., Ackermann, M., Althouse, W., and Anderson, B., e. a. (2009). The Large Area Telescope on the Fermi Gamma-Ray Space Telescope Mission. *APJ*, 697:1071–1102.

Atwood, W. B., Baldini, L., Bregeon, J., Bruel, P., and Chekhtman, A., e. a. (2013). New Fermi-LAT Event Reconstruction Reveals More High-energy Gamma Rays from Gamma-Ray Bursts. *APJ*, 774:76.

Axelsson, M., Baldini, L., Barbiellini, G., Baring, M. G., and Bellazzini, R., e. a. (2012). GRB110721A: An Extreme Peak Energy and Signatures of the Photosphere. *APJL*, 757:L31.

Ballesteros, F. J. (2001). Speeding up image reconstruction methods in coded mask γ cameras using neural networks: application to the em algorithm. `http://www.dmae.upm.es/WebpersonalBartolo/papers/speeding1.pdf`.

Band, D., Matteson, J., Ford, L., Schaefer, B., and Palmer, D., e. a. (1993). BATSE observations of gamma-ray burst spectra. I - Spectral diversity. *APJ*, 413:281–292.

Baring, M. G. and Harding, A. K. (1997). The Escape of High-Energy Photons from Gamma-Ray Bursts. *APJ*, 491:663–686.

Barraud, C., Olive, J.-F., Lestrade, J. P., Atteia, J.-L., and Hurley, K., e. a. (2003). Spectral analysis of 35 GRBs/XRFs observed with HETE-2/FREGATE. *AAP*, 400:1021–1030.

Barthelmy, S. D., Barbier, L. M., Cummings, J. R., Fenimore, E. E., and Gehrels, N., e. a. (2005). The Burst Alert Telescope (BAT) on the SWIFT Midex Mission. *SSR*, 120:143–164.

Bellazzini, R., Angelini, F., Bagagli, R., Baldini, L., and Brez, A., e. a. (2003). The silicon-strip tracker of the Gamma ray Large Area Space Telescope. *Nuclear Instruments and Methods in Physics Research A*, 512:136–142.

Beloborodov, A. M. (2013). Regulation of the Spectral Peak in Gamma-Ray Bursts. *APJ*, 764:157.

Beniamini, P. and Piran, T. (2013). Constraints on the Synchrotron Emission Mechanism in Gamma-Ray Bursts. , 769:69.

Berger, E., Kulkarni, S. R., and Frail, D. A. (2004). The Nonrelativistic Evolution of GRBs 980703 and 970508: Beaming-independent Calorimetry. *APJ*, 612:966–973.

Bloom, J. S., Djorgovski, S. G., Kulkarni, S. R., and Frail, D. A. (1998). The Host Galaxy of GRB 970508. *APJL*, 507:L25–L28.

Boella, G., Butler, R. C., Perola, G. C., Piro, L., Scarsi, L., and Bleeker, J. A. M. (1997). BeppoSAX, the wide band mission for X-ray astronomy. , 122.

Bonnell, J. (1995). `https://apod.nasa.gov/htmltest/jbonnell/www/grbhist.html`.

Bošnjak, Ž. and Daigne, F. (2014). Spectral evolution in gamma-ray bursts: Predictions of the internal shock model and comparison to observations. *AAP*, 568:A45.

Bošnjak, Ž., Daigne, F., and Dubus, G. (2009). Prompt high-energy emission from gamma-ray bursts in the internal shock model. *AAP*, 498:677–703.

Briggs, M. S., Band, D. L., Kippen, R. M., Preece, R. D., and Kouveliotou, C., e. a. (1999). Observations of GRB 990123 by the Compton Gamma Ray Observatory. *APJ*, 524:82–91.

Briggs, M. S., Paciesas, W. S., Pendleton, G. N., Meegan, C. A., and Fishman, G. J., e. a. (1996). BATSE Observations of the Large-Scale Isotropy of Gamma-Ray Bursts. *APJ*, 459:40.

Burrows, D. N., Hill, J. E., Nousek, J. A., Kennea, J. A., and Wells, A., e. a. (2005). The Swift X-Ray Telescope. *SSR*, 120:165–195.

Butler, N. R. and Kocevski, D. (2007). X-Ray Hardness Evolution in GRB Afterglows and Flares: Late-Time GRB Activity without N_H Variations. *APJ*, 663:407–419.

Cash, W. (1979). Parameter estimation in astronomy through application of the likelihood ratio. *APJ*, 228:939–947.

Cavallo, G. and Rees, M. J. (1978). A qualitative study of cosmic fireballs and gamma-ray bursts. *MNRAS*, 183:359–365.

Chandra, P. (2016). Gamma-Ray Bursts: A Radio Perspective. *Advances in Astronomy*, 2016:296781.

Chincarini, G., Mao, J., Margutti, R., Bernardini, M. G., and Guidorzi, C., e. a. (2010). Unveiling the origin of X-ray flares in gamma-ray bursts. *MNRAS*, 406:2113–2148.

Cieslak, M. J. (2016). Coded-aperture imaging systems: Past, present and future development - a review. `http://ac.els-cdn.com/S1350448716301524/1-s2.0-S1350448716301524-main.pdf?_tid=75983cdc-2bdd-11e7-af64-00000aacb360&acdnat=1493361761_14e6edb2d78c46055f988a95188229b9`.

Connaughton, V., Briggs, M. S., Goldstein, A., Meegan, C. A., and Paciesas, W. S., e. a. (2015). Localization of Gamma-Ray Bursts Using the Fermi Gamma-Ray Burst Monitor. *APJS*, 216:32.

Connaughton, V., Burns, E., Goldstein, A., Blackburn, L., and Briggs, M. S., e. a. (2016). Fermi GBM Observations of LIGO Gravitational-wave Event GW150914. *APJL*, 826:L6.

Costa, E., Frontera, F., Heise, J., Feroci, M., and in't Zand, J., e. a. (1997). Discovery of an X-ray afterglow associated with the γ-ray burst of 28 February 1997. *NAT*, 387:783–785.

Coward, D. M., Howell, E. J., Branchesi, M., Stratta, G., and Guetta, D., e. a. (2013). The Swift gamma-ray burst redshift distribution: selection biases and optical brightness evolution at high z? *MNRAS*, 432:2141–2149.

Cucchiara, A., Levan, A. J., Fox, D. B., Tanvir, N. R., and Ukwatta, T. N., e. a. (2011). A Photometric Redshift of z ˜ 9.4 for GRB 090429B. *APJ*, 736:7.

Daigne, F., Bošnjak, Ž., and Dubus, G. (2011). Reconciling observed GRB prompt spectra with synchrotron radiation? *AAP*, 526:A110.

Daigne, F. and Mochkovitch, R. (1998). Gamma-ray bursts from internal shocks in a relativistic wind: temporal and spectral properties. *MNRAS*, 296:275–286.

Daigne, F. and Mochkovitch, R. (2000). Gamma-ray bursts from internal shocks in a relativistic wind: a hydrodynamical study. *AAP*, 358:1157–1166.

Daigne, F. and Mochkovitch, R. (2002). The expected thermal precursors of gamma-ray bursts in the internal shock model. *MNRAS*, 336:1271–1280.

D'Avanzo, P. (2015). Short gamma-ray bursts: A review. *Journal of High Energy Astrophysics*, 7:73–80.

D'Elia, V., Fynbo, J. P. U., Covino, S., Goldoni, P., and Jakobsson, P., e. a. (2010). VLT/X-shooter spectroscopy of the GRB 090926A afterglow. *AAP*, 523:A36.

Dezalay, J.-P., Barat, C., Talon, R., Syunyaev, R., Terekhov, O., and Kuznetsov, A. (1992). Short cosmic events - A subset of classical GRBs? In Paciesas, W. S. and Fishman, G. J., editors, *American Institute of Physics Conference Series*, volume 265 of *American Institute of Physics Conference Series*, pages 304–309.

Estulin, I. V., Dyachkov, A. V., Zenchenko, V. M., Kuznetsov, A. V., and Mersov, G. A., e. a. (1981). Three Gamma-Ray Bursts Recorded by VENERA-11 VENERA-12 and PROGNOZ-7. *Soviet Astronomy Letters*, 7:12–14.

Fenimore, E. E., Conner, J. P., Epstein, R. I., Klebesadel, R. W., and Laros, J. G., e. a. (1988). Interpretations of multiple absorption features in a gamma-ray burst spectrum. *APJL*, 335:L71–L74.

Feroci, M. (1999). Observation of gamma-ray bursts by BeppoSAX. *MEMSAI*, 70:905–931.

Fishman, G. J., Meegan, C. A., Wilson, R. B., Paciesas, W. S., and Pendleton, G. N. (1992). The BATSE experiment on the Compton Gamma Ray Observatory: Status and some early results. In Shrader, C. R., Gehrels, N., and Dennis, B., editors, *NASA Conference Publication*, volume 3137 of *NASA Conference Publication*.

Fong, W., Berger, E., and Fox, D. B. (2010). Hubble Space Telescope Observations of Short Gamma-Ray Burst Host Galaxies: Morphologies, Offsets, and Local Environments. *APJ*, 708:9–25.

Ford, L. A., Band, D. L., Matteson, J. L., Briggs, M. S., and Pendleton, G. N., e. a. (1995). BATSE observations of gamma-ray burst spectra. 2: Peak energy evolution in bright, long bursts. *APJ*, 439:307–321.

Fox, D. B., Frail, D. A., Price, P. A., Kulkarni, S. R., and Berger, E., e. a. (2005). The afterglow of GRB 050709 and the nature of the short-hard γ-ray bursts. *NAT*, 437:845–850.

Fox, D. W. (2002). GRB021004: optical afterglow. *GRB Coordinates Network*, 1564.

Frail, D. A. (1997). Radio Afterglows: Constraints on Fireball Evolution. In *American Astronomical Society Meeting Abstracts*, volume 29 of *Bulletin of the American Astronomical Society*, page 1303.

Frail, D. A., Kulkarni, S. R., Nicastro, L., Feroci, M., and Taylor, G. B. (1997). The radio afterglow from the γ-ray burst of 8 May 1997. *NAT*, 389:261–263.

Frail, D. A., Kulkarni, S. R., Sari, R., Djorgovski, S. G., and Bloom, J. S., e. a. (2001). Beaming in Gamma-Ray Bursts: Evidence for a Standard Energy Reservoir. *APJL*, 562:L55–L58.

Fruchter, A. S., Levan, A. J., Strolger, L., Vreeswijk, P. M., and Thorsett, S. E., e. a. (2006). Long γ-ray bursts and core-collapse supernovae have different environments. *NAT*, 441:463–468.

Galama, T. J., Vreeswijk, P. M., van Paradijs, J., Kouveliotou, C., and Augusteijn, T., e. a. (1998). An unusual supernova in the error box of the γ-ray burst of 25 April 1998. *NAT*, 395:670–672.

Galli, M., Marisaldi, M., Fuschino, F., Labanti, C., and Argan, A., e. a. (2013). AGILE mini-calorimeter gamma-ray burst catalog. *AAP*, 553:A33.

Gehrels, N. (2007). Swift observations of gamma-ray bursts. *Philosophical Transactions of the Royal Society of London Series A*, 365:1119–1128.

Gehrels, N., Chincarini, G., Giommi, P., Mason, K. O., and Nousek, J. A., e. a. (2004). The Swift Gamma-Ray Burst Mission. *APJ*, 611:1005–1020.

Gehrels, N. and Razzaque, S. (2013). Gamma-ray bursts in the swift-Fermi era. *Frontiers of Physics*, 8:661–678.

Gehrels, N., Sarazin, C. L., O'Brien, P. T., Zhang, B., and Barbier, L., e. a. (2005). A short γ-ray burst apparently associated with an elliptical galaxy at redshift z = 0.225. *NAT*, 437:851–854.

Ghirlanda, G., Celotti, A., and Ghisellini, G. (2003). Extremely hard GRB spectra prune down the forest of emission models. *AAP*, 406:879–892.

Ghirlanda, G., Ghisellini, G., and Lazzati, D. (2004). The Collimation-corrected Gamma-Ray Burst Energies Correlate with the Peak Energy of Their $\nu F_{\frac{1}{2}}$ Spectrum. *APJ*, 616:331–338.

Ghisellini, G., Ghirlanda, G., Nava, L., and Firmani, C. (2007). "Late Prompt" Emission in Gamma-Ray Bursts? *APJL*, 658:L75–L78.

Ghisellini, G. and Lazzati, D. (1999). Polarization light curves and position angle variation of beamed gamma-ray bursts. *MNRAS*, 309:L7–L11.

Gilmore, R. C., Bouvier, A., Connaughton, V., Goldstein, A., and Otte, N., e. a. (2013). IACT observations of gamma-ray bursts: prospects for the Cherenkov Telescope Array. *Experimental Astronomy*, 35:413–457.

Giuliani, A., Fuschino, F., Vianello, G., Marisaldi, M., and Mereghetti, S., e. a. (2010). AGILE Detection of Delayed Gamma-ray Emission From the Short Gamma-Ray Burst GRB 090510. *APJL*, 708:L84–L88.

Giuliani, A., Mereghetti, S., Fornari, F., Del Monte, E., and Feroci, M., e. a. (2008). AGILE detection of delayed gamma-ray emission from GRB 080514B. *AAP*, 491:L25–L28.

Goldstein, A., Burgess, J. M., Preece, R. D., Briggs, M. S., and Guiriec, S., e. a. (2012). The Fermi GBM Gamma-Ray Burst Spectral Catalog: The First Two Years. *APJS*, 199:19.

Goldstein, A., Preece, R. D., Mallozzi, R. S., Briggs, M. S., and Fishman, G. J., e. a. (2013). The BATSE 5B Gamma-Ray Burst Spectral Catalog. *APJS*, 208:21.

González, M. M., Dingus, B. L., Kaneko, Y., Preece, R. D., and Dermer, C. D., e. a. (2003a). A γ-ray burst with a high-energy spectral component inconsistent with the synchrotron shock model. *NAT*, 424:749–751.

González, M. M., Dingus, B. L., Kaneko, Y., Preece, R. D., and Dermer, C. D., e. a. (2003b). A γ-ray burst with a high-energy spectral component inconsistent with the synchrotron shock model. *NAT*, 424:749–751.

Götz, D., Laurent, P., Lebrun, F., Daigne, F., and Bošnjak, Ž. (2009). Variable Polarization Measured in the Prompt Emission of GRB 041219A Using IBIS on Board INTEGRAL. *APJL*, 695:L208–L212.

Granot, J., Cohen-Tanugi, J., and Silva, E. d. C. e. (2008). Opacity Buildup in Impulsive Relativistic Sources. *APJ*, 677:92–126.

Granot, J., Fermi LAT Collaboration, and GBM Collaboration (2009). GRB Theory in the Fermi Era. *ArXiv e-prints*.

Granot, J. and Guetta, D. (2003). Explaining the High-Energy Spectral Component in GRB 941017. *APJL*, 598:L11–L14.

Greiner, J., Clemens, C., Krühler, T., von Kienlin, A., and Rau, A., e. a. (2009). The redshift and afterglow of the extremely energetic gamma-ray burst GRB 080916C. *AAP*, 498:89–94.

Groot, P. J., Galama, T. J., van Paradijs, J., Strom, R., and Telting, J., e. a. (1997). GRB 970228. *IAUCIRC*, 6584.

Gruber, D., Goldstein, A., Weller von Ahlefeld, V., Narayana Bhat, P., and Bissaldi, E., e. a. (2014). The Fermi GBM Gamma-Ray Burst Spectral Catalog: Four Years of Data. *APJS*, 211:12.

Guiriec, S., Connaughton, V., Briggs, M. S., Burgess, M., and Ryde, F., e. a. (2011). Detection of a Thermal Spectral Component in the Prompt Emission of GRB 100724B. *APJL*, 727:L33.

Guiriec, S., Daigne, F., Hascoët, R., Vianello, G., and Ryde, F., e. a. (2013). Evidence for a Photospheric Component in the Prompt Emission of the Short GRB 120323A and Its Effects on the GRB Hardness-Luminosity Relation. *APJ*, 770:32.

Guiriec, S., Kouveliotou, C., Daigne, F., Zhang, B., and Hascoët, R., e. a. (2015a). Toward a Better Understanding of the GRB Phenomenon: a New Model for GRB Prompt Emission and its Effects on the New $L_i{}^{NT}$- $E_{peak,i}{}^{rest,NT}$ Relation. *APJ*, 807:148.

Guiriec, S., Mochkovitch, R., Piran, T., Daigne, F., Kouveliotou, C., and Racusin, J. e. a. (2015b). GRB 131014A: A Laboratory for Studying the Thermal-like and Non-thermal Emissions in Gamma-Ray Bursts, and the New $L^{nTh}{}_i$-$E^{nTh,rest}{}_{peak,i}$ Relation. *APJ*, 814:10.

Harrison, F. A., Bloom, J. S., Frail, D. A., Sari, R., and Kulkarni, S. R., e. a. (1999). Optical and Radio Observations of the Afterglow from GRB 990510: Evidence for a Jet. *APJL*, 523:L121–L124.

Hartman, R. C., Bertsch, D. L., Fichtel, C. E., Hunter, S. D., and Kanbach, G., e. a. (1992). The EGRET high energy gamma ray telescope. In Shrader, C. R., Gehrels, N., and Dennis, B., editors, *NASA Conference Publication*, volume 3137 of *NASA Conference Publication*.

Hascoet, R. (2012). *Modeling Gamma-Ray Bursts in the Swift-Fermi era*. Theses, Université Pierre et Marie Curie - Paris VI.

Hascoët, R., Daigne, F., and Mochkovitch, R. (2013). Prompt thermal emission in gamma-ray bursts. *AAP*, 551:A124.

Hascoët, R., Daigne, F., Mochkovitch, R., and Vennin, V. (2012). Do Fermi Large Area Telescope observations imply very large Lorentz factors in gamma-ray burst outflows? *MNRAS*, 421:525–545.

HAWC Collaboration (2012). HAWC - The High Altitude Water Cherenkov Detector. In *Journal of Physics Conference Series*, volume 375 of *Journal of Physics Conference Series*, page 052026.

HEASARC, N. (2003a). `https://heasarc.gsfc.nasa.gov/docs/heasarc/missions/vela5a.html`.

HEASARC, N. (2003b). `https://heasarc.nasa.gov/docs/objects/grbs/grb_profiles.html`.

HEASARC, N. (2004). https://heasarc.gsfc.nasa.gov/docs/granat/granat_about.html.

Hjorth, J., Sollerman, J., Gorosabel, J., Granot, J., and Klose, S., e. a. (2005). GRB 050509B: Constraints on Short Gamma-Ray Burst Models. *APJL*, 630:L117–L120.

Hurley, K. (1986). Cosmic Gamma-Ray Bursts. In Kylafis, N., Papamastorakis, J., and Ventura, J., editors, *Plasma Penetration into Magnetospheres*, page 165.

Hurley, K., Cline, T., Mitrofanov, I., Mazets, E., Golenetskii, S., Frontera, F., Montanari, E., Guidorzi, C., and Feroci, M. (2003). The Current Performance of the Third Interplanetary Network. In Ricker, G. R. and Vanderspek, R. K., editors, *Gamma-Ray Burst and Afterglow Astronomy 2001: A Workshop Celebrating the First Year of the HETE Mission*, volume 662 of *American Institute of Physics Conference Series*, pages 473–476.

Hurley, K., Dingus, B. L., Mukherjee, R., Sreekumar, P., and Kouveliotou, C., e. a. (1994). Detection of a γ-ray burst of very long duration and very high energy. *NAT*, 372:652–654.

Inoue, S., Granot, J., O'Brien, P. T., Asano, K., and Bouvier, A., e. a. (2013). Gamma-ray burst science in the era of the Cherenkov Telescope Array. *Astroparticle Physics*, 43:252–275.

Kann, D. A., Klose, S., Zhang, B., Malesani, D., and Nakar, E., e. a. (2010). The Afterglows of Swift-era Gamma-ray Bursts. I. Comparing pre-Swift and Swift-era Long/Soft (Type II) GRB Optical Afterglows. *APJ*, 720:1513–1558.

Klebesadel, R. W., Strong, I. B., and Olson, R. A. (1973). Observations of Gamma-Ray Bursts of Cosmic Origin. *APJL*, 182:L85.

Kocevski, D. and Butler, N. (2008). Gamma-Ray Burst Energetics in the Swift Era. *APJ*, 680:531–538.

Kocevski, D. and Longo, F. (2016). Fermi-LAT Observations of GRB 160509A. *LPI Contributions*, 1962:4092.

Kouveliotou, C., Meegan, C. A., Fishman, G. J., Bhat, N. P., and Briggs, M. S., e. a. (1993). Identification of two classes of gamma-ray bursts. *APJL*, 413:L101–L104.

Krimm, H. A., Granot, J., Marshall, F. E., Perri, M., and Barthelmy, S. D., e. a. (2007). GRB 060714: No Clear Dividing Line between Prompt Emission and X-Ray Flares. *APJ*, 665:554–568.

Labanti, C., Di Cocco, G., Ferro, G., Gianotti, F., and Mauri, A., e. a. (2003). The Ibis-Picsit detector onboard Integral. *AAP*, 411:L149–L152.

Lebrun, F., Leray, J. P., Lavocat, P., Crétolle, J., and Arquès, M., e. a. (2003). ISGRI: The INTEGRAL Soft Gamma-Ray Imager. *AAP*, 411:L141–L148.

Lien, A., Sakamoto, T., Barthelmy, S. D., Baumgartner, W. H., and Cannizzo, J. K., e. a. (2016). The Third Swift Burst Alert Telescope Gamma-Ray Burst Catalog. *APJ*, 829:7.

Longo, F., Bissaldi, E., Bregeon, J., McEnery, J., Ohno, M., and Zhu, S. (2016a). GRB 160509A: Fermi-LAT prompt detection of a very bright burst. *GRB Coordinates Network*, 19403.

Longo, F., Bissaldi, E., Vianello, G., Moretti, E., and Omodei, N., e. a. (2016b). GRB 160509A: Fermi-LAT refined analysis. *GRB Coordinates Network*, 19413.

Lyutikov, M. (2006). The electromagnetic model of gamma-ray bursts. *New Journal of Physics*, 8:119.

Lyutikov, M. and Blandford, R. (2003). Gamma Ray Bursts as Electromagnetic Outflows. *ArXiv Astrophysics e-prints*.

MacFadyen, A. I. and Woosley, S. E. (1999). Collapsars: Gamma-Ray Bursts and Explosions in "Failed Supernovae". *APJ*, 524:262–289.

Marisaldi, M., Barbiellini, G., Costa, E., Cutini, S., and Del Monte, E., e. a. (2009). Observation of GRBs with AGILE. *ArXiv e-prints*.

Marshall, F. E. (2016). GRB 160422A: Swift/UVOT Afterglow Confirmation. *GRB Coordinates Network*, 19346.

Maselli, A., Malesani, D., Page, K. L., and Evans, P. A. (2016). GRB 160422A: XRT Afterglow Confirmation. *GRB Coordinates Network*, 19359.

Massaro, F., Grindlay, J. E., and Paggi, A. (2010). Gamma-ray Bursts in the Fermi Era: The Spectral Energy Distribution of the Prompt Emission. *APJL*, 714:L299–L302.

Mattox, J. R., Bertsch, D. L., Chiang, J., Dingus, B. L., and Digel, S. W., e. a. (1996). The Likelihood Analysis of EGRET Data. *APJ*, 461:396.

Mazets, E. P., Golenetskii, S. V., Aptekar, R. L., Gurian, I. A., and Ilinskii, V. N. (1981). Cyclotron and annihilation lines in gamma-ray burst. *NAT*, 290:378–382.

McEnery, J., Thayer, G., Russell, J. J., Zhu, S., and Omodei, N. (2010). Update to the configuration of the Fermi-LAT onboard GRB search. *GRB Coordinates Network*, 10777.

McGlynn, S., Clark, D. J., Dean, A. J., Hanlon, L., McBreen, S., Willis, D. R., McBreen, B., Bird, A. J., and Foley, S. (2007). Polarisation studies of the prompt gamma-ray emission from GRB 041219a using the spectrometer aboard INTEGRAL. , 466:895–904.

Medvedev, M. V. (2000). Theory of "Jitter" Radiation from Small-Scale Random Magnetic Fields and Prompt Emission from Gamma-Ray Burst Shocks. *APJ*, 540:704–714.

Meegan, C., Connaughton, V., Fishman, G., Kippen, R. M., and Kouveliotou, C., e. a. (1996). Gamma-Ray Bursts. *IAUCIRC*, 6518.

Meegan, C., Lichti, G., Bhat, P. N., Bissaldi, E., and Briggs, M. S., e. a. (2009). The Fermi Gamma-ray Burst Monitor. *APJ*, 702:791–804.

Meegan, C. A., Fishman, G. J., Wilson, R. B., Horack, J. M., and Brock, M. N., e. a. (1992). Spatial distribution of gamma-ray bursts observed by BATSE. *NAT*, 355:143–145.

Mereghetti, S. (2013). Ten years of the INTEGRAL Burst Alert System (IBAS). *ArXiv e-prints*.

Mereghetti, S., Götz, D., Borkowski, J., Beck, M., and von Kienlin, A., e. a. (2004). The INTEGRAL Burst Alert System: Results and Future Perspectives. In Schoenfelder, V., Lichti, G., and Winkler, C., editors, *5th INTEGRAL Workshop on the INTEGRAL Universe*, volume 552 of *ESA Special Publication*, page 599.

Mészáros, P. (2006). Gamma-ray bursts. *Reports on Progress in Physics*, 69:2259–2321.

Meszaros, P. and Rees, M. J. (1993). Relativistic fireballs and their impact on external matter - Models for cosmological gamma-ray bursts. *APJ*, 405:278–284.

Meszaros, P., Rees, M. J., and Papathanassiou, H. (1994). Spectral properties of blast-wave models of gamma-ray burst sources. *APJ*, 432:181–193.

Moiseev, A. A., Hartman, R. C., Ormes, J. F., Thompson, D. J., and Amato, M. J., e. a. (2007). The anti-coincidence detector for the GLAST large area telescope. *Astroparticle Physics*, 27:339–358.

Murakami, T., Fujii, M., Hayashida, K., Itoh, M., and Nishimura, J. (1988). Evidence for cyclotron absorption from spectral features in gamma-ray bursts seen with Ginga. *NAT*, 335:234.

Narayana Bhat, P., Meegan, C. A., von Kienlin, A., Paciesas, W. S., and Briggs, M. S., e. a. (2016a). The Third Fermi GBM Gamma-Ray Burst Catalog: The First Six Years. *APJS*, 223:28.

Narayana Bhat, P., Meegan, C. A., von Kienlin, A., Paciesas, W. S., and Briggs, M. S., e. a. (2016b). The Third Fermi GBM Gamma-Ray Burst Catalog: The First Six Years. *APJS*, 223:28.

Neyman, J. and Pearson, E. S. (1928). *On the Use and Interpretation of Certain Test Criteria for Purposes of Statistical Inference, Part I*. Cambridge University Press, London.

Niel, M., Hurley, K., Vedrenne, G., Estkhulin, I. V., and Melioranskii, A. S. (1976). The French-Russian 3 satellite gamma-burst experiment. *APSS*, 42:99–102.

Nolan, P. L., Abdo, A. A., Ackermann, M., Ajello, M., and Allafort, A., e. a. (2012). Fermi Large Area Telescope Second Source Catalog. *APJS*, 199:31.

Norris, J. P., Bonnell, J. T., Kazanas, D., Scargle, J. D., and Hakkila, J., e. a. (2005). Long-Lag, Wide-Pulse Gamma-Ray Bursts. *APJ*, 627:324–345.

Nousek, J. A., Kouveliotou, C., Grupe, D., Page, K. L., and Granot, J., e. a. (2006). Evidence for a Canonical Gamma-Ray Burst Afterglow Light Curve in the Swift XRT Data. *APJ*, 642:389–400.

Oates, S. R., Page, M. J., Schady, P., de Pasquale, M., and Evans, P. A., e. a. (2011). A statistical comparison of the optical/UV and X-ray afterglows of gamma-ray bursts using the Swift Ultraviolet Optical and X-ray Telescopes. *MNRAS*, 412:561–579.

Oates, S. R., Page, M. J., Schady, P., de Pasquale, M., Koch, T. S., and Breeveld, A. A., e. a. (2009). A statistical study of gamma-ray burst afterglows measured by the Swift Ultraviolet Optical Telescope. *MNRAS*, 395:490–503.

O'Brien, P. T., Willingale, R., Osborne, J. P., and Goad, M. R. (2006). Early multi-wavelength emission from gamma-ray bursts: from gamma-ray to x-ray. *New Journal of Physics*, 8:121.

Ohno, M. and Pelassa, V. (2009). Fermi LAT detection of GRB 090510. *GRB Coordinates Network*, 9334.

Paciesas, W. S., Meegan, C. A., von Kienlin, A., Bhat, P. N., and Bissaldi, E., e. a. (2012). The Fermi GBM Gamma-Ray Burst Catalog: The First Two Years. *APJS*, 199:18.

Paczynski, B. (1986). Gamma-ray bursters at cosmological distances. *APJL*, 308:L43–L46.

Palmer, D. M., Teegarden, B. J., Schaefer, B. E., Cline, T. L., and Band, D. L., e. a. (1994). BATSE gamma-ray burst line search. 1: Search for narrow lines in spectroscopy detector data. *APJL*, 433:L77–L80.

Perley, D. A., Krühler, T., Schulze, S., de Ugarte Postigo, A., and Hjorth, J., e. a. (2016). The Swift Gamma-Ray Burst Host Galaxy Legacy Survey. I. Sample Selection and Redshift Distribution. *APJ*, 817:7.

Preece, R. D., Briggs, M. S., Mallozzi, R. S., Pendleton, G. N., and Paciesas, W. S., e. a. (1998). The Synchrotron Shock Model Confronts a "Line of Death" in the BATSE Gamma-Ray Burst Data. *APJL*, 506:L23–L26.

Qin, Y.-P., Xie, G.-Z., Xue, S.-J., Liang, E.-W., and Zheng, X.-T., e. a. (2000). The Hardness-Duration Correlation in the Two Classes of Gamma-Ray Bursts. *PASJ*, 52:759.

Racusin, J. L., Axelsson, M., Yassine, M., and Kocevski, D. (2015). GRB 150510A: Fermi-LAT Refined Analysis. *GRB Coordinates Network*, 17806.

Racusin, J. L., Liang, E. W., Burrows, D. N., Falcone, A., and Sakamoto, T., e. a. (2009). Jet Breaks and Energetics of Swift Gamma-Ray Burst X-Ray Afterglows. *APJ*, 698:43–74.

Rau, A., Kienlin, A. V., Hurley, K., and Lichti, G. G. (2005). The 1st INTEGRAL SPI-ACS gamma-ray burst catalogue. *AAP*, 438:1175–1183.

Rau, A., Savaglio, S., Krühler, T., Afonso, P., Greiner, J., Klose, S., Schady, P., McBreen, S., Filgas, R., Olivares E., F., Rossi, A., and Updike, A. (2010). A Very Metal-poor Damped Lyman-α System Revealed Through the Most Energetic GRB 090926A. , 720:862–871.

Razzaque, S. (2010). A Leptonic-Hadronic Model for the Afterglow of Gamma-ray Burst 090510. *APJL*, 724:L109–L112.

Razzaque, S., Dermer, C. D., and Finke, J. D. (2010). Synchrotron Radiation from Ultra-High Energy Protons and the Fermi Observations of GRB 080916C. *The Open Astronomy Journal*, 3:150–155.

Rees, M. J. and Mészáros, P. (2005). Dissipative Photosphere Models of Gamma-Ray Bursts and X-Ray Flashes. *APJ*, 628:847–852.

Reichart, D. E. (1998). The Redshift of GRB 970508. *APJL*, 495:L99–L101.

Rolke, W. A., López, A. M., and Conrad, J. (2005). Limits and confidence intervals in the presence of nuisance parameters. *Nuclear Instruments and Methods in Physics Research A*, 551:493–503.

Roming, P. W. A., Kennedy, T. E., Mason, K. O., Nousek, J. A., and Ahr, L., e. a. (2005). The Swift Ultra-Violet/Optical Telescope. *SSR*, 120:95–142.

Ryde, F. (2004). The Cooling Behavior of Thermal Pulses in Gamma-Ray Bursts. *APJ*, 614:827–846.

Ryde, F., Axelsson, M., Zhang, B. B., McGlynn, S., and Pe'er, A., e. a. (2010). Identification and Properties of the Photospheric Emission in GRB090902B. *APJL*, 709:L172–L177.

Sakamoto, T., Barthelmy, S. D., Barbier, L., Cummings, J. R., and Fenimore, E. E., e. a. (2008). The First Swift BAT Gamma-Ray Burst Catalog. *APJS*, 175:179–190.

Sakamoto, T., Lamb, D. Q., Kawai, N., Yoshida, A., and Graziani, C., e. a. (2005). Global Characteristics of X-Ray Flashes and X-Ray-Rich Gamma-Ray Bursts Observed by HETE-2. *APJ*, 629:311–327.

Sari, R., Piran, T., and Narayan, R. (1998). Spectra and Light Curves of Gamma-Ray Burst Afterglows. *APJL*, 497:L17–L20.

Savchenko, V., Ferrigno, C., Mereghetti, S., Natalucci, L., Bazzano, A., Bozzo, E., Brandt, S., Courvoisier, T. J.-L., Diehl, R., Hanlon, L., von Kienlin, A., Kuulkers, E., Laurent, P., Lebrun, F., Roques, J. P., Ubertini, P., and Weidenspointner, G. (2016). INTEGRAL Upper Limits on Gamma-Ray Emission Associated with the Gravitational Wave Event GW150914. , 820:L36.

Schmidt, M., Higdon, J. C., and Hueter, G. (1988). Application of the V/V(max) test to gamma-ray bursts. *APJL*, 329:L85–L87.

Schweyer, T., Bolmer, J., Greiner, J., and Kann, D. A. (2016). GRB 160422A: GROND NIR afterglow detection. *GRB Coordinates Network*, 19352.

Sommer, M., Bertsch, D. L., Dingus, B. L., Fichtel, C. E., and Fishman, G. J., e. a. (1994a). High-energy gamma rays from the intense 1993 January 31 gamma-ray burst. *APJL*, 422:L63–L66.

Sommer, M., Bertsch, D. L., Dingus, B. L., Fichtel, C. E., and Fishman, G. J., e. a. (1994b). High-energy gamma rays from the intense 1993 January 31 gamma-ray burst. *APJL*, 422:L63–L66.

Stanek, K. Z., Matheson, T., Garnavich, P. M., Martini, P., and Berlind, P., e. a. (2003). Spectroscopic Discovery of the Supernova 2003dh Associated with GRB 030329. *APJL*, 591:L17–L20.

Tanvir, N. R., Fox, D. B., Levan, A. J., Berger, E., and Wiersema, K., e. a. (2009). A γ-ray burst at a redshift of z˜8.2. *NAT*, 461:1254–1257.

Tanvir, N. R., Levan, A. J., Cenko, S. B., Perley, D., and Cucchiara, A., e. a. (2016). GRB 160509A Gemini North redshift. *GRB Coordinates Network*, 19419.

Tanvir, N. R., Levan, A. J., Fruchter, A. S., Hjorth, J., and Hounsell, R. A., e. a. (2013). A 'kilonova' associated with the short-duration γ-ray burst GRB 130603B. *NAT*, 500:547–549.

Tavani, M., Barbiellini, G., Argan, A., Basset, M., and Boffelli, F., e. a. (2006). The AGILE mission and its scientific instrument. In *Society of Photo-Optical Instrumentation Engineers (SPIE) Conference Series*, volume 6266 of *PROCSPIE*, page 626603.

Tavani, M., Barbiellini, G., Argan, A., Bulgarelli, A., and Caraveo, P., e. a. (2008). The AGILE space mission. *Nuclear Instruments and Methods in Physics Research A*, 588:52–62.

Thompson, C. (1994). A Model of Gamma-Ray Bursts. *MNRAS*, 270:480.

Thompson, C., Mészáros, P., and Rees, M. J. (2007). Thermalization in Relativistic Outflows and the Correlation between Spectral Hardness and Apparent Luminosity in Gamma-Ray Bursts. *APJ*, 666:1012–1023.

Tierney, D., McBreen, S., Preece, R. D., Fitzpatrick, G., and Foley, S., e. a. (2013). Anomalies in low-energy gamma-ray burst spectra with the Fermi Gamma-ray Burst Monitor. *AAP*, 550:A102.

Ubertini, P., Lebrun, F., Di Cocco, G., Bazzano, A., and Bird, A. J., e. a. (2003). IBIS: The Imager on-board INTEGRAL. *AAP*, 411:L131–L139.

van der Horst, A. J., Kamble, A., Resmi, L., Wijers, R. A. M. J., and Bhattacharya, D., e. a. (2008). Detailed study of the GRB 030329 radio afterglow deep into the non-relativistic phase. *AAP*, 480:35–43.

Vedrenne, G., Roques, J.-P., Schönfelder, V., Mandrou, P., and Lichti, G. G., e. a. (2003). SPI: The spectrometer aboard INTEGRAL. *AAP*, 411:L63–L70.

Vianello, G., Gill, R., Granot, J., Omodei, N., and Cohen-Tanugi, J., e. a. (2017). The Bright and the Slow – GRBs 100724B \ 160509A with high-energy cutoffs at $\lesssim 100$ MeV. *ArXiv e-prints*.

Vianello, G., Omodei, N., and Fermi/LAT collaboration (2015). The First 100 LAT Gamma-Ray Bursts: A New Detection Algorithm and Pass 8. *ArXiv e-prints*.

Vianello, G., Yassine, M., and Moretti, E. (2016). GRB 160310A: Fermi-LAT detection. *GRB Coordinates Network*, 19158.

Vietri, M., De Marco, D., and Guetta, D. (2003). On the Generation of Ultra-High-Energy Cosmic Rays in Gamma-Ray Bursts: A Reappraisal. *APJ*, 592:378–389.

von Kienlin, A., Meegan, C. A., Paciesas, W. S., Bhat, P. N., and Bissaldi, E., e. a. (2014). The Second Fermi GBM Gamma-Ray Burst Catalog: The First Four Years. *APJS*, 211:13.

Wei, J., Cordier, B., Antier, S., Antilogus, P., and Atteia, J.-L., e. a. (2016). The Deep and Transient Universe in the SVOM Era: New Challenges and Opportunities - Scientific prospects of the SVOM mission. *ArXiv e-prints,1610.06892, astro-ph.HE*.

Wijers, R. A. M. J., Rees, M. J., and Meszaros, P. (1997). Shocked by GRB 970228: the afterglow of a cosmological fireball. *MNRAS*, 288:L51–L56.

Winkler, C., Courvoisier, T. J.-L., Di Cocco, G., Gehrels, N., and Giménez, A., e. a. (2003). The INTEGRAL mission. *AAP*, 411:L1–L6.

Yassine, M., Piron, F., Mochkovitch, R., and Daigne, F. (2017). Time evolution of the spectral break in the high-energy extra component of GRB 090926A. *ArXiv e-prints*.

Yassine, M., Racusin, J. L., and Omodei, N. (2016). GRB 160422A: Fermi-LAT Detection. *GRB Coordinates Network*, 19329.

Yu, H.-F., van Eerten, H. J., Greiner, J., Sari, R., and Narayana Bhat, P., e. a. (2015). The sharpness of gamma-ray burst prompt emission spectra. *AAP*, 583:A129.

Zhang, B., Fan, Y. Z., Dyks, J., Kobayashi, S., and Mészáros, P., e. a. (2006). Physical Processes Shaping Gamma-Ray Burst X-Ray Afterglow Light Curves: Theoretical Implications from the Swift X-Ray Telescope Observations. *APJ*, 642:354–370.

Zhang, B. and Mészáros, P. (2002). Gamma-Ray Burst Beaming: A Universal Configuration with a Standard Energy Reservoir? *APJ*, 571:876–879.

Zhang, B. and Yan, H. (2011). The Internal-collision-induced Magnetic Reconnection and Turbulence (ICMART) Model of Gamma-ray Bursts. *APJ*, 726:90.

Zhu, S., Bissaldi, E., Racusin, J., Sonbas, E., Kocevski, D., and Yassine, M. (2015). GRB 150210A: Fermi-LAT detection. *GRB Coordinates Network*, 17438.

List of Tables

List of Figures

Résumé

Les sursauts gamma (GRBs pour "Gamma-Ray Bursts" en anglais) sont de bréves bouffées trés énergétiques de rayonnement de haute énergie qui sont émises sur de courtes échelles de temps (fraction de seconde à plusieurs minutes). L'émission intense des sursauts gamma à haute énergie est supposée provenir d'un trou noir de masse stellaire nouvellement formé, accompagné d'un vent collimaté (i.e. un jet) se propageant à vitesse relativiste. L'émission est observée suivant deux phases successives, la phase prompte trés erratique, et la phase de rémanence, moins lumineuse. Les deux instruments embarqués sur le satellite *Fermi*, le "Gamma-ray Burst Monitor" (GBM) et le "Large Area Telescope" (LAT), permettent d'étudier l'émission prompte des sursauts gamma sur une grande plage d'énergie (de ∼10 keV à ∼100 GeV). L'objectif principal de ma thése est l'analyse et l'interprétation des propriétés spectrales et temporelles de l'émission prompte des GRBs observés par *Fermi*, en particulier avec les nouvelles données du LAT (Pass 8) qui ont été rendues publiques en juin 2015.

La premiére partie de mon travail est une analyse spectrale résolue en temps de la phase prompte du sursaut GRB 090926A avec les données du GBM et du LAT. Mes résultats confirment avec un meilleur niveau de confiance la présence d'une cassure spectrale à ∼400 MeV, qui est observée en coincidence avec un pic d'émission trés court. Ils révélent que cette atténuation spectrale est présente durant toute l'émission prompte du sursaut, et que l'énergie de cassure augmente jusqu'au GeV. L'interprétation de la cassure spectrale en termes d'absorption gamma ou de courbure naturelle du spectre d'émission Compton inverse (CI) dans le régime Klein-Nishina fournit des contraintes fortes sur le facteur de Lorentz du jet. Mes résultats conduisent en outre à des rayons d'émission R $\sim 10^{14}$ cm qui sont compatibles avec une origine interne de l'émission du keV au GeV au-dessus de la photosphére du jet.

La seconde partie de mon travail est une exploration du modéle de chocs internes développé par des collaborateurs à l'Institut d'Astrophysique de Paris (IAP). Ce modéle simule la dynamique du jet et les processus d'émission (synchrotron et CI) d'une population d'électrons accélérés aux chocs. J'ai simulé la réponse instrumentale de *Fermi* à un sursaut synthétique fourni par ce code numérique, et j'ai construit une fonction paramétrique qui peut être utilisée pour ajuster le modéle aux spectres de sursauts du keV au MeV. J'ai appliqué cette fonction avec succés à un échantillon de 64 sursauts brillants détectés par le GBM. J'ai aussi confronté le modéle de l'IAP au spectre d'émission prompte de GRB 090926A. Mes résultats montrent un bon accord, et j'ai identifié quelques pistes pour les améliorer. Les spectres synthétiques sont plus larges que tous les spectres dans l'échantillon du GBM. En conséquence, je discute briévement quelques pistes de développements théoriques qui pourraient améliorer l'accord du modéle avec les observations, ainsi que des avancées observationnelles attendues dans le futur.

Mots clés: sursauts gamma - émission prompte - opacité γ à la création de paires - facteur de Lorentz du jet - émissions synchrotron et inverse Compton - satellite *Fermi*

Abstract

Gamma-Ray Bursts (GRBs) are very energetic and brief flashes of high-energy radiations which are emitted in a short time scale (fraction of a second to several minutes). The GRB bright emission is thought to be powered by a newly formed stellar-mass black hole that is accompanied by a collimated outflow (i.e. a jet) moving at a relativistic speed. The emission is observed as two successive phases: the highly variable "prompt" phase and the late and less luminous "afterglow" phase. The two instruments on board the *Fermi* space telescope, the Gamma-ray Burst Monitor (GBM) and the Large Area Telescope (LAT), allow the study of GRB prompt emission over a broad energy range (from ∼10 keV to ∼100 GeV). In June 2015, a new set of LAT data (Pass 8) was publicly released, which were generated using improved algorithms of reconstruction and classification of γ-ray events. The main goal of my thesis is the analysis and interpretation of the spectral and temporal properties of the prompt emission phase of the GRBs observed by *Fermi*, especially using LAT Pass8 data.

In the first part of my work, I performed a detailed time-resolved spectral analysis of the prompt phase of GRB 090926A with GBM and LAT data. My results confirm with a greater significance the spectral break at ∼400 MeV that is observed during a short spike, and they also reveal the presence of a spectral attenuation throughout the GRB prompt emission, as well as an increase of the break energy up to the GeV domain. I interpreted the spectral break in terms of γ-ray absorption or as a natural curvature of the inverse Compton (IC) emission in the Klein-Nishina regime. Strong constraints on the jet Lorentz factor were obtained in both scenarios. My results lead also to emission radii R $\sim 10^{14}$ cm, which are consistent with an internal origin of both the keV-MeV and GeV prompt emissions above the jet photosphere.

The second part of my work is an exploration of the internal shock model that has been developed by collaborators at the "Institut d'Astrophysique de Paris" (IAP). This model simulates the GRB jet dynamics and the radiations (synchrotron and IC processes) from a population of shock-accelerated electrons. I simulated the response of the *Fermi* instruments to the synthetic GRB spectra provided by this numerical code. From these simulations, I built a new parametric function that can be used to fit the keV-MeV spectra of GRBs with the model. I applied successfully this function to a sample of 64 GBM bright GRBs. I confronted also the IAP model to the prompt emission spectrum of GRB 090926A. I obtained a relatively good agreement and I identified a couple of solutions that may improve it. The synthetic spectra are wider than any GRB spectra in the GBM sample. I present some theoretical developments that could improve the data-model agreement in the future, and I discuss possible advances from future GRB missions as well.

Keywords: gamma-ray bursts - prompt emission - γ-ray opacity to pair creation - jet Lorentz factor - radiations synchrotron and Compton inverse - *Fermi* gamma-ray space telescope